

Ministry of Education and Science of the Russian Federation
Saint Petersburg National Research University of Information
Technologies, Mechanics, and Optics

NANOSYSTEMS:
PHYSICS, CHEMISTRY, MATHEMATICS

2014, volume 5(6)

Наносистемы: физика, химия, математика

2014, том 5, № 6



NANOSYSTEMS:

PHYSICS, CHEMISTRY, MATHEMATICS

ADVISORY BOARD MEMBERS

Chairman: V.N. Vasiliev (*St. Petersburg, Russia*),
V.M. Ievlev (*Voronezh*), P.S. Kop'ev (*St. Petersburg, Russia*),
V.N. Parmon (*Novosibirsk*), A.I. Rusanov (*St. Petersburg, Russia*).

EDITORIAL BOARD

Editor-in-Chief: N.F. Morozov (*St. Petersburg, Russia*)
Deputy Editor-in-Chief: I.Yu. Popov (*St. Petersburg, Russia*)

Section Co-Editors:

Physics – V.M. Uzdin (*St. Petersburg, Russia*),
Chemistry, material science – V.V. Gusarov (*St. Petersburg, Russia*),
Mechanics – A.K. Belyaev (*St. Petersburg, Russia*),
Mathematics – I.Yu. Popov (*St. Petersburg, Russia*).

Editorial Board Members:

V.M. Adamyan (*Odessa, Ukraine*); O.V. Al'myasheva (*St. Petersburg, Russia*); S. Bechta (*Stockholm, Sweden*); V.G. Bepalov (*St. Petersburg, Russia*); A. Chatterjee (*Hyderabad, India*); S.A. Chivilikhin (*St. Petersburg, Russia*); A.V. Chizhov (*Dubna, Russia*); P.P. Fedorov (*Moscow, Russia*); E.A. Gudilin (*Moscow, Russia*); D.A. Indeitsev (*St. Petersburg, Russia*); H. Jónsson (*Reykjavik, Iceland*); A.A. Kiselev (*Madison, USA*); Yu.S. Kivshar (*Canberra, Australia*); S.A. Kozlov (*St. Petersburg, Russia*); Yu.B. Kudasov (*Sarov, Russia*); S.E. Kul'kova (*Tomsk, Russia*); P.A. Kurasov (*Stockholm, Sweden*); A.V. Lukashin (*Moscow, Russia*); V.A. Margulis (*Saransk, Russia*); I.V. Melikhov (*Moscow, Russia*); G.P. Miroshnichenko (*St. Petersburg, Russia*); H. Neidhardt (*Berlin, Germany*); K. Pankrashkin (*Orsay, France*); B.S. Pavlov (*Auckland, New Zealand*); A.V. Ragulya (*Kiev, Ukraine*); V. Rajendran (*Tamil Nadu, India*); A.A. Rempel (*Ekaterinburg, Russia*); V.P. Romanov (*St. Petersburg, Russia*); V.Ya. Rudyak (*Novosibirsk, Russia*); V.M. Talanov (*Novocherkassk, Russia*); A.Ya. Vul' (*St. Petersburg, Russia*).

Editors:

I.V. Blinova; A.I. Popov; A.I. Trifanov; E.S. Trifanova (*St. Petersburg, Russia*),
R. Simoneaux (*USA*).

Address: University ITMO, Kronverkskiy pr., 49, St. Petersburg 197101, Russia.

Phone: +7(812)232-67-65, **Journal site:** <http://nanojournal.ifmo.ru/>,

E-mail: popov1955@gmail.com

AIM AND SCOPE

The scope of the journal includes all areas of nano-sciences. Papers devoted to basic problems of physics, chemistry, material science and mathematics inspired by nanosystems investigations are welcomed. Both theoretical and experimental works concerning the properties and behavior of nanosystems, problems of its creation and application, mathematical methods of nanosystem studies are considered.

The journal publishes scientific reviews (up to 30 journal pages), research papers (up to 15 pages) and letters (up to 5 pages). All manuscripts are peer-reviewed. Authors are informed about the referee opinion and the Editorial decision.

Content

PHYSICS

- M.R. Mohebbifar, M. Ahmadi daryakenari,
G. Mosallanezhad, M. Zohrabi
Effect of the elimination of the barrier layer period in productive process and its simulation of absorption spectra for anodic alumina membrane 737
- S.Kh. Batygov, M.N. Mayakova, S.V. Kuznetsov, P.P. Fedorov
X-ray luminescence of BaF₂:Ce³⁺ powders 752
- P.F. Bessarab, A. Skorodumov, V. M. Uzdin, H. Jónsson
Navigation on the energy surface of the noncollinear Alexander-Anderson model 757
- A.A. Bogdanov, S.P. Denisov, A.A. Karetnikov,
A.P. Kovshik, V.P. Romanov, D. Brukkel
The effect of the cell phone radiation on a freely suspended liquid-crystal film 782
- V.F. Gremenok, V.A. Ivanov, H. Izadneshan,
V.V. Lazenka, A. Bakouie
Physical properties of hot wall deposited Sn_{1-x}Pb_xS thin films 789
- M.A. Jafarov, E.F. Nasirov, R. Mammadov, R. Jafarli
Fabrication and Characterization ZnCdS nanowire 796
- A.V. Kalenskii, M.V. Ananyeva
Spectral regularities of the critical energy density of the pentaerythriol tetranitrate- aluminum nanosystems initiated by the laser pulse 803
- V.V. Zakharov, M.A. Baranov, A.S. Zlatov, A.V. Veniaminov
Measuring local quantum yield of photoluminescence and phototransformations with laser scanning microscope 811

CHEMISTRY AND MATERIAL SCIENCE

- Bassem Assfour, Thaer assaad, adnan odeh
Hydrogen adsorption properties of metal-organic frameworks within the density-functional based tight-binding approach 820
- Jun Li, Zhen Hu, Yuanjun Song, Yudong Huang, V.V. Zuev
New route to poly (2, 6 – diimidaazo (4,5-b: 4',5' - e) pyridinylene-1,4 (2,5-dihydroxy)-phenylene) (pipd) and high modulus fiber on it basis 829
- N.A. Lomanova
Dielectric properties of Aurivillius phase $\text{Bi}_{10}\text{Fe}_6\text{Ti}_3\text{O}_{30}$ with a nano-sized pseudo-perovskite blocks 836
- Sidheshwar G. Gaurkhede
Synthesis and studies room temperature conductivity, dielectric analysis of LaF_3 nanocrystals 843
- V.V. Sokolov, N.A. Petrov, M.V. Tomkovich, V.V. Gusarov
Porous structure of carbon nanoparticles prepared by chlorination of nanoparticles of silicon carbid 849
- E.A. Tugova, O.N. Karpov
Nanocrystalline perovskite-like oxides formation in $\text{Ln}_2\text{O}_3 - \text{Fe}_2\text{O}_3 - \text{H}_2\text{O}$ ($\text{Ln} = \text{La}, \text{Gd}$) systems 854
- Information for authors** 861

EFFECT OF THE ELIMINATION OF THE BARRIER LAYER PERIOD IN PRODUCTIVE PROCESS AND ITS SIMULATION OF ABSORPTION SPECTRA FOR ANODIC ALUMINA MEMBRANE

M. R. Mohebbifar^{1,*}, M. Ahmadi daryakenari², G. Mosallanezhad³, M. Zohrabi¹

¹Institute of Physics, Optics and Nanophotonics Department, Kazan Federal University, Kazan, Russia

²Kazan National Research Technological University, Kazan, Russia

³Faculty of Electrical and Computer Engineering, University of Sistan and Baluchestan, Zahedan, Iran

mmohebbifar@gmail.com

PACS 78.66.Bz , 81.05.Bx

An anodic alumina membrane is produced in two levels by performing the anodization process in various type of acidic electrolyte. Holes are characterized by hexagonal structure of varying diameters (from 40 to 420 nm). The heat and chemical stability as well as the regularity of the formed holes make the membranes appropriate for use in gas separating process, drug delivery and for fuel cell membrane applications. Detachment of the membrane from the aluminum base is the most important step in the membrane production process. In this research, initially, the synthesis of the aluminum based layer omitted the use of CuSO_4 and HCl . In the second step, the barrier layer at the end of the holes was removed via treatment with an aqueous phosphoric acid solution. The aim of this work is to analyze the effect of time upon the barrier layer removal process and, assuming that we have added gold to the alumina membrane, i.e. the alumina membrane has its empty pores filled with gold, simulations were done in order investigate its absorption spectra. Simulations were done using the FDTD method for all structures evaluated. The values for the structures' absorption and their spectra were calculated and plotted. In the case when the aluminum membrane pores are filled with gold, the curve of gold absorption spectrum has the highest absorption, so in practical terms, this means that making this membrane can have different applications.

Keywords: Anodizing, Alumina, Membrane, Absorption spectra, Removal of the barrier layer and Simulation.

Received: 4 November 2014

Revised: 27 November 2014

Final revision: 2 December 2014

1. Introduction

The initial use of anodized aluminum occurred in the last century. The anodic behavior of aluminum was intensively investigated to obtain protective and attractive films on its surface. Currently, anodizing is defined as an electrochemical process of converting metal (usually aluminum) to metal oxide on the metal surface. The electrochemical anodizing cell consists of a cathode, an anode (the metal substrate to be converted to metal oxide) and a

direct current (DC) power supply. The anodic aluminum oxide thin film starts to grow at the anode (aluminum surface) as the anodic current or voltage is applied [1, 2].

An anodic alumina membrane (AAM) can provide a simple template for the deposition and growth of various materials with ordered structure. A new bi-level method of anodizing for the synthesis of porous aluminum oxide with regular structure in oxalic acid was invented by H. Masuda in 1995 [3]. Since then, scientists have tried to discover new ways to synthesize this structure with different features.

The success of anodic alumina membrane is owed to its attractive physical and chemical properties: its ceramic temperament involves high thermal strength (up to several hundred degrees) and excellent chemical insensitivity in many environments (within the pH range of 5 to 9). It has highly-ordered nanopores with controllable and uniform dimensions arranged in a close-packed hexagonal framework. Anodic alumina membranes with pore diameters ranging from 4 nm to 420 nm, density as high as 10^{11} pores/cm², and film thickness variable from 0.1 μm to 300 μm has been obtained using two-step anodization or nanoimprint methods. These materials can be synthesized in slightly soluble electrolytes such as sulfuric, phosphoric and oxalic acids [4, 5].

The synthesis of nanomaterials such as polymeric nanowire, metallic nanowire [6], 3D nanodots [7], polymeric [8] and metallic nanotubes [9] and others provides many potential research directions for anodic alumina membrane, also because it can be used as membrane in various applications such as gas separation [10], drug delivery [11], membrane in solid acid fuel cell [12] and solar cells [13].

A key difficulty encountered in the above-mentioned applications is how to attain through-hole porous anodic alumina which is previously produced on an alumina barrier layer covering aluminum substrate in the anodization process. Wet chemical etching, based on H_3PO_4 , is commonly viewed as the most reliable method for custom pore opening of AAM [14, 15]. The difficulty of this method is that the process of pore opening is controlled by the etching time, usually from 50–90 minutes. Different etching conditions such as concentration of H_3PO_4 (5–10 wt %), temperatures (25–50°C) have been reported for pore opening of AAM, but there are no details on how these variations affect the pore diameters of AAM [14,15]. One aim of this work is to analyze the effect of time on the barrier layer removal process. Another aim is to perform simulations assuming that gold has been added to the membrane, i.e. the empty pores are filled with gold, in order investigate its absorption spectra. The morphological modifications were monitored by Scanning Electron Microscopy (SEM) and Clemex software.

A hemispherical shell with homogeneous thickness known as the barrier layer develops at the bottom of every nanopore during the anodization process. To date, this barrier layer has not attracted much attention in the literature, even though many applications require its removal to create through-hole membranes. Examples for such applications include energy-efficient gas separation and pattern-transfer masks for e-beam evaporation,[16] reactive ion etching,[17] or molecular-beam epitaxial growth.[18] Through a carefully controlled barrier layer etching process, one can systematically prepare a tunable pore opening. Three methods have been used to open the barrier oxide layer: wet chemical etching,[3,20] ion milling,[19] and plasma etching.[17] Of these, the wet etching has been regarded as difficult to control and only ion milling has received more detailed analysis in the literature.[19] Both ion milling and plasma etching have the advantage of maintaining intact pores after barrier layer removal, but require expensive equipment, and a typical setup allows only a small area around 1 x 1 mm to be removed at any given time and, thus, they are cost- and time-intensive. Wet chemical etching, when properly controlled, can be used to etch samples with larger dimensions (for

example, 2 x 2 cm) and is fast, convenient, inexpensive, and reliable. This method has been used routinely in our laboratory for opening the barrier layers of AAO membranes. Experimental results show that if the chemical etching is done with proper control, 10–95 nm openings in the barrier layer can be obtained systematically for AAO membranes generated in oxalic acid. In addition, very interesting double hexagon nanostructures were observed for the first time through AFM imaging before complete removal of the barrier layer. These nanostructures reveal the impurity distribution in the membranes that bear significant implication for catalysis and sensing applications [21].

During anodization, a U-shaped aluminum oxide layer or barrier layer with a thickness of 30–40 nm forms at the bottom of every nanopore. A protective polymer layer made of a mixture of nitrocellulose and polyester resin was coated on the top surface of the AAO membrane that is opposite to the barrier layer to prevent overetching of the surface structure and uneven diffusion of acid into the nanopores.[22]

2. AAO Barrier Layer

2.1. AAO Barrier Layer Opening

In addition, the membrane was then immersed in 200 mL of 5.00 wt% phosphoric acid at 30.0°C for different periods of time, rinsed with distilled water, and dried under ambient conditions. The barrier layer removal and pore widening process was then studied with use of atomic force microscopy (AFM) (Digital Instruments, Dimension 3000 with a type IIIa controller and TESP Si cantilevers) and SEM (Hitachi S-4700-II). Effective pore diameters were determined by analyzing the total pore area of each image using Scion Image based on NIH Image to ascertain the average area per pore and, hence, the average pore diameter [21].

This study utilizes a freestanding anodic aluminum oxide (AAO) film with a protective polymer layer made of a mixture of nitrocellulose and polyester resin on the porous side of the film [22]. The polymer layer is used to block the pores and thus prevent uneven etching of the AAO barrier layer from inside, which may be caused by the uneven acid diffusion through the AAO pores. The presence of the protective layer also focuses the etching process on the bottom side of the barrier layer, which is comprised of a hexagonally close packed array of hemispherical domes that are 120 nm in diameter and 27 nm in height (Fig. 1a). The domes begin to shrink both in diameter and height once the etching process starts. After 18 min of etching, the domes have decreased in size to approximately 100 nm in diameter and 24 nm in height (Fig. 1b). It is interesting to note that, at this early stage of the etching process, the walls of each individual cell are becoming more pronounced, which suggests that the area in-between individual domes is not etched as quickly as the domes themselves. This trend continues through 30 min of etching, with the domes continuing to decrease in size (85 nm in diameter and 16 nm in height) and the hexagonal cell walls becoming clearly visible to form a double hexagon nanostructure (Fig. 1c). After 40 min of etching, the barrier layer is finally breached by the acid (Fig. 1d). Note that the initial opening is uneven across the surface. The majority of the cells have an opening of ~10 nm, while some of the cells remain closed. While the aluminum surface used to create the AAO membrane was annealed and electropolished before anodization, the surface still maintains a certain degree of roughness. This roughness translates into a subtle variation in the thickness of the barrier layer [23]. Those domes that are thinner would obviously be etched through earlier. It should also be noted that the walls of each individual cell have become distinct enough to completely encircle each dome. Once the domes have been breached initially, the openings

begin to widen to generate a unique surface topography which combines a hexagonal cell wall surrounding each opened dome. This process can be used to create membranes with a wide range of pore diameters with fixed pore-to-pore distance, from sub-10 nm, to 34 nm, to 48 nm, and to 70 nm just by terminating the etching process at 40, 50, 60, and 70 min, respectively (Figs. 1d-1f and Fig. 2a). The pronounced hexagonal walls persist through the entire procedure, even after the barrier layer has been completely removed at 70 min of etching [21].

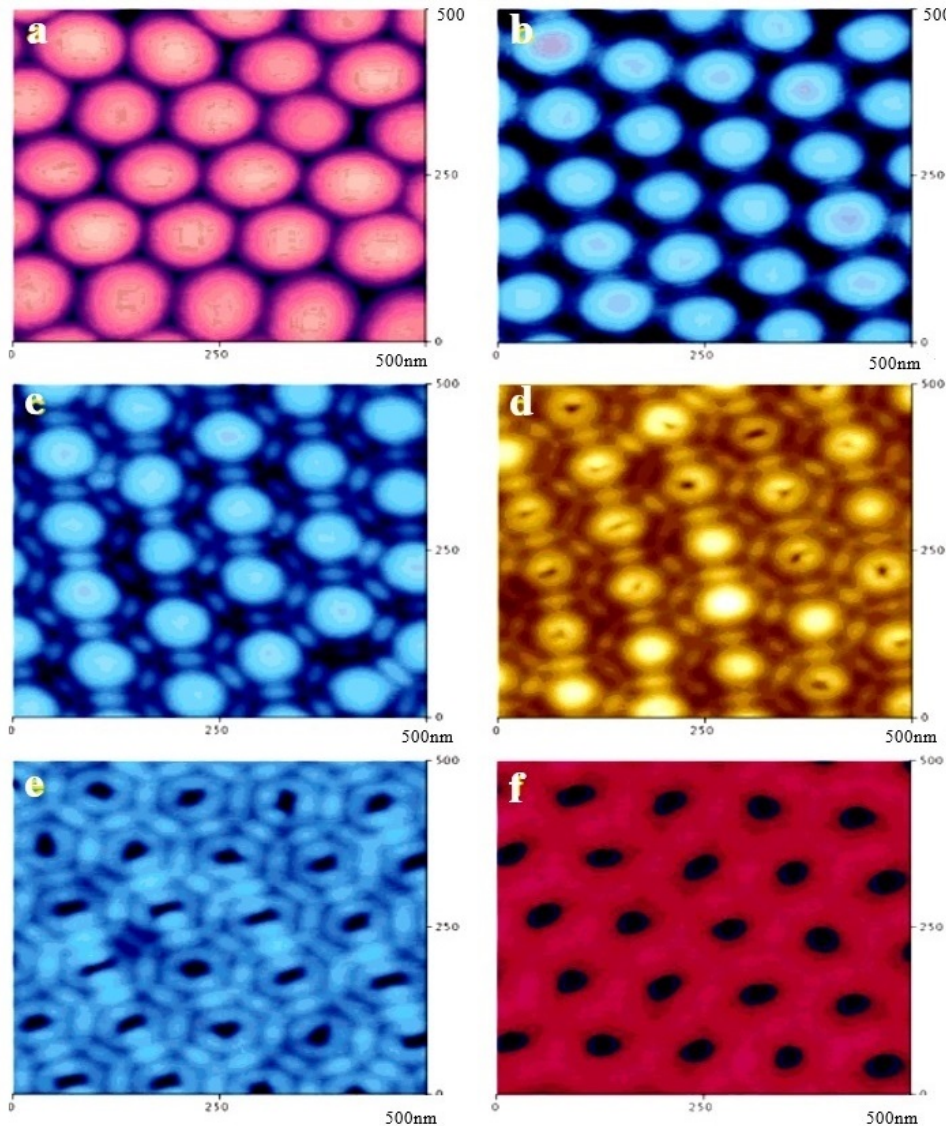


FIG. 1. Stages of chemical etching process of the anodic aluminum oxide barrier layer. Etching progress after (a) 0 min, (b) 18 min, (c) 30 min, (d) 40 min, (e) 50 min, and (f) 60 min [21]

Note that the two techniques give fairly consistent results, especially before the complete removal of the barrier layer. From 40 to 90 min of etching, the pore opening rate is about 1.3 nm/min, but the following pore expansion rate is much slower, at about 0.5 nm/min. This is attributed to the fact that the barrier layer is the growth front of the anodization process; [24] it is constantly building up and redissolving. This action allows the oxalate

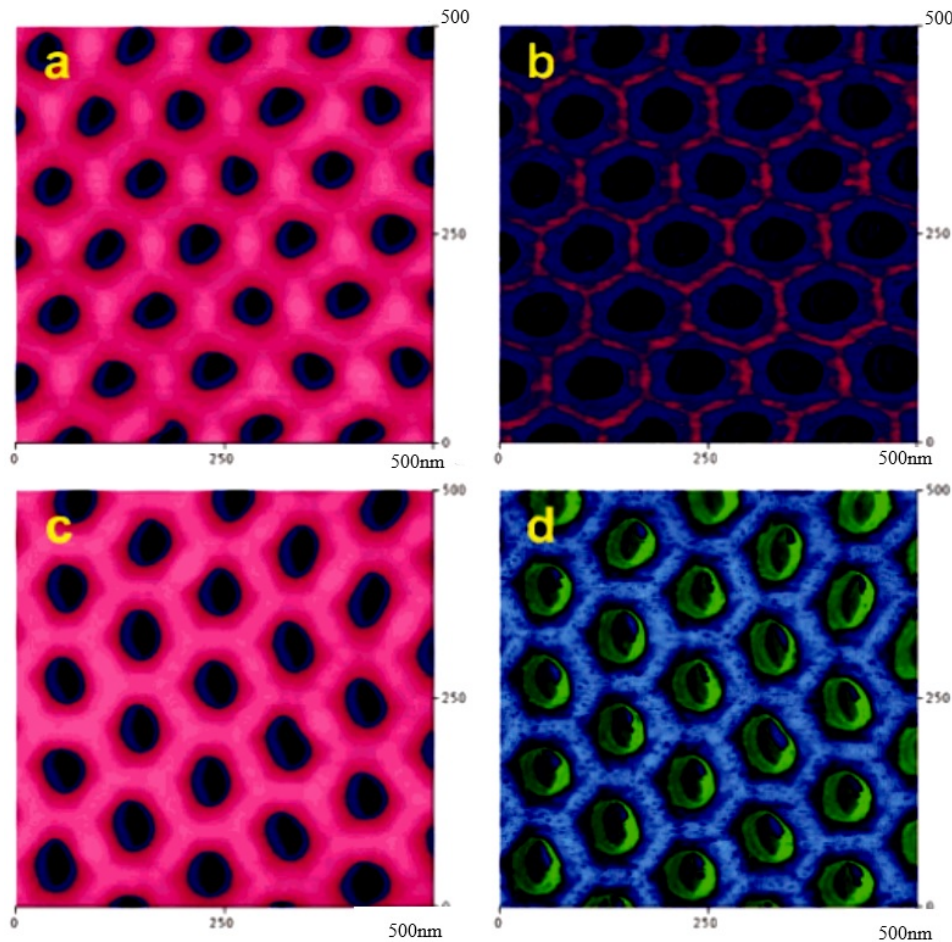


FIG. 2. AFM topography and phase images of the AAO membrane after (a and b) 70 min and (c and d) 90 min of etching

anion (Ox), $\text{C}_2\text{O}_4^{2-}$, and H_2O to be mixed with the alumina within the barrier layer, leading to a less dense composite material, Al_2O_3 mixed with $\text{Al}_2(\text{Ox})_3$ [21].

The results, as seen in Figure 3 (measured by SEM), show that there are also two different regimes. The first regime, which runs from 10 to 60 min, shows the pore diameter increasing at a rate of 0.93 nm/min, which means the cell walls are etched at a slower rate than the domes of the barrier layer (1.3 nm/min). As can be seen from Figure 3, the change in diameter versus time is fairly linear. The second regime, which begins at 60 min, has an etching rate of only 0.17 nm/min. The two different etching rates clearly indicate that the cell wall is comprised of two different material layers. Earlier studies of AAO have suggested that there is a measurable difference in the alumina of these two areas arising from the entrapment of conjugated base anions in the alumina near the pore [25].

Figures 4a and 4b show the section analyses of the AAO membranes just before (30 min etching) and after (50 min) the barrier layer was breached, respectively. The double-dip features with 25 nm separation and 2.5 nm height at the 30 min etching (Figure 4a) and 31 nm separation and 2.9 nm height at the 50 min etching (marked in Figure 4b) are clearly observed in both figures and indicate the boundary of pure alumina between the cells as depicted schematically in Figure 4c. In addition, the two types of alumina as indicated in the cell wall of Figure 4c can be observed from the AFM phase imaging technique, which is sensitive to changes in elastic modulus and surface hardness of the AAO membrane. The

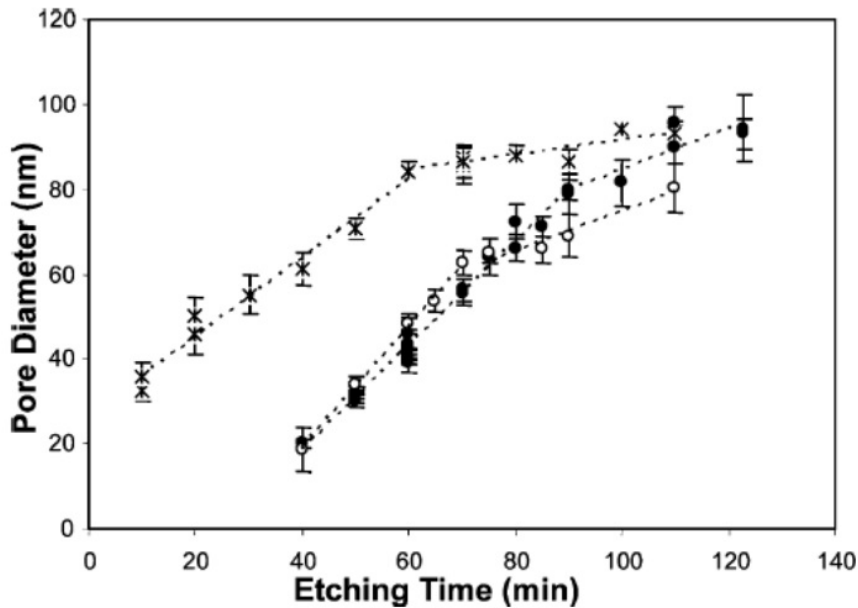


FIG. 3. Etching of the barrier side (●, SEM; ○, AFM) and front side (*, SEM) of AAO membranes in 5.00 wt % H_3PO_4 at 30.0°C

cell wall nanostructures can be observed from both topography (Figure 1c-1f) and phase imaging (not shown here). At the early etching stage (18 min, Figure 1b) and just after the barrier layer has been removed (70 min, Figure 2a), while topography imaging simply showed the actual cell size and shape, phase imaging continued to reveal the underlying cell wall nanostructures. As shown in pseudo color (Figure 2b, 70 min), the contaminated alumina is indicated with light blue next to the dark blue pore, while the pure alumina of the cell wall, which is harder than the alumina near the pore, is indicated as pink. As the pores are etched further (90 min etching, Figure 2c), this contaminated layer is quickly removed, leaving behind only the pure alumina wall indicated as blue walls in Figure 2d and empty pores in green [21].

2.2. Implications of the Barrier Layer

If the barrier layer was made of concentric layers of the same material throughout the whole curvature, the whole barrier layer should be etched away all at once under homogeneous etching without diffusion limit, which is not supported by the aforementioned observation. It is quite obvious from Figure 1d-1f that the barrier layer is first breached at the very top or center of the domes, and then the small opening is gradually enlarged and eventually the whole dome is etched away as the chemical etching process proceeds. Based on our etching results, the barrier layer cannot consist of simple concentric layers with different purities [21].

Pore opening and removal of the oxide barrier layer by wet chemical etching is the last and most critical step in the fabrication of AAO with through-hole pore morphology. The time controlled etching method is dependent on many parameters that can't provide reproducible pore diameters of fabricated AAO. The removal of the AAO barrier layer was performed using a two-half permeation cell assembled with disposable plastic cuvettes with a hole in middle of the cell (Fig. 5.) AAO is sandwiched between the two cells and sealed using flat silicon rubber with a hole that corresponds to the hole in the cuvettes. The cells were then filled, by the etching solution (5 wt % H_3PO_4) for the cell that faces AAO with

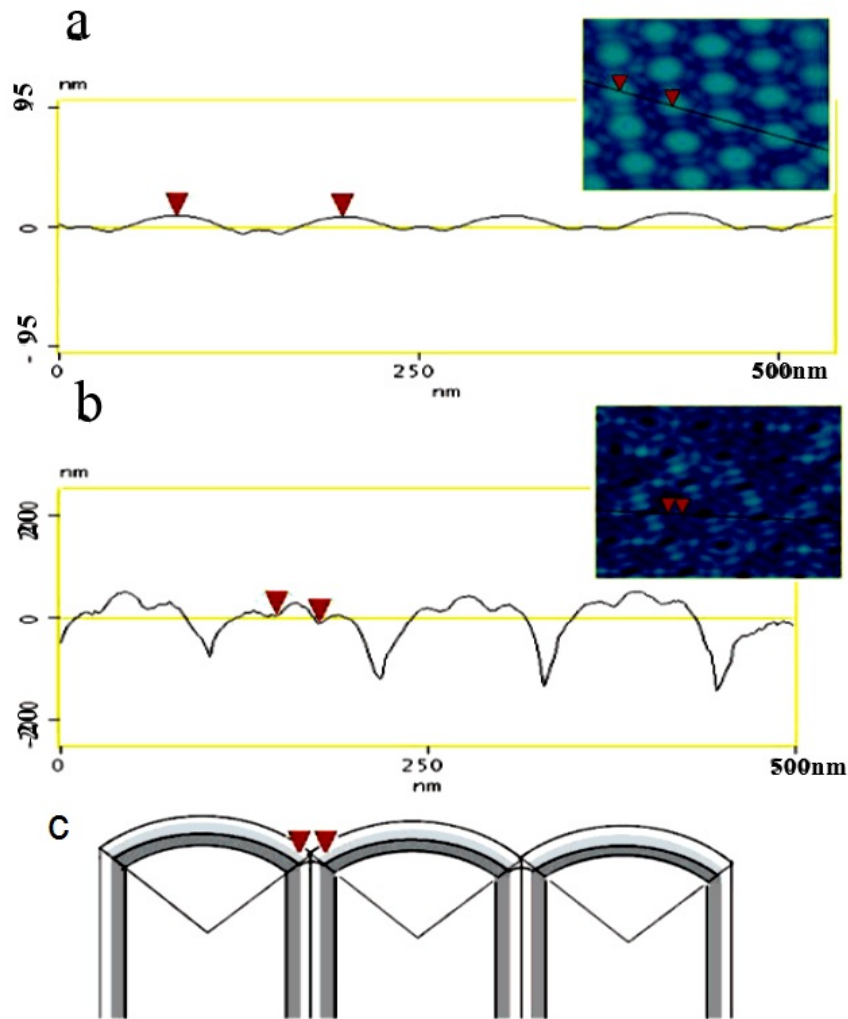


FIG. 4. (a) Section analysis of AAO membrane at 30 min etching (same sample as Figure 2c) showing a cross section of the barrier layer and the double-dip feature. (b) Section analysis of AAO membrane at 50 min etching (same as Figure 2e) showing the collapsed dome and the double-dip feature (marked with red arrows). (c) Schematic drawing of the bilayered cell wall (gray area, oxalate contaminated alumina; white, pure alumina), the barrier layer (shown with thicker oxalate contaminated layer), and the double-dip feature observed during etching

oxide barrier layer, and by KCl (0.2 M) for the second cell with front surface of AAO. A small voltage 1.5-2V is applied between two platinum electrodes immersed in both cells, and both solutions were stirred using a magnetic stirrer [26].

To investigate how structural changes during the pore opening process correlate with pore opening curves, a series of SEM images of the barrier oxide layer were taken at different time intervals representing different stages of barrier layer dissolution, and presented in Figure 4. The SEM image (Fig. 4 a) of the barrier layer after about 25 minutes of etching didn't show morphological differences in comparison with structures before etching (Fig. 2 a). Characteristic black spots seen in the middle of the cell verify that the initial dissolution process starts at the top of the convex domes of the barrier layer. These spots suggest that

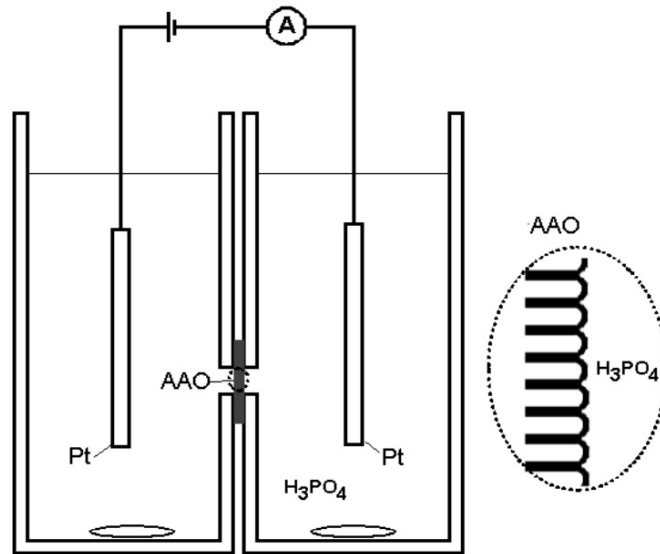


FIG. 5. Schematic diagram of the method for controlled dissolution of anodic aluminium oxide (AAO) barrier layer that combines wet chemical etching and electrochemical detection of the pore opening

the barrier layer is not homogenous and that dissolution of oxide layer is more extensive at the top than at the edge of AAO cells. Similar results are reported in previous studies describing the underlying black layer as electrolyte-rich alumina [27, 28]. A structure of the barrier layer after 42 minutes of etching or 2 min after the pore opening point was detected is shown in Figure 4 b. From the pore opening curves we expected to see very small holes in the centre of the cell as an indication of the initial pore opening and progressive dissolution of black spots. However, this initial breaching of the barrier layer was not clearly visualized by SEM images, likely due to the limitation of the SEM technique to observe structures less than 5 nm [26].

3. Materials and method

3.1. Anodic alumina membrane production

AA1057 aluminum (diameter 14 mm, thickness 0.3 mm) was used as the starting material. Active surface diameter of the samples was 10 mm. The samples were disc-shaped to minimize both the uneven electric field during Electro Polishing (EP) and anodizing, and the undesirable effects of heat treatment such as remaining stress. Before anodizing, the aluminum was degreased with acetone and then annealed at 450°C for 15 min. During the EP, the aluminum specimens were electropolished in a mixture of ethanol-perchloric acid solution (1:4) at 35V for 1 min. To speed up the anodization, a poly-ethylene chemical reactor was designed to treat 4 specimens simultaneously. The temperature of the electrolyte was maintained at $17 \pm 0.1^\circ\text{C}$ by means of isotherm Lauda circular bath (RE106). Anodic alumina membranes were prepared in a two-step anodizing process. In the first step, aluminum specimens were anodized in 0.3M oxalic acid ($\text{C}_2\text{H}_2\text{O}_4$) electrolyte 40 V and 17°C . After 15 h of anodization, the specimens were immersed in a mixture of 0.5 wt% H_3PO_4 and 0.2wt% H_2CrO_4 at 70°C for 6 h to remove the alumina layers. The aluminum specimens were then anodized again for 24 h under the same anodization conditions used previously.

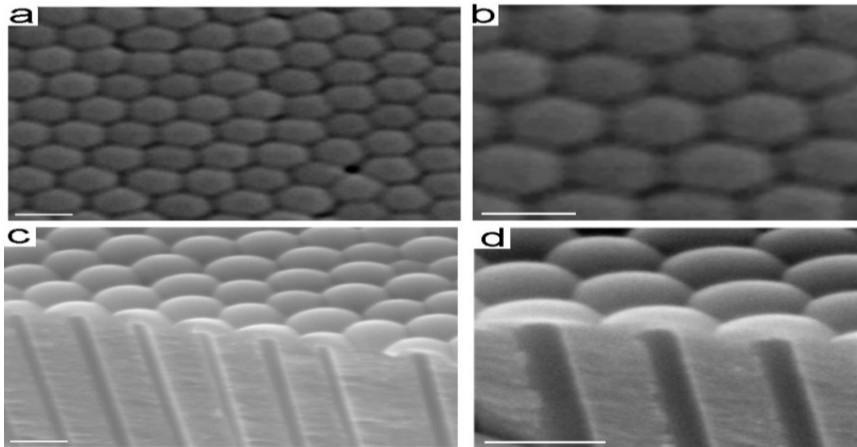


FIG. 6. SEM images of a bottom surface of anodic aluminium oxide (AAO) with the barrier film before pore opening. AAO was fabricated by anodization at 40 V, temperature -0.5°C in 0.3 M oxalic acid. a-b) Low and high-resolution image of the top topography of barrier layer with an array of highly ordered hexagonal cells. c-d) Cross-sectional images showing internal pore structure with the barrier layer at the top. Bar scale is 100 nm

The Current-Time diagram of the 2nd anodizing at different voltages was drawn using multi-meter (Lutron 801) software. The film thickness was measured by using a scanning electron microscope (SEM, XL30, Philips Company). Since the layers are fragile, they are deeply cracked when curved. Hence, the thickness of oxide layer will be observed more easily using Scanning Electron Microscopy. X-Ray Diffraction (XRD) patterns of AAM were obtained by Philips PW1140 system. Using Clemex software, the pore diameter distribution diagram, the average pore diameter and the number of pores per unit surface of samples were measured. A saturated solution of copper sulfate and perchloric acid was used for dissolving the metallic base. Then, the membrane was immersed in 100 mL of 5.00wt% phosphoric acid at 30.0°C for different periods of time (30 min, 60 min and 90 min). Finally, assuming that we have added gold to the membrane, i.e. the alumina membrane has its empty pores are filled with gold, simulations were done in order investigate its absorption spectra.

4. Simulation and results

Further recent work investigated the behavior of gold nanorod arrays coupled with a semicontinuous nanoparticle film developed using AAM substrates as templates. Nonlinear enhancement effects occurred upon plasmonic coupling and interference between a percolating Au nanoparticle film and a free standing Au nanorod array [29]. In this paper, in addition to analyzing the effect of time on the barrier layer removal process, we also performed simulations assuming that the aluminum holes are filled with gold. Simulations were done using the finite-difference time domain (FDTD) method, assuming the alumina membrane has had its empty pores filled with gold. These simulations were performed in order to evaluate the absorption spectrum. In this work, we used a structure with the following properties (Fig. 8):

1. the surface underside had the following dimensions: $X= 10.18 \mu\text{m}$ and $Y=6.2 \mu\text{m}$ depth $1 \mu\text{m}$ and was made of aluminum.
2. the structure had a total of 71 holes with depth of $0.5 \mu\text{m}$ and empty / full of gold.
3. the layer's upper surface , including the walls between the holes, is made of Al_2O_3 .

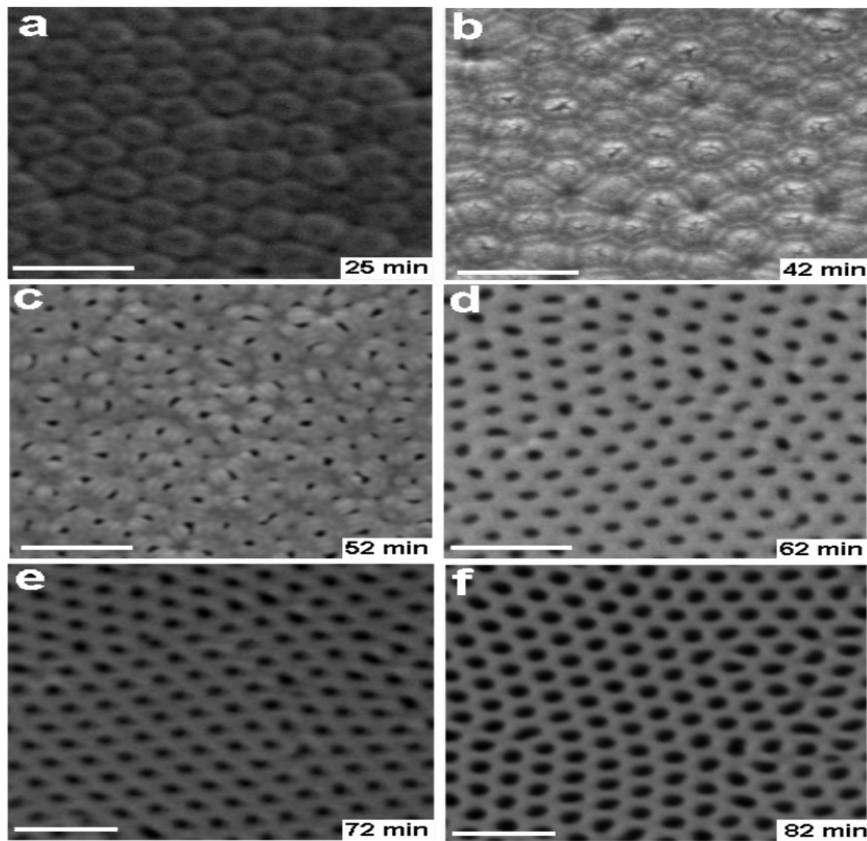


FIG. 7. Scanning electron microscopy (SEM) images of the barrier oxide layer obtained during different stages of chemical etching process of anodic aluminum oxide (AAO). AAO was fabricated by anodization in 0.3 M oxalic acid at 40 V and -0.5°C . Etching condition was 5 wt % phosphoric acid at 25°C . SEM images of barrier oxide layer after etching of a) 25 min, b) 40 + 2 min, c) 40 + 12 min, d) 40 + 22 min, e) 40 + 32 min and f) 40 + 52 min. The etching time $t = 40$ min was determined as the average pore opening point

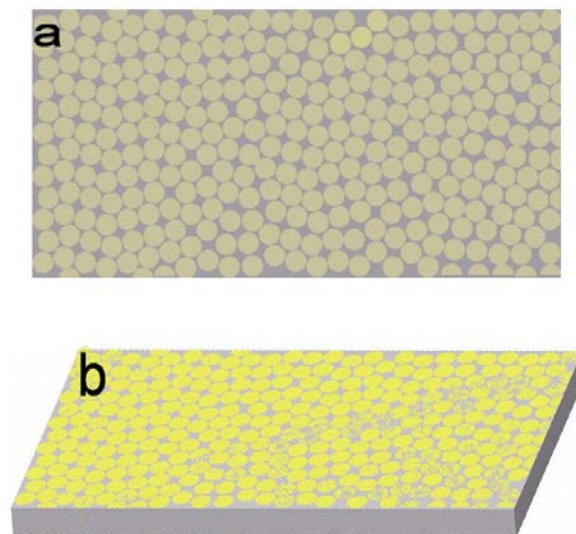


FIG. 8. Aluminum structure with empty / full of gold holes, a) in the two dimensions and b) in the three dimensions

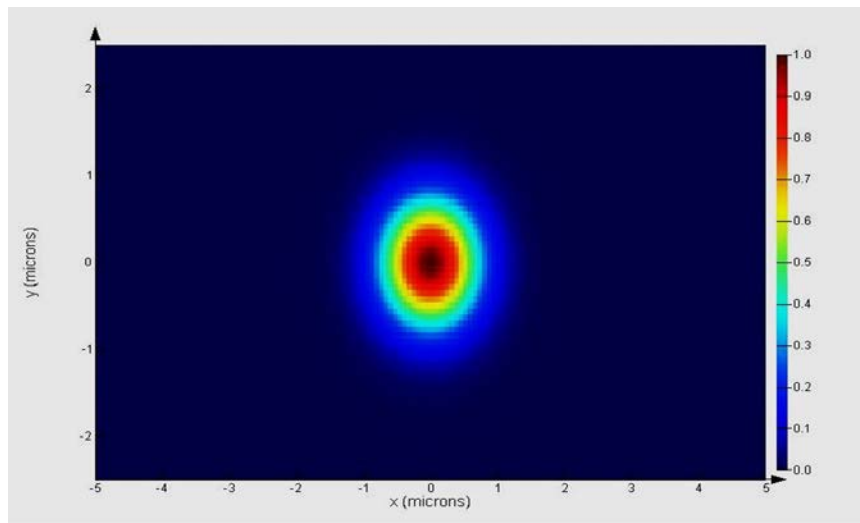


FIG. 9. Source (Aluminum structure with empty holes)[2D]

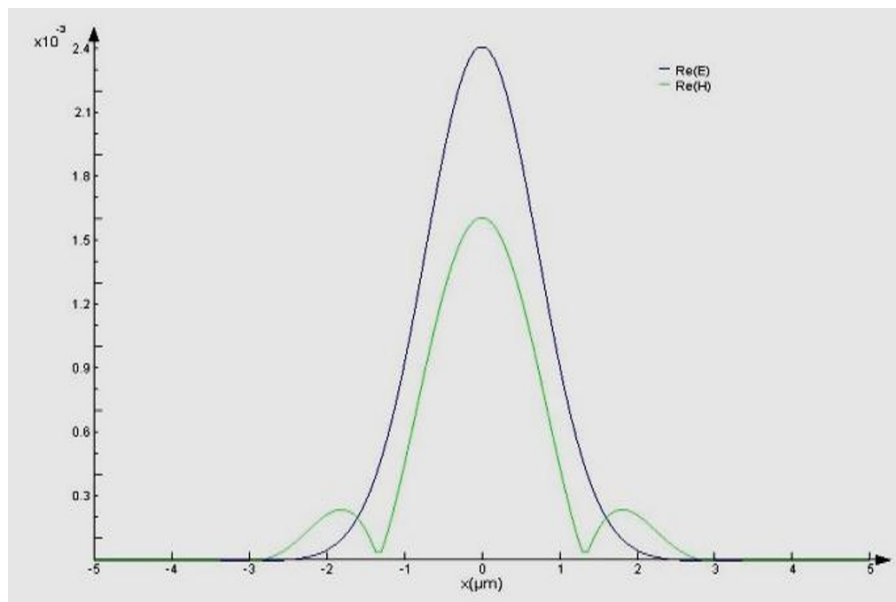


FIG. 10. Source (Aluminum structure with empty holes)[1D]

When using the FDTD method, all structures had mesh $dx=dy=dz=0.05 \mu\text{m}$ and were done with times of 100 fs. Light or Gaussian wave with domain 2, phase 0, pulse length of 45 fs, frequency of 650 THz and a radiation angle of 55° to the surface. All the boundary conditions are perfectly matched layers (PML). The magnitude of the structure's absorption and its spectrum were calculated and plotted. In the empty holes or source state (aluminum structure with empty holes), its spectrum and diagram are shown in Fig. 9 and 10, and field on the aluminum membrane surface[2D] shown in Fig. 11 and 12, also In the state where Au occupies the holes, its spectrum and diagram are shown in Fig. 13 and 14.

In the beginning of the gold absorption spectrum curve, shown in Figure 13 (Wavelengths greater than $20 \mu\text{m}$) the amount of absorption is very trivial and with a slight increase in the wavelength, the absorption increases until it reaches a maximum slightly above $22 \mu\text{m}$. After that maximum, with increasing wavelength, the absorption is reduced, finally reaching

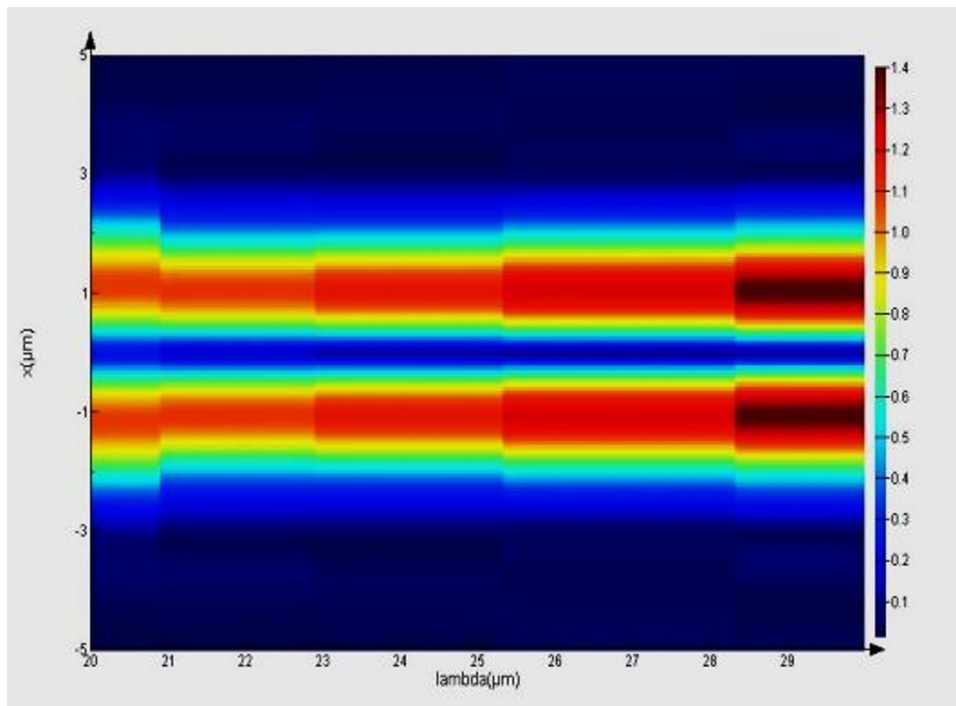


FIG. 11. Field on the Aluminum membrane surface[2D]

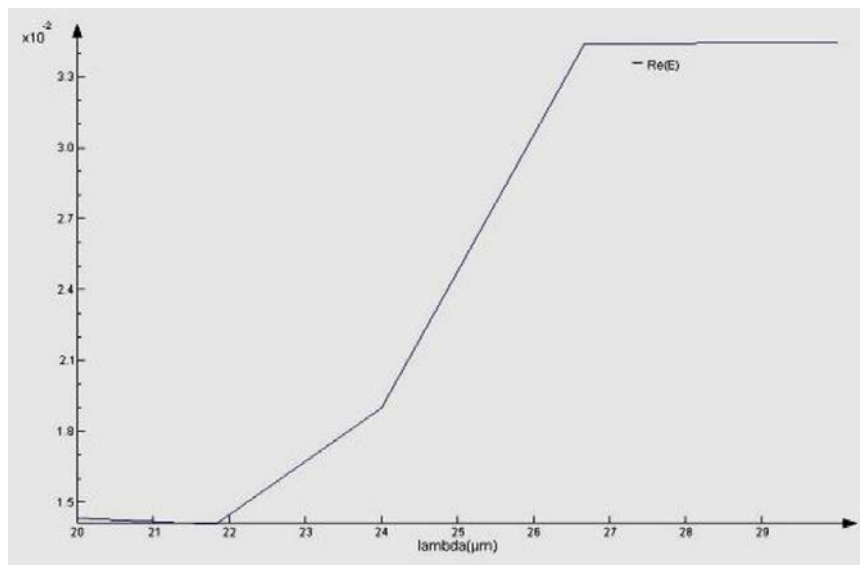


FIG. 12. Field on the Aluminum membrane surface[1D]

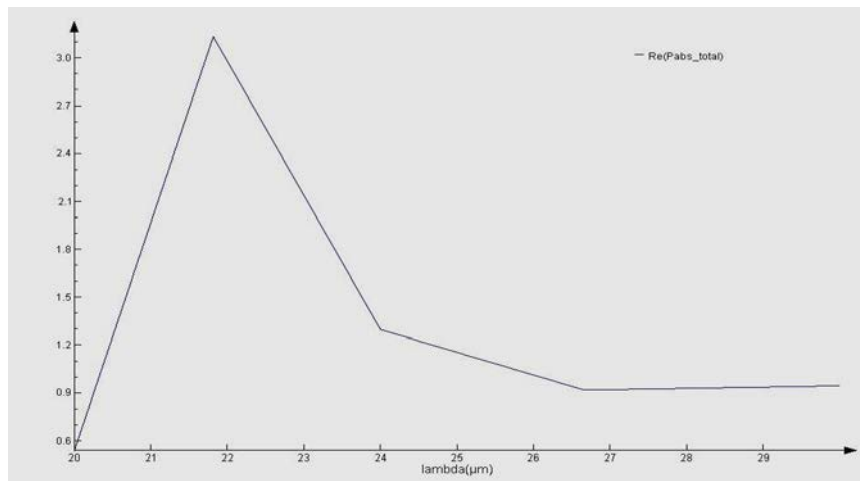


FIG. 13. Total absorption of the Aluminum membrane according to wavelength

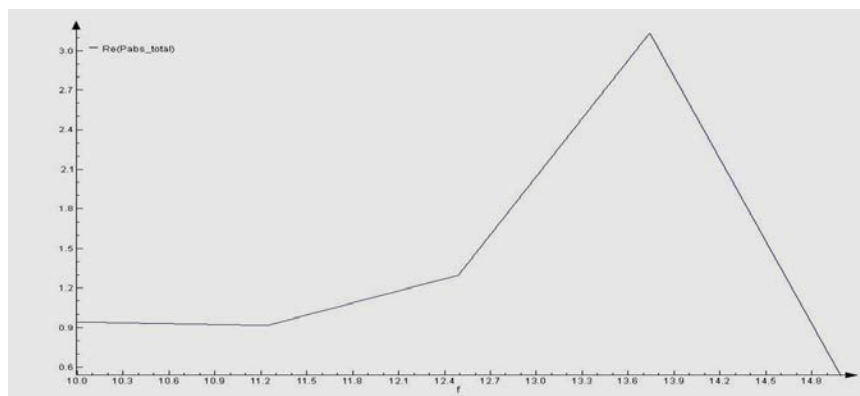


FIG. 14. Total absorption of the Aluminum membrane according to frequency

a plateau for wavelengths greater than $27 \mu\text{m}$, where the absorption values remain fairly low and constant. When comparing the curves of gold absorption spectrum, one can clearly say that in the case when the aluminum membrane pores are filled with gold, the curve of gold absorption spectrum has the highest absorption, so in practicality, this makes the membrane amenable to different applications.

5. Conclusion

Porous alumina membranes were prepared in a two-step anodizing process. In the first step, aluminum specimens were anodized. After 15 h of anodization, the specimens were immersed in a mixture for 6 h to remove the alumina layers. The 2nd anodizing at different voltages was drawn using multi-meter software. The aim of this work was to analyze the effect of time on the barrier layer removal process. Additionally, simulations were performed using the FDTD method, assuming that gold occupied the once-empty pores of the model membrane. This was done in order to investigate its absorption spectra. Adding gold to the holes of an anodic alumina membrane causes its absorption spectrum to change. We note that the absorption spectrum of an anodic alumina membrane will have the greatest absorption by the results of the simulation done when gold was added to the anodic alumina membrane.

References

- [1] F. Reidenbach, Surface Engineering, ASM International, Ohio, 124 p. (2007).
- [2] K. Itaya, S. Sugawara, K. Arai, and S. Saito. Properties of porous anodic aluminum oxide films as membranes. *Journal of Chemical Engineering of Japan*, **17**(6), P. 514–520 (1984).
- [3] H. Masuda, K. Yada and A. Osaka. Self-Ordering of Cell Configuration of Anodic Porous Alumina with Large-Size Pores in Phosphoric Acid Solution. *Japanese Journal of Applied Physics*, **37**(11A), P. 212–219 (1998).
- [4] F. Keller, M.S. Hunter, D.L. Robinson, Structural Features of Oxide Coatings on Aluminum, The Electrochemical Society, 1953, 100 (9), 411-419.
- [5] D. Crouse, Y.H. Lo, A.E. Miller, M. Crouse. Self-ordered pore structure of anodized aluminum on silicon and pattern transfer. *Appl. Phys. Lett.*, **76**(1), P. 49–51 (2000).
- [6] D.Qin , M.Lu , H.Li. Magnetic force microscopy of magnetic domain structure in highly ordered Co nanowire arrays. *Chem. Phys. Lett.*, **350**(10), P. 51–56 (2001).
- [7] T. Imai, S. Nomura. Quantum dot arrays prepared with self-organized nanopore and its photoluminescence spectra. *Physica E: Low-dimensional Systems and Nanostructures*, **21**(2), P. 1093–1097 (2004).
- [8] M. Steinhart, R.B. Wehrspohn,U. Gosele, J. Wendorff. Nanotubes by Template Wetting: A Modular Assembly System. *Chem. Int. Ed.*, **43**(9), P. 1334–1344 (2004).
- [9] J. Justin Gooding. Nanostructuring electrodes with carbon nanotubes: A review on electrochemistry and applications for sensing. *Electrochim. Acta.*, **50**(15), P. 3049–3060 (2005).
- [10] D. Gong, V. Yadavalli, M. Paulose, M. Pishko, C. Grimes. Controlled molecular release using nanoporous alumina, *Biomed. Microdevices.*, **5**(1), P. 75–80 (2003).
- [11] M. Darder, P. Aranda, M. Hernández-Vélez, E. Manova, E. Ruiz-Hitzky. Encapsulation of enzymes in alumina membranes of controlled pore size. *Thin Solid Films.*, **495**(8), P. 321–326 (2005).
- [12] P. Bocchetta, R. Ferraro, F. Di Quarto. Advances in anodic alumina membranes thin film fuel cell: CsH₂PO₄ pore-filler as proton conductor at room temperature. *Power Sources.*, **187**(11), P. 49–56 (2009).
- [13] M. J. Zheng, L. D. Zhang, G. H. Li, W. Z. Shen. Fabrication and optical properties of large-scale uniform zinc oxide nanowire arrays by one-step electrochemical deposition technique. *Chemical Physics Letters.*, **363**(3), P. 123–128 (2002).
- [14] W. Lee, R. Ji, U. Gosele, K. Nielsch. Fast fabrication of long-range ordered porous alumina membranes by hard anodization. *Nature Materials*, **5**(6), P. 741–747 (2006).
- [15] I. Vrubevsky, V. Parkoun, J. Schreckenbach, G. Marx. Study of porous oxide film growth on aluminum in oxalic acid using a re-anodizing technique. *Applied Surface Science*, **227**(4), P. 282–292 (2004).
- [16] H. Masuda, K. Yasui, Nishio. Fabrication of Ordered Arrays of Multiple Nanodots Using Anodic Porous Alumina as an Evaporation Mask. *Advanced Materials.*, **12**(14), P. 1031–1033 (2000).
- [17] J. Liang, H. Chik, A. Yin, J.J. Xu. Two-dimensional lateral superlattices of nanostructures: Nonlithographic formation by anodic membrane template. *Appl. Phys.*, **91**(12), P. 2544–2553 (2002).
- [18] X. Mei, D. Kim, H. E. Ruda, Q. X. Guo. Molecular-beam epitaxial growth of GaAs and InGaAs/GaAs nanodot arrays using anodic Al₂O₃ nanohole array template masks. *Appl. Phys. Lett.*, **81**(11), P. 361–363 (2002).
- [19] T. Xu, G. Zangari, R. M. Metzger. Periodic Holes with 10 nm Diameter Produced by Grazing Ar+ Milling of the Barrier Layer in Hexagonally Ordered Nanoporous Alumina. *Nano Lett.*, **2**(1), P. 37–41 (2002).
- [20] H. Masuda and M. Satoh. Fabrication of Gold Nanodot Array Using Anodic Porous Alumina as an Evaporation Mask. *J. Appl. Phys.*, **35**(1), P. 126–129 (1996).
- [21] Catherine Y. Han, Gerold A. Willing, Zhili Xiao, and H. Hau Wang. Control of the Anodic Aluminum Oxide Barrier Layer Opening Process by Wet Chemical Etching. *Langmuir*, **23**(3), P. 1564–1568 (2007).
- [22] T.T. Xu, R. Piner and R.S.Ruoff. An Improved Method to Strip Aluminum from Porous Anodic Alumina Films. *Langmuir*, **19**(5) P. 1443–1449 (2003).
- [23] H. Masuda, A. Abe, M. Nakao, A. Yokoo, T. Tamamura, K. Nishio, Ordered Mosaic Nanocomposites in Anodic Porous Alumina. *Adv. Mater.*, **15**(2), P. 161–164 (2003).
- [24] J. P. O’Sullivan and G. C. Wood. Proc. R. Soc. London, Ser. A. **317**(2), P. 511–519 (1970).
- [25] G. E. Thompson, and G. C. Wood. Porous anodic film formation on aluminium. *Nature*, **290**(9), P. 230–232 (1981).

- [26] Mickael Lillo, Dusan Losic. Pore opening detection for controlled dissolution of barrier oxide layer and fabrication of nanoporous alumina with through-hole morphology. *Journal of Membrane Science*, **237**(1), P. 11–17 (2008).
- [27] C. Y. Han, G. A. Willing, Z. L. Xiao, H. H. Wang. Control of the anodic aluminum oxide barrier layer opening process by wet chemical etching. *Langmuir*, **23**(3), P. 1564–1568 (2007).
- [28] J. J. Schneider, N. Engstler, K. P. Budna, C. Teichert, S. Franzka, Freestanding, highly flexible, large area, “nanoporous alumina membranes with complete through-hole pore morphology”. *European Journal of Inorganic Chemistry*, **2005**(12), P. 2352–2359 (2005).
- [29] Zhou Z-K et al. Tuning gold nanorod-nanoparticle hybrids into plasmonic fano resonance for dramatically enhanced light emission and transmission. *Nano Lett.*, **11**(1), P. 49–55 (2011).

X-RAY LUMINESCENCE OF $\text{BaF}_2:\text{Ce}^{3+}$ POWDERS

S. Kh. Batygov, M. N. Mayakova, S. V. Kuznetsov, P. P. Fedorov

A. M. Prokhorov General Physics Institute, Russian Academy of Sciences, Moscow, Russia
ppfedorov@yandex.ru

PACS 61.46

We studied the mechanism for the formation of cerium-activated barium fluoride scintillation ceramics and especially X-ray luminescence of its powdered precursors, prepared by co-precipitation of barium and cerium fluorides from aqueous solutions. We have found that the Ce^{3+} luminescence, which is typical for cerium (III)-containing ceramics and single crystals, was not observed for such polycrystalline precursors, and the intensity of barium fluoride's own luminescence decreases with increasing amounts of the cerium dopant in the specimens. We have interpreted our results as two-phase precipitation of barium hydrofluoride ($\text{BaF}_2 \cdot \text{HF}$) and cerium fluoride, respectively. Cerium (III) became incorporated in fluorite-type barium fluoride lattice only later, in the course of ceramics synthesis by the hot-pressing technique.

Keywords: Fluoride powder, nanoparticles, scintillators, X-ray luminescence.

Received: 30 October 2014

1. Introduction

The study of fluoride nanoceramics is one of the most promising areas of modern photonics [1–3], and barium fluoride is one of the most interesting and actively studied fast scintillators [3–8]. BaF_2 ceramics and single crystals exhibit two types of emission: a broad excitonic line with maximum near 300 nm (slow luminescence, $\tau = 600 - 800$ ns), and a short-wavelength line at 220 nm, corresponding to the superfast luminescence core-valence transitions ($\tau = 0.8$ ns). Addition of CeF_3 to the BaF_2 matrix leads to the transfer of exciton energy to cerium ion and powerful Ce^{3+} -luminescence at 300 – 350 nm [7, 9–12]. Because $\text{BaF}_2:\text{Ce}^{3+}$ ceramics have an enhanced scintillation yield compared to the same composition single crystals [11, 12], we have developed a technology for the further improvement of its optical quality that included precipitation of barium hydrofluoride $\text{BaF}_2 \cdot \text{HF}$ from aqueous solutions followed by its thermal decomposition with HF evolution. The latter has been found to be an active fluorinating reagent that eliminated oxygen impurities from the batch materials [13, 14]. Thus, the topic of the present paper concerns the influence of cerium doping on the synthesis of barium fluoride scintillation ceramics and its precursors.

2. Experimental

99.99 wt. % pure $\text{Ba}(\text{NO}_3)_2$, $\text{Ce}(\text{NO}_3)_3$, HF and doubly-distilled water were used as starting materials. All precipitation experiments were carried in polypropylene reactors at room temperature under air. All samples were prepared by co-precipitation from aqueous solutions [13–15]. Premixed corresponding amounts of starting 0.17 M metal nitrate solutions ($\text{Ce}/(\text{Ce}+\text{Ba})$) (molar ratios varied from 0.01 to 1%) were treated in a dropwise manner with concentrated aqueous HF under vigorous stirring. The HF content in the formed matrix solution was maintained at about 47 vol. %. Formed precipitates were additionally treated with conc. HF, decanted, thoroughly washed with doubly-distilled water and dried under air at 40 °C.

Further thermal treatment included heating of the synthesized precipitates at 10 °C/min to 550 °C followed by 1-hour annealing at the same (550 °C) temperature under air.

The phase composition of the synthesized samples was determined by X-ray diffraction analysis (Bruker D8 diffractometer, $\text{CuK}\alpha$ radiation, TOPAS software for lattice parameter calculations and profile treatment of the X-ray diffraction pattern lines). All sample X-ray-initiated luminescence spectra were recorded at room temperature (KSVU spectrometer, Cu anode, 10 kV, 10 mA).

3. Results and discussion

Typical X-ray diffraction patterns of the synthesized samples are presented in Fig. 1.

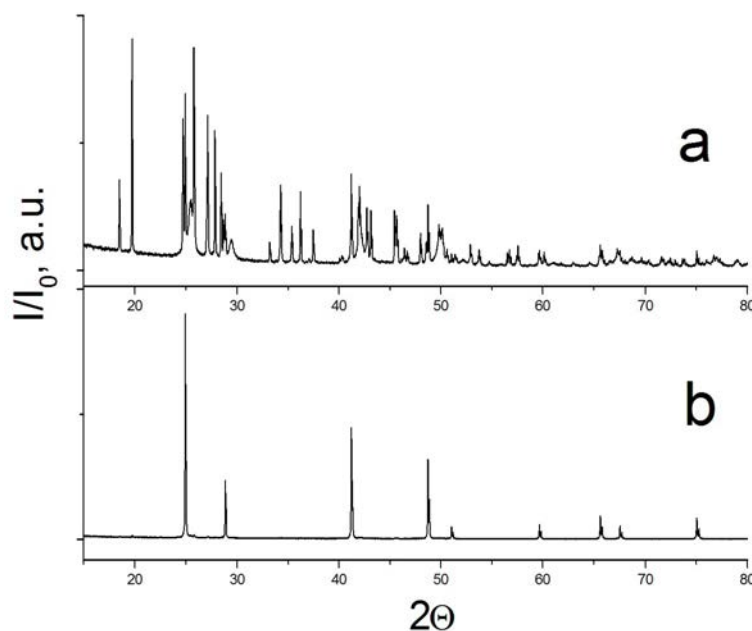


FIG. 1. Typical X-ray diffraction patterns of barium fluoride samples: monoclinic $\text{BaF}_2\cdot\text{HF}$ [13, 14] precipitated by HF from aqueous solution at room temperature (a); and the same sample after its washing with water, cubic BaF_2 (b)

All barium difluoride samples had $a_0 = 6.189 - 6.200$ Å lattice parameters that were in a good agreement with the known literature data for pure BaF_2 [15].

These precipitates did not exhibit any luminescence without additional treatment, but after annealing at 550 °C, intrinsic BaF_2 produced luminescence at 320 nm if excited by X-ray radiation (Fig. 2; for comparison, please see there a similar spectrum of monocrystalline BaF_2 , too).

Lines in both spectra have about the same maximum wavelengths (its location for the single crystals is associated with self-trapped exciton irradiation), and luminescence intensity for the powdered BaF_2 batch is comparable to that of single crystals.

The luminescence spectra for cerium-doped BaF_2 batch powders are presented in Fig. 3.

The addition of cerium to BaF_2 samples decreases the intensity of its own line at ca. 320 nm, but – in contrast with cerium-doped single crystals and ceramics – such spectra also lack of Ce^{3+} -related luminescence lines (i.e., lines attributed to Ce^{3+} ions in BaF_2 matrix) (Fig. 4).

0.1% Ce-doped ceramics and single crystals have BaF_2 -related luminescence almost completely suppressed, and the only lines visible in the luminescence spectra are those related

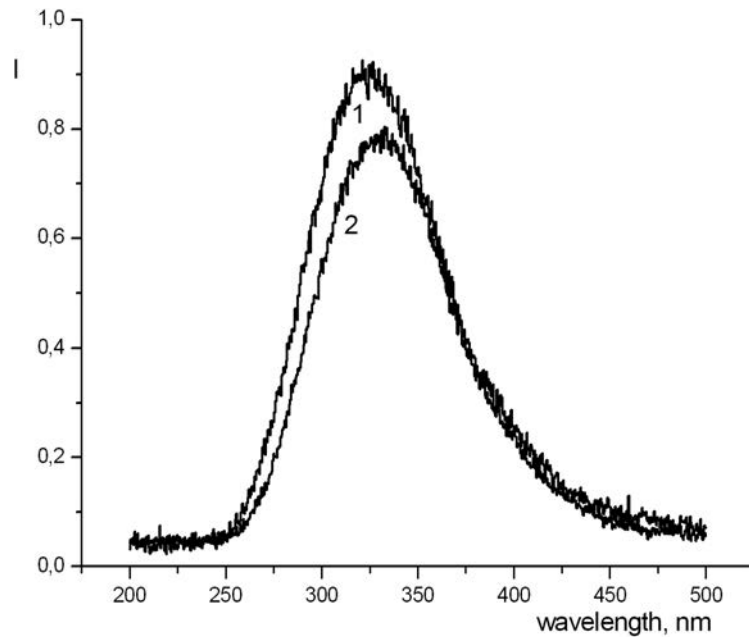


FIG. 2. X-Ray luminescence spectra of intrinsic BaF_2 : single crystal (1) and powder (2) (recorded under the same ambient conditions)

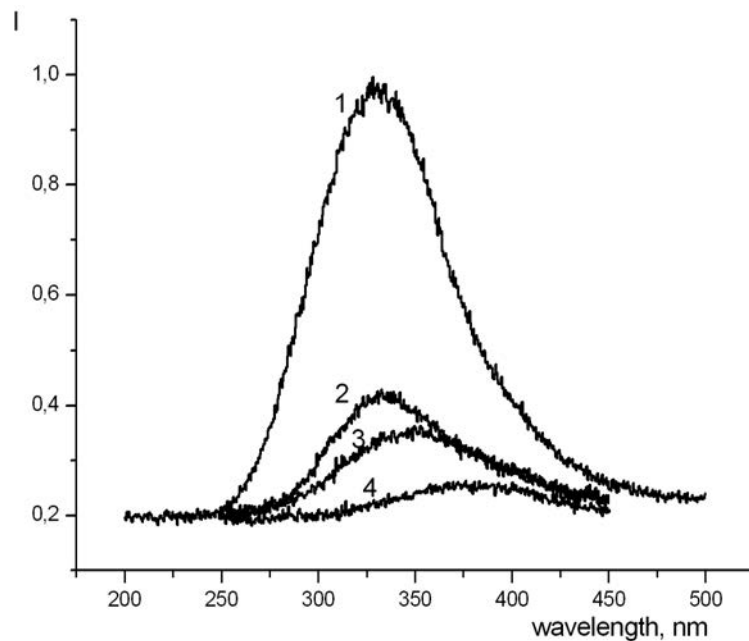


FIG. 3. Luminescence spectra of intrinsic (1) and cerium-doped BaF_2 batch powders: 0.01% Ce (2), 0.1% Ce (3), and 1% Ce (4)

to the $5d - 4f$ transitions in Ce^{3+} ions [8–12]. However, our cerium-doped BaF_2 batch samples did not exhibit such Ce^{3+} -related lines, and suppression of the BaF_2 -related luminescence line was much less than expected. Also, increasing the cerium concentration in the doped samples caused a shift of the line toward the higher wavelength part of the spectrum (Fig. 3). The negligible influence of cerium dopant on BaF_2 luminescence and lack of Ce^{3+} -related lines in

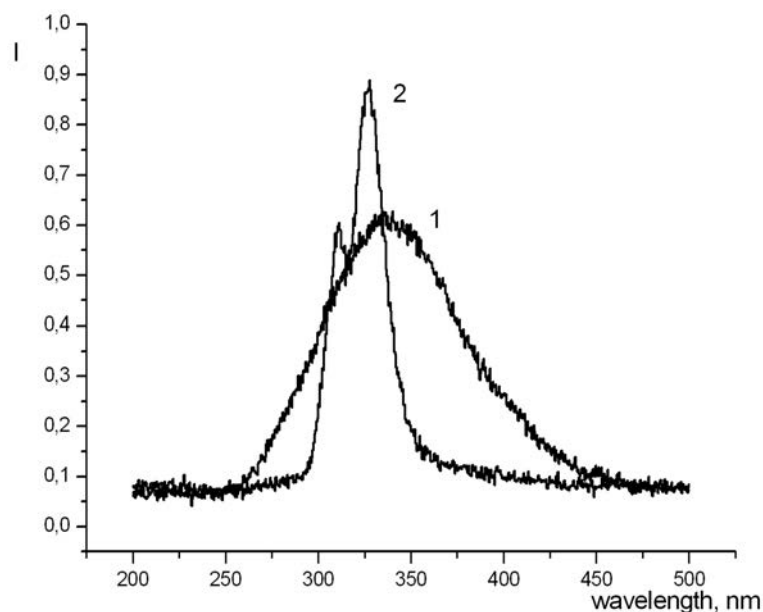


FIG. 4. X-ray luminescence spectra of polycrystalline (1) and ceramic (2) $\text{BaF}_2 - 0.1\% \text{Ce}$

the recorded spectra may indicate that cerium did not get incorporated in BaF_2 matrix during precipitation (co-precipitation) from aqueous solutions and formed an additional solid phase.

4. Conclusions

1. X-Ray radiation excitation produces luminescence at ca. 320 nm in co-precipitated barium-cerium fluoride powders, which is typical for intrinsic BaF_2 and is usually associated with the auto-localized exciton in intrinsic BaF_2 single crystals and BaF_2 ceramics (intensity of such lines for monocrystalline and polycrystalline (ceramic) BaF_2 is about the same under similar conditions).
2. Doping of BaF_2 with cerium during their co-precipitation from aqueous solutions leads to a decrease in the intensity of the BaF_2 -related luminescence line, and there is no cerium-related luminescence line observed (in contrast to the same composition $\text{BaF}_2:\text{Ce}$ ceramics or single crystals).
3. The latter indicates that co-precipitation of BaF_2 and CeF_3 from aqueous solutions results in the formation of two separate fluoride phases, and cerium only becomes incorporated in fluorite-type BaF_2 crystalline lattice only during hot-pressing ceramics synthesis.

Acknowledgements

This work was supported by the Scholarship of the President of Russian Federation (SP-6467.2013.2) and RFBR grant No. 13-02-12162-ofi-m. Authors thank V. V. Voronov and R. P. Ermakov for their help with X-ray diffraction experiments.

References

- [1] F.K. Volynets. Fabrication, structure, and physico-chemical properties of optical ceramics. *Opt. Mekh. Prom.*, **9**, P. 48–60 (1973) (in Russian).
- [2] P.P. Fedorov. Fluoride laser ceramics. In: Handbook on solid-state lasers: materials, systems and applications. Ed. by B. Denker and E. Shklovsky. Oxford Cambridge Philadelphia New Delhi, Woodhead Publishing Limited, UK, P. 82–109 (2013).

- [3] P.P. Fedorov, S.V. Kuznetsov, et al. Microstructure and scintillation characteristics of BaF₂ ceramics. *Inorganic Materials*, **50** (7), P. 738–744 (2014).
- [4] P. Schotanus, P. Dorenbos, C.W.E. van Eijk, R.W. Hollander. Recent development in scintillator research. *IEEE Trans. Nucl. Sci.*, **36** (1), P. 132–136 (1989).
- [5] M. Laval, M. Moszynski, R. Allemann. Barium fluoride-inorganic scintillator for subnanosecond timing. *Nucl. Instrum. Methods*, **206** (1), P. 169–176 (1983).
- [6] P.A. Rodnyi. Core-valence transitions in wide-band-gap ionic crystals. *Phys. Solid State*, **34** (7), P. 1975–1998 (1992).
- [7] B.P. Sobolev. *Multicomponent crystals based on heavy metal fluorides for radiation detectors*. Barcelona: Inst. d'Estudis Catalans (1994).
- [8] D.M. Seliverstov, A.A. Demidenko, et al. New fast scintillators on the base of BaF₂ crystals with increased light yield of 0.9 ns luminescence for TOF PET. *Nuclear Instruments and Methods in Physics Research A*, **695**, P. 369–372 (2012).
- [9] P. Schotanus, P. Dorenbos, C.W.E. van Eijk, and R.W. Hollander. Recent development in scintillator research. *IEEE Trans. Nucl. Sci.*, **36** (1), P. 132–136 (1989).
- [10] A.J. Wojtowicz, P. Szupryczynski, et al., Radioluminescence and recombination processes in BaF₂:Ce. *J. Phys.: Condens. Matter*, **12**, P. 4097–4124 (2000).
- [11] Kh.S. Batygov, L.S. Bolyasnikova, et al. BaF₂:Ce³⁺ scintillation ceramics. *Doklady Physics*, **53** (9), P. 485–488 (2008).
- [12] P.A. Rodnyi, S.D. Gain, et al. Spectral-kinetic characteristics of crystals and nanoceramics based on BaF₂ and BaF₂:Ce. *Phys. Solid State*, **52** (9), P. 1910–1914 (2010).
- [13] A.A. Luginina, P.P. Fedorov, et al. Synthesis of BaF₂·HF and BaF₂ from nitric solutions. *Nanosystems: Physics, Chemistry, Mathematics*, **3** (5), P. 125–137 (2012) (in Russian).
- [14] A.A. Luginina, A.E. Baranchikov, A.I. Popov, P.P. Fedorov. Preparation of barium monohydrofluoride BaF₂·HF from nitrate aqueous solutions. *Mater. Res. Bull.*, **49** (1), P. 199–205 (2014).
- [15] P.P. Fedorov, M.N. Mayakova, et al. Co-Precipitation of Yttrium and Barium Fluorides from Aqueous Solutions. *Mater. Res. Bull.*, **47**, P. 1794–1799 (2012).

NAVIGATION ON THE ENERGY SURFACE OF THE NONCOLLINEAR ALEXANDER-ANDERSON MODEL

P. F. Bessarab^{1,2}, A. Skorodumov³, V. M. Uzdin^{2,3}, H. Jónsson^{4,5}

¹ Royal Institute of Technology KTH, Stockholm, Sweden

² St. Petersburg State University, St. Petersburg, Russia

³ ITMO University, St. Petersburg, Russia

⁴ University of Iceland, Reykjavík, Iceland

⁵ Aalto University, Espoo, Finland

bessarab@kth.se, skorodumov@vingrad.ru, v_uzdin@mail.ru, hj@hi.is

PACS 05.20.Dd, 75.10.-b

Implementation of the multiple impurity, noncollinear Alexander-Anderson model is described in detail and an analytical expression given for the force which determines the orientation of the magnetic momenta as well as a corresponding magnetic force theorem. Applications to trimers of Cr, Mn and Fe adsorbed on a metal surface are described, including the energy surface as a function of the the angles specifying the orientation of the magnetic momenta and minimum energy paths for transitions between stable states, which necessarily involve noncollinear ordering. A simple model for the interaction of a magnetic STM tip with a Cr dimer on a surface is briefly described. A finite range approximation is also formulated, which simplifies the self-consistency calculations and results in linear scaling of the computational effort with the number of magnetic atoms in the system. The theoretical approach described here can be used to study magnetic systems with complex energy landscapes, including stable states and magnetic transitions in frustrated magnetic systems, over a range in length scale, from a few to several thousands of magnetic atoms.

Keywords: itinerant magnetism, Alexander-Anderson model, magnetic force theorem, noncollinear ordering, energy surface, minimum energy path.

Received: 7 November 2014

Revised: 15 November 2014

1. Introduction

Noncollinear magnetic states are of great importance, not only because the stable states of many systems are noncollinear, as has been demonstrated in recent experimental measurements of nano-scale islands [1] and thin layers [2,3], but also because magnetic systems driven out of equilibrium by some external perturbation such as a magnetic field, spin-polarized current or thermal fluctuation, as well as spin dynamics at finite temperature necessarily involve configurations where the magnetic momenta can be far from parallel to each other. In particular, a proper description of non-stationary, noncollinear magnetic states is important in studies of thermally activated magnetic transitions. Within harmonic transition state theory (TST) [4], minimum energy paths (MEPs) in a configuration space connecting stable states have to be found. Following an MEP means rotating the magnetic momenta in an optimal way so as to minimize the energy with respect to all degrees of freedom perpendicular to the path. Of particular importance for estimating the rate are the maxima along the path which correspond to first order saddle points on the energy surface. These define the activation energy for transitions between

stable magnetic states and give the temperature dependence of the transition rate. Being a path of maximal statistical weight, an MEP also gives a detailed description of the optimal transition mechanism. Even if the stable states of the system are collinear, the configurations along the MEP can be noncollinear, representing complex, non-uniform rotations of the spins [5–7].

The basic physical quantity from which most magnetic properties of an electronic system can be derived is the electron density, which becomes a 2×2 matrix in a noncollinear, spin-polarized theory:

$$\rho(\vec{r}) = \begin{pmatrix} \rho^{++}(\vec{r}) & \rho^{+-}(\vec{r}) \\ \rho^{-+}(\vec{r}) & \rho^{--}(\vec{r}) \end{pmatrix}, \quad (1)$$

where $+$ and $-$ denote the spin projections. The sum of the diagonal elements of $\rho(\vec{r})$ gives the charge density while their difference gives the projection of the spin density on the quantization axis. The off-diagonal elements of the matrix (1) determine in quasi-classical framework the components of the magnetization density perpendicular to the quantization axis. In general, at any point in space, the expectation value of magnetization density can be calculated from

$$\vec{m}(\vec{r}) = \text{Tr}_s [\vec{\sigma} \rho(\vec{r})]. \quad (2)$$

Here, $\vec{\sigma} = (\sigma_x, \sigma_y, \sigma_z)$ are the Pauli matrices and Tr_s means the trace operation in spin space. A continuous vector field of magnetization density can be calculated using, for example, density functional theory (DFT) [8–10], for many important magnetic materials including $3d$ -transition metals and rare-earth magnets. But, in most cases, the magnetization density is highly localized on atomic sites. An atomic moment approximation can then be used where the orientation of the magnetization within a region surrounding each atom is considered to be fixed and the magnetization density is assumed to be zero in the interstitial regions between the atomic sites. A magnetic configuration is then defined by a set of magnetic momentum vectors, one vector associated with each of the magnetic atoms.

A further approximation can be made based on the hierarchy of relaxation times. The relaxation of charge and magnitude of the magnetic moments is assumed to be much faster than the relaxation of the orientation of the magnetic vectors [11]. The fast degrees of freedom, charge and magnitude of magnetic moments, are assumed to adjust instantaneously to changes in the slow degrees of freedom, the direction of the magnetic moments as defined by polar and azimuthal angles θ and ϕ . The magnetic properties of a system, including the total energy, are then completely characterized by the slow degrees of freedom only. This is analogous to the Born-Oppenheimer approximation in atomic systems where the fast degrees of freedom are associated with the electrons while the positions of the nuclei are the slowly varying degrees of freedom.

Within the atomic moment and adiabatic approximations, spin dynamics simulations as well as iterative searches for stable magnetic states and MEPs between them can be viewed as navigation on the systems energy surface as a function of the angles defining the orientation of the magnetic moments. Efficient navigation requires efficient evaluation of not only the energy but also the changes in energy with orientation, that is the ‘forces’, or ‘torques’ acting on the magnetic moments. The energy surface can in principle be characterized within the tight-binding approach [12] and DFT [13, 14]. Such calculations are, however, complicated and computationally intensive. In order to describe nonstationary magnetic states, local constraining fields are needed to orient the magnetic vectors in the predefined orientations [15]. These local fields are not known *a priori*, so an additional iterative cycle needs to be added to the self-consistency procedure to find them. As a result, the calculation of an arbitrary, nonstationary, noncollinear state in a system of several non-equivalent magnetic moments is a challenging task within DFT and tight-binding methods.

In most cases, the evolution of extended magnetic systems is described using simple, phenomenological models, in particular Heisenberg-type models, where the total energy and gradients of the energy can be obtained analytically. However, in order to describe magnetic systems accurately enough, the model Hamiltonian may need to include several phenomenological terms. In addition to the usual magnetic exchange, anisotropy and dipole-dipole interaction, more elaborate interactions, such as biquadratic exchange and Dzyaloshinsky-Moriya interaction have been invoked to reproduce experimental observations accurately enough [2]. The magnitude of the magnetic moments and interaction parameters in such Heisenberg-type models are typically kept unchanged as the magnetic vectors rotate. This approach can be accurate enough for small deviations from collinear stable states, but is expected to fail for large rotation angles in itinerant electron systems [16] where the magnitude of the magnetic moments and coupling parameters depend on the relative orientation of the moments. While additional parameters and elaborate expressions for the dependence of the parameters on the orientation of the magnetic moments can, in principle, be used to make a Heisenberg-type model reproduce any magnetic system, the transferability of the parameter values obtained in this way may be quite limited. Models that better describe the underlying physics and rely on only a few, well defined parameters are then preferable.

The Alexander-Anderson (AA) model [17, 18] describes the interaction of magnetic impurities in a system containing itinerant electrons. It includes two electronic bands: a quasilocalized band of d -electrons and a band of itinerant $s(p)$ -electrons. A noncollinear extension of the AA model (NCAA) has been developed within mean-field approximation as well as an efficient implementation of the self-consistency calculations for an arbitrary number of non-equivalent magnetic impurities using the recursive Green function method [19, 20] and analytical transformations of the density of states [21–23]. The NCAA model can be applied to large and complex magnetic systems where a self-consistent calculation of the number of d -electrons and magnitude of the magnetic moments is carried out for a given orientation. For an arbitrary, stationary or non-stationary orientation, only the number of d -electrons and magnitude of the magnetic moments are modified during the self-consistency calculations. The orientation of the magnetic vectors remains unaffected, i.e. in the NCAA model, changes in orientation are completely decoupled from the self-consistency procedure. This is different from DFT calculations, where the orientation of the magnetic moments at a non-stationary point is modified during self-consistency calculations unless local constraining fields fixing the orientation of the magnetic moments to the predefined direction are included [15].

In our recent paper [23], a magnetic force theorem for the NCAA model has been derived which makes it possible to calculate the energy gradient without repeated self-consistency calculations and also provides analytic expression for the force acting on the orientation of the magnetic moments. This theorem is particularly important for large scale simulation of dynamics, calculation of minimum energy paths, or, in general, navigation on the energy surface of a magnetic system.

The NCAA model, however, does not describe the band structure of an itinerant magnet in detail. Similar to the Heisenberg-type models, the NCAA model only focuses on the energetics due to magnetic interactions. But, unlike Heisenberg-type models, the NCAA model correctly accounts for the itinerant nature of $3d$ -transition metal systems: both the magnitude of the magnetic moments and the interatomic exchange parameters (analogous to exchange parameters in a Heisenberg Hamiltonian), are predicted to vary upon rotation of the magnetic momentum vectors. The NCAA model has, for example, been used successfully to describe

magnetism of 3d-metal surfaces and interfaces [22]. Moreover, a noncollinear ordering of magnetic moments in nanoclusters of 3d-metal atoms was obtained in calculations using the NCAA model [24–26], and this prediction was later confirmed by DFT calculations [27,28].

This article is organized as follows. In the following section, the NCAA model is described as well as the method used in the self-consistency calculations. In Sec. III, the magnetic force theorem is presented and an expression given for the magnetic force. In Sec. IV, the method is applied to magnetic trimers and to a simple model of a magnetic tip of a scanning tunneling microscope (STM) interacting with a dimer adsorbed on a metal surface. In Sec. V, the finite range approximation is discussed as well as an application to Fe-atoms adsorbed on a W(110) surface, as both a full monolayer and a large island. Section VI gives a summary.

2. Noncollinear Alexander-Anderson model

The AA model [18] extended to multiple-impurities and noncollinear magnetic ordering has been described elsewhere [21,24]. However, we present here a comprehensive description of the model and its implementation for completeness.

The electronic structure of a 3d transition metal system is approximated by an itinerant $s(p)$ -electron band and five degenerate, quasi-localized d -orbitals. The Hamiltonian is as follows:

$$\begin{aligned} \mathcal{H} = & \sum_{\mathbf{k},\alpha} \varepsilon_{\mathbf{k}} n_{\mathbf{k}\alpha} + \sum_{i,\alpha} \varepsilon_i^0 n_{i\alpha} + \sum_{\mathbf{k},i,\alpha} \left(v_{i\mathbf{k}} d_{i\alpha}^\dagger c_{\mathbf{k}\alpha} + v_{\mathbf{k}i} c_{\mathbf{k}\alpha}^\dagger d_{i\alpha} \right) \\ & + \sum_{i \neq j, \alpha} v_{ij} d_{i\alpha}^\dagger d_{j\alpha} + \frac{1}{2} \sum_{i,\alpha} U_i n_{i\alpha} n_{i-\alpha}, \end{aligned} \quad (3)$$

where only one of the five d -orbitals is considered explicitly. Here, $d_{i\alpha}^\dagger$ ($d_{i\alpha}$) and $c_{\mathbf{k}\alpha}^\dagger$ ($c_{\mathbf{k}\alpha}$) are creation (annihilation) operators for d -electrons localized on atom i and itinerant $s(p)$ -electrons with the wave vector \mathbf{k} , respectively; $n_{i\alpha} = d_{i\alpha}^\dagger d_{i\alpha}$, $n_{\mathbf{k}\alpha} = c_{\mathbf{k}\alpha}^\dagger c_{\mathbf{k}\alpha}$ are the corresponding occupation number operators. Greek indices denote spin projection ($\alpha, \beta = \pm$). The energy of non-interacting $s(p)$ electrons, $\varepsilon_{\mathbf{k}}$, and d -electrons, ε_i^0 , hybridization parameters, $v_{i\mathbf{k}}$, hopping parameters, v_{ij} , and Coulomb repulsion between electrons with opposite spin projection, U_i , are spin independent. The last term in the Hamiltonian, $U_i n_{i\alpha} n_{i-\alpha}$, describes the interaction between d -electrons localized on atom i .

This Hamiltonian is invariant with respect to the choice of quantization axis. In order to describe noncollinear magnetic states, a mean field approximation is invoked at each site i for the d -electron operators, $\tilde{d}_{i\alpha}^\dagger$ and $\tilde{d}_{i\alpha}$, where the quantization axis, z_i , is chosen to be along the local magnetic moment associated with atom i . The last term in Eqn.(3) is transformed according to

$$\tilde{n}_{i\alpha} \tilde{n}_{i-\alpha} \approx \tilde{n}_{i\alpha} \langle \tilde{n}_{i-\alpha} \rangle + \langle \tilde{n}_{i\alpha} \rangle \tilde{n}_{i-\alpha} - \langle \tilde{n}_{i\alpha} \rangle \langle \tilde{n}_{i-\alpha} \rangle. \quad (4)$$

Operators with a tilde correspond to a local reference frame associated with the quantization axis z_i and angular parentheses denote expectation values of operators. The last term in Eqn. (4) represents the double counting term. The mean-field Hamiltonian is rewritten in terms of $\tilde{d}_{i\alpha}^\dagger$ and $\tilde{d}_{i\alpha}$ whose quantization axis is the laboratory z axis, the same for all sites i . Creation (annihilation) operators are transformed using the spin- $\frac{1}{2}$ rotation matrix [29]:

$$\begin{pmatrix} \tilde{d}_{i+} \\ \tilde{d}_{i-} \end{pmatrix} = \mathbf{U} \begin{pmatrix} d_{i+} \\ d_{i-} \end{pmatrix}, \quad (5)$$

where \mathbf{U} is given by:

$$\mathbf{U} = \begin{pmatrix} \exp(i\phi_i/2) \cos(\theta_i/2) & \exp(-i\phi_i/2) \sin(\theta_i/2) \\ -\exp(i\phi_i/2) \sin(\theta_i/2) & \exp(-i\phi_i/2) \cos(\theta_i/2) \end{pmatrix}. \quad (6)$$

Here, the polar angle θ_i and the azimuthal angle ϕ_i define the direction of i th magnetic moment with respect to the laboratory quantization axis z . After performing the operations (4) and (5) for each site i , the mean-field Hamiltonian is given by:

$$\begin{aligned} \mathcal{H}_{MF} = & \sum_{\mathbf{k}, \alpha} \varepsilon_{\mathbf{k}} n_{\mathbf{k}\alpha} + \sum_{i, \alpha} \varepsilon_i^\alpha n_{i\alpha} + \sum_{\mathbf{k}, i, \alpha} \left(v_{i\mathbf{k}} d_{i\alpha}^\dagger c_{\mathbf{k}\alpha} + v_{\mathbf{k}i} c_{\mathbf{k}\alpha}^\dagger d_{i\alpha} \right) \\ & + \sum_{i, j, \alpha, \beta} v_{ij}^{\alpha\beta} d_{i\alpha}^\dagger d_{j\beta} - \frac{1}{4} \sum_i U_i (N_i^2 - M_i^2), \end{aligned} \quad (7)$$

where

$$\varepsilon_i^\alpha = \varepsilon_i^0 + \frac{U_i}{2} (N_i - \alpha \cos \theta_i M_i), \quad (8)$$

$$v_{ij}^{\alpha\beta} = \frac{U_i}{2} (\delta^{\alpha\beta} - 1) \delta_{ij} \exp(-\alpha i \phi_i) \sin \theta_i M_i + (1 - \delta_{ij}) \delta^{\alpha\beta} v_{ij}. \quad (9)$$

The number of d -electrons, N_i , and the magnitude of the magnetic moments, M_i , in Eqs. (7)-(9) are defined in terms of the expectation value of occupation number operators:

$$N_i = \langle \tilde{d}_{i+}^\dagger \tilde{d}_{i+} \rangle + \langle \tilde{d}_{i-}^\dagger \tilde{d}_{i-} \rangle = \langle \tilde{n}_{i+} \rangle + \langle \tilde{n}_{i-} \rangle, \quad (10)$$

$$M_i = \langle \tilde{d}_{i+}^\dagger \tilde{d}_{i+} \rangle - \langle \tilde{d}_{i-}^\dagger \tilde{d}_{i-} \rangle = \langle \tilde{n}_{i+} \rangle - \langle \tilde{n}_{i-} \rangle. \quad (11)$$

In this model, the magnetic structure of a system consisting of P $3d$ -metal atoms supported on a metallic substrate is described by a set of values of N_i and M_i , $i = 1, \dots, P$, which need to be found from self-consistency iterations for any given orientation of the magnetic moments. The number of d -electrons, N_i , and the magnitude of the magnetic moments, M_i , can be obtained from the Green's function, $\mathcal{G}(\epsilon - is) = [\epsilon - is - \mathcal{H}_{MF}]^{-1}$, $s = +0$. Equations for the matrix elements of the Green function are derived from

$$(\mathcal{E} - \mathcal{H}_{MF}) \mathcal{G}(\mathcal{E}) = I, \quad (12)$$

where

$$\mathcal{E} = \epsilon - is. \quad (13)$$

This gives the following:

$$(\mathcal{E} - \epsilon_{\mathbf{k}}) \mathcal{G}_{\mathbf{k}i}^{\alpha\beta}(\mathcal{E}) - \sum_l v_{\mathbf{k}l} \mathcal{G}_{li}^{\alpha\beta}(\mathcal{E}) = 0, \quad (14)$$

$$(\mathcal{E} - \epsilon_i^\alpha) \mathcal{G}_{ij}^{\alpha\beta}(\mathcal{E}) - \sum_{l, \gamma} v_{il}^{\alpha\gamma} \mathcal{G}_{lj}^{\gamma\beta}(\mathcal{E}) - \sum_{\mathbf{k}} v_{i\mathbf{k}} \mathcal{G}_{\mathbf{k}j}^{\alpha\beta}(\mathcal{E}) = \delta_{ij} \delta^{\alpha\beta}. \quad (15)$$

By substituting the matrix elements $\mathcal{G}_{\mathbf{k}i}^{\alpha\beta}(\mathcal{E})$ derived from Eqn. (14) into Eqn. (15), an equation for the matrix elements of the d -electron Green function can be obtained as:

$$\begin{aligned} \left(\mathcal{E} - \epsilon_i^\alpha - \sum_{\mathbf{k}} \frac{v_{i\mathbf{k}} v_{\mathbf{k}i}}{\mathcal{E} - \epsilon_{\mathbf{k}}} \right) \mathcal{G}_{ij}^{\alpha\beta}(\mathcal{E}) - \sum_{l \neq i} \left(v_{il} + \sum_{\mathbf{k}} \frac{v_{i\mathbf{k}} v_{\mathbf{k}l}}{\mathcal{E} - \epsilon_{\mathbf{k}}} \right) \mathcal{G}_{lj}^{\alpha\beta}(\mathcal{E}) \\ + \sum_{\gamma} v_{ii}^{\alpha\gamma} \mathcal{G}_{ij}^{\gamma\beta}(\mathcal{E}) = \delta_{ij} \delta^{\alpha\beta}. \end{aligned} \quad (16)$$

The magnetism of $3d$ -transition metal systems is mostly determined by the d -electrons. Therefore, only the Green function for d -electrons, $G(\mathcal{E}) \equiv \mathcal{G}^{(d)}(\mathcal{E})$, will be considered explicitly

in what follows. According to Eqn. (16), $G(\mathcal{E})$ is a resolvent of an effective, mean field Hamiltonian for the d -electrons, $H \equiv \mathcal{H}_{MF}^{(d)}$, with parameters that are renormalized due to the influence of the itinerant $s(p)$ -electrons. This Hamiltonian is given by:

$$H = \sum_{i,\alpha} E_i^\alpha n_{i\alpha} + \sum_{i,j,\alpha,\beta} V_{ij}^{\alpha\beta} d_{i\alpha}^\dagger d_{j\beta} - \frac{1}{4} \sum_i U_i (N_i^2 - M_i^2), \quad (17)$$

where

$$E_i^\alpha = E_i^0 + \frac{U_i}{2} (N_i - \alpha \cos \theta_i M_i), \quad (18)$$

$$V_{ij}^{\alpha\beta} = \frac{U_i}{2} (\delta^{\alpha\beta} - 1) \delta_{ij} \exp(-\alpha i \phi_i) \sin \theta_i M_i + (1 - \delta_{ij}) \delta^{\alpha\beta} V_{ij}. \quad (19)$$

Here, E_i^0 is a renormalized energy of unperturbed d -states:

$$E_i^0 \equiv \varepsilon_i^0 + \text{Re} \sum_{\mathbf{k}} \frac{v_{i\mathbf{k}} v_{\mathbf{k}i}}{\mathcal{E} - \varepsilon_{\mathbf{k}}}, \quad (20)$$

which now acquires non-zero width due to the $s(p)$ - d hybridization and the width parameter, Γ , is given by

$$\Gamma \equiv \text{Im} \sum_{\mathbf{k}} \frac{v_{i\mathbf{k}} v_{\mathbf{k}i}}{\mathcal{E} - \varepsilon_{\mathbf{k}}}. \quad (21)$$

Γ is included in the argument of the Green function when computing the density of states [17]. The V_{ij} are referred to as hopping parameters. They represent both a direct exchange between d -states localized on sites i and j and as well as a contribution from indirect d - $s(p)$ - d coupling through the conduction band

$$V_{ij} \equiv v_{ij} + \sum_{\mathbf{k}} \frac{v_{i\mathbf{k}} v_{\mathbf{k}j}}{\mathcal{E} - \varepsilon_{\mathbf{k}}}. \quad (22)$$

Following [18], it is assumed that the on-site $s(p)$ - d coupling is stronger than d - $s(p)$ - d interaction of d -electrons at different sites and, hence, the imaginary part of V_{ij} is neglected. E_i^0 , U_i , V_{ij} and Γ are assumed to be constant parameters for the model. The choice of values for E_i^0 and U_i depends mainly on the type of atom i , while the hopping parameters V_{ij} also depend on the geometry of the system, in particular the distance between atoms i and j .

The number of d -electrons, N_i , and the magnitude of the magnetic moments, M_i , defined in Eqs. (10) and (11), are expressed in terms of the Green function in the local frame of reference, $\tilde{G}(\mathcal{E})$, using the following standard relations:

$$N_i = \frac{1}{\pi} \int_{-\infty}^0 d\epsilon \text{Im Tr } \tilde{G}_{ii}(\epsilon - i\Gamma), \quad (23)$$

$$M_i = \frac{1}{\pi} \int_{-\infty}^0 d\epsilon \text{Im Tr } \left[\sigma_z \tilde{G}_{ii}(\epsilon - i\Gamma) \right]. \quad (24)$$

Here, $\tilde{G}_{ii}(\epsilon - i\Gamma)$ is a 2×2 matrix with elements $\tilde{G}_{ii}^{\alpha\beta}(\epsilon - i\Gamma)$ and σ_z is the z component of the Pauli spin matrix. It is assumed that the magnetic system is in contact with a bath of $s(p)$ -electrons which fixes the Fermi level. The zero of energy is set to be at the Fermi level ($\varepsilon_F = 0$).

In order to be able to use Eqs. (23) and (24) in self-consistency calculations, the Green function has to be transformed from the local reference frame to a global one using the spin- $\frac{1}{2}$ rotation matrix \mathbf{U} , Eq. (6):

$$\tilde{G}(\mathcal{E}) = \mathbf{U}G(\mathcal{E})\mathbf{U}^\dagger. \quad (25)$$

By substituting this relation into Eqs. (23) and (24), one obtains the following:

$$N_i = \frac{1}{\pi} \int_{-\infty}^0 d\epsilon \operatorname{Im} [G_{ii}^{++}(\epsilon - i\Gamma) + G_{ii}^{--}(\epsilon - i\Gamma)], \quad (26)$$

$$\begin{aligned} M_i = & \frac{1}{\pi} \int_{-\infty}^0 d\epsilon \operatorname{Im} [G_{ii}^{++}(\epsilon - i\Gamma) - G_{ii}^{--}(\epsilon - i\Gamma)] \cos \theta_i \\ & + \frac{1}{\pi} \int_{-\infty}^0 d\epsilon \operatorname{Im} [G_{ii}^{+-}(\epsilon - i\Gamma)e^{i\phi_i} + G_{ii}^{-+}(\epsilon - i\Gamma)e^{-i\phi_i}] \sin \theta_i. \end{aligned} \quad (27)$$

Since the matrix elements of the Green function depend on N and M , Eqs. (26) and (27) should be solved self-consistently for a given orientation of the magnetic vectors starting from some initial estimate for the number of d -electrons and magnitude of the magnetic moments. If the system consists of more than one atom, the self-consistency procedure contains two nested loops. The inner loop involves finding the constrained solution of Eqs. (26) and (27) for each individual atom, while the number of d -electrons and magnitude of magnetic moments at all other atoms are kept fixed. Values of N and M found in the output of the inner loop are then used as the revised constraints for the next iteration of the outer loop. The iterations are repeated until N and M change by less than a predefined magnitude in an iteration. The implementation of the self-consistency procedure is illustrated in Fig. 1.

It is important to realize that this procedure is the same for both stationary and non-stationary orientations of the magnetic momentum vectors and that only the number of d -electrons and magnitude of the magnetic moments are modified during the self-consistency calculation. The orientations of the magnetic vectors remain unaffected, i.e. spin rotations are completely decoupled from the self-consistency procedure in the NCAA model. This is different from DFT calculations, where the orientations of magnetic moments at a non-stationary point are modified during self-consistency calculations, unless local constraining fields are introduced [15].

After self-consistency has been achieved, the total energy of d -electrons can be found from:

$$E = \frac{5}{\pi} \int_{-\infty}^0 d\epsilon \epsilon \operatorname{Im} \operatorname{Tr} G^*(\epsilon - i\Gamma) - 5 \sum_i \frac{U_i}{4} (N_i^{*2} - M_i^{*2}), \quad (28)$$

where the factor of 5 is due to the five-fold degeneracy of the d -orbitals. Quantities marked with an asterisk correspond to self-consistent values.

In practice, the procedure described above implies that integration over the density of d -states needs to be carried out repeatedly (see Eqs. (26) and (27)). An efficient approach for this has been described in the literature [19–21]. It is reviewed in Appendices A and B for completeness. Initially, the recursive Green's function method is applied in order to represent the Green function in terms of a continued fraction (see §3 in [19] and §2 in [20]). Then, the

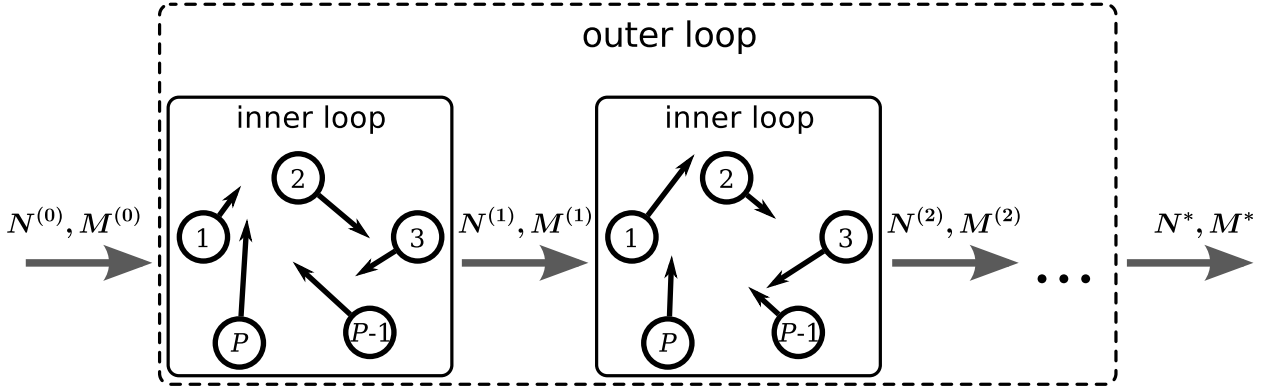


FIG. 1. An illustration of the self-consistency procedure. The magnetic system consists of P atoms whose magnetic moments are denoted by arrows. The direction of the magnetic vectors is fixed. Self-consistent values of the magnitude, M^* , of the magnetic moments and the number of d -electrons, N^* , are found using the nested loop scheme. In the inner loop, the constrained solution of Eqns. (26) and (27) is found for each atom separately, keeping the number of d -electrons and magnitude of the magnetic moments for all other atoms fixed. After the k -th iteration, the inner loop produces a set of $N^{(k)}$ and $M^{(k)}$ values that are then used as revised constraints in iteration $(k+1)$ of the outer loop. Self-consistency is reached when all the N_i and M_i do not change upon further iterations.

continued fraction is expanded in a series of partial fractions [21]. A matrix element of the Green function then takes the form (see Appendix B)

$$G_{ij}^{\alpha\beta}(\epsilon) = \sum_k \frac{p_k}{\epsilon - q_k}, \quad (29)$$

where the numbers p_k, q_k depend on the orientation of the magnetic moments as well as on indices i, j, α and β . The density of states is expressed in terms of Lorentzian functions and the integration then carried out analytically. Namely, since the d -levels contain an imaginary part, $i\Gamma$, integrands in Eqns. (26) and (27) include the terms

$$\text{Im} \sum_k \frac{p_k}{\epsilon - q_k - i\Gamma} = \Gamma \sum_k \frac{p_k}{(\epsilon - q_k)^2 + \Gamma^2},$$

that can be integrated analytically to give

$$\int_{-\infty}^0 d\epsilon \Gamma \sum_k \frac{p_k}{(\epsilon - q_k)^2 + \Gamma^2} = \sum_k p_k \text{arccot} \left(\frac{q_k}{\Gamma} \right).$$

The total energy of the system is also expressed analytically in terms of parameters of the self-consistent Hamiltonian as:

$$\begin{aligned} E &= \frac{5}{\pi} \int_{-\infty}^0 d\epsilon \epsilon \sum_{\mu=1}^{2P} \frac{\Gamma}{(\epsilon - \epsilon_{\mu}^*)^2 + \Gamma^2} - 5 \sum_{i=1}^P \frac{U_i}{4} (N_i^{*2} - M_i^{*2}) \\ &= \frac{5}{\pi} \sum_{\mu=1}^{2P} \left[\epsilon_{\mu}^* \text{arccot} \frac{\epsilon_{\mu}^*}{\Gamma} + \frac{\Gamma}{2} \ln \left(\frac{\epsilon_{\mu}^{*2}}{\Gamma^2} + 1 \right) \right] - 5 \sum_{i=1}^P \frac{U_i}{4} (N_i^{*2} - M_i^{*2}), \end{aligned} \quad (30)$$

where ϵ_μ^* are the eigenvalues of H^* . Integral in Eq. (30) diverges at the lower limit. However, this infinite contribution is the same for all magnetic states and, therefore, can be omitted.

In the self-consistency procedure, the number of d -electrons and the magnitude of the magnetic moments are found for a given orientation of the magnetic momentum vectors. This assumes a hierarchy of relaxation times. The relaxation of the diagonal components of the spin density matrix, which give the number of d -electrons and magnitude of the magnetic moments, is assumed to be much faster than the relaxation of the off-diagonal components which give the orientation of the magnetic momentum vectors [11]. Thus, N and M , are treated as fast degrees of freedom that adjust instantaneously to changes in the orientation of the magnetic moments, the slow degrees of freedom. This is analogous to the Born-Oppenheimer approximation for electronic and nuclear degrees of freedom.

3. Magnetic force theorem

Gradients of the energy with respect to the orientation of the magnetic momentum vectors, i.e. magnetic forces, can be used to guide the search for minimum energy configurations of the magnetic moments, identify minimum energy paths, and to simulate dynamics of magnetic systems. A simple approach for evaluating the energy gradient is to approximate it by finite differences where the energy is evaluated self-consistently for slightly different orientations. However, this is inefficient for large systems as at least $2P + 1$ self-consistency calculations need to be carried out for a system with P magnetic moments each time the force is evaluated.

Below, a method is presented for evaluating all components of the energy gradient without having to perform any additional self-consistency calculations. The method is based on a magnetic force theorem (MFT) for the NCAA model. The theorem states that for an arbitrary orientation of the magnetic vectors, stationary or non-stationary, the energy as a function of the fast degrees of freedom, N and M , reaches an extremum at the self-consistent values, N^* and M^*

$$\forall i: \quad \left. \frac{\partial E}{\partial N_i} \right|_{\substack{N=N^* \\ M=M^*}} = 0 \quad \text{and} \quad \left. \frac{\partial E}{\partial M_i} \right|_{\substack{N=N^* \\ M=M^*}} = 0. \quad (31)$$

This simplifies greatly the calculation of the gradient and speeds up exploration of the energy surface of the system.

Two lemmas for the Green function that are proved in Appendix C are needed to derive the MFT:

$$\frac{\partial \text{Tr} G(\epsilon)}{\partial N_i} = -\frac{U_i}{2} \frac{\partial}{\partial \epsilon} (G_{ii}^{++}(\epsilon) + G_{ii}^{--}(\epsilon)), \quad (32)$$

and

$$\begin{aligned} \frac{\partial \text{Tr} G(\epsilon)}{\partial M_i} = & \frac{U_i}{2} \frac{\partial}{\partial \epsilon} [(G_{ii}^{++}(\epsilon) - G_{ii}^{--}(\epsilon)) \cos \theta_i \\ & + (G_{ii}^{+-}(\epsilon)e^{i\phi_i} + G_{ii}^{-+}(\epsilon)e^{-i\phi_i}) \sin \theta_i]. \end{aligned} \quad (33)$$

According to eqns. (28) and (32)

$$\begin{aligned} \frac{\partial E}{\partial N_i} &= \frac{5}{\pi} \int_{-\infty}^0 d\epsilon \epsilon \text{Im} \frac{\partial}{\partial N_i} \text{Tr} G(\epsilon - i\Gamma) - 5 \frac{U_i}{2} N_i \\ &= 5 \frac{U_i}{2} \left[\frac{1}{\pi} \int_{-\infty}^0 d\epsilon \text{Im} (G_{ii}^{++}(\epsilon - i\Gamma) + G_{ii}^{--}(\epsilon - i\Gamma)) - N_i \right], \end{aligned}$$

where integration by parts has been invoked. According to Eqn. (26), the expression in square brackets is equal to zero when self-consistency has been reached.

The equation for the derivative of the energy with respect to M_i in Eq. (31) is proved in the same way. Using (28) and (33), we obtain the following:

$$\begin{aligned} \frac{\partial E}{\partial M_i} &= \frac{5}{\pi} \int_{-\infty}^0 d\epsilon \epsilon \operatorname{Im} \frac{\partial}{\partial M_i} \operatorname{Tr} G(\epsilon - i\Gamma) + 5 \frac{U_i}{2} M_i \\ &= 5 \frac{U_i}{2} \left\{ -\frac{1}{\pi} \int_{-\infty}^0 d\epsilon \operatorname{Im} [(G_{ii}^{++}(\epsilon - i\Gamma) - G_{ii}^{--}(\epsilon - i\Gamma)) \cos \theta_i \right. \\ &\quad \left. + (G_{ii}^{+-}(\epsilon - i\Gamma)e^{i\phi_i} + G_{ii}^{-+}(\epsilon - i\Gamma)e^{-i\phi_i}) \sin \theta_i] + M_i \right\}. \end{aligned}$$

Due to Eqn. (27), the expression in curly brackets vanishes when M has the self-consistent value, M^* .

By using the MFT, the computational effort involved in the calculation of magnetic forces in NCAA is significantly reduced. According to the MFT, the energy change due to the infinitesimal rotation of magnetic vectors does not contain a contribution from the variation of the number of d -electrons and the magnitude of the magnetic moments, i.e. fast degrees of freedom. In particular, this means that in the finite difference scheme, the energy of the perturbed spin state obtained by a small rotation of magnetic vectors from a particular orientation can be approximated using the same values for the fast degrees of freedom as those calculated self-consistently for the unperturbed spin state and, therefore, no additional self-consistency calculations are needed.

A simple finite difference scheme is, however, problematic because it involves evaluating the difference between two numbers of similar magnitude. This procedure can lead to a significant loss of accuracy. Instead, first order perturbation theory can be used to derive an expression for the magnetic force in terms of the self-consistent values. According to the MFT, a derivative of the energy, $E = E(\lambda)$, with respect to any adiabatic parameter λ (a slow degree of freedom) can be computed from the explicit λ dependence only, without having to include implicit dependence

$$\frac{dE(\lambda)}{d\lambda} = \frac{\partial E(\lambda)}{\partial \lambda} = \frac{5}{\pi} \int_{-\infty}^0 d\epsilon \epsilon \operatorname{Im} \operatorname{Tr} \frac{\partial G^*(\epsilon - i\Gamma; \lambda)}{\partial \lambda}. \quad (34)$$

Here, $\partial G^*(\epsilon - i\Gamma; \lambda)/\partial \lambda$ can be found by using the resolvent identity

$$\frac{\partial G(\epsilon; \lambda)}{\partial \lambda} = G(\epsilon; \lambda) \frac{\partial H(\lambda)}{\partial \lambda} G(\epsilon; \lambda), \quad (35)$$

which, together with Eqn. (34), gives

$$\begin{aligned} \frac{dE(\lambda)}{d\lambda} &= \frac{5}{\pi} \int_{-\infty}^0 d\epsilon \epsilon \operatorname{Im} \operatorname{Tr} \left[G^*(\epsilon - i\Gamma; \lambda) \frac{\partial H^*(\lambda)}{\partial \lambda} G^*(\epsilon - i\Gamma; \lambda) \right] \\ &= \frac{5}{\pi} \int_{-\infty}^0 d\epsilon \operatorname{Im} \operatorname{Tr} \left[G^*(\epsilon - i\Gamma; \lambda) \frac{\partial H^*(\lambda)}{\partial \lambda} \right], \end{aligned} \quad (36)$$

that is, the derivative of the total energy with respect to a parameter coincides with the expectation value of the derivative of the Hamiltonian with respect to that parameter. This is analogous to the Hellmann-Feynman theorem.

In practice, it is convenient to calculate the trace in Eqn. (36) using the basis in which $H^*(\lambda)$ and $G^*(\epsilon; \lambda)$ are diagonal

$$\text{Tr} \left[G^*(\epsilon; \lambda) \frac{\partial H^*(\lambda)}{\partial \lambda} \right] = \sum_{\mu=1}^{2P} \frac{\xi_{\mu}^*}{(\epsilon - \epsilon_{\mu}^*)}, \quad (37)$$

where ξ_{μ}^* are the diagonal elements of $\partial H^*(\lambda)/\partial \lambda$ in the relevant basis. The integral in Eqn. (36) can then be evaluated analytically leading to

$$\frac{dE(\lambda)}{d\lambda} = \frac{5}{\pi} \sum_{\mu=1}^{2P} \xi_{\mu}^* \text{arccot} \left(\frac{\epsilon_{\mu}^*}{\Gamma} \right). \quad (38)$$

With $\lambda = \theta_i$ or $\lambda = \phi_i$ and $i = 1, \dots, P$, this gives the gradient of the energy with respect to the angles defining the orientation of the magnetic moments.

The procedure for evaluating the energy gradient is as follows: First, derivatives of the self-consistent Hamiltonian, $\partial H^*(\boldsymbol{\theta}, \boldsymbol{\phi})/\partial \theta_i$ and $\partial H^*(\boldsymbol{\theta}, \boldsymbol{\phi})/\partial \phi_i$, which are given explicitly by

$$\left(\frac{\partial H^*(\boldsymbol{\theta}, \boldsymbol{\phi})}{\partial \theta_i} \right)_{kj}^{\alpha\beta} = \frac{1}{2} \delta_{ji} \delta_{ki} U_i M_i^* [\alpha \delta^{\alpha\beta} \sin \theta_i + (\delta^{\alpha\beta} - 1) \exp(-\alpha i \phi_i) \cos \theta_i], \quad (39)$$

$$\left(\frac{\partial H^*(\boldsymbol{\theta}, \boldsymbol{\phi})}{\partial \phi_i} \right)_{kj}^{\alpha\beta} = \frac{i\alpha}{2} (1 - \delta^{\alpha\beta}) \delta_{ji} \delta_{ki} U_i M_i^* e^{-\alpha i \phi_i} \sin \theta_i \quad (40)$$

are transformed to a basis where $H^*(\boldsymbol{\theta}, \boldsymbol{\phi})$ is diagonal. Then, their diagonal matrix elements, $\xi_{\mu}^*(\theta_i)$, $\xi_{\mu}^*(\phi_i)$, are inserted into Eqn. (38) and the derivatives with respect to θ and ϕ evaluated.

The MFT significantly reduces the computational effort involved in calculations of the first derivatives of the energy with respect to θ and ϕ . Second derivatives of the energy are also important, because they are used to calculate magnetic exchange interaction parameters, J_{ij} , between magnetic moments i and j . However, the MFT is not valid for the second derivatives. One cannot neglect the change in the fast degrees of freedom when computing the second variation of the energy.

4. Applications

4.1. Trimers adsorbed on a metallic substrate

Trimers of $3d$ transition metal atoms supported on a metallic surface are good test systems for studying noncollinear magnetism at the atomic scale. Noncollinear magnetic ordering in Cr, Mn, Fe trimers was predicted theoretically using a model Hamiltonian approach [24–26] and was later obtained in *ab initio* calculations [27, 28, 30, 31]. The angles formed between the magnetic moments in the stable magnetic states depend on the type of atoms in the trimer and the geometrical arrangement of the atoms. Without spin-orbit interaction, the configuration and spin spaces are uncoupled. For coplanar magnetic ordering, two angles completely determine the configuration of the three magnetic momentum vectors. Therefore, the energy surface for such systems can be visualized easily.

Within the NCAA model, the parameters E_i^0 and U_i are determined mainly by the chemical element whereas the hopping parameters V_{ij} depend also on the arrangement of the atoms in the trimer and the hybridization of the $3d$ -states with electronic states of the substrate. The parameter associated with the width of the d -states, Γ , may depend on the position of the

trimer on the surface as well as on the trimer geometry. The unit of energy is taken to be Γ and we give below the values chosen for the scaled energy parameters, $\tilde{U} \equiv U/\Gamma$, $\tilde{E}^0 \equiv E^0/\Gamma$ and $\tilde{V}_{ij} \equiv V_{ij}/\Gamma$.

Magnetic ordering in the Cr, Mn and Fe trimers is expected to be quite different. To illustrate this, we choose the Coulomb integral, $\tilde{U} = 13$, and the hopping parameters, \tilde{V}_{12} , \tilde{V}_{13} and \tilde{V}_{23} , to be the same for all the trimers, while the value of \tilde{E}^0 is chosen to ensure that the number of d -electrons per atom in each case is the same as in the corresponding solid ($N \approx 5$, 6 and 7, for Cr, Mn and Fe, respectively). The definitions of the two variables, the angles θ_2 and θ_3 , are shown in Fig. 2.

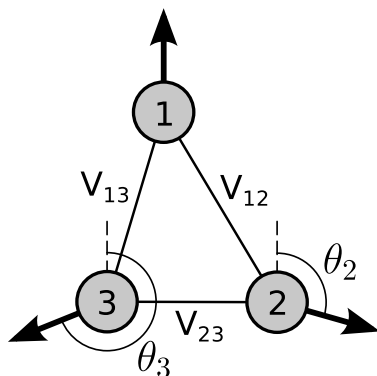


FIG. 2. A noncollinear magnetic state of a trimer of atoms adsorbed on a surface. The definitions of the atom labeling, 1, 2 and 3, are shown as well as the two angles, θ_2 and θ_3 , specifying the two degrees of freedom. All three distances between the atom pairs are different, leading to different values for the three hopping parameters, \tilde{V}_{ij} .

The calculated energy surfaces for the three trimers, Cr_3 , Mn_3 and Fe_3 , are shown in Fig. 3. The stable configurations of the magnetic momentum vectors, corresponding to minima on the energy surface, are shown, as well as MEPs for transitions between these states calculated using the climbing image nudged elastic band (NEB) method [32,33]. The MEP gives the mechanism for low energy collective excitations of the magnetic trimers and the maximum energy along the MEP gives the minimum energy needed for the transitions.

A Cr crystal has spin density wave magnetic structure with antiferromagnetic coupling of near neighbor spins. In an equilateral Cr trimer, the ground state is noncollinear with angles $2\pi/3$ between the magnetic momentum vectors [24–27]. However, a collinear ordering of the magnetic moments is also possible for a different choice of distances between the Cr atoms and, thereby, the hopping parameters \tilde{V}_{ij} . Such a case is shown in Fig. 3a, where $\tilde{V}_{23} = 1.0$, $\tilde{V}_{12} = 0.6$ and $\tilde{V}_{13} = 0.9$. Maxima on the energy surface correspond to ferromagnetic ordering of two of the magnetic moments, while the magnetic moment of the third atom is pointing in the opposite direction. All minima on the energy surface correspond to the same magnetic state. There are two different MEPs for transitions between these states, as shown in Fig. 3a. One of the MEPs corresponds to an almost coherent rotation of the magnetic moments of atoms 2 and 3, maintaining a nearly antiparallel ordering during the rotation. At the saddle point, both moments have reversed their direction. The activation energy for this transition is $5.4 \cdot 10^{-2}$ in Γ -units. Along the second MEP, the magnetic moment of atom 2 rotates monotonously by an angle of 2π , while the magnetic moment of atom 3 only rotates slightly from the initial orientation and then returns. At the saddle point, the magnetic moment of atom 3 is aligned in the same direction as in the ground state but the moment of atom 2 has been reversed. The activation

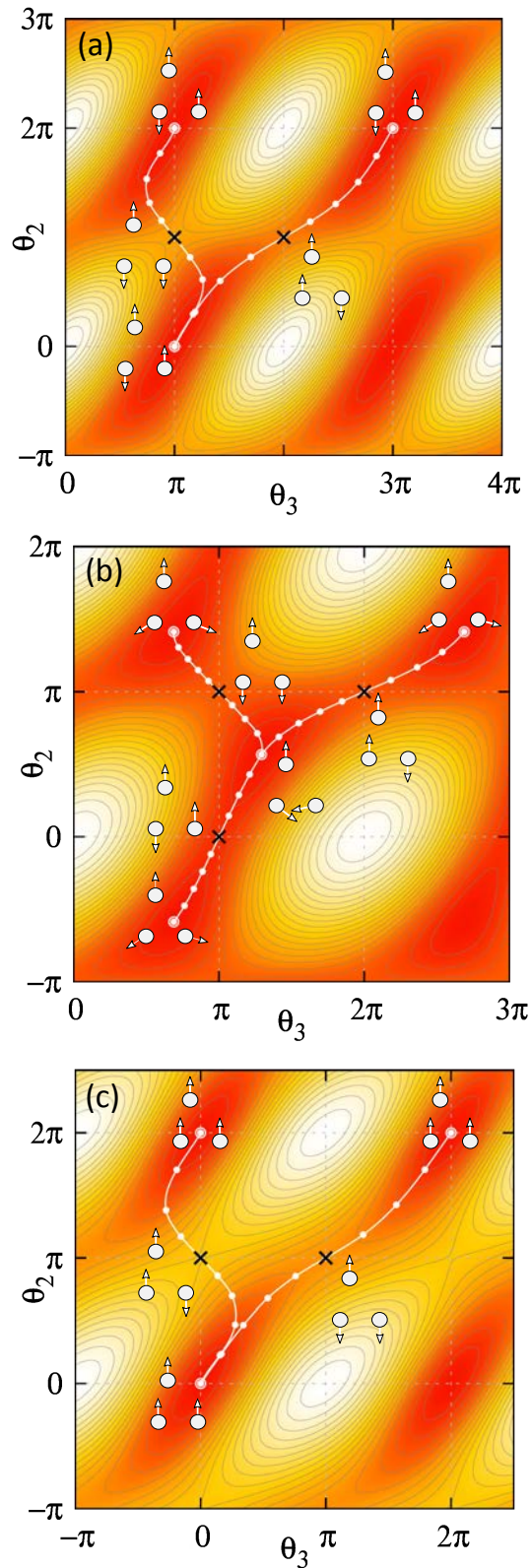


FIG. 3. Energy surfaces of supported trimers: (a) Cr₃, (b) Mn₃ and (c) Fe₃. The zero of energy (red) is the energy for the lowest energy configuration of the magnetic moments. White lines represent minimum energy paths and the dots indicate positions of images in the NEB calculations. Minima are marked with circles, while saddle points are indicated with crosses. The insets show the magnetic momentum vectors at the minima and at the saddle points.

energy is larger for this second mechanism, $7.8 \cdot 10^{-2} \Gamma$, because of strong antiferromagnetic coupling between atoms 2 and 3. Note that all minima and saddle points on the energy surface correspond to collinear ordering of the magnetic moments.

For the Mn trimer, we obtain two distinct stable states, both corresponding to non-collinear magnetic ordering, as shown in Fig 3b. Mn atoms often form noncollinear structures [24,26,28]. The two stable states have the same energy, but the MEPs between them are quite different and give different activation energies. The saddle points correspond to collinear magnetic ordering. The activation energy is $1.9 \cdot 10^{-2} \Gamma$ for the saddle point at $\theta_2 = \pi$, $\theta_3 = \pi$, $1.7 \cdot 10^{-2} \Gamma$ for the saddle point at $\theta_2 = \pi$, $\theta_3 = 2\pi$ and $0.7 \cdot 10^{-2} \Gamma$ for the saddle points at $\theta_2 = 0$, $\theta_3 = \pi$.

For the Fe trimer, all the minima on the energy surface correspond to the same ferromagnetic state (see Fig. 3c). The saddle points between those states also correspond to collinear magnetic ordering, but with one of the magnetic moments pointing in the opposite direction to the other two. The energy surface for the Fe trimer is similar to the one for the Cr trimer, but shifted by π along the θ_3 axis. There are also two possible MEPs between the states. The MEP with the lower activation energy, $2.7 \cdot 10^{-2} \Gamma$, corresponds to nearly coherent rotation of the second and the third magnetic moments. The other MEP corresponds to relatively small deviation of θ_3 from zero. The barrier for this transition mechanism is higher, $4.5 \cdot 10^{-2} \Gamma$.

4.2. STM tip interacting with adsorbed dimer

The energy surface of a magnetic cluster can be modified by applying a local external magnetic field. Another way to deform the surface is by hybridization with an additional atom placed close enough to the cluster. The latter effect was recently demonstrated experimentally by using magnetic atoms at the tip of a scanning-tunneling microscope (STM) [34]. The magnetic tip was used to modify the energy barrier between two magnetic states of a magnetic nanostructure on a non-magnetic substrate.

As a simple model of this experiment, we consider the isosceles Cr trimer, where atom 1 represents the STM tip and atoms 2 and 3 represent the dimer adsorbed on a non-magnetic substrate. The hopping parameters between the tip atom and each one of the two dimer atoms are set to be the same, $\tilde{V}_{12} = \tilde{V}_{13} \equiv \tilde{V}$, and are varied to mimic changes in the distance between the tip and the dimer, while the third hopping parameter is kept fixed with a value of $\tilde{V}_{23} = 1$. For each value of \tilde{V} , the energy of the system is minimized with respect to the angles θ_2 and θ_3 defining the orientation of the magnetic moments in the dimer. Due to the symmetry of the system, θ_2 differs from θ_3 by an angle of π at the minimum energy configuration. The value obtained for one of the angles, θ_2 , is shown as a function of \tilde{V} in Fig. 4. For small \tilde{V} , the magnetic moments of the dimer point in the opposite direction and are perpendicular to the magnetic moment of the tip. However, when \tilde{V} becomes larger than \tilde{V}_{23} , the magnetic moments of the dimer tend to point in the same direction and opposite to the magnetic moment of the tip. The energy surface of the system for three different values of \tilde{V} is shown in the insets of Fig. 4.

5. Finite range approximation

In the self-consistency calculations, the computational effort of the tridiagonalization of the NCAA Hamiltonian which is needed to evaluate the matrix elements of the Green function scales as P^3 , where P is the number of magnetic atoms in the system. This operation has to be performed for each magnetic atom, so the computational effort in each iteration of the self-consistency procedure scales as P^4 . The number of iterations needed to reach self-consistency

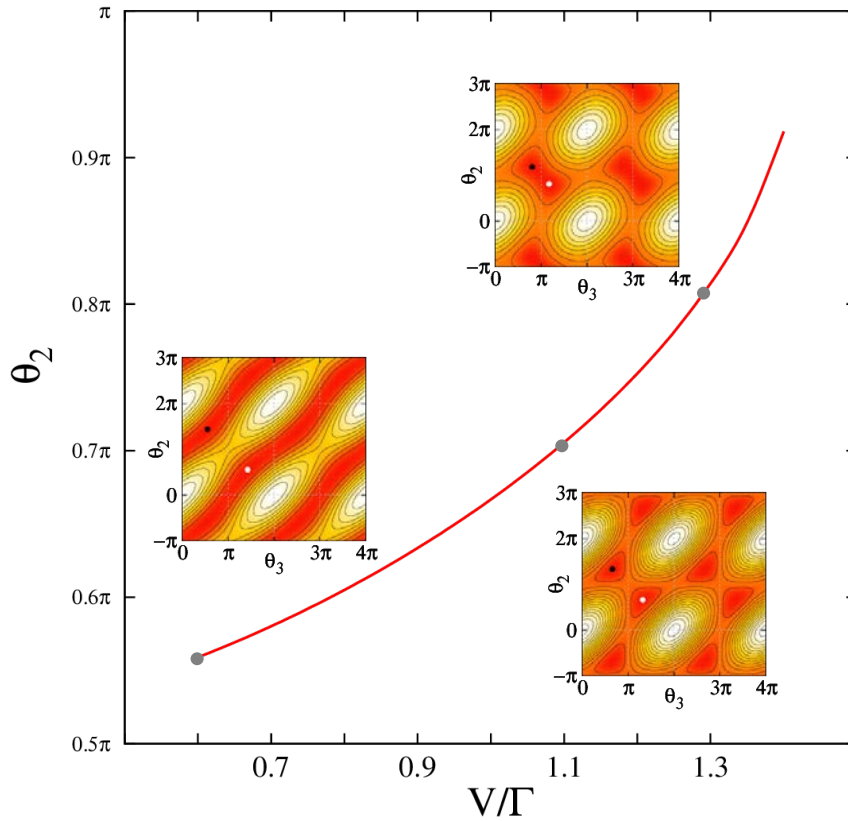


FIG. 4. Angle between the magnetic moment of an STM tip and the magnetic moment of one of the Cr-atoms in a Cr_2 addimer as a function of the corresponding hopping parameter. The three insets show the energy surface of the system for the values indicated by the three gray circles on the curve. White and black dots in the insets mark energy minima.

could also have some dependence on the system size, but is difficult to assess. The self-consistency calculations become too demanding when the number of non-equivalent magnetic atoms becomes large, on the order of thousands. One way of addressing this problem is to use parallel computing as the self-consistency algorithm can be parallelized efficiently. Another option is to use approximations in order to make the computational effort scale linearly with P .

One approach is to assume that the magnetic state of an atom is mostly affected by its neighbors, while the effect of distant atoms can be neglected in the self-consistency calculations. More specifically, when calculating the number of d -electrons and the magnitude of the magnetic moment of a particular atom, only neighbors within a sphere of a certain radius, r_c , centered on the atom are included. The accuracy of this approximation can be controlled by varying the radius, r_c . Typically, the calculated results converge quite fast as r_c increases. This is demonstrated below in calculations for the electronic and magnetic structure of a monolayer island of Fe-atoms on a W(110) surface.

The position of the Fe-atoms in the monolayer are determined by the atomic structure of the W(110) substrate. Each Fe-atom has four nearest neighbors at a distance of $\sqrt{3}/2a$, where a is a lattice constant of the W-crystal (see Fig. 5(a)). For the Fe monolayer, the number of atoms inside the sphere, N_c , changes stepwise as a function of r_c as shown in Fig. 5(b). The position of the steps, $r_c^{(\zeta)}$, $\zeta = 0, 1, 2, \dots$, is defined by the distance between the neighbors.

Any value of r_c in the range $[r_c^{(\zeta)}; r_c^{(\zeta+1)}]$ will result in the same self-consistent values for the number of d -electrons and magnitude of the magnetic moments. Below, we will refer to ζ as the number of shells of interacting neighbors and study how the choice of ζ affects the results of the self-consistency calculations.

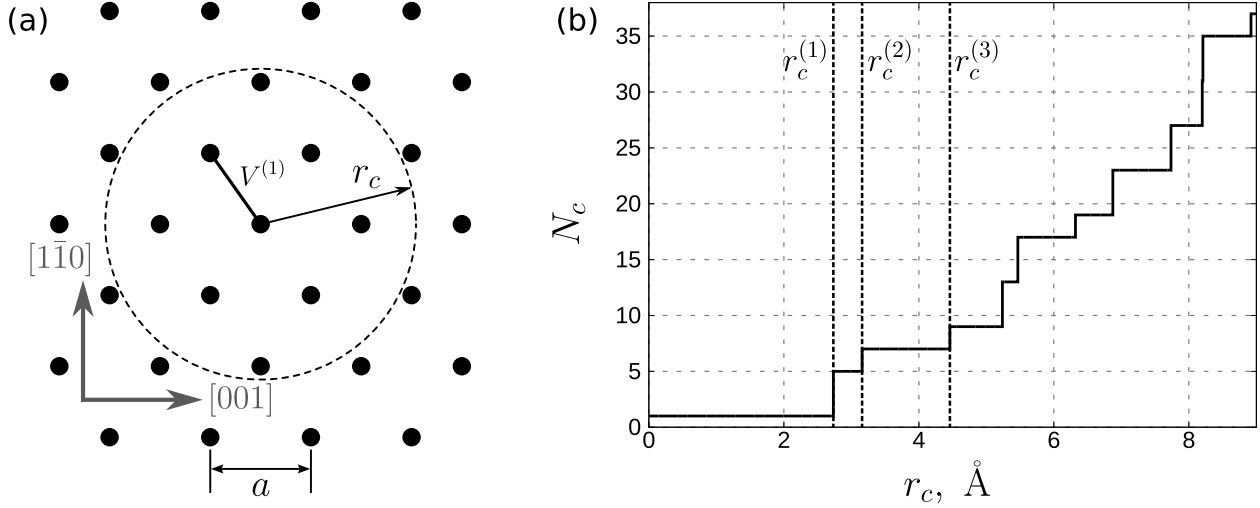


FIG. 5. (a) Positions of Fe-atoms in a monolayer of Fe on a W(110) surface. (b) Number of Fe atoms inside a coordination sphere of radius, r_c , in a Fe monolayer on a W(110) surface.

The parameters \tilde{E}^0 and \tilde{U} in the NCAA model were chosen to have values that are typical for Fe: -12 and 13, respectively [7]. For simplicity, only nearest neighbor hopping parameters were included and the value $\tilde{V} = 0.9$ was chosen to reproduce DFT calculated magnetization of an Fe overlayer on a W(110) surface [35].

A self-consistent calculation was carried out for a relatively large Fe island containing 17×17 atomic rows. Observe that due to the structure of the (110) surface the total number of atoms in the island is not equal to the product of the number of atomic rows along $[001]$ and $[1\bar{1}0]$ directions. Reference values of N^{ref} and M^{ref} at each Fe-atom were first calculated by including all 144 atoms explicitly. Then, approximate calculations were carried out for the same orientation of the magnetic vectors. The coordination sphere of a particular size was chosen for each atom in the island and corresponding self-consistent values of N and M evaluated and compared with the reference values. Fig. 6(a) shows the deviation in the number of d -electrons and the magnitude of the magnetic moments from the reference values as a function of the number of coordination spheres included. For both N and M , the error drops rapidly as ζ increases.

The MFT is a rigorous statement only when all atoms in the system are included explicitly. When the coordination sphere approximation is used, the theorem is, strictly speaking, not satisfied and the self-consistency state is no longer a stationary point of the energy as a function of the number of d -electrons and magnitude of the magnetic moments. This is illustrated in Fig. 6(b) where the derivative of the energy with respect to N and M as a function of ζ is shown. The magnitude of the derivative, however, vanishes as ζ increases.

Thus, the coordination sphere approximation can provide reasonably accurate results while significantly reducing the computational effort. After the system becomes larger than the

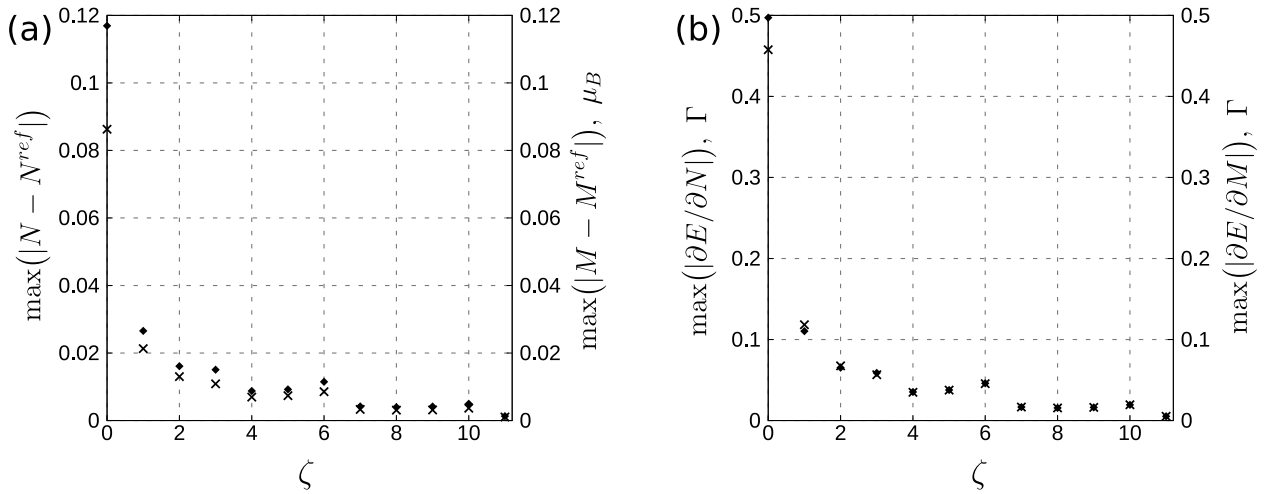


FIG. 6. (a) Maximum deviation of the number of d -electrons (crosses, and left vertical axis) and the magnitude of the magnetic momentum vectors (diamonds, and right vertical axis) from the reference values, N^{ref} and M^{ref} , as a function of the number of coordination shells included in the self-consistency calculation. (b) Maximum derivative of the energy, E , with respect to N (crosses) and M (diamonds), as a function of the number of coordination shells included in the self-consistency calculation.

chosen number of coordination shells included in the self-consistency calculation, the computational effort increases only linearly with the system size. The level of approximation can readily be increased by increasing ζ , i.e. including more coordination shells.

With this approximation, the NCAA model can be used to study large systems including thousands of non-equivalent atoms.

6. Summary

A detailed description of the NCAA model and its implementation is given in this article as well as an application to trimers of Cr, Mn and Fe adsorbed on a metal surface and a simple model for STM tip interaction with a dimer. While the Cr and Fe trimers are found to have collinear stable states, the former with antiferromagnetic ordering and the latter ferromagnetic, the Mn trimer has two different stable states, both non-collinear. In all three cases, the maximum energy configurations along the minimum energy path, i.e. first order saddle points on the energy surface, correspond to collinear ordering. These simple systems were chosen as illustrations of the method because the energy surface can be visualized easily. A finite range approximation is also presented which leads to linear scaling of the computational effort with the number of magnetic atoms in large systems. The theoretical approach described here can be used in studies of magnetism in $3d$ -metal systems, including simulations of spin dynamics and, in general, navigation on the energy surface characterizing such systems to find stable state and transition state for magnetic transitions.

Acknowledgements

This work was supported by the Government of Russian Federation (Grant No. 074-U01), RFBR Grants No. 14-02-00102, and No. 14-22-01113 ofi-m, the Icelandic Research Fund, University of Iceland research fund and the Nordic-Russian Training Network for Magnetic

Nanotechnology (NCM-RU10121). PB greatly acknowledges support from Göran Gustafsson Foundation.

APPENDIX

A. Recursion method and continued-fraction expansion of the Green function

An efficient algorithm for calculating the matrix elements of the Green function G (in this Appendix, a dependence of G on ϵ is implied) using the recursion method involves finding a new orthonormal basis in which the Hamiltonian has a tridiagonal form, while the matrix element to be evaluated, $G_{ij}^{\alpha\beta}$, remains unchanged.

We begin by discussing how diagonal matrix elements, $G_{\mu\mu} = \langle x_\mu | G | x_\mu \rangle$, can be evaluated. Here, $\{|x_1\rangle, \dots, |x_{2P}\rangle\}$ is an initial basis set and indices μ, ν enumerate both atomic site and spin projection. The first vector of the new basis is chosen so that $|y_1\rangle = |x_\mu\rangle$. Then, the diagonal matrix element of the Green function is given by:

$$G_{\mu\mu} = \langle y_1 | G | y_1 \rangle = \tilde{G}_{11}, \quad (41)$$

where tilde indicates a quantity in the new basis. Other vectors of the new basis $\{|y_1\rangle, \dots, |y_{2P}\rangle\}$ are found given that the Hamiltonian has a tridiagonal form:

$$\tilde{H}_{\mu\nu} = \begin{pmatrix} a_1 & b_1 & 0 & 0 & \dots & 0 & 0 & 0 \\ b_1 & a_2 & b_2 & 0 & \dots & 0 & 0 & 0 \\ 0 & b_2 & a_3 & b_3 & \dots & 0 & 0 & 0 \\ \vdots & \vdots & \vdots & \vdots & \ddots & \vdots & \vdots & \vdots \\ 0 & 0 & 0 & 0 & \dots & a_{2P-2} & b_{2P-2} & 0 \\ 0 & 0 & 0 & 0 & \dots & b_{2P-2} & a_{2P-1} & b_{2P-1} \\ 0 & 0 & 0 & 0 & \dots & 0 & b_{2P-1} & a_{2P} \end{pmatrix}. \quad (42)$$

Not only basis vectors $|y_\mu\rangle$ are found within the recursion scheme, but also elements $\{a_1, a_2, \dots, a_{2P}\}$ and $\{b_1, b_2, \dots, b_{2P-1}\}$ are successively calculated. From the equation:

$$H |y_1\rangle = a_1 |y_1\rangle + b_1 |y_2\rangle, \quad (43)$$

the second basis vector $|y_2\rangle$ as well as a_1 and b_1 can be found as follows:

$$a_1 = \langle y_1 | H |y_1\rangle, \quad (44)$$

$$b_1 = \|H |y_1\rangle - a_1 |y_1\rangle\|, \quad (45)$$

$$|y_2\rangle = \frac{H |y_1\rangle - a_1 |y_1\rangle}{b_1}. \quad (46)$$

Then, the Hamiltonian acts upon the second basis vector and the next portion of elements of the tridiagonal matrix is found. This operation is reapplied until all elements of H in the new basis have been calculated. For example, on the k -th step ($k < 2P$), when a_1, \dots, a_{k-1} , b_1, \dots, b_{k-1} and $|y_1\rangle, \dots, |y_k\rangle$ are known, we have:

$$a_k = \langle y_k | H |y_k\rangle, \quad (47)$$

$$b_k = \|H |y_k\rangle - b_{k-1} |y_{k-1}\rangle - a_k |y_k\rangle\|, \quad (48)$$

$$|y_{k+1}\rangle = \frac{H |y_k\rangle - b_{k-1} |y_{k-1}\rangle - a_k |y_k\rangle}{b_k}. \quad (49)$$

\tilde{G}_{11} is found in the following way. Let us introduce a notation:

$$\lambda_k = \langle y_1 | G | y_k \rangle. \quad (50)$$

The following set of equations is then valid for λ_k , which follows from the definition of the Green function, $(\epsilon - H)G = I$:

$$\begin{cases} (\epsilon - a_1) \lambda_1 - b_1 \lambda_2 = 1, \\ (\epsilon - a_k) \lambda_k - b_{k-1} \lambda_{k-1} - b_k \lambda_{k+1} = 0, & k \neq 1, k \neq 2P, \\ (\epsilon - a_{2P}) \lambda_{2P} - b_{2P-1} \lambda_{2P-1} = 0. \end{cases}$$

After straightforward algebra, we obtain the representation of \tilde{G}_{11} in the continued-fraction form:

$$G_{\mu\mu} = \tilde{G}_{11} = \lambda_1 = \frac{1}{\epsilon - a_1 - \frac{b_1^2}{\epsilon - a_2 - \frac{b_2^2}{\dots - \frac{b_{2P-1}^2}{\epsilon - a_{2P}}}}} \quad (51)$$

The nondiagonal elements of the Green function can also be expanded in terms of continued fractions. Namely, if $G_{\mu\nu}$, $\mu \neq \nu$, is to be found, one has to perform tridiagonalization four times, where the starting vectors are:

$$\begin{aligned} |y_1^a\rangle &= \frac{1}{\sqrt{2}} (|x_\mu\rangle + |x_\nu\rangle), \\ |y_1^b\rangle &= \frac{1}{\sqrt{2}} (|x_\mu\rangle - |x_\nu\rangle), \\ |y_1^c\rangle &= \frac{1}{\sqrt{2}} (|x_\mu\rangle + i|x_\nu\rangle), \\ |y_1^d\rangle &= \frac{1}{\sqrt{2}} (|x_\mu\rangle - i|x_\nu\rangle). \end{aligned}$$

In each basis, matrix element $\tilde{G}_{11}^\zeta = \langle y_1^\zeta | G | y_1^\zeta \rangle$, $\zeta = a, b, c, d$, is expanded in terms of continued fractions as described above. Continued-fraction representation of the real and imaginary part of the nondiagonal element, $G_{\mu\nu}$, is thus given by:

$$\text{Re } G_{\mu\nu} = \frac{1}{2} (\tilde{G}_{11}^a - \tilde{G}_{11}^b), \quad (52)$$

$$\text{Im } G_{\mu\nu} = \frac{1}{2} (\tilde{G}_{11}^d - \tilde{G}_{11}^c). \quad (53)$$

B. Partial-fraction expansion of the Green function

We proceed with the continued-fraction representation of the matrix element of the Green function, Eqn. (51). Let us consider the last level of the continued fraction:

$$f^{(1)}(\epsilon) = \epsilon - a_{2P-1} - \frac{b_{2P-1}^2}{\epsilon - a_{2P}}. \quad (54)$$

If $b_{2P-1} \neq 0$, then the equation $f^{(1)}(\epsilon) = 0$ has two real roots, $q_1^{(2)}$ and $q_2^{(2)}$, $q_1^{(2)} < q_2^{(2)}$, which can be found either analytically or numerically. Then:

$$f^{(1)}(\epsilon) = \frac{(\epsilon - q_1^{(2)}) (\epsilon - q_2^{(2)})}{\epsilon - q_1^{(1)}},$$

where $q_1^{(1)} \equiv a_{2P}$. As a result, the next level of the continued fraction acquires the form:

$$f^{(2)}(\epsilon) = \epsilon - a_{2P-2} - \frac{b_{2P-2}^2 (\epsilon - q_1^{(1)})}{(\epsilon - q_1^{(2)}) (\epsilon - q_2^{(2)})}.$$

The ratio of polynomials here can be transformed into a sum of two partial fractions:

$$\frac{b_{2P-2}^2 (\epsilon - q_1^{(1)})}{(\epsilon - q_1^{(2)}) (\epsilon - q_2^{(2)})} = \frac{p_1^{(2)}}{\epsilon - q_1^{(2)}} + \frac{p_2^{(2)}}{\epsilon - q_2^{(2)}},$$

where

$$p_1^{(2)} = b_{2P-2}^2 \frac{q_1^{(2)} - q_1^{(1)}}{q_1^{(2)} - q_2^{(2)}}, \quad p_2^{(2)} = b_{2P-2}^2 \frac{q_2^{(2)} - q_1^{(1)}}{q_2^{(2)} - q_1^{(2)}}.$$

Thus, the function $f^2(\epsilon)$ is represented in the form analogous to Eqn. (54):

$$f^{(2)}(\epsilon) = \epsilon - a_{2P-2} - \frac{p_1^{(2)}}{\epsilon - q_1^{(2)}} - \frac{p_2^{(2)}}{\epsilon - q_2^{(2)}}, \tag{55}$$

and the number of levels in the continued fraction is reduced by one.

The same technique is sequentially applied in order to transform the continued fraction into a sum of partial fractions. For example, at the k -th step we have:

$$f^{(k)}(\epsilon) = \epsilon - a_{2P-k} - \sum_{j=1}^k \frac{p_j^{(k)}}{\epsilon - q_j^{(k)}}. \tag{56}$$

Zeros of the function $f^{(k)}(\epsilon)$ are well separated (see Fig. 7) and can be found numerically without problems.

The function $f^{(k+1)}(\epsilon)$ is then represented as follows:

$$f^{(k+1)}(\epsilon) = \epsilon - a_{2P-k-1} - \sum_{j=1}^{k+1} \frac{p_j^{(k+1)}}{\epsilon - q_j^{(k+1)}}.$$

Here $q_1^{(k+1)}, \dots, q_{k+1}^{(k+1)}$ are the roots of $f^{(k)}(\epsilon) = 0$ and $p_j^{(k+1)}$ are given by:

$$p_j^{(k+1)} = b_{2P-k-1}^2 \frac{\prod_{i=1}^k (q_j^{(k+1)} - q_i^{(k)})}{\prod_{\substack{i=1 \\ i \neq j}}^{k+1} (q_j^{(k+1)} - q_i^{(k+1)})}.$$

As a result, any continued fraction of the form (51) and thus an arbitrary element of the Green function can be expanded in a sum of partial fractions (see Eqn. (29)).

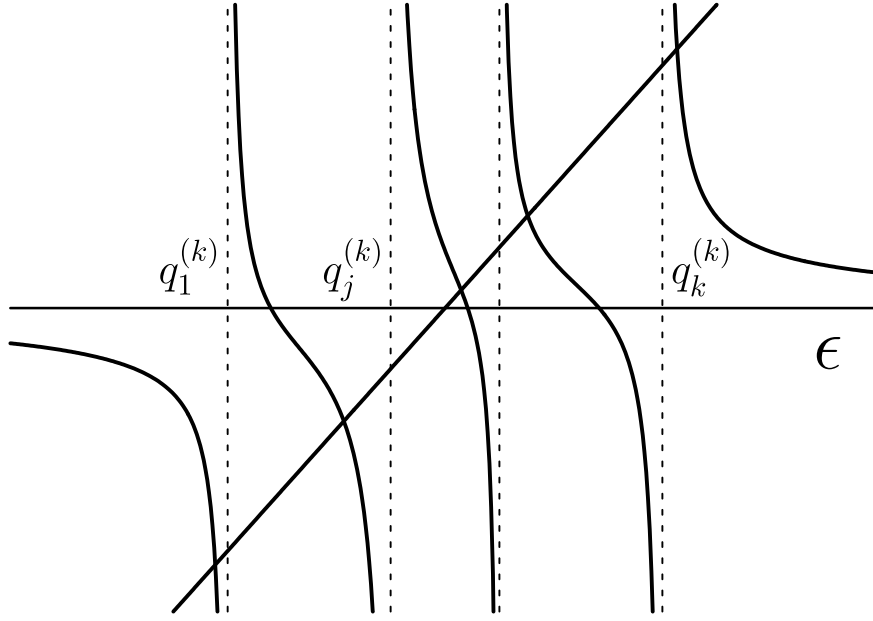


FIG. 7. Graphical solution of the equation $f^{(k)}(\epsilon) = 0$. Exactly one root is located between poles $q_1^{(k)}, \dots, q_k^{(k)}$ of $f^{(k)}(\epsilon)$.

C. Proof of lemmas (32) and (33)

We proceed with the equation for the matrix elements of the Green function:

$$(\epsilon - E_i^\alpha) G_{ij}^{\alpha\beta}(\epsilon) - \sum_{k,\gamma} V_{ik}^{\alpha\gamma} G_{kj}^{\gamma\beta}(\epsilon) = \delta^{\alpha\beta} \delta_{ij}. \quad (57)$$

This equation can be solved iteratively giving the following result for the diagonal elements of the Green function:

$$\begin{aligned} G_{ii}^{\alpha\alpha}(\epsilon) = & \frac{1}{\epsilon - E_i^\alpha} + \sum_{\gamma,k} \frac{V_{ik}^{\alpha\gamma} V_{ki}^{\gamma\alpha}}{(\epsilon - E_i^\alpha)(\epsilon - E_k^\gamma)(\epsilon - E_i^\alpha)} + \dots \\ & + \sum_{\substack{\gamma_1, \dots, \gamma_n \\ k_1, \dots, k_n}} \frac{V_{ik_1}^{\alpha\gamma_1} V_{k_1 k_2}^{\gamma_1 \gamma_2} \dots V_{k_n i}^{\gamma_n \alpha}}{(\epsilon - E_i^\alpha)(\epsilon - E_{k_1}^{\gamma_1}) \dots (\epsilon - E_{k_n}^{\gamma_n})(\epsilon - E_i^\alpha)} + \dots \end{aligned} \quad (58)$$

where summation over k_1, k_2, \dots, k_n and $\gamma_1, \gamma_2, \dots, \gamma_n$ runs over all atomic sites and spin projections, respectively. Each term in Eq. (58) can be considered as a sequence of vertices forming a path with endpoints at (α, i) :

$$(\alpha, i) \rightarrow (\gamma_1, k_1) \rightarrow (\gamma_2, k_2) \rightarrow \dots \rightarrow (\gamma_n, k_n) \rightarrow (\alpha, i) \equiv \frac{V_{ik_1}^{\alpha\gamma_1} V_{k_1 k_2}^{\gamma_1 \gamma_2} \dots V_{k_n i}^{\gamma_n \alpha}}{(\epsilon - E_i^\alpha)(\epsilon - E_{k_1}^{\gamma_1}) \dots (\epsilon - E_{k_n}^{\gamma_n})}. \quad (59)$$

Therefore, $G_{ii}^{\alpha\alpha}(\epsilon)$ can be thought of as the sum of all such closed paths. Each path describes some multiple scattering process, where a single scattering event ('hopping') can be either an on-site spin-flip or a non-spin-flip intersite transition. The sum of all possible paths of the same

length and endpoints fixed at (α, i) can be represented as:

$$\sum_{\substack{\gamma_1, \dots, \gamma_n \\ k_1, \dots, k_n}} \frac{V_{ik_1}^{\alpha\gamma_1} V_{k_1 k_2}^{\gamma_1 \gamma_2} \dots V_{k_n i}^{\gamma_n \alpha}}{(\epsilon - E_i^\alpha)(\epsilon - E_{k_1}^{\gamma_1}) \dots (\epsilon - E_{k_n}^{\gamma_n})(\epsilon - E_i^\alpha)} = [G_0(\epsilon) \underbrace{V G_0(\epsilon) V \dots V G_0(\epsilon)}_{n+1 \text{ V-factors}}]_{ii}^{\alpha\alpha} \equiv S_{ii}^{\alpha\alpha}(\epsilon; n). \quad (60)$$

Here, V is a hopping matrix (see Eq. (19)) which contains information about all scattering events in the system and $G_0(\epsilon)$ is the Green function for the non-interacting magnetic impurities. $G_0(\epsilon)$ is diagonal and its matrix elements are given by:

$$[G_0(\epsilon)]_{ii}^{\alpha\alpha} = \frac{1}{(\epsilon - E_i^\alpha)}. \quad (61)$$

In order to prove lemmas (32)-(33), it is sufficient to derive corresponding identities for the sum of the paths, $S(\epsilon; n)$, for an arbitrary path length, n . The derivative of $\text{Tr } S(\epsilon; n)$ with respect to N_i is given by:

$$\begin{aligned} \frac{\partial}{\partial N_i} \text{Tr } S(\epsilon; n) &= \frac{\partial}{\partial N_i} \text{Tr} [G_0(\epsilon) V G_0(\epsilon) V \dots V G_0(\epsilon)] = \text{Tr} \left[\frac{\partial G_0(\epsilon)}{\partial N_i} V G_0(\epsilon) V \dots V G_0(\epsilon) \right] \\ &+ \text{Tr} \left[G_0(\epsilon) V \frac{\partial G_0(\epsilon)}{\partial N_i} V \dots V G_0(\epsilon) \right] + \dots + \text{Tr} \left[G_0(\epsilon) V G_0(\epsilon) V \dots V \frac{\partial G_0(\epsilon)}{\partial N_i} \right]. \end{aligned} \quad (62)$$

Only two matrix elements of $\frac{\partial G_0(\epsilon)}{\partial N_i}$ are non-zero (see Eq. (61)). According to Eqs. (61) and (18), they can be expressed in terms of derivatives with respect to ϵ :

$$\frac{\partial G_0(\epsilon)}{\partial N_i} = -\frac{U_i}{2} \frac{\partial G_0(\epsilon)}{\partial \epsilon} \Sigma_i^0, \quad (63)$$

where Σ_i^0 is $2P \times 2P$ matrix defined so that only the elements $(+, +, ii)$ and $(-, -, ii)$ are equal to unity, while the others are zero. Therefore, Eq. (62) takes the form:

$$\begin{aligned} \frac{\partial}{\partial N_i} \text{Tr } S(\epsilon; n) &= -\frac{U_i}{2} \left\{ \text{Tr} \left[\frac{\partial G_0(\epsilon)}{\partial \epsilon} \Sigma_i^0 V G_0(\epsilon) V \dots V G_0(\epsilon) \right] \right. \\ &+ \text{Tr} \left[G_0(\epsilon) V \frac{\partial G_0(\epsilon)}{\partial \epsilon} \Sigma_i^0 V \dots V G_0(\epsilon) \right] \\ &+ \dots + \text{Tr} \left[G_0(\epsilon) V G_0(\epsilon) V \dots V \frac{\partial G_0(\epsilon)}{\partial \epsilon} \Sigma_i^0 \right] \left. \right\}. \end{aligned} \quad (64)$$

The factor $\frac{\partial G_0(\epsilon)}{\partial \epsilon} \Sigma_i^0$ found in every term in the curly brackets can be transformed into:

$$\frac{\partial G_0(\epsilon)}{\partial \epsilon} \Sigma_i^0 = -G_0(\epsilon) \Sigma_i^0 G_0(\epsilon), \quad (65)$$

where use has been made of the identity

$$\frac{\partial G_0(\epsilon)}{\partial \epsilon} = -G_0^2(\epsilon), \quad (66)$$

as well as commutativity of $G_0(\epsilon)$ and Σ_i^0 . Using Eqs. (65) and (66) and invariance of a trace under cyclic permutations, each term in Eq. (64) is transformed to obtain the following:

$$\begin{aligned} \frac{\partial}{\partial N_i} \text{Tr} S(\epsilon; n) &= -\frac{U_i}{2} \left\{ \text{Tr} \left[\Sigma_i^0 \frac{\partial G_0(\epsilon)}{\partial \epsilon} V G_0(\epsilon) V \dots V G_0(\epsilon) \right] \right. \\ &+ \text{Tr} \left[\Sigma_i^0 G_0(\epsilon) V \frac{\partial G_0(\epsilon)}{\partial \epsilon} V \dots V G_0(\epsilon) \right] \\ &+ \dots + \text{Tr} \left[\Sigma_i^0 G_0(\epsilon) V G_0(\epsilon) V \dots V \frac{\partial G_0(\epsilon)}{\partial \epsilon} \right] \left. \right\} = -\frac{U_i}{2} \frac{\partial}{\partial \epsilon} \text{Tr} \left[\Sigma_i^0 G_0(\epsilon) V G_0(\epsilon) V \dots V G_0(\epsilon) \right] = \\ &= -\frac{U_i}{2} \frac{\partial}{\partial \epsilon} \text{Tr} \left[\Sigma_i^0 S(\epsilon; n) \right] = -\frac{U_i}{2} \frac{\partial}{\partial \epsilon} \left(S_{ii}^{++}(\epsilon; n) + S_{ii}^{--}(\epsilon; n) \right), \end{aligned} \quad (67)$$

which proves Lemma (32).

Lemma (33) is proved in a similar way. However, when computing the derivative of $\text{Tr} S(\epsilon; n)$ with respect to M_i , one needs to observe that both $G_0(\epsilon)$ and V depend on M_i . More specifically:

$$\frac{\partial G_0(\epsilon)}{\partial M_i} = \frac{U_i}{2} \cos \theta_i \frac{\partial G_0(\epsilon)}{\partial \epsilon} \Sigma_i^z, \quad (68)$$

$$\frac{\partial V}{\partial M_i} = -\frac{U_i}{2} \sin \theta_i (\cos \phi_i \Sigma_i^x + \sin \phi_i \Sigma_i^y). \quad (69)$$

The only nonzero matrix elements of Σ_i^x , Σ_i^y and Σ_i^z are defined as follows:

$$(\Sigma_i^x)_{ii}^{+-} = 1 \quad (\Sigma_i^x)_{ii}^{-+} = 1, \quad (70)$$

$$(\Sigma_i^y)_{ii}^{+-} = -i \quad (\Sigma_i^y)_{ii}^{-+} = i, \quad (71)$$

$$(\Sigma_i^z)_{ii}^{++} = 1 \quad (\Sigma_i^z)_{ii}^{--} = -1. \quad (72)$$

Note that if only one magnetic impurity is present in the system, Σ_i^x , Σ_i^y and Σ_i^z coincide with ordinary 2×2 Pauli matrices. This gives the following:

$$\begin{aligned} \frac{\partial}{\partial M_i} \text{Tr} S(\epsilon; n) &= \frac{U_i}{2} \cos \theta_i \frac{\partial}{\partial \epsilon} \text{Tr} \left[\Sigma_i^z G_0(\epsilon) V G_0(\epsilon) V \dots V G_0(\epsilon) \right] + \\ &\frac{U_i}{2} \sin \theta_i \frac{\partial}{\partial \epsilon} \left(\cos \phi_i \text{Tr} \left[\Sigma_i^x G_0(\epsilon) V G_0(\epsilon) V \dots V G_0(\epsilon) \right] + \sin \phi_i \text{Tr} \left[\Sigma_i^y G_0(\epsilon) V G_0(\epsilon) V \dots V G_0(\epsilon) \right] \right) \\ &= \frac{U_i}{2} \frac{\partial}{\partial \epsilon} \left\{ \cos \theta_i \text{Tr} \left[\Sigma_i^z S(\epsilon; n) \right] + \sin \theta_i \left(\cos \phi_i \text{Tr} \left[\Sigma_i^x S(\epsilon; n-1) \right] + \sin \phi_i \text{Tr} \left[\Sigma_i^y S(\epsilon; n-1) \right] \right) \right\} \\ &= \frac{U_i}{2} \frac{\partial}{\partial \epsilon} \left[\left(S_{ii}^{++}(\epsilon; n) - S_{ii}^{--}(\epsilon; n) \right) \cos \theta_i + \left(S_{ii}^{+-}(\epsilon; n-1) e^{\phi_i} + S_{ii}^{-+}(\epsilon; n-1) e^{-\phi_i} \right) \sin \theta_i \right], \end{aligned} \quad (73)$$

which proves lemma (33).

For large (or infinite) systems, the calculation of Green functions is often performed approximately, using a finite range approximation (see Sec. 5) or by truncating the recursion method (see appendix A) at a certain step. In this case, the scattering matrix V_i may be different for different sites i and Lemmas (32)-(33) and, therefore, the MFT, are strictly not valid. This was demonstrated in Sec. 5 where direct calculations of the derivatives of energy with respect to N_i and M_i for the self-consistent values N_i^* and M_i^* were found not to equal zero because of the finite range approximation. However, if any subsystem of atoms is chosen and the same

set of hopping contributions are included for all the atoms of this subsystem, then the scattering matrix will be the same for all atoms in the system and the proof of Lemmas (32)-(33) will hold just as in the case when all atoms and hopping contributions are included. In particular, one can choose as a subsystem the atoms included in one closed loop in Eqn.(59) and the corresponding hopping contributions to form the scattering matrix V . Then, the MFT will be valid for this subsystem. Formally, it is a consequence of the fact that all closed paths in Eqn.(59) which make a contribution to the matrix element of the Green function G_{ii} , make the same contribution to any G_{jj} if the path in Eqn.(59) goes through site j . If, however, we try to improve the calculation by taking into account additional atoms and hopping contributions that are different for different atoms, as in the case of the finite range approximation described in Sec. 5, then the MFT is violated.

References

- [1] R. Wiesendanger. Spin mapping at the nanoscale and atomic scale. *Rev. Mod. Phys.*, **81**, 1495 (2009).
- [2] S. Heinze, K. von Bergmann, et al. Spontaneous atomic-scale magnetic skyrmion lattice in two dimensions. *Nature Phys.* **7**, 713 (2011).
- [3] M. Bode, O. Pietzsch, et al. Experimental Evidence for Intra-Atomic Noncollinear Magnetism at Thin Film Probe Tips. *Phys. Rev. Lett.* **86**, 2142 (2001).
- [4] P.F. Bessarab, V.M. Uzdin, H. Jónsson. Harmonic transition state theory of thermal spin transitions. *Phys. Rev. B* **85**, 184409 (2012).
- [5] H.B. Braun. Topological effects in nanomagnetism: from superparamagnetism to chiral quantum solitons. *Advances in Physics* **61**, 1 (2012).
- [6] P.F. Bessarab, V.M. Uzdin, H. Jónsson. Size and shape dependence of thermal spin transitions in nanoislands. *Phys. Rev. Lett.* **110**, 020604 (2013).
- [7] P.F. Bessarab, V.M. Uzdin, H. Jónsson. Potential Energy Surfaces and Rates of Spin Transitions. *Z. Phys. Chem.* **227**, 1543 (2013).
- [8] T. Oda, A. Pasquarello, R. Car. Fully Unconstrained Approach to Noncollinear Magnetism: Application to Small Fe Clusters. *Phys. Rev. Lett.* **80**, 3622 (1998).
- [9] O. Ivanov, V.P. Antropov. Molecular magnetism: Noncollinear ordering and spin dynamics. *J. Appl. Phys.* **85**, 4821 (1999).
- [10] L. Nordström, D.J. Singh. Noncollinear intra-atomic magnetism. *Phys. Rev. Lett.* **76**, 4420 (1996).
- [11] V.P. Antropov, M.I. Katsnelson, et al. Spin dynamics in magnets: equation of motion and finite temperature effects. *Phys. Rev. B* **54**, 1019-1035 (1996).
- [12] L.M. Small, V. Heine. A couple method for calculating interatomic interactions in itinerant electron magnetic systems. *J. Phys. F* **14**, 3041 (1986).
- [13] G. Bihlmayer, 'Density-functional theory of magnetism', in '*Handbook of magnetism and advanced magnetic materials*', ed. H. Kronmüller, S. Parkin. Vol. 1, page 3.
- [14] L.M. Sandratskii. Noncollinear magnetism in itinerant-electron systems: Theory and applications. *Advances in Physics* **47**, 91 (1998).
- [15] G.M. Stocks, B. Ujfalussy, et al. Towards a constrained local moment model for first principles spin dynamics. *Philos. Mag. B* **78**, 665 (1998).
- [16] S. Lounis, P.H. Dederichs. Mapping the magnetic exchange interactions from first principles: Anisotropy anomaly and application to Fe, Ni, and Co. *Phys. Rev. B* **82**, 180404(R) (2010).
- [17] P.W. Anderson. Localized Magnetic States in Metals. *Phys. Rev.* **124**, 41 (1961).
- [18] S. Alexander, P.W. Anderson. Interaction between localized states in metals. *Phys. Rev.* **133**, A1594 (1964).
- [19] R. Haydock, V. Heine, M.J. Kelly. Electronic structure based on the local atomic environment for tight-binding bands. *J. Phys. C: Solid State Phys.* **5**, 2845 (1972).
- [20] R. Haydock, V. Heine, M.J. Kelly. Electronic structure based on the local atomic environment for tight-binding bands: II. *J. Phys. C: Solid State Phys.* **8**, 2591 (1975).
- [21] V.M. Uzdin, N.S. Yartseva. Periodic Anderson model for the description of noncollinear magnetic structure in low-dimensional 3d-systems. *Comput. Mater. Sci.* **10**, 211 (1998).
- [22] S.V. Uzdin. On the calculation of the magnetic structure of surfaces, near surface layers, and interfaces of 3d metals. *Physics of the Solid State* **51**, 1260 (2009).

- [23] P.F. Bessarab, V.M. Uzdin, H. Jónsson. Calculations of magnetic states and minimum energy paths of transitions using a noncollinear extension of the Alexander-Anderson model and a magnetic force theorem. *Phys. Rev. B* **89**, 214424 (2014).
- [24] S. Uzdin, V. Uzdin, C. Demangeat. Magnetic trimer on non-magnetic substrate: from frustration towards non-collinearity. *Europhys. Lett.* **47**, 556 (1999).
- [25] S. Uzdin, V. Uzdin, C. Demangeat. Non-collinear structure of Cr trimer on the surface of non-magnetic metals. *Comput. Mater. Sci.* **17**, 441 (2000).
- [26] S. Uzdin, V. Uzdin, C. Demangeat. Non-collinear magnetism of Cr, Mn and Fe trimers supported on the non-magnetic metal surface. *Surf. Sci.* **482**, 965 (2001).
- [27] H.J. Gotsis, N. Kioussis, D.A. Papaconstantopoulos. Evolution of magnetism of Cr nanoclusters on Au(111): First-principles electronic structure calculations. *Phys. Rev. B* **73**, 014436 (2006).
- [28] A. Bergman, L. Nordström, et al. Magnetic interactions of Mn clusters supported on Cu. *Phys. Rev. B* **73**, 174434 (2006).
- [29] K. Hirai. Electronic Structure of Helical Spin Density Wave State in fcc Iron. *J. Phys. Soc. of Jpn.* **61**, 2491 (1992).
- [30] S. Lounis, P. Mavropoulos, P.H. Dederichs, S. Blügel. Noncollinear Korringa-Kohn-Rostoker Green function method: Application to 3d nanostructures on Ni (001). *Phys. Rev. B* **72**, 224437 (2005).
- [31] R. Robles, L. Nordström. Noncollinear magnetism of Cr clusters on Fe surfaces. *Phys. Rev. B* **74**, 094403 (2006).
- [32] H. Jónsson, G. Mills, K.W. Jacobsen. In *Classical and Quantum Dynamics in Condensed Phase Simulations*, edited by B.J. Berne, G. Ciccotti, D. F. Coker (World Scientific, Singapore, 1998), p. 385.
- [33] G. Henkelman, H. Jónsson. 'Improved Tangent Estimate in the NEB Method for Finding Minimum Energy Paths and Saddle Points'. *J. Chem. Phys.* **113**, 9978 (2000).
- [34] R. Schmidt, A. Schwarz, R. Wiesendanger. Ground State of Magnetic Dimers on Metal Surfaces. *Phys. Rev. B* **86** 174402 (2012).
- [35] A.T. Costa, R.B. Muniz, et al. Magnetism of an Fe monolayer on W(110). *Phys. Rev. B* **78** 054439 (2008).

THE EFFECT OF THE CELL PHONE RADIATION ON A FREELY SUSPENDED LIQUID-CRYSTAL FILMS

A. A. Bogdanov¹, S. P. Denisov², A. A. Karetnikov³,
A. P. Kovshik³, V. P. Romanov³, D. Brukkel²

¹The Federal State Budgetary Institute “The Nikiforov Russian Center of Emergency and Radiation Medicine”, Saint Petersburg, Russia

²Center of Informatics “GAMMA-7”, Moscow, Russia

³Saint Petersburg State University, Saint Petersburg, Russia
sashakovshik@yandex.ru

PACS 61.30.-v, 42.25.Lc, 42.70.Df, 41.85.Ct

The article presents the results of an experimental study of the effect of the radiofrequency radiation (RF) of a cell phone on a freely suspended liquid-crystal film (FSLCF) as a system that simulates biological structures. The selection of the FSLCF model is theoretically substantiated. A polarizing microscope with a video camera was used to visualize the process under study. The reaction of the FSLCF was analyzed using a specially developed software. The responses of the FSLCF were studied for exposure to the RF radiation in the presence of protective device Gamma 7.N-RT and for the action of a static magnetic field of strength 500 Oe. The RF radiation of a cell phone was found to change the orientation structure of the FSLCF, which, after some time, returns to the nearly initial level despite the presence of external field. The protective device Gamma 7.N-RT attenuates the reaction of the FSLCF. The response of the FSLCF in a static magnetic field remains unchanged during the exposure to the field. These experimental results are evidence that the structure of the freely suspended liquid-crystal film is a viable model for biological structures, and is capable of adapting to the effect of the RF radiation emitted by a cell phone.

Keywords: biological structures, liquid-crystal film, electromagnetic fields, orientation structure.

Received: 31 October 2014

1. Introduction

The intense advancement of wireless technologies and the spread of mobile telecommunication facilities in every-day life are among the primary reasons that people are persistently under the influence of low-energy RF electromagnetic fields. Despite the fact that there are numerous studies [1–4] on the matter, the issue of the biological effects of low-intensity electromagnetic fields on human and other organisms remains debatable [5–7].

The electromagnetic wave energy of a cell phone’s RF radiation is known to be insufficient to break chemical bonds. The revealed biological effects are discussed primarily in terms of the thermal exposure of electromagnetic radiation (EMR) [8]. However, a number of nonthermal biological effects caused by low-energy electromagnetic radiation are described in the literature [3,4]. These studies have questioned the hypothesis of the thermal nature of the biological effects and the currently accepted safety levels of the EMR. These effects, caused by the low-energy electromagnetic radiation comprise the increased permeability of the blood-brain barrier, changing the expression of heat shock genes, impaired calcium homeostasis, reduction of melatonin synthesis, etc. [4,9–11]. These biological effects can modify adaptive

processes in the organism. Therefore, studying the adaptive response patterns at different levels for the organism structure under exposure to low-energy EMR is an important and urgent task both in terms of understanding of the biological action mechanisms and assessing the hazard this factor presents to human health.

In addition to the biological research, it is of interest to study the effect of the RF radiation on the systems that simulate real biological objects. The advantage for such studies is that these make it possible to obtain quantitative data, permitting rigorous theoretical analysis.

Many biological structures are known to possess a number of properties which are typical for liquid crystals [12]. These include chloroplasts, visual receptors, muscle, nerve, cell membranes, etc. Therefore, a study of the influence of the RF radiation on the model crystal structures may elucidate some of the mechanisms of biological reactions to this radiation.

Nematic liquid crystals are highly sensitive to the effects of external electric and magnetic fields [13]. This makes liquid crystals the basis for displays as well as systems of information transfer and storage. First of all, these are light modulators, displays, monitors, etc. In these devices, a thin layer of the liquid crystal is placed between the glass surfaces that preset the specific direction of the optical axis of the liquid crystal (the direction of the preferred orientation of the molecules). Under the action of an external electric field of a sufficient strength that exceeds the threshold value, the direction of the optical axis alters, which affects the intensity of light passing through the liquid-crystal layer.

The energy density W required to change the orientation direction of the liquid crystal placed between the glass surfaces is estimated by the relation [14]:

$$W \sim \frac{K}{d^2},$$

where d is the layer thickness and K is the modulus of orientation elasticity of the order of 10^{-6} dyn [13]. For the oriented layers with a thickness of 3 to 30 μm the energy density required to change the direction of orientation of the liquid crystal is on the order of $W \sim 0.1 - 10 \text{ erg/cm}^3$, which is much larger than that of cell phone RF radiation.

In all likelihood, the orientation of liquid-crystal structures in biological objects is fixed more weakly than on the solid surfaces of technical devices. Therefore, to cope with the stated problem, we used a freely suspended film of a nematic liquid crystal as a liquid-crystal system, which, in our opinion, is most similar to biological structures and could be responsive to the RF radiation of cell phones. In such a film, the process of changing the direction of the preferred orientation of the liquid crystal molecules is nonthreshold [15]. The energy density required for the reorientation of the liquid crystal in a freely suspended film or for the disordered-to-ordered state formation by an external field is estimated as K/L^2 , where L is the dimension within which the external field can be considered homogeneous. This value is on the order of several fractions of millimeter to several millimeters. For these fields, the energy density required for the reorientation is on the order of $W \sim K/L^2 \sim 10^{-5} - 10^{-3} \text{ erg/cm}^2$, that is, by several orders of magnitude lower than that required for the reorientation of a liquid crystal placed between the solid surfaces. It is the nonthreshold nature of the reorientation in a freely suspended liquid-crystal film that can provide its extremely high sensitivity to the external effects.

Cell phone radiation density near the phone is known to be on the order of 2-20 mW/cm^2 . The dielectric constant of liquid crystal at frequencies of several GHz is approximately 3. This means that the energy density acting on the liquid crystal inside the film amounts to $10^{-6} - 10^{-5} \text{ erg/cm}^3$. By an order of magnitude, this energy density is comparable with the energy of the orientational ordering. The aim of this study is to

investigate the effect of cell phone RF radiation on freely suspended films of a nematic liquid crystal.

2. Materials and Methods

To study the effects of the RF radiation on the freely suspended liquid-crystal film, we used an experimental setup that enabled us to visually observe and record the structural changes in the film. The setup comprised a polarizing microscope POLAM L-213M equipped with a video camera DCM-130 with a 1.3 megapixel photodetector array, and a PC with a display. The liquid-crystal film was composed of a binary mixture of alkylcyanobiphenyls was suspended on the wall of a circular aperture 2 mm in diameter in a plastic plate 0.5-mm thick and placed on the stage of the polarizing microscope. A cell phone Nokia-3110, operating in the signal transmission mode, was placed at a distance of 2 cm from the film. The linearly polarized light flux was directed normal to the film surface and arrived at the video camera through the objective of the microscope. The digitized 40-fold zoomed image was transmitted to the PC for viewing and recording. The light source was an incandescent lamp energized from a rectifier or a battery-powered LED.

The response of the liquid-crystal film to the influence of the RF radiation was assessed visually by changes in the distribution of light intensity and its color spectrum.

To compare the responses to different EM field effects, the freely suspended liquid-crystal film was also subjected to the action of a static magnetic field of strength 500 Oe.

Quantification of the freely suspended liquid-crystal film's reaction was performed using specially developed software. The observation field was selected as a section of the film free of the boundary effects occurring at the contact of the film with the aperture wall [16]. The image analysis technique is based on the count of the number of pixels with different color codes in the RGB24 system. At the first stage, the number of pixels of each color code in each frame was calculated and a histogram was constructed. At the second stage, the number of non-recurrent color codes was determined from the histogram (the number of columns that contain non-zero values).

At the third stage, the ratio of the absolute number of the color codes per frame K and the minimum number of the color codes during the observation period M was calculated. The time dependences of the expression $(K/M) - 1 = N$ were plotted as graphs of the dynamic series.

3. The results of measurements

In the absence of a cell phone electromagnetic field (Fig. 1a), the freely suspended liquid-crystal film has, at equilibrium, an anisotropic structure with a nonuniform spatial distribution of the predominant direction of the long axes of the molecules (the local optical axis). This structure is formed under the action of the orienting forces of the molecules of the surface layer, the cylindrical wall of the aperture at which the film is attached and, possibly, the electromagnetic fields acting in this spatial region. The light flux passing through the system has a nonuniform distribution of the intensity and spectral composition in the field of observation due to the inhomogeneous distribution of the local optical axis of the film.

During the first minute of exposure to the cell phone's electromagnetic field the brightness and color of the film alter (interference fringes appear), which may be associated with a local change in the spatial distribution of the optical axis in the film. Having reached a maximum difference from the initial pattern (Fig. 1b), the image of the film changes again (interference fringes appear) and becomes similar to the original pattern (Fig. 1c). It should be noted that, throughout this time, the film was exposed to the RF radiation of the cell

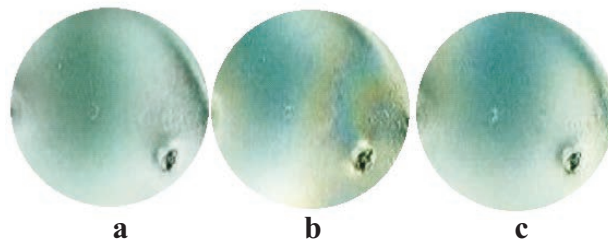


FIG. 1. Photomicrograph of a liquid crystal film before the impact of RF cell phone radiation (a), one minute (b) and two minute (c) after the start of exposure

phone. This may mean that the structure of the liquid-crystal film adapts to the cell phone radiation, and the local distribution of the optical axis recovers to a value similar to the original undisturbed condition.

The results of mathematical processing for the dynamic behavior of the video characteristics of the luminous flux are presented graphically in Fig. 2 (curve 1). It can be seen that, after the onset of liquid-crystal film exposure to cell phone radiation, the value $(K/M) - 1 = N$ which describes the reaction of liquid crystal increases and reaches a maximum in one minute, and then decreases and returns to the baseline level within two minutes from the start of the experiment.

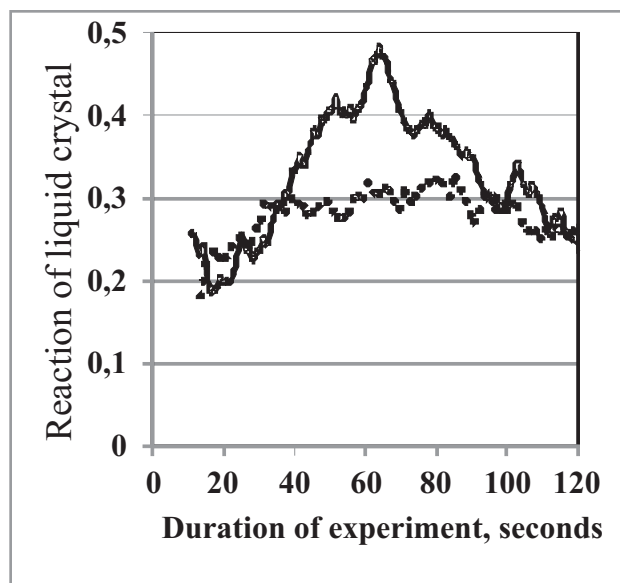


FIG. 2. Graphical display of a liquid crystal film reaction (quantity of image colors relative to the minimum) on the impact from the field of a cell phone in the absence and presence of the device “Gamma-7.N-RT”

A similar response of the liquid-crystal film was observed for the influence of cell phone EMR equipped with a protective device (Gamma 7.N-RT), which eliminates the negative impact of biotropic components of radiation from mobile phones [17, 18]. Photographs in Fig. 3 show the brightness and color distribution of the film before exposure to the cell phone electromagnetic field (Fig. 3a), and at one minute (Fig. 3b) and two minutes (Fig. 3c) after the onset of the RF radiation. Alteration of the brightness and color of the film in

the presence of the protective device Gamma 7.N-RT differs from that in its absence. The observed phenomenon quantitatively confirms the results of the mathematical processing of the dynamic behavior of the video characteristics of the light flux presented graphically in Fig. 2, which demonstrates that, although the value $(K/M) - 1 = N$ also increased under the action the mobile phone with the Gamma 7.N-RT device, it was 1.3 times smaller than that in the case without this device. This could mean that the Gamma 7.N-RT device partially attenuates the effect of the cell phone RF radiation on the local distribution of the optical axis in the freely suspended liquid-crystal film.

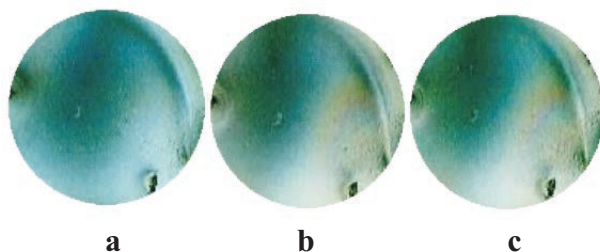


FIG. 3. Photomicrograph of a liquid crystal film phone in the presence of the device “Gamma-7.N-RT” before the impact of RF cell phone radiation (a), one minute (b) and two minute (c) after the start of exposure

The observed response of the freely suspended liquid-crystal film to the cell phone’s low-energy electromagnetic field significantly differs from the response to a constant magnetic field of high strength. Photographs in Fig. 4 show the brightness and color distribution of the films under the action of a magnetic field of 500 Oe after one minute (Fig. 4b), and three minutes (Fig. 4c) from the start of the experiment.

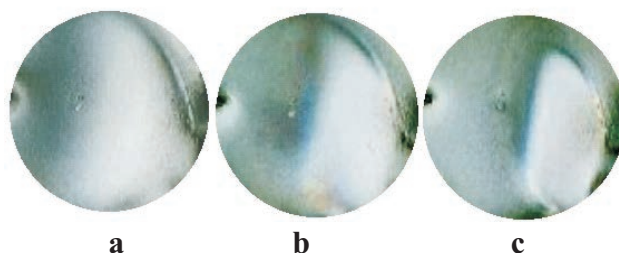


FIG. 4. Photomicrograph of a liquid crystal film before the impact of a static magnetic field of strength intensity 500 oersted (a), one minute and two minute (c) after the start of exposure

After the initial sharp change, the characteristics of the light flux remained constant throughout the action of the magnetic field and did not recover to the original undisturbed condition of the liquid-crystal film structure. This is illustrated in Fig. 5, which shows the behavior of the value $(K/M) - 1 = N$ over the course of the experiment.

The structure of the liquid crystal film recovered to the original unperturbed state only after the cessation of the constant magnetic field’s action.

4. Conclusion

The experiment revealed that the structure of a freely suspended liquid-crystal film changes in the low-energy electromagnetic field of a cell phone. The liquid crystal transforms

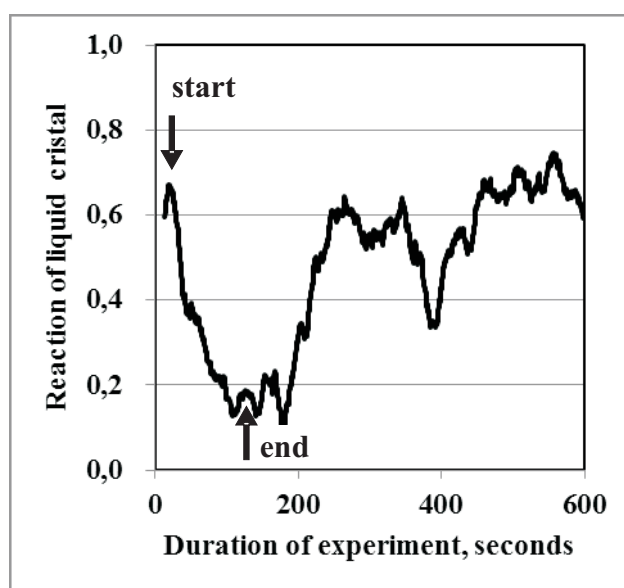


FIG. 5. Graphical display of a liquid crystal film reaction (quantity of image colors relative to the minimum) on the impact from a static magnetic field of strength intensity 500 oersted

to a quasi-equilibrium state, and, in the presence of the same field, recovers to equilibrium after some time. The structure of a freely suspended liquid-crystal film shows the property of adaptation to the effects of the RF radiation of a cell phone. In the presence of protective device Gamma 7.N-RT, the reaction of the liquid crystal is diminished and attenuated, which indirectly indicates a decrease in the energy consumption in the process of adaptation. In earlier studies [19], the data was obtained that provided evidence of a decrease of the tension of functions of the human body under the influence of high physical and psychic loads using devices Gamma 7.N-RT. This observation indirectly reflects the reduction of load on the system of the body responsible for its adaptation to the environment, in particular, to the influence of physical fields of different nature. The totality of the experimental results and published data suggest that the response of the liquid-crystal structure is one of the essential elements of adaptation of organism to the action of the RF radiation of cell phones.

References

- [1] Goodman R., Blank M., Cell phone safety standards should incorporate the bio-logical differences between thermal and electromagnetic responses, Abstract Book 22 Annual Meeting. Munich, Germany, P. 18 (2000).
- [2] Sandstrom M., Wilen J., Oftedal G. et al. Mobile phone use and subjective symptoms comparison of symptoms experienced users of analogue and digital mobile phones. *Occup. Med.*, **51**(1), P. 25–35 (2001).
- [3] Foster K. R., Repacholi, M. H. Biological Effects of Radiofrequency Fields: Does Modulation Matter? *Radiat. Res.*, **162**, P. 219–225 (2004).
- [4] Grigoriev Yu. 2005. Elektromagnitnye polya sotovikh telefonov i zdorovye detei i podrostkov (Situatsiya, trebuyushchya prinyatiya neotlozhnykh mer), Radiatsionnaya biologiya. *Radioekologiya*, **45**(4), P. 442–450 (2005).
- [5] Frey A.H. Headaches from cellular telephones: are real and what are the implication? *Environmental Health Perspectives*, **6**(3), P. 101–103 (1998).
- [6] Koivisto M., Haarala Ch., Krause Ch. et al. 2001. GSM phone signal does not produce subjective symptoms. *Bioelectromagnetics*, **2**(3), P. 212–215 (2001).

- [7] Grigoriev Yu. Mobile Phones and Children: Is Precaution Warranted? *Bioelectromagnetics*, **25**(5), P. 322–323 (2004).
- [8] Pickard W.F., Moros E.G. 2001. Energy deposition processes in biological, tissue: Nonthermal biohazards seem unlikely in the ultra-high frequency range. *Bioelectromagnetics*, **22**(2), P. 97–105 (2001).
- [9] Kim Yu., Montrell ., Akoyev V., Akoyev I., Phesenko E. 2001. Issledova-niye vliyaniya EMI maloy intensivnosti na hydrotatsiyu plynok DNK Radiatsionnaya Biologiya. *Radioekologiya*, **41**(4), P. 395–398 (2001).
- [10] Vijayalaxmi and Prihoda T. J., Genetic Damage in Mammalian So-matic Cells Exposed to Radiofrequency Radiation: A Meta-analysis of Data from 63 Publications (1990-2005). *Radiat. Res.*, **169**, P. 561–574 (2008).
- [11] Luria R., Eliyahu I., Hareuveny R., Margaliot M., Meiran N. Cognitive effects of radiation emitted by cellular phones: The influence of exposure side and time. *Bioelectromagnetics*, **30**(3), P. 198–204 (2009).
- [12] Brawn G.H. *Liquid Crystals and Biological Structures*. Academic Press, 1979, New York, San Francisco, London.
- [13] De Gennes P.G. and Prost J. *The Physics of Liquid Crystals*. Clarendon Press, Oxford, p. 597 (1993).
- [14] Blinov L.M. *Electro- i magnitooptika zhidkikh kristallov*. M.: Nauka (1978).
- [15] Pikin S.A. *Structural Transformations in Liquid Crystals*. Gordon and Breach Science Publishers (1991).
- [16] Romanov V.P., Ul'anov S.V. Dynamic properties of smectic films. *Advances in Physical Sciences*, **173**(6), P. 941–963 (2003).
- [17] Denisov S. 2003. Neitralizatotri izluchenii. *Science in Russia*, **6**(138), P. 24–26 (2003).
- [18] Liberman A.N., Denisov S.G. *Mobile phone and health*. M.: Moscow University Press, 90 p. (2011).
- [19] Aleksanin S.S., Bogdanov A.A., Zagarov E.S. Physiological monitoring operators ACS in audio-visual simulation of an emergency. *Radiation Hygiene*, **3**(3), P. 43–46 (2010).

PHYSICAL PROPERTIES OF HOT WALL DEPOSITED $\text{Sn}_{1-x}\text{Pb}_x\text{S}$ THIN FILMS

V. F. Gremenok¹, V. A. Ivanov¹, H. Izadneshan¹, V. V. Lazenka², A. Bakouie³

¹State Scientific and Production Association “Scientific-Practical Materials Research Centre of the National Academy of Sciences of Belarus”,
P. Brovka Street 19, 220072 Minsk, Belarus

²Institute for Nuclear and radiation physics (IKS),
KU Leuven, Celestijnenlaan 65/84, 3001 Leuven, Belgium

³Department of Physics, Marvdasht Branch, Islamic Azad University, Marvdasht, Iran
4-Tarbiat Modares University, Teheran, Iran

vasil@physics.by

PACS 73.50.-h

Thin films and nanorods of $\text{Sn}_{1-x}\text{Pb}_x\text{S}$ ($0.00 \leq x \leq 0.45$) with orthorhombic crystal structure and *c*-axis oriented perpendicular to the substrate surface were grown by hot wall vacuum deposition (HWVD) method. The nanorods grew via a self consuming vapor–liquid–solid (VLS) mechanism by means of Sn-droplets onto the surface of an underlying thin film. The former one consists of stacked blocks with their *c*-axis always parallel to the growth direction. However, each block is alternately rotated around the [001] against its underlying and subsequent one. As revealed by composition analysis, there is no composition gradient across or within the nanorods and the underlying film. The rods were about 500 nm high and 250 nm in diameter. The droplet at the top of rods consists of Sn with small trace of Pb and S. The density of rods, arranged like a lawn, depends on the metal ratio and substrate temperature. The as-grown $\text{Sn}_{1-x}\text{Pb}_x\text{S}$ samples showed p-type electrical conductivity. Increasing the lead atom concentration results in a decreased Seebeck coefficient and lower conductivity.

Keywords: Hot Wall Deposition, Physical Properties, Thin Films.

Received: 26 August 2014

Revised: 29 September 2014

1. Introduction

Novel inexpensive materials with high photovoltaic efficiencies are needed for thin film solar cells, replacing most extensively studied materials as CdTe and $\text{Cu}(\text{In,Ga})\text{Se}_2$. Recently, a considerable effort has been invested to gain a better and deeper understanding of physical properties of the lead tin chalcogenide semiconductors because of their potential application in electrical and photonic devices [1-4]. The most interesting candidates are (Sn,Pb)S mixed crystals. SnS has an orthorhombic structure and consists of double layers weakly bound to each other, while PbS has a cubic structure. The crystal structures of SnS–PbS bulk materials have been examined and linear relationships between cell parameters *a*, *b* and *c* and composition have been established [5-7]. Both PbS (optical band gap of 0.4 eV) and SnS (optical band gap of 1.1–1.7 eV) semiconductors are promising materials in photovoltaic, infrared detection and other optoelectronic devices. To evaluate these materials for such applications, their microstructure, optical, electrical properties should be thoroughly understood. In addition, lead and tin containing sulfides in photovoltaic structures would

decrease the production costs of solar cells, because the materials involved are cost effective, abundant in nature, and somewhat less-toxic.

A few techniques have been applied for the preparation of $\text{Sn}_{1-x}\text{Pb}_x\text{S}$ thin films. The first report was by Thangaraju and co-workers [8], who prepared PbSnS_2 films by a spray pyrolysis method. Unuchak et al. deposited PbSnS_2 thin film by thermal evaporation [4]. The preliminary structural and optical characteristics have been reported.

New approaches and various techniques must be developed to control the deposition of photoactive materials with minimum density of defects, so that carrier generation, transport, and collection are optimized. Shape and size of nanostructures have considerable influence on physical properties of such semiconductors especially for the phonons due to the lattice part of the thermal conductivity for which nanorods constitute an important class of corresponding 1D nanostructures [9-11]. At the same time, bicontinuous morphology is necessary to decrease the distance needed for excitons to diffuse to interfaces and to allow charges to efficiently diffuse to electrode interfaces. Nanorods constitute an important class of 1D nanostructure and can also act as active components in devices. Previously, much effort has been made to develop novel methods for fabrication of nanostructured chalcogenide semiconductors [12]. Among these technologies, the vapor-liquid-solid (VLS) method seems to be the most successful for generating nanocrystalline nanowires with relatively large quantities [13,14].

In our continuing effort to prepare the SnS-PbS semiconductor films, we have used a hot wall vacuum deposition (HWVD) method. Among the various thin films deposition techniques, HWVD has become a popular and reliable synthesis for films preparation [15-21]. This deposition technology yields high quality thin films with smooth surfaces grown under conditions very close to a quasi thermal equilibrium. The high quality of the electrical and optical properties thin films of the different II-VI materials produced by this method didn't require additional post-growth heat treatments [22,23].

Here, we report on the preparation of $\text{Sn}_{1-x}\text{Pb}_x\text{S}$ thin films and nanorods by the hot wall vacuum deposition of bulk materials onto glass substrates using different synthetic parameters. Microstructure and electrical properties of the as deposited materials are also described.

2. Experimental details

The polycrystalline $\text{Sn}_{1-x}\text{Pb}_x\text{S}$ ($0.00 \leq x \leq 0.45$) ingots used as targets were synthesized by reaction of Sn, S of high purity 99.999% and natural galena (PbS) containing 0.04 at.% Ag and Sb, 0.06 at.% Cu, 0.07 at.% Zn, and 0.08 at.% Au in silica ampoules. Mixtures of constituent elements in stoichiometric proportions (with an accuracy of 5×10^{-7} kg) were sealed into evacuated ampoules at the pressure of 10^{-3} Torr. The evacuated tube was then placed into an electric furnace and kept at 730 K for 7 days and after that at 970 K for 10 days. In order to avoid explosions due to the sulfur vapor pressure, the tube was heated slowly (300 K/h). The tubes were cooled gradually, with a cooling rate of about 295 K/h to room temperature in order to obtain polycrystalline $\text{Sn}_{1-x}\text{Pb}_x\text{S}$ compounds.

The main feature of the hot wall deposition system is the heated linear quartz tube of 1.2×10^{-2} m diameter, which served to enclose and direct the vapor from the source to the substrate. The quartz tube and substrates were heated independently. The quartz tube was charged with $\text{Sn}_{1-x}\text{Pb}_x\text{S}$ powder and the films were deposited by keeping the quartz tube temperatures around 870 K. Glass plates were chemically cleaned, rinsed with distilled water before deposition. Substrate temperature was varied from 520 to 680 K. The substrate was held at a distance of about 10^{-4} m above the open end of the quartz tube acting almost

as a lid closing the tube with the help of a substrate holder heater. The pressure in the chamber was about 10^{-5} Torr during evaporation. Chromel–alumel thermocouples were used to measure the temperatures of quartz tube and the substrate.

The crystal structure of the $\text{Sn}_{1-x}\text{Pb}_x\text{S}$ in both powder and thin film forms were investigated by X-ray diffraction (XRD) using a Siemens D-5000 diffractometer with $\text{CuK}\alpha$ ($\lambda = 1.5418 \text{ \AA}$) radiation. Silicon powder suspended in acetone and covering the samples was used as a standard. The 2θ -range for the diffractometer was set from 10 to 100° with a step size of 0.038° . The observed phases were determined by comparing the d -spacing with the Joint Committee on Powder Diffraction Standard (JCPDS) data files. Surface morphology and cross-section of the films were investigated with scanning electron microscope (SEM) (Hitachi S-806). The elemental composition of the obtained films was determined from energy dispersive X-ray (EDX) data, using Scanning electron microscope Stereoscan-360 with EDX spectrometer AN 10000 with an accuracy of about 2 %. The depth profiling was done by Auger electron spectroscopy (AES) using a Perkin Elmer Physical Electronics model 590 with simultaneous sputter etching. The nature of the crystalline surface was also analyzed using atomic force microscopy (AFM, Model: NT-206) and the grain size was evaluated. The TEM examinations have been performed by means of a Philips CM-200 STEM operating at 200 kV accelerating voltage and equipped with a calibrated EDX system. The cross-sections needed for TEM were prepared by mechanical grinding, dimpling and Ar^+ ion milling using a Gatan PIPS machine.

Electrical conductivity measurements were made by using a dc two-probe configuration in a special cryostat. The temperature range of investigation was extended from 150–420 K. All measurements were carried out under vacuum condition of about 5×10^{-4} Torr. The “Leit-C” paste was used as ohmic contact. The ohmic nature of the contacts was checked by recording the current–voltage characteristics.

3. Results and discussion

The physical properties of $\text{Sn}_{1-x}\text{Pb}_x\text{S}$ thin films are influenced by the elemental composition and substrate temperature. The characteristics of layers were studied by appropriate techniques and are discussed in the following section. The as-deposited films were pinhole free and strongly adherent to the surface of the substrate. $\text{Sn}_{1-x}\text{Pb}_x\text{S}$ layers appeared grey in color; the valuated thickness varied from 2.0 to 4.0 μm .

The influence of substrate temperature and Pb content on the phase formation and crystalline structure of the $\text{Sn}_{1-x}\text{Pb}_x\text{S}$ structures were characterized by XRD measurements. Teallite pattern (PDF # 44-1437) was used as reference for qualitative analysis of the samples. The structures obtained were single phase in nature and had an orthorhombic crystal structure. All films showed strong orientation along [001] axes with strong 004 peak [24]. A linear relationship between the lattice parameters and the composition of $\text{Sn}_{1-x}\text{Pb}_x\text{S}$ thin films were established. These relationships, calculated mathematically by least-squares analysis, are:

$$a = 4.333 - 0,0745 \cdot x(\text{\AA}), \quad b = 3,977 + 0,1435 \cdot x(\text{\AA}), \quad c = 11,219 + 0,4402 \cdot x(\text{\AA}).$$

The value of the a parameter gradually decreases with increasing Pb content in films, while value of the b and c parameters increase and agree with data of previously synthesized herzenbergite–teallite bulk minerals [6]. The change of lattice parameters with substrate temperature is marginal. SEM examinations (Fig. 1) of the as-grown structures showed that the nanorods lawn was formed onto a thin film interlayer (about 1500 nm thick) on the glass substrate.

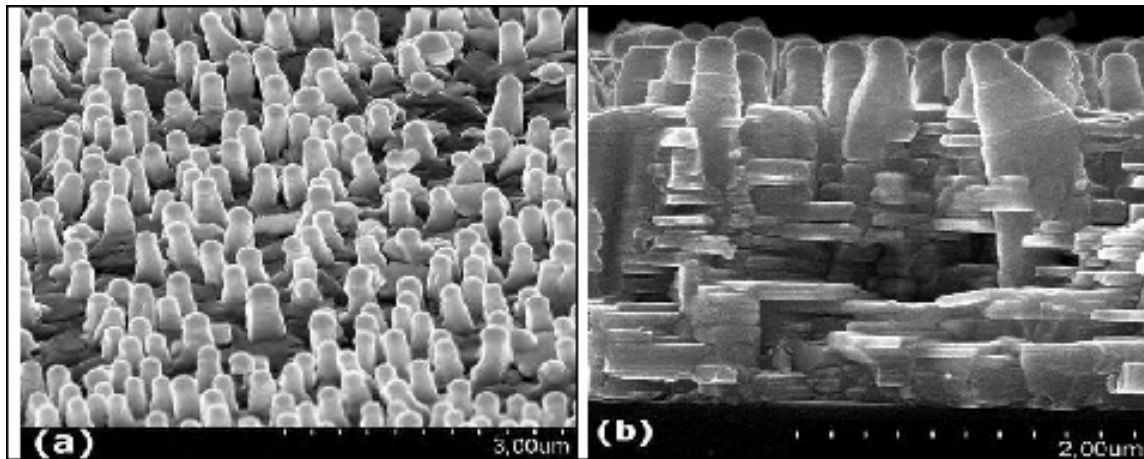


FIG. 1. SEM images of $\text{Sn}_{0.92}\text{Pb}_{0.08}\text{S}$ nanorods grown onto underlying thin film (a) top view, (b) cross sectional view

The average length and diameter of rods for the $\text{Sn}_{0.92}\text{Pb}_{0.08}\text{S}$ sample are 500 nm and 250 nm respectively. The underlying thin film is composed by single-crystalline blocks with their orthorhombic 11.2 Å axis (c-axis) always perpendicular to the substrate surface (Fig. 2).

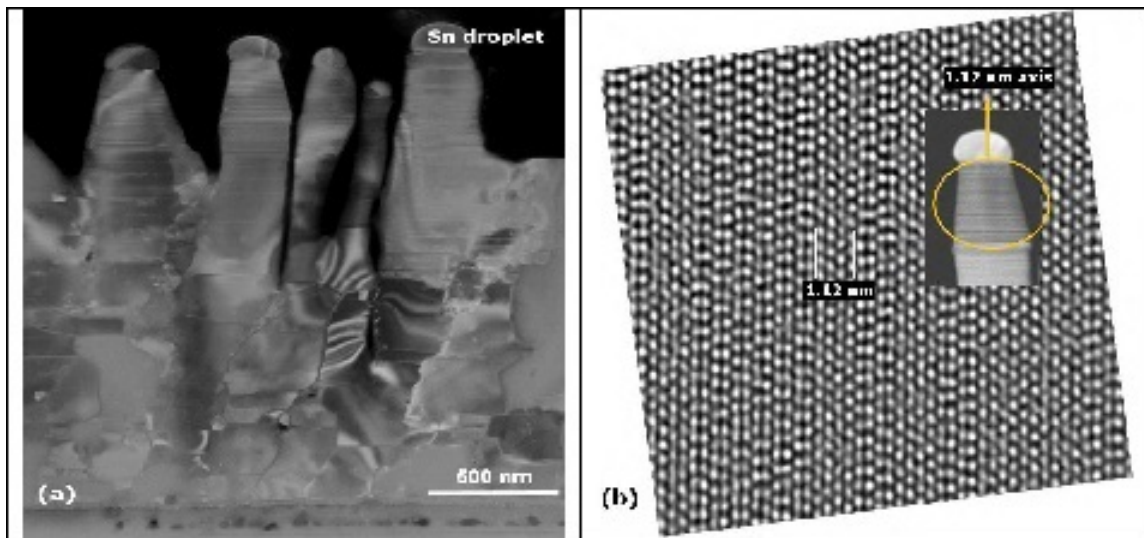


FIG. 2. (a) TEM bright-field image of nanorods and block structured underlying thin film of $\text{Sn}_{0.92}\text{Pb}_{0.08}\text{S}$, (b) bragg-filtered experimental HRTEM image of plane defects

The individual adjacent blocks, which differ in their azimuthal orientation, are randomly directed. Therefore, the whole grown $\text{Sn}_{1-x}\text{Pb}_x\text{S}$ displays polycrystalline behavior but has a well-distinct (001) texture, which is in agreement with XRD results [24]. However, between blocks that are stacked over each other to form columns there are well-defined twist boundaries. The whiskers are formed either by thicker blocks (see Fig. 2,b) separated by twist boundaries containing dislocations or they are composed of many extremely thin lamellae with the same orientation relationship as the blocks but without dislocations. This means that in the former case, plastic relaxation between stacked blocks took place. In the

latter one, pseudomorphic intergrowth between stacked thin strained lamellae occurs, i.e., there is elastic relaxation without forming dislocations. As revealed by TEM-EDX analysis, the average composition of the blocks and rods is the same without any composition gradient across the whole $\text{Sn}_{1-x}\text{Pb}_x\text{S}$ sample structure (Fig. 3). As seen from the Fig. 1 and Fig. 2 the droplets were formed at the tip of the rods. TEM-EDX experiments showed that these droplets consist of Sn and about 0.6 at.% Pb and 1.2 at.% S.

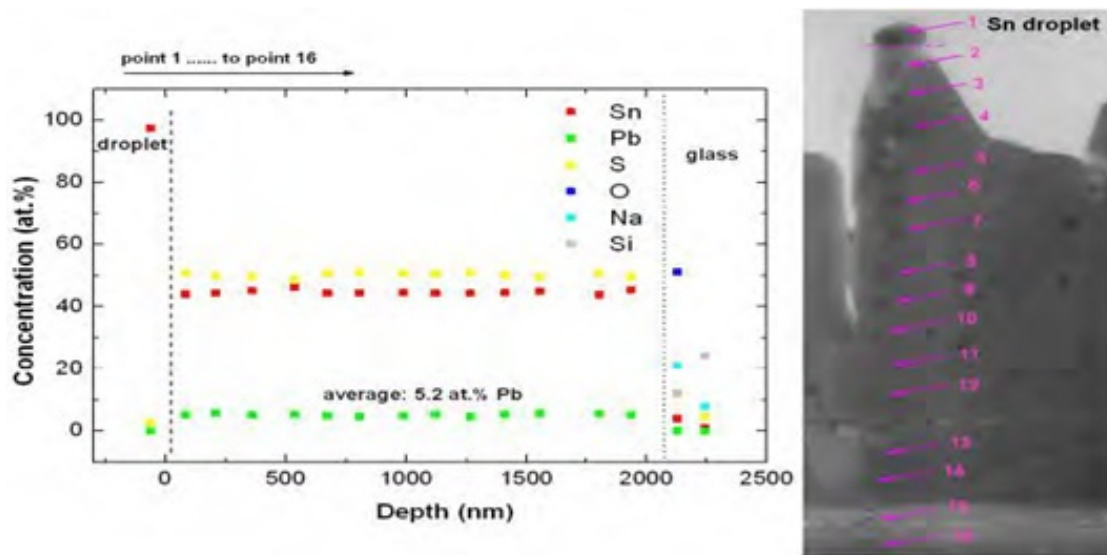


FIG. 3. Compositional distribution along $\text{Sn}_{0.9}\text{Pb}_{0.1}\text{S}$ sample determined by calibrated TEM-EDX. The points for quantitative TEM-EDX measurements are indicated by 1 to 16

It was suggested that these droplets are liquid at growth temperature and act as a solute for the sulfur and lead, and tin may also come from the vapor phase during the growth process. Therefore, it is assumed the rods grew via a self-consuming vapor–liquid–solid (VLS) mechanism [13-14].

The experiments confirm that the nanorod growth depends strongly on the lead concentration and substrate temperature. The lawn of nanorods with lead concentration ranging from 4 at.% to 6 at.% was formed onto the underlying $\text{Sn}_{1-x}\text{Pb}_x\text{S}$ thin film at substrate temperatures of 570–590 K. Thin films containing ca. 8 at.% Pb grown on glass at temperatures less than 540 K have few droplets on their surfaces only (Fig. 4).

At a substrate temperature of 600 K, the droplets required for VLS growth begin to form (Fig. 4b) and at 630 K an array of whiskers 500 nm high and 250 nm in diameter can be observed (Figs. 4c). However, at substrate temperatures of 670 K and higher, lawn-growth could not be found even though some few droplets and single nanorods appeared. Thus, it can be concluded that for higher Pb content, higher substrate temperatures are required to produce nanorods. The as-grown $\text{Sn}_{1-x}\text{Pb}_x\text{S}$ films showed p-type electrical conductivity, which is confirmed by the thermoelectric probe measurement. The Seebeck coefficient and conductivity of the layers was in the range of $\alpha = 6\text{--}360 \mu\text{V}/\text{K}$ and $\sigma = 4.8 \times 10^{-5} - 1.5 \times 10^{-2} \Omega^{-1} \cdot \text{cm}^{-1}$ respectively at room temperature, depending on concentration of the lead in the films.

An increase of the Pb concentration leads to a decrease of the Seebeck coefficient and decrease of conductivity [4]. If Na deriving from diffusion from the glass substrate is

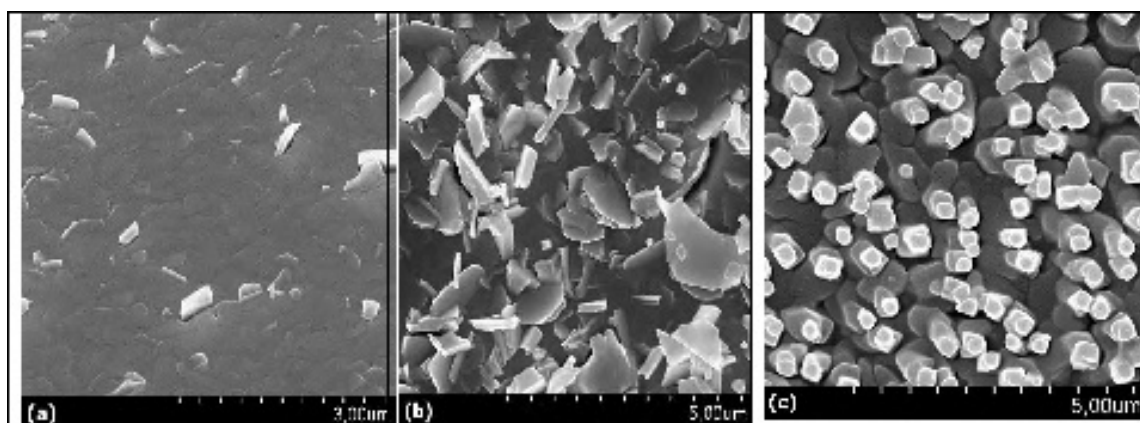


FIG. 4. SEM images of $\text{Sn}_{0.84}\text{Pb}_{0.16}\text{S}$ thin film samples deposited at different substrate temperature: (a) 540 K; (b) 600 K; (c) 630 K

incorporated within the thin film and nanorods, the electrical conductivity can be increased up to $\sigma = 10^2 \Omega^{-1}\cdot\text{cm}^{-1}$ and the Seebeck coefficient up to about $800 \mu\text{V}/\text{K}$. First data on structural and electrical characteristics of $\text{Sn}_{1-x}\text{Pb}_x\text{S}$ thin films grown by hot wall vacuum deposition method promise optimal conditions for application within photovoltaic and thermoelectrical devices.

4. Conclusion

$\text{Sn}_{1-x}\text{Pb}_x\text{S}$ films and nanorods were deposited by hot wall vacuum technique on glass substrates at temperatures of 520–680 K. The nanorods and film it self are composed of well-defined stacked blocks with orthorhombic crystal structure like $\alpha\text{-SnS}$ and show a preferential orientation along [001] perpendicular to the substrate surface. There is no composition gradient across the rods and the underlying thin film. Nanorod growth strongly depends on the lead concentration and substrate temperature. Increasing the Pb content requires the substrate temperature to be increased in order to realize whisker growth via VLS. Electrical measurements showed that $\text{Sn}_{1-x}\text{Pb}_x\text{S}$ films were of p-type conductivity. The values of Seebeck coefficient and conductivity at room temperature depended on the lead concentration were in the range of $6\text{--}360 \mu\text{V}/\text{K}$ and $4.8 \times 10^{-5} - 1.5 \times 10^{-2} \Omega^{-1}\cdot\text{cm}^{-1}$ respectively.

Acknowledgments

We acknowledge PD Dr. G. Wagner (Leipzig University) for TEM investigations and A. Bernstein (LMU München) for the EPMA analyses of natural PbS. This work has been supported by Belarusian Republican Foundation for Fundamental Research.

References

- [1] Razykov T.M. Solar photovoltaic electricity: Current status and future prospects. *Solar Energy*, **85**, P. 1580–1608 (2011).
- [2] Versavel M.Y., Haber J.A. Lead antimony sulfides as potential solar absorbers for thin film solar cells. *Thin Solid Films*, **515**, P. 5767–5770 (2007).
- [3] Dittrich H., Bieniok A., Brendel U., Grodzicki M. A new class of compound semiconductors for photovoltaic applications. *Thin Solid Films*, **515**, P. 5745–5750 (2007).
- [4] Unuchak D.M., Bente K., Kloess G., Schmitz W., Gremenok V.F., Ivanov V.A., Ukhov V. Structure and optical properties of PbS-SnS mixed crystal thin films. *Physics Status Solidi C*, **6**, P. 1191–1194 (2009).

- [5] Krebs H. and Langner D. Über struktur und eigenschaften der halbmatalle. XVI. Mischkristallsysteme zwischen halbleitenden chalcogeniden der vierten hauptgruppe. *Zeitschrift für anorganische und allgemeine Chemie*, **334**, P. 37–49 (1964).
- [6] Hayashi K., Kitakaze A., Sugaki A. A re-examination of herzenbergite-teallite solid solution at temperatures between 300 and 700°C. *Mineralogical Magazine*, **65**, P. 645–651 (2001).
- [7] Lebedev A.I., Sluchinskaya I.A., Munro I.H. An EXAFS study of the local structure of the $\text{Pb}_x\text{Sn}_{1-x}\text{S}$ solid solution. *Physics of the Solid State*, **44**, P. 1643–1647 (2002).
- [8] Thangaraju B. and Kaliannan P. Polycrystalline Lead Tin Chalcogenide Thin Film Grown by Spray Pyrolysis Crystal Research Technology, **35**, P. 71–75 (2000).
- [9] Lieber C.M. One-Dimensional Nanostructures: Chemistry, Physics & Applications. *Solid State Communications*, **107**, P. 607–616 (1998).
- [10] Manna L., Scher E.C., Alivisatos A.P. Synthesis of soluble and processable rod-, arrow-, teardrop-, and tetrapod-shaped CdSe nanocrystals. *J. American Chemistry Society*, **122**, P. 12700–12706 (2000).
- [11] Deng Z.X., Wang C., Sun X.M., Li Y.D. Structure-Directing Coordination Template Effect of Ethylenediamine in Formations of ZnS and ZnSe Nanocrystallites via Solvothermal Route. *Inorganic Chemistry*, **41**, P. 869–873 (2002).
- [12] Rao C.N., Deepak F.L., Gundiah. G., Govindaraj A. Inorganic nanowires. *Progress Solid State Chemistry*, **31**, P. 5–147 (2003).
- [13] Xia Y.N., Yang P.D., Sun Y.G., Wu Y.Y., Mayers B., Gates B., Yin Y.D., Kim F., Yan H.Q. One-Dimensional Nanostructures: Synthesis, Characterization, and Applications. *Advanced Materials*, **15**, P. 353–389 (2003).
- [14] Wagner R.S., Ellis W.S. Vapor-liquid-solid mechanism of single crystal growth. *Applied Physics Letters*, **4**, P. 89–90 (1964).
- [15] Lopez-Otero, A. Hot wall epitaxy. *Thin Solid Films*, **49**, P. 3–57 (1978).
- [16] Chaudhuri S., Mondal A., Pal A.K. Structural studies of CdSe films deposited onto glass, NaCl and substrates by a hot-wall technique. *Journal of Materials Science Letters*, **6**, P. 366–369 (1987).
- [17] Seto S., Yamada S., Suzuki K. Growth kinetics and structural characterization of polycrystalline CdTe films grown by hot-wall vacuum evaporation. *Solar Energy Materials and Solar Cells*, **50**, P. 133–139 (1998).
- [18] Velumani S., Narayandass S.K., Mangalara D. Structural characterization of hot wall deposited cadmium selenide thin films. *Semiconductors Science and Technology*, **13**, P. 1016–1024 (1998).
- [19] Velumani, S., Mathew, X., Sebastian, P.J. Thickness dependent properties of hot wall deposited CdSe films. *Journal of Materials Science Letters*, **22**, P. 25–28 (2003).
- [20] Muthukumarasamy N., Balasundaraprabhu R., Jayakumar S., Kannan M.D. Photoconductive properties of hot wall deposited $\text{CdSe}_{0.6}\text{Te}_{0.4}$ thin films. *Materials Science and Engineering B*, **137**, P. 1–4 (2007).
- [21] Agilan S., Venkatachalam S., Mangalraj D., Narayandass Sa.K., Velumani S., Singh Vijay P. Structural and photoelectrical characterization of hot wall deposited CuInSe_2 thin films and the fabrication of CuInSe_2 based solar cells. *Materials Characterization*, **58**, P. 701–707 (2007).
- [22] Schikora D., Sitter H., Humenberger J., Lischka K. High quality CdTe epilayers on GaAs grown by hotwall epitaxy. *Applied Physics Letters*, **48**, P. 1276–1278 (1986).
- [23] Pal A.K., Mondal A., Chaudhuri S. Preparation and characterization of ZnTe/CdSe solar cells. *Vacuum*, **41**, P. 1460–1462 (1990).
- [24] Bente K, Lazenka V.V., Unuchak D.G., Wagner G., Gremenok V.F. Epitaxial $\text{Sn}_{1-x}\text{Pb}_x\text{S}$ nanorods on iso-compositional thin films, Crystal. *Research Technology*, **45**, P. 643–646 (2010).

FABRICATION AND CHARACTERIZATION ZnCdS NANOWIRE

M. A. Jafarov, E. F. Nasirov, R. Mammadov, R. Jafarli

Baku State University, Baku 1045, Z. Khalilov st. 23, Azerbaijan

maarif.jafarov@mail.ru

PACS 71.55.Gs, 78.20.-e, 85.30.-z, 85.60.Dw

Semiconductor ZnCdS nanowire arrays have been synthesized by electrochemical deposition from aqueous solutions into porous anodic alumina substrates. X-ray diffraction analyses show that the as-synthesized nanowires have a highly preferential orientation. Scanning electron microscopy indicates that high-filling, ordered, and single-crystalline nanowire arrays have been obtained. The optical absorption spectra of the nanowire arrays show that the optical absorption band edge of the ZnCdS nanowire array exhibits a blue shift compared with that of bulk ZnCdS. The growth mechanism and the electrochemical deposition process are discussed together with the chemical compositions analysis.

Keywords: Nanowire, electrochemical deposition, nanoparticle, ZnCdS.

Received: 30 November 2014

1. Introduction

Sulfides or selenides, as wide-band gap II-VI semiconductor materials, have been studied extensively due to their wide applications in the fields of light-emitting devices, solar cells, sensors, and optical recording materials [1–3]. ZnS is a wide band gap semiconductor, commercially used in a variety of applications, including optical coatings, solid-state solar cell windows, in thin film electroluminescent devices, photoconductors, field effect transistors, sensors, and light-emitting applications. To date, there are many methodologies available for synthesizing ZnS powders, such as laser ablation, electrochemical fabrication and solvothermal methods. The synthesis of ZnS nanowires, ZnS nanorods by a surfactant-assisted soft chemistry approach and ZnS nanocrystals in colloids are all known methods.

One-dimensional (1D) semiconductor nanostructures have received much attention due to their novel properties and potential applications in nanoscale electronics and optoelectronics [4, 5]. Among these semiconductor systems, the II-VI family of the compound semiconductors, including ZnS, CdS, and CdTe, has been widely studied because of their potential applications in solar cells, photodetectors, and light emitting diodes [6,7]. Many attempts have been made to fabricate 1D nanostructures, such as high-temperature chemical vapor deposition (CVD) [8,9]. Among these methods, the anodic alumina substrate (AAS)-based synthesis is a widely used route for fabricating 1D nanostructures, because the AAS's possess a uniform and parallel porous structure, which can be used as templates to assemble high-quality nanowire and nanotube arrays [10,11].

Cadmium sulfide (CdS), an important semiconductor material with a direct optical band gap of 2.4 – 2.45 eV at room temperature, has potential applications in optoelectronic and thermoelectric devices. To the best of our knowledge, there are no reports on the fabrication of the CdS nanowire (NW) arrays.

In this paper, large-scale, ordered, and single-crystalline ZnCdS nanowire arrays have been fabricated in AAS using an electrochemical deposition technique from an aqueous solution for the first time. For the as-formed ZnCdS NWs, systematic morphological, compositional, structural characterizations are carried.

2. Experimental Section

The AAS templates were prepared using a two-step anodization process as described previously. The pore size of the anodic alumina membrane (AAM) used was about 60 nm. A layer of Au film (thickness, 200 nm) was sputtered onto one side of the AAM to serve as the working electrode in a two-electrode plating cell, and a graphite plate was used as the counter electrode. The pulsed electrochemical deposition was carried out at a constant current density of 10 mA/cm² at 330 K. During the pulsed time, species were reduced on the pore ground. The delayed time provided time for the recovery of the ion concentration. Here, both the pulsed time and delayed time were 100 ms. The electrolyte was prepared by dissolving 10 mM CdSO₄, 10 mM ZnSO₄, 0.15 mM Na₂S₂O₃, 0.2 M C₆H₈O₇·H₂O (H₃Cit.H₂O), and 0.2 M NaOH in water. Due to the low solubility of Na₂S₂O₃ continuous heating and stirring for several hours is required. The pH of the final electrolyte was adjusted to 3.5 with H₂SO₄.

Powder X-ray diffraction (XRD, D/MAX-rA), field-emission scanning electron microscopy (FE-SEM, JEOL JSM-6700F), transmission electron microscopy (TEM, H-800), selected area electron diffraction (SAED), and high-resolution transmission electron microscopy (HRTEM, JEOL-2010) were used to study the crystalline structure and morphology of nanowire arrays. The chemical compositions of the nanowires were determined by energy dispersive spectrometer (EDS). The band structure of the nanowires was obtained by measuring the optical absorption spectra on UV-visible spectrophotometer (Cary-5E). For XRD and optical absorption measurements, the overfilled nanowires on the surface of the AAM and the back Au film were mechanically polished away using Al₂O₃ nanopowders. For SEM observation, the AAM was partly dissolved with 0.5 M NaOH solution and then carefully rinsed with deionized water several times.

The SEM images and elemental compositions [energy-dispersive X-ray analysis] of the ZnCdS NWs were analyzed by scanning electron microscope (HR-SEM, JSM, 7000F). The particles' morphology and structure were also studied by transmission electron microscopy (TEM) with a JEOL-2010HRTEM instrument. The 632.8 nm line of an He-Ne laser was used as the excitation source, focused to a 1 – 2 μm spot size. The X-ray diffraction patterns of the products were measured with a Bruker AXSD* Advance Powder X-ray diffractometer (using CuK α 1.5418 Å radiation). The collection of the emission was done through an objective with 40× magnification, then into an optical fiber connected to a SHAMROCK spectrometer SR-303I-A from ANDOR Technology onto a cooled CCD camera, connected to a computer.

3. Results and Discussion

The SEM images were taken of the reactant Zn, Cd and S powders for the realization of morphological difference between them. Typically, poly dispersed Zn and Cd particles possess spherical shape, submicron size and smooth surfaces. The Cd submicrometer sized particles reacted with an S vapor environment at 450 °C in a closed reactor, yielding ZnCdS particles (Fig. 1). A close observation (high resolution SEM micrograph) of ZnCdS particles showed that they were 50 – 300 nm in diameter and closely packed. The HR-SEM image confirmed the diameters of the formed ZnCdS are in the range of 100 – 400 nm. The existence of Zn, Cd and S elements was confirmed with an atomic ratio of S/Zn, Cd very close to 1 – 3. The insert plot for as-prepared ZnCdS powder also confirmed the atomic ratio of S/Zn, Cd close to 3.

Figure 1 shows the XRD pattern of the as-prepared ZnCdS nanowire array. The intensity of the (220) diffraction is much higher than all the other peaks, indicating that the ZnCdS nanowires have a preferential orientation along the [220] direction, which will be further confirmed by HRTEM analysis. In addition, no diffraction peaks for elemental Cd and S can be detected.

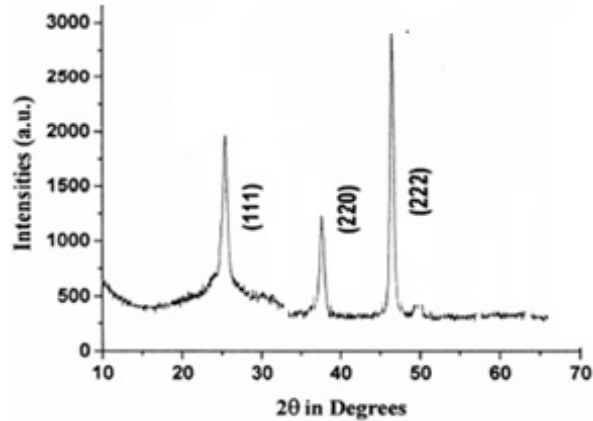


FIG. 1. XRD pattern of ZnCdS nanowire array

Figure 2 shows the dependence of the (220) peak intensity of XRD patterns of the ZnCdS nanowires on the current density and pulsed time. One can see that the peak intensity first increases, after reaching a maximum value at the current density of 10 mA/cm^2 , and then decreases with further increasing of the current density.

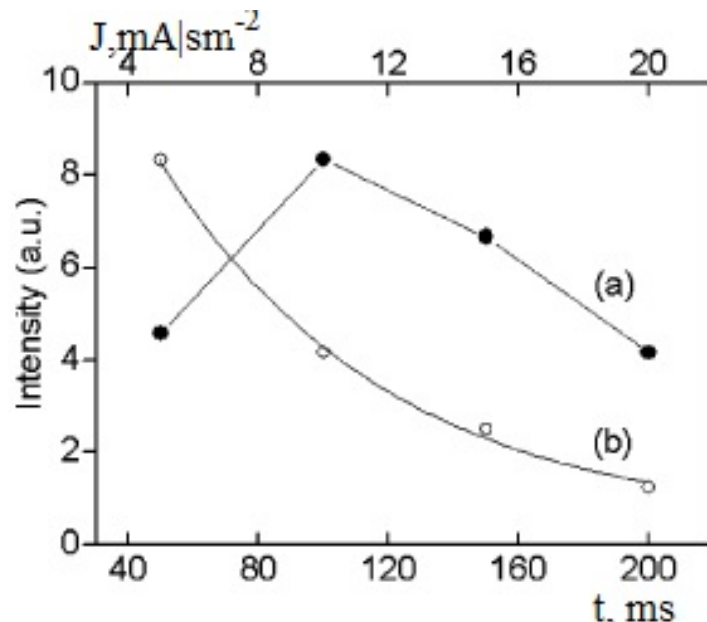


FIG. 2. Relative intensity of the (220) peak of ZnCdS nanowires as a function of (a) current density (I) and (b) pulsed time (t), keeping the delayed time at 100 ms

The reduction in the peak intensity might be due to hydrogen evolution at larger current densities, which suppresses the growth of the nanowires along the (220) orientation. Keeping

the delayed time at constant 100 ms, the (220) peak intensity always decreased with increasing pulse time. This result indicates that the best crystallinity of the ZnCdS nanowires can be obtained at a current density of ~ 10 mA/cm² and pulse time of about 100 ms.

Figure 3 shows SEM images of the as-prepared AAS and the ZnCdS nanowire array. Fig. 3a is a typical image of the as-prepared empty AAS. One can see that the AAS has a highly ordered pore array with an average pore size of about 60 nm. The morphologies of the ZnCdS nanowire arrays after different etching times are represented in Fig. 3b-c. Parts b and c of Fig. 3 are the surface images of the nanowire arrays after etching for 10 and 20 min, respectively.

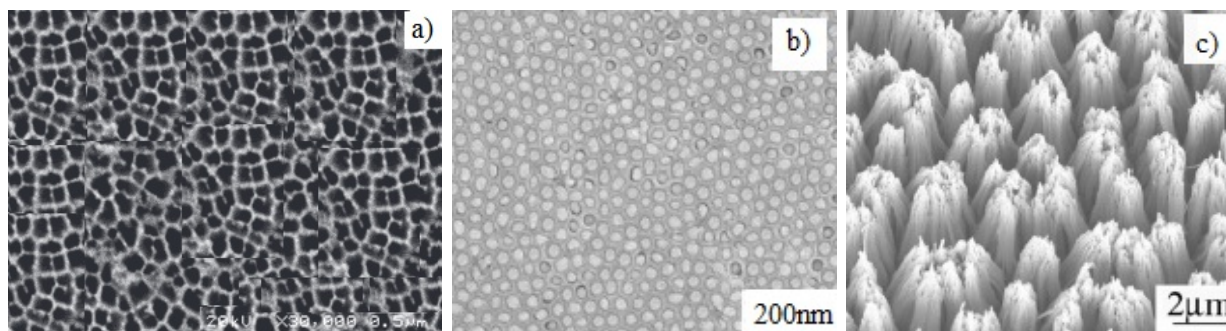


FIG. 3. SEM images of empty AAS (a) and ZnCdS nanowire arrays: (b and c) top views of the ZnCdS nanowire array after etching for 10 and 20 min

Apparently, the nanowires are highly filled (nearly 100%) and the exposed parts of the nanowires increase with increasing etching time. The length of the nanowires is the same as the thickness of the AAS used, because the deposition of the nanowires starts at the Au cathode on the bottom of the pores, and then the nanowires grow along the pores until the top of the AAS. It is noted that all the ZnCdS nanowires have the same length, implying that the electrodeposition process is well-controlled and all the nanowires grow along the pores at the same rate. It is evident that the ZnCdS nanowires with a smooth surface and a high aspect ratio still inside the nanochannels of AAM can be clearly seen. The diameters of the nanowires are uniform and equal to the pore size of the AAS used. One can see that the nanowire is dense and uniform in diameter corresponding to the pore size of the AAS. Some contrast variations were observed along the nanowires. The variation in the intensity of the individual spots might arise from slight structural deformation along the length in the release process of the nanowires from the substrate. The lattice-resolved image of the nanowire further reveals that the nanowire is structurally uniform and single-crystalline, with an interplanar spacing corresponding to the (220) plane of cubic ZnCdS. This result indicates that the growth direction of ZnCdS nanowire is along the [220] direction, which is in agreement with XRD results.

The EDS spectrum of ZnCdS nanowires is shown in Fig. 4, which proves that the nanowires consist of only Zn, Cd and S. Quantitative analysis of the EDS spectrum indicates that the atomic ratio of Zn/Cd/S is close to 1:1:1. It is well-known that a high Zn, Cd²⁺ concentration in the electrolyte is necessary for the deposition of ZnCdS thin films in order to bring the electrode potentials of the Cd²⁺ closer to S²⁺. To confirm the feasibility for nanowire growth, electrolytes with different Cd²⁺ concentrations were used to grow ZnCdS nanowires.

That the compositions of the nanowires are stoichiometric despite the wide range of Cd²⁺ concentration in the electrolytes, which indicates that we can use a high Cd²⁺ concentration in the electrolyte to co-deposit a ZnCdS nanowire array. It is worth noting that the potential has a very important influence on the compositions of ZnCdS nanowires. The ZnCdS nanowires deposited at about -2.0 V were found to exhibit a stoichiometric composition with Zn/Cd/S

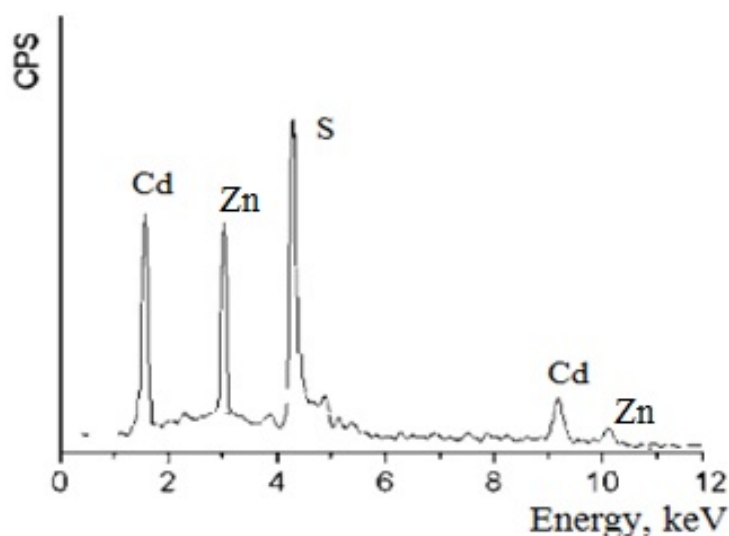


FIG. 4. EDS spectrum of the ZnCdS nanowire array

ratio of 1:1:3, and that deposited at more negative potentials (< -2.1 V) exhibited a Cd-rich phase, while that deposited at more positive potentials (> -1.5 V) revealed a S-rich phase. Fig. 5 shows the optical absorption spectra of the ZnCdS nanowires/AAS assembly system with the diameter of 60 nm and 40 nm. The absorption spectrum of the ZnCdS nanowires/AAS assembly system was shown to be quite different from that of the blank AAS, which is due to the absorption of ZnCdS nanowires. The relationship between the absorption coefficient (α) near the absorption edge and the optical band gap (E_g) for direct interband transitions are known to obey the following formula: $(\alpha h\nu)^2 = A(h\nu - E_g)$, where A is the parameter that related to the effective masses associated with the valence and conduction bands, and $h\nu$ is the photon energy. Hence, the optical band gap for the absorption edge can be obtained by extrapolating the linear portion of the plot $(\alpha h\nu)^2$ versus $\alpha = 0$. The two insets (topright corner in Fig. 5) show the $(\alpha h\nu)^2$ versus $h\nu$ plots for the two samples. For all samples, the optical absorption in the edge region can be well-fitted by the relation $(\alpha h\nu)^2 \sim h\nu - E_g$, which shows that the ZnCdS nanowires embedded in the AAS have a direct band gap. The band gap of nanowires with diameters of 60 and 40 nm is about 2.83 and 2.88 eV, respectively. The shift of 40 nm nanowires is higher than that of 60 nm nanowires. This result indicates that the optical band edge of the ZnCdS nanowires embedded in AAS exhibits a marked blue shift with respect to that of the bulk and thin-film ZnCdS (2.83 – 2.88 eV). The blue shift could be attributed to the quantum size effect, which has also been observed in other semiconductor nanosystems.

Therefore, ZnCdS nanowires have a relatively strong quantum confinement effect and exhibit a marked blue shift. The shift for 40 nm ZnCdS nanowires is larger than that for 60 nm ZnCdS nanowires. Simple electrochemical calculation indicates that the formation of ZnCdS alloy can be realized by using the basic electrochemical reactions for the simultaneous co-deposition of Zn, Cd and S, as described in the present experimental conditions. To obtain a highly-filled, uniform, and single-crystalline ZnCdS nanowire array by the electrochemical deposition into the nanochannels of the AAS, several factors should be considered. First, before electrodeposition the AAS should be treated ultrasonically in water for a few minutes to remove the impurities and air bubble inside the nanochannels, because the ZnCdS ions will preferentially nucleate and grow at the sites of the impurities, causing the inhomogeneous growth of nanowires, and the air bubbles will hinder ion diffusion into the nanopores of the AAS,

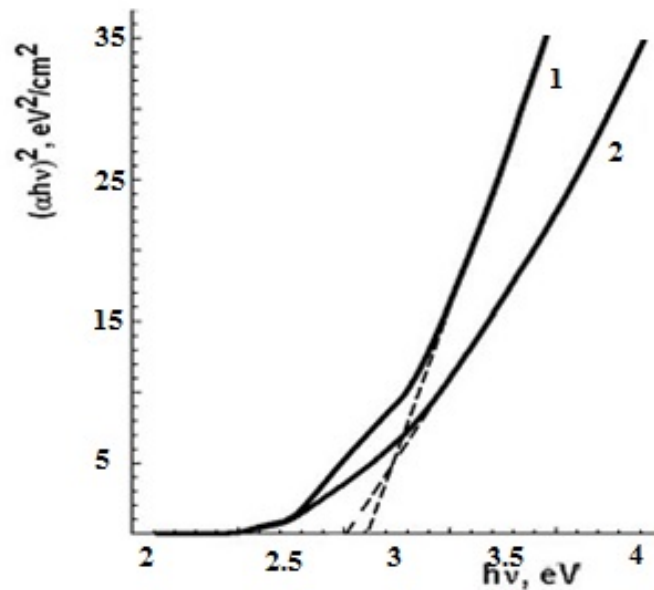


FIG. 5. Optical absorption spectra of the ZnCdS /AAS nanowire arrays with different diameters: (1) 60 and (2) 40 nm

causing the electrodeposition on the surface of the AAS. Second, a suitable deposition rate is critical to obtain dense, ordered, and singly-crystalline nanowires. To avoid rapid nucleation and growth and inhomogeneous concentration gradient in the nanopores, a pulsed electrodeposition technique is employed, which allows a better control over the deposition parameters, such as deposition rate and ion concentration at the deposition interface, as compared with the direct and alternating current deposition. In this paper, the pulsed time in each pulse cycle was so short (100 ms) that only a small number of metal ions at the interfaces were consumed. The delayed time (100 ms) provided enough time for the concentration of the metal ions at the pore tips to achieve steady state through diffusion. No evident concentration gradient near the reaction interface exists during the deposition, and the pulsed time controls the atom-by-atom deposition of nanowires, which improves the homogeneity of the deposition and makes the deposited nanowires have a highly preferential orientation and good crystallization. The proper choice of electrolyte pH value and deposition potential is also important.

4. Conclusions

In summary, highly-filled and ordered ZnCdS nanowire arrays have been prepared from aqueous solutions by the electrochemical deposition into the pores of AAS. The ZnCdS nanowires are single-crystalline and have a preferential orientation along the [220] direction. The optical absorption band edge of ZnCdS nanowires exhibits a marked blue-shift compared with that of bulk ZnCdS due to quantum size effect. We believe that the ZnCdS nanowire arrays will find interesting applications in optoelectronic and thermoelectric nanodevices in the future.

References

- [1] Wang Y.B., Wang Y.S., Xu R. Photochemical deposition of Pt on CdS for H₂ evolution from water: markedly enhanced activity by controlling Pt reduction environment. *J. Phys. Chem. C*, **117**, P. 783–790 (2013).
- [2] Bai Y., et al. In situ growth of a ZnO nanowire network within a TiO₂ nanoparticle film for enhanced dye-sensitized solar cell performance. *Adv. Mater.*, **24**, P. 5850–5856 (2012).
- [3] Ali Z., Shakira I., Kang D.J. Highly efficient photoelectrochemical response by sea-urchin shaped ZnO/TiO₂ nano/micro hybrid heterostructures co-sensitized with CdS/CdSe. *J. Mater. Chem. A*, **2**, P. 6474–6479 (2014).
- [4] Xu D.S., Xu Y.J., et al. Preparation and characterization of CdS nanowire arrays by dc electrodeposit in porous anodic aluminum oxide templates. *Chemical Physics Letters*, **325**, P. 340–34 (2000).
- [5] Huang M.H., Mao S., et al. Room-temperature ultraviolet nanowire nanolasers. *Science*, **292**, P. 1897–1899 (2001).
- [6] Barrelet C.J., Greytak A.B., Lieber C.M. Nanowire photonic circuit elements. *Nano Letters*, **4**, P. 1981–1985 (2004).
- [7] Li Q., Penner R.M. Photoconductive cadmium sulfide hemicylindrical shell nanowire ensembles. *Nano Letters*, **5**, P. 1720–1725 (2005).
- [8] Mondal S.P., Dhar A., Ray S.K. Optical properties of CdS nanowires prepared by dc electrochemical deposition in porous alumina template. *Materials Science in Semiconductor Processing*, **10**, P. 185–193 (2007).
- [9] Tak Y., Hong S.J., Lee J.S., Yong K. Fabrication of ZnO/CdS core/shell nanowire arrays for efficient solar energy conversion. *J. Mater. Chem.*, **19**, P. 5945–5951 (2009).
- [10] Sankar P.R., Tiwari P., et al. Synthesis and characterization of cadmium selenide nanostructures on porous aluminum oxide templates by high frequency alternating current electrolysis. *Applied Surface Science*, **256**, P. 2097–2103 (2010).
- [11] Kung S.C., van der Veer W.E., et al. 20 μ s Photocurrent Response from Lithographically Patterned Nanocrystalline Cadmium Selenide Nanowires. *Nano Letters*, **10**, P. 1481–1485 (2010).

SPECTRAL REGULARITIES OF THE CRITICAL ENERGY DENSITY OF THE PENTAERYTHRIOL TETRANITRATE -ALUMINUM NANOSYSTEMS INITIATED BY THE LASER PULSE

A. V. Kalenskii, M. V. Ananyeva

Kemerovo state University, Kemerovo, 650043, Russia

kriger@kemsu.ru

PACS 42.25.Gy, 82.33.Vx

In this work, the absorption of aluminum nanoparticles and the critical energy densities of the pentaerythritol tetranitrate -aluminum nanosystems, initiated by laser pulses, were calculated for wavelengths from 400 to 1200 nm. Data showed that it is necessary to consider both thermal and optical characteristics in order to calculate the critical initiation energy density and the radius of the most dangerous inclusion. The nanoparticle's radius, corresponding to the maximum on the curve of absorptivities, and the maximum's amplitude and critical energy density of the explosive materials, were all shown to depend on the initiating wavelength. The maximum of the aluminum nanoparticles' absorptivity and minimum of the critical energy density of the explosive decomposition were observed for the 400 nm wavelength, there is also a local maximum at 850 nm. The results from the experiment qualitatively and quantitatively agree with our calculations. These results are very important to optimize the cap composition for the optical detonators.

Keywords: Hot spot model, laser initiation, metal nanoparticles absorption, pentaerythritol tetranitrate.

Received: 10 November 2014

1. Introduction

The process of discovering energetic materials which have selective sensitivity to laser irradiation, in order to determine the ideal cap compositions for optical detonators has been carried out for almost 20 years. The first optical detonators were based on silver and lead azides. Their disadvantages were the high sensitivity not only to the laser impulse but also to the stroke, friction and heating. Because of their low selectivity, optical detonators based on priming powder were not widely adopted. The main direction of current research is now based on composite materials consisting of explosive materials and photosensitive metal particles [1-3]. The initiation threshold values for composites of pentaerythritol tetranitrate (PETN) and aluminum nanoparticles were obtained. Sensibility to laser initiation for these composites was shown to be about 1 J/cm^2 , while their sensibility to striking remained the same [1-4]. This proves both the possibility of using disruptive explosives, containing metal nanoparticles, as a cup of the optical detonators, and the role of the metal nanoparticles as the centers for light absorption in the bulk matrix of the transparent media. To find the ideal material, optimal sizes for the metal inclusions and parameters for the initiating system, it is necessary to consider several factors, which used to be considered negligible: the dependence of the metal nanoparticles' absorption on their sizes and the initiation wavelength. The aim of this work is to theoretically estimate the aluminum nanoparticles' absorption in the PETN matrix for the initiating wavelengths from 400 to 1200 nm; calculation of the minimal values

of the critical energy density for PETN – aluminum composites for different inclusion sizes and initiating wavelengths.

2. Hot spot model

The hot spot model [1-4] is based on the assumption that in the matrix of the energetic material there are nanoparticles, which can absorb irradiation very efficiently. In this model, it is assumed that the main result of light absorption is the heating of these particles. The heating causes growth of the surrounding energetic material's temperature and formation of the center of the self-accelerating exothermic reaction. The system of equations, describing conductive heat-transfer processes in the nanoparticles and media and the exothermal decomposition in case of the spherical symmetry, are [2-5]:

$$\begin{aligned} \frac{\partial T}{\partial t} &= \alpha \cdot \left(\frac{\partial^2 T}{\partial x^2} + \frac{2}{x} \cdot \frac{\partial T}{\partial x} \right) + \frac{Q}{c} k_0 n \cdot \exp \left(-\frac{E}{k_B T} \right), & x > R, \\ \frac{\partial n}{\partial t} &= -k_0 n \cdot \exp \left(-\frac{E}{k_B T} \right), & x > R, \\ \frac{\partial T}{\partial t} &= \alpha_M \cdot \left(\frac{\partial^2 T}{\partial x^2} + \frac{2}{x} \cdot \frac{\partial T}{\partial x} \right), & x < R, \end{aligned} \quad (1)$$

where T – temperature, n – relative concentration of the explosive material (PETN), which decreases during the reaction from 1 to 0, α and α_M – are the coefficients of thermal conductivity of the matrix and inclusion materials, R is the inclusion radius, k_B – Boltzmann constant, E – energy of activation, Q – heat efficiency of the decomposition, k_0 – preexponential factor, c is the volumetric heat capacity of the matrix. The boundary conditions for $x = R$ are:

$$J - c_M \alpha_M \cdot \left. \frac{\partial T}{\partial x} \right|_{x \rightarrow R-0} + c \alpha \cdot \left. \frac{\partial T}{\partial x} \right|_{x \rightarrow R+0} = 0, \quad (2)$$

where c_M is the volumetric heat capacity of the nanoparticle, $J(t)$ – is the absorbed density of the laser pulse radiation power. During the calculations the following parameters were used (the same as in works [2-5]): $J = 2.22 \text{ J}/(\text{cm}^3\text{K})$, $c_M = 2.7 \text{ J}/(\text{cm}^3\text{K})$, $E = 165 \text{ kJ}/(\text{mole}\cdot\text{K})$, $k_0 = 1.210^{16} \text{ s}^{-1}$, $\alpha = 1.1 \cdot 10^{-3} \text{ cm}^2\text{s}^{-1}$, $\alpha_M = 0.97 \text{ cm}^2\text{s}^{-1}$, $Q = 9.64 \text{ kJ}/\text{cm}^3$.

To research the explosive decomposition of energetic materials, the Nd:Yag based laser system is often used [6-7]. The dependence of the laser's radiating power on time is close to the function of the normal distribution [7-8]. Taking as a zero-time the moment of the impulse's maximum, one can obtain for $J(t)$ the following equation [9-10]:

$$J(t) = \sqrt{\pi} \cdot Q_{abs} R^2 k_i H_0 \cdot \exp(-k_i^2 t^2), \quad (3)$$

where $k_i = 8.325 \cdot 10^7 \text{ c}^{-1}$ – parameter, determining the impulse duration (corresponds to the impulse duration on the half-height 20 ns); H_0 – impulse energy density; Q_{abs} – the coefficient of absorption efficiency equal to the ratio of intensities of radiation absorbed and incident on the inclusion. The value of Q_{abs} depends on different factors – the inclusion radius and material of inclusion, and radiation wavelength. Multipliers of Eq. (3) normalize the integral of $J(t)$ over time by H_0 .

Q_{abs} of the spherical inclusion was calculated in terms of Mie theory. According to this theory, Q_{abs} might be calculated as a difference between coefficients of extinction (Q)

and the scattering coefficient (Q_{sca}) ($Q_{abs} = Q - Q_{sca}$) [11]:

$$Q_{sca} = \frac{2}{\rho^2} \sum_{l=1}^{\infty} (2l+1) \cdot (|c_l|^2 + |b_l|^2), \quad Q = \frac{2}{\rho^2} \text{Im} \sum_{l=1}^{\infty} (2l+1) \cdot (c_l - b_l), \quad (4)$$

where $\rho = 2\pi R m_0 / \lambda$, $m_0 = 1.54$ [12] – PETN's refractive index. c_l and b_l coefficients, which can be obtained using the boundary conditions for the nanoinclusion's surface [11-12]:

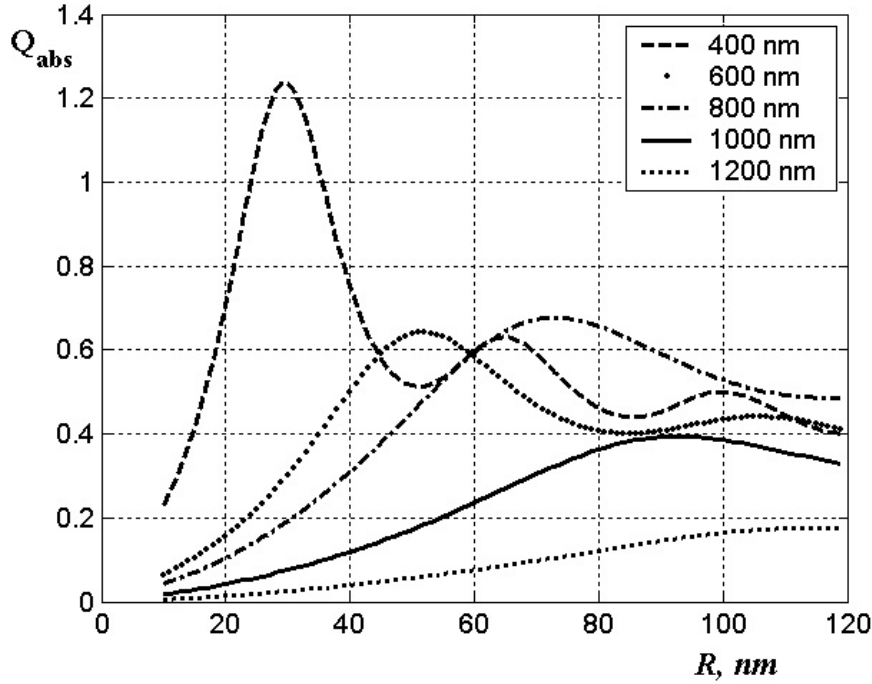


FIG. 1. Calculated dependences of the aluminium nanoparticles' absorptivity (Q_{abs}) in PETN-matrix on the particles' sizes for wavelengths 400, 600, 800, 1000, 1200 nm

$$c_l = i \frac{\psi_l(\rho)\psi'_l(n\rho) - n\psi'_l(\rho)\psi_l(n\rho)}{\zeta_l(\rho)\psi'_l(n\rho) - n\zeta'_l(\rho)\psi_l(n\rho)},$$

$$b_l = -i \frac{\psi'_l(\rho)\psi_l(n\rho) - n\psi_l(\rho)\psi'_l(n\rho)}{\zeta'_l(\rho)\psi_l(n\rho) - n\zeta_l(\rho)\psi'_l(n\rho)}, \quad (5)$$

where $n = m_i / m_0$ – complex refractive index of the nanoparticle relative to the matrix. To calculate the functions (ψ_l and ζ_l) and their derivatives (ψ'_l and ζ'_l) the following recurrence relations were used:

$$\psi_{l+1}(z) = \frac{2l+1}{z} \psi_l(z) - \psi_{l-1}(z), \quad (6)$$

$$\psi'_l(z) = \psi_{l-1}(z) - \frac{l}{z} \psi_l(z). \quad (7)$$

If $l = 1; 2$ the special functions are:

$$\psi_0(z) = \sin z \quad \psi_1(z) = \frac{\sin z}{z} - \cos z, \quad (8)$$

$$\zeta_0(z) = ie^{-iz} \quad \zeta_1(z) = -e^{-iz}(1 - i/z). \quad (9)$$

The use of recurrence relations (6-9) greatly shortened the time required for calculation. Dependences of the aluminum nanoparticles' absorptivity in the PETN-matrix on the particles' sizes, calculated using equation (4-9) are presented in fig. 1. Calculations were done for different initiating wavelengths – 400, 600, 800, 1000, and 1200 nm. Each dependence has a maximum ($Q_{abs \ max}$), its position (R_{max}) depending on the irradiation wavelength. For smaller radii, the curve decreases to zero, and in the extreme case $R \rightarrow 0$, the dependence changes according to Rayleigh–Jeans law. For nanoparticles having larger radii, the curve plateaus with some oscillations. In terms of the Mie theory, the wavelength influences the Q_{abs} because the factorial expansion arguments of the special functions are $\rho = 2\pi R m_0 / \lambda$ and $m_i \rho / m_0$. If m_i did not depend on the wavelength, the $Q_{abs}(\rho)$ dependences would coincide. The real and imaginary parts of m_i change considerably over the range of the examined wavelengths (Table 1). Table 1 shows the following: complex refractive index of aluminum [13], the calculated radii of aluminum particles having the largest absorptivity and those absorptivity values. The results presented for the wavelengths from 400 to 1200 nm, for which the complex refractive index of aluminum are well known [13-14], and for wavelengths of 1064 and 532 nm – the first and the second harmonic of the Nd:YAG laser using in the experimental work [2-3]. If the wavelength increases, the absorptivity maximum moves to the area of the larger radii (fig. 1), the maximum's amplitude – decreases (fig. 2). But for $\lambda = 850$ nm there is a local maximum, caused by the local maxima of the real and imaginary parts of the complex refractive index. Thus, for the $Q_{abs \ max}(\lambda)$ dependence for aluminum in a PETN-matrix, there is a local maximum, and so, there must be corresponding minimum of critical initiation energy for explosive decomposition. The calculated $Q_{abs \ max}(\lambda)$ dependence over wavelengths ranging from 400–1200 nm is presented on fig. 2.

In order to calculate the critical parameters for explosive decomposition, a numerical solution for models (1)–(3) was made using a variable-pitch grid. A step in the vicinity of the inclusions with the radii $R \geq 30$ nm was no more than $1/20$ of the thickness of the inert substance heated during the pulse ($\sqrt{2\alpha/k_i}$), then the cell size increased exponentially, so that the total thickness of the surrounding material was no less than $7R$. For a half-height pulse duration of 20 ns, the heating length was equal to ≈ 50 nm and the size of cells near the inclusion was about 2.5 nm. The step of the grid inside the inclusion exceeded the step outside by $\sqrt{\alpha_M/\alpha}$ times. The cell on the bound inclusion-matrix contained both the matrix material and the inclusion material with the thickness equal to the half step of the grid. For the mentioned characteristics, the size of the cell inside the inclusion was about 10 nm, which is approximately the thickness of the light absorption layer. This layer does not exceed 10 nm for most metals. This method allows one to make a reasonable consideration of light absorption by means of boundary conditions (2) [15].

The ordinary differential equation set obtained after dividing the space into cells was solved by the Runge — Kutta method of 1–5 orders with a variable time step. A relative error at an integration step does not exceed 10^{-9} , whereas the integral relative error estimated by the precision of performance of the law of conservation of energy did not exceed $2.5 \cdot 10^{-5}$.

Calculation of the radius of the most dangerous inclusion was made using the following method. First the absorptivities for the different particles' radii were calculated. Then, the critical energy density was calculated for these radii in terms of models (1-3). Next, quadratic

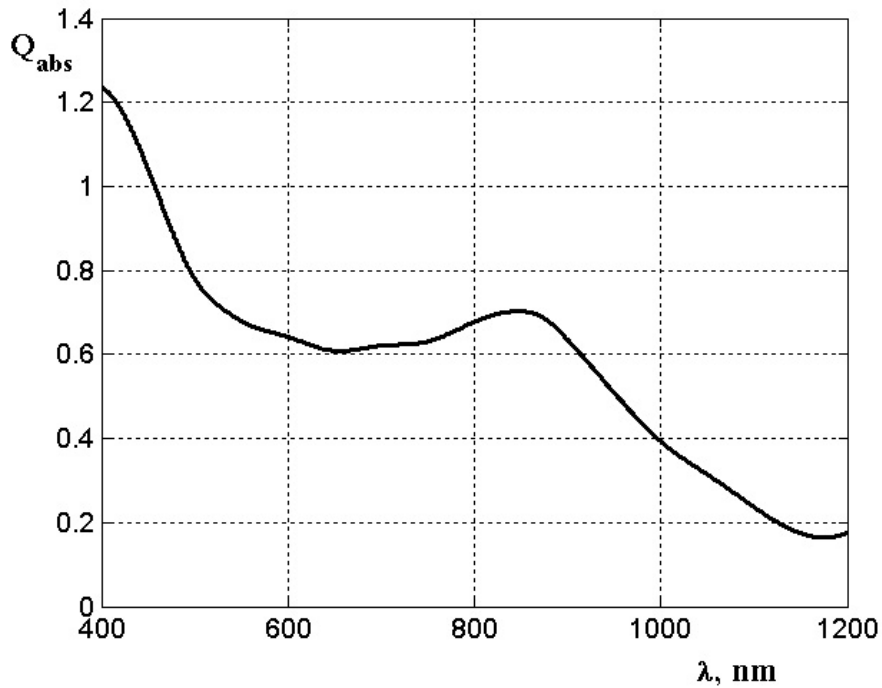


FIG. 2. Dependences of the aluminum nanoparticles' maximal absorptivity in PETN matrix on the initiating wavelength in a spectral range 400 – 1200 nm

interpolation was done to obtain the minimal value results. After that, the critical energy density was calculated at the point of this minimum. All these steps were repeated until the most dangerous inclusion's radius accuracy became 0.1 nm.

Fig. 3 shows dependences of the critical energy density on the radius of the aluminum inclusion in the PETN-matrix for initiating wavelengths of 532, 700, 850, 900, and 1064 nm. For each wavelength, there is an optimum radius of the nanoparticle (R_c), which corresponds to the minimum critical energy density (H_c), for the definite impulse duration. Values R_c and R_{max} for each wavelength have some differences (see table), this is due to the particularities of the nanoparticle heating by the laser pulse in solid-state matrix. For 20 ns pulse duration, there is a size of the nanoparticles, which is heated to the maximum temperature (particularities of the absorption were not considered – $Q_{abs} = 1$). The absorption cross section of the particle is πR^2 , heat capacity of the system nanoparticle – matrix layer might be written as $\frac{4\pi}{3} \cdot \left(c_M R^3 + c \left(\left(R + \sqrt{2\alpha/k_i} \right)^3 - R^3 \right) \right)$ [11], where $h \approx \sqrt{2\alpha/k_i}$ – thickness of the energetic material's layer, which is heated during the laser action. Therefore, the dependence of the heat rate (ΔT) of the particle on the nanoparticle's sizes during the pulse action is:

$$\Delta T = \frac{HR/4c}{R\xi_1\sqrt{2\alpha/k_i} + \xi_1^2 \cdot 2\alpha/k_i + c_M R^2/3c}, \quad (10)$$

where ξ_1 – variable parameter, its value is about 1 [11].

TABLE 1. Calculated parameters for the absorption and explosive decomposition process of the aluminum-PETN composites – complex refractive index (m_i), maximum of absorptivity ($Q_{abs\ max}$) and particle's radius R_{max} corresponding to this maximum, minimum of critical energy density (H_c), optimal particle's radius R_c

λ , nm	m_i	$Q_{abs\ max}$	R_{max} , nm	H_c , $\mu\text{J}/\text{cm}^2$	R_c , nm
400	0.32-3.72i	1.2358	30	7.25	30.7
450	0.41-4.06i	1.0410	35	7.93	36.1
500	0.5-4.59i	0.7815	41	9.93	42.1
532	0.56-4.86i	0.7064	44	10.66	45.8
550	0.6-5.01i	0.6799	46	10.93	47.6
600	0.77-5.46i	0.6419	52	11.25	53.1
650	0.98-5.97i	0.6090	57	11.59	58.6
700	1.26-6.4i	0.6210	63	11.22	63.8
750	1.5-6.72i	0.6307	68	10.95	68.8
800	1.78-6.87i	0.6771	73	10.16	73.5
850	1.91-6.9i	0.7027	78	9.77	77.7
875	1.82-6.87i	0.6871	80	9.99	79.7
900	1.7-6.97i	0.6364	82	10.79	81.8
950	1.4-7.22i	0.51	87	13.52	86.6
1000	1.17-7.58i	0.3939	93	17.58	92.1
1064	0.98-8.03i	0.2942	100	23.66	98.7
1100	0.85-8.33i	0.2375	104	29.43	102.2
1200	0.78-9.16i	0.1757	115	40.48	111.6

Maximum of the dependence corresponds to the $R_m = \xi_1 \sqrt{3c/c_M} \cdot \sqrt{2\alpha/k_i}$. The existence of the optimal nanoparticle's size for which the heating rate is maximal was postulated in previous works. If the half-height pulse duration is 20 ns, then $R_m=75$ nm. Table 1 shows the calculated minimum energy densities for the explosive decomposition of aluminum-PETN composites, optimal radius with the minimal initiating energy density for the laser wavelengths from 400 to 1200 nm. If $\lambda \leq 800$ nm, the radius, corresponding to the absorptivity maximum, $R_{max} < R_m$ (75 nm), and so the optimal radius, corresponding to the minimal critical energy density, $R_c > R_{max}$, i.e. the optimal radius for explosive decomposition initiation is larger than the radius, corresponding to the absorptivity maximum. If $\lambda \geq 850$ nm $R_{max} > R_m$, and so the optimal radius of the particle is smaller than the radius, corresponding to the maximum of absorptivity. Calculated critical energy densities are minimal if $\lambda = 400$ nm and have local minimum at $\lambda = 850$ nm. Minimal critical energy densities for the first harmonic of the Nd:YAG laser is 2.2 times bigger than the same values for the second harmonic. This fact is in good agreement with the experimental data (for the first harmonic – 1.15 J/cm², for the second – 0.7 J/cm² [3]), where this difference is 1.6.

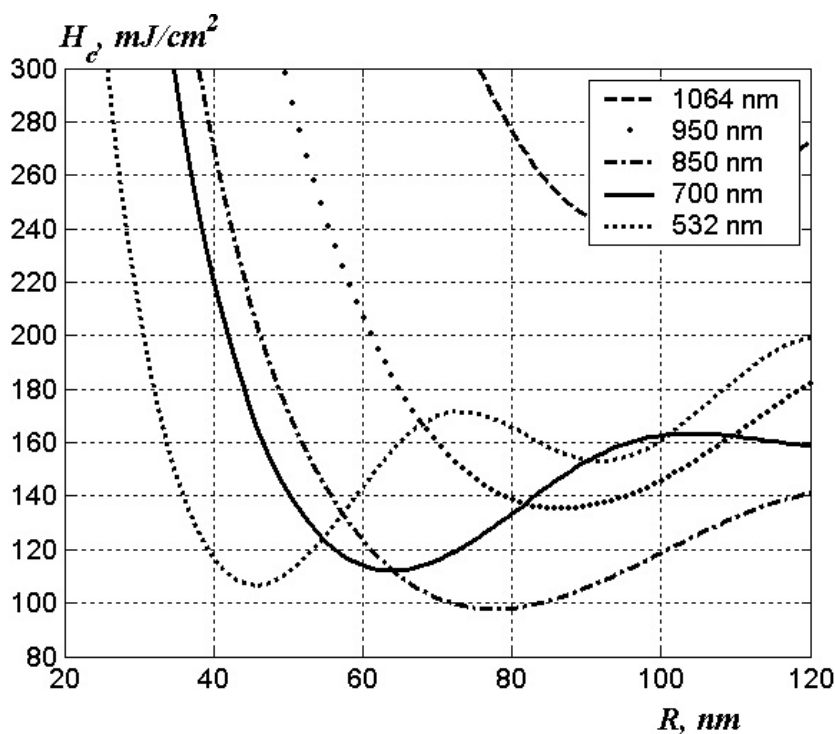


FIG. 3. Dependences of the critical energy density on the aluminum nanoparticle's radius in PETN matrix for the initiating wavelengths 532, 700, 850, 900 and 1064 nm

3. Conclusion

In this work, the dependences of the absorption of the aluminum nanoparticles and the critical energy densities of the pentaerythritol tetranitrate-aluminum composites were calculated for the wavelengths from 400 nm to 1200 nm. It was shown that it is necessary to consider both thermal and optical characteristics in order to calculate the critical initiation energy density and the radius of the most dangerous inclusion. The nanoparticle's radius, corresponding to the maximum on the curve of absorptivities, the maximum's amplitude and critical energy density of the explosive materials, were all shown to be dependent upon the initiating wavelength. The maximum of the aluminum nanoparticles' absorptivity and minimum of its critical energy density of the explosive decomposition are observed for the 400 nm wavelength, there is also a local maximum at the 850 nm wavelength. The results of the experiment qualitatively and quantitatively agree with our calculations. These results are necessary to determine the ideal cap composition for optical detonators.

Acknowledgments

This work was supported by Ministry of Education and Science of the Russian Federation (governmental project No. 2014/64) and Russian Foundation for Basic Research for the financial support (grant 14-03-00534).

References

- [1] Chumakov Yu.A., Knyazeva A.G. Initiation of reaction in the vicinity of a single particle heated by microwave radiation. *Fizika goreniiya i vzryva*, **48**(2), P. 24–30 (2012).
- [2] Ananyeva M.V., Zvekov A.A., et al. Promising compounds for the cap of optical detonator. *Perspektivnye materialy*, **7**, P. 5–12 (2014).
- [3] Aduiev B.P., Nurmukhametov D.R., et al. Vzryvchatoye razlozheniye TENa s nanodobavkami alyuminiya pri vozdeystvii impulsnogo lazernogo izlucheniya razlichnoy dliny volny. *Khimicheskaya fizika*, **32**(8), P. 39–42 (2013).
- [4] Kalenskii A.V., Zvekov A.A., et al. Influence of the laser irradiation wavelength on the energetic materials' initiation critical energy. *Fizika goreniiya i vzryva*, **50**(3), P. 98–104 (2014).
- [5] Kalenskii A.V., Ananyeva M.V., Zvekov A.A., Zykov I.Yu. Spectrum dependence of the critical energy density of composites based on pentaerythritol tetranitrate with nikel nanoparticles. *Fundamental'nye problemy sovremennogo materialovedeniya*, **11**(3), P. 340–345 (2014).
- [6] Kriger V.G., Kalenskii A.V., et al. Opredelenie shiriny fronta volny reakcii vzryvnogo razlozheniya azida serebra. *Fizika goreniiya i vzryva*, **48**(4), P. 129–136 (2012).
- [7] Korepanov V.I., Lisicyn V.M., Oleshko V.I., Cipilev V.P. K voprosu o kinetike i mehanizme vzryvnogo razlozheniya azidov tzhzhelyh metallov. *Fizika goreniiya i vzryva*, **42**(1), P. 106–119 (2006).
- [8] Aduiev B.P., Nurmukhametov D.R., Cipilev V.P., Furega R.I. Vliyanie dobavok ul' tradispersnyh chastic al-c na chuvstvitel'nost' tjena k lazernomu vozdeystviyu. *Fizika goreniiya i vzryva*, **49**(2), P. 102–105 (2013).
- [9] Kriger V.G., Kalenskii A.V., Ananyeva M.V., Borovikova A.P. Critical initiation-energy density as a function of single-crystal size in explosive decomposition of silver azide. *Fizika goreniiya i vzryva*, **44**(2), P. 76–78 (2008).
- [10] Aduiev B.P., Ananyeva M.V., et al. Mikroochagovaya model' lazernogo iniciirovaniya vzryvnogo razlozheniya jenergeticheskikh materialov s uchetom plavljeniya. *Fizika goreniiya i vzryva*, **50**(6), P. 92–99 (2014).
- [11] Kriger V.G., Kalenskii A.V., et al. Vliyaniye effektivnosti pogloshcheniya lazernogo izlucheniya na temperaturu razogreva vklyucheniya v prozrachnykh sredakh. *Fizika goreniiya i vzryva*, **48**(6), P. 54–58 (2012).
- [12] Nikitin A.P. Raschet kriticheskikh parametrov iniciirovaniya teplovogo vzryva tjena s nanochasticami medi na raznyh dlinah voln. *Mezhdunarodnoe nauchnoe izdanie Sovremennye fundamental'nye i prikladnye issledovaniya*, **4**(11), P. 68–75 (2013).
- [13] Zolotarev V.M., Morozov V.N., Smirnova E.V. *Opticheskie postojannye prirodnyh i tehniceskikh sred*. L.: Himija, 216 p. (1984).
- [14] Aduiev B.P., Nurmukhametov D.R., et al. Integrating Sphere Study of the Optical Properties of Aluminum Nanoparticles in Tetranitropentaerytrite. *Zhurnal Tekhnicheskoi Fiziki*, **84**(9), P. 126–131 (2014).
- [15] Kriger V.G., Kalenskii A.V., Zvekov A.A., Zykov I.Yu., Nikitin A.P. Protsessy teploperenosa pri lazerom razogreve vklyucheny v inertnoy matritse. *Teplofizika i aeromekhanika*, **20**(3), P. 375–382 (2013).
- [16] Aleksandrov E. I., Cipilev V. P. Issledovanie vliyanija dlitel'nosti vzbuzhdajushhego impul'sa na chuvstvitel'nost' azida svinca k dejstviyu lazernogo izlucheniya. *Fizika goreniiya i vzryva*, **20**(6), P. 104–108 (1984).
- [17] Burkina R.S., Morozova E.Ju., Cipilev V.P. Iniciirovanie reakcionno-sposobnogo veshhestva potokom izlucheniya pri pogloshhenii ego neodnorodnostjami veshhestva. *Fizika goreniiya i vzryva*, **47**(5), P. 95–105 (2011).

MEASURING LOCAL QUANTUM YIELD OF PHOTOLUMINESCENCE AND PHOTOTRANSFORMATIONS WITH LASER SCANNING MICROSCOPE

V. V. Zakharov^{1,2}, M. A. Baranov¹, A. S. Zlatov¹, A. V. Veniaminov¹

¹ITMO University, St. Petersburg, Russia

²Optec LLC, St. Petersburg, Russia

Viktor-zah@yandex.ru, mbaranov@mail.ru, zlatov.andrei@gmail.com,
veniaminov@phoi.ifmo.ru

PACS 78.55.Qr, 82.50.-m, 68.37.-d, 82.30.Qt

Measurement of local quantum yields for the photoluminescence of semiconductor nanocrystals (quantum dots) and photoinduced transformations of dye molecules in polymer films is demonstrated using a laser scanning microscope capable of mapping luminescence spectra and intensities of transmitted laser light. The confocal scanning microscope (Zeiss LSM710) was applied for both the induction of photochemical transformations and measurement. The luminescence quantum yield values for quantum dots in different locations of a polymer film were found to differ, ostensibly depending on their aggregation. To measure photoisomerization quantum yield, the effects of scanning a tiny area of a polymer film with a focused beam on the intensities of luminescence and transmitted light were monitored.

Keywords: Confocal microscopy, luminescence, photoisomerization, quantum dot, thioindigo.

Received: 24 November 2014

Revised: 29 November 2014

1. Introduction

Quantum yield (QY) is one of the most important characteristics of photoinduced processes such as photoluminescence and photochemical transformations. The quantum yield depends on intrinsic properties of molecules, nanocrystals, and other species as well as on their interactions with the environment. As a rule, only values for QY averaged over relatively large areas can be measured, while information about their microscopic local values remains hidden.

Nanocomposites with luminescent semiconductor nanocrystals (quantum dots, QD) are widely used in different areas, such as microelectronics, solar energy conversion, biology and medicine [1, 2] due to their unusual optical, electrical and structural properties [3]. Spatial heterogeneity of properties is a common feature of nanocomposite materials. Aggregation of nanoparticles may lead to considerable inhomogeneity of light intensity, decrease of luminescence caused by nonradiative energy transfer. The distribution of the QY could be regarded as a quantitative measure of nanocrystal and molecular interactions and provide information about efficiency of nanocrystal incorporation in the polymeric matrix. Bulk polymers are known to be spatially inhomogeneous, and luminescent dyes dissolved in them may serve efficient probes for testing microheterogeneous environment, provided local QY becomes available.

There are two different approaches to measuring QY of luminescence: (i) direct, or absolute, which typically requires a spectrophotometer with an integrating sphere, and (ii) comparative, based on relative measurements of light emitted by a specimen under study and

a fluorescent standard with known QY. Traditional techniques of QY measurements, as well as possible sources of errors, have been analyzed and described in detail [4–9]. In a similar way, the QY of photochemical reactions can be obtained from spectroscopic monitoring of photoreaction progress and comparison with phototransformations of etalon substances whose QY are well established (chemical actinometers) [10] or by direct measurement of exposure.

Various techniques intended for the measurement of absolute luminescence and photoreaction QY are known, such as that using a spectrophotometer with integrating sphere [11] or the dual-beam thermal lens technique [12], but only in a few publications local characteristics with microscopic resolution have been revealed. Thus, a combined map of topography and single-particle fluorescence QY of single particles was obtained using correlated atomic-force and single-particle fluorescence microscopy [13], however such a technique could hardly be applied to investigate the inhomogeneous bulk of thick samples.

The present work is aimed at the development of a technique utilizing a confocal laser scanning microscope (LSM) for the measurement of local QY of exemplary photoprocesses induced by laser light in doped polymer films: quantum dot luminescence and phototransformations of organic molecules such as *trans-cis* photoisomerization of a thioindigo derivative and photoreduction of phenanthrenequinone.

2. Experimental

2.1. Instrumentation and calibration

In this study, a Zeiss LSM710 scanning microscope based on Axio Imager Z1 stand, Carl Zeiss Microimaging GmbH, Germany, was used to measure QY. Confocal scanning microscopy allows one to obtain digital images with high spatial resolution due to the filtering-out of light scattered and emitted by out-of-focus optical slices. The LSM is capable of measuring the intensity of laser light transmitted by specimens and obtaining local luminescence spectra.

Prior to applying the microscope for numerical measurements of QY, we needed to assess the accuracy of light transmittance measured with its help and calibrate the spectral response of the microscope photodetector system, in order to ensure correct calculation of photons absorbed by the species and inducing their luminescence or phototransformations.

To verify the accuracy of quantitative measurements using LSM, the transmittance of laser light by several neutral gray light absorbers (glass plates with thin metal coating of controlled thickness) with well defined optical densities was measured. The measured optical densities versus their etalon values are presented in Fig. 1 that demonstrates perfect agreement within the range of optical densities up to 1 and slight deviation at O.D.=2.4, for the small aperture (0.2) lens. In the case of large numerical aperture (0.95), a significant deviation from linearity shall be taken into account already for O.D.>0.6, which is already far beyond absorbance values considered acceptable for luminescence measurements.

For the present study, objective lenses were chosen with sufficiently small numerical aperture (predominantly 0.1 to 0.2) that ensured, along with correct transmittance measurements, ‘optical slice thickness’ larger than the sample thickness, to avoid possible uncertainties caused by absorption heterogeneity along the optical axis. Axial resolution of luminescence images strongly depends not only on numerical aperture, but also on the diameter of the confocal pinhole (Fig. 2); however, this does not apply to transmittance measurements that do not involve the pinhole.

Spectral calibration of LSM photodetector system was performed using an etalon incandescent lamp verified at S. I. Vavilov Optical institute (St. Petersburg) as black body with color

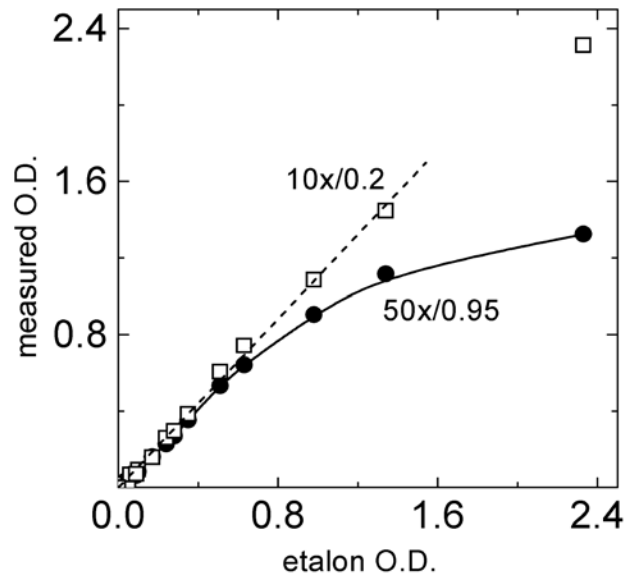


FIG. 1. Optical density of neutral gray etalon absorbers at 543 nm measured with LSM using two different objective lenses (magnification / numerical aperture: $10 \times / 0.2$, squares and $50 \times / 0.95$, circles), vs. nominal etalon optical density. The dashed line is the best linear fit for the low aperture dependence; the solid curve is exponential fit for the large aperture drawn as a guide to the eye

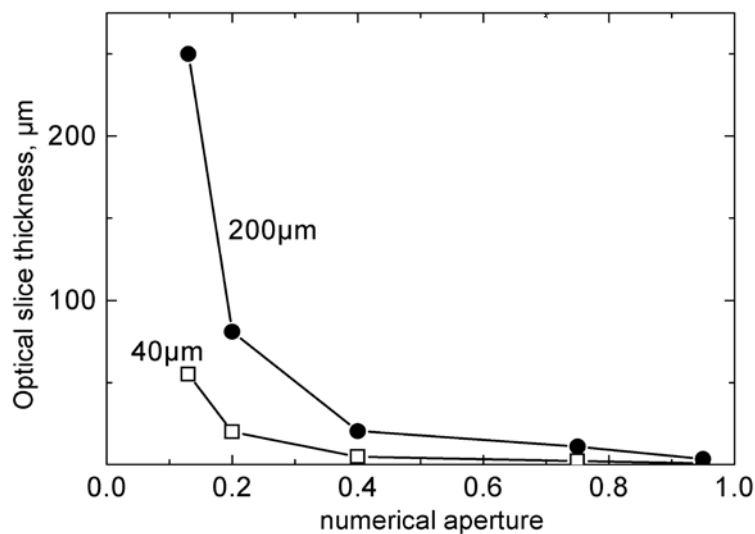


FIG. 2. Optical slice thickness as a function of numerical apertures of the objective lenses, at confocal pinhole diameters 40 (squares) and 200 μm (circles)

temperature $T = 2856 \text{ K}$; the spectra of its emission measured with the LSM was used for correction of the luminescence spectra.

Diode (405 nm), Ar^+ (488 nm) and He-Ne (543 nm) lasers served as light sources for luminescence excitation and the induction of phototransformations. In order to avoid overheating of specimens by focused laser beams, not more than a few per cent of maximum power was used in the measurements. Within these limits, no effect of varied power on the results of measurements was revealed.

The temperature of specimens could be monitored and stabilized during the measurements within the range from room temperature up to 100 °C with an accuracy of ± 0.125 °C using a glass substrate with conductive coating serving as a heater run by a specially designed LabView-compatible controller. Almost all the measurements were fulfilled at 24 °C.

2.2. Sample preparation

The polymer films were made by casting from tetrahydrofuran solutions of polymers: polybutylmethacrylate (PBMA), polymethylmethacrylate (PMMA), polyvinylbutyral, or polycarbonate mixed in appropriate proportions with solutions of either semiconductor quantum dots (QD), thioindigo dye (TI), phenanthrenequinone (PQ), or Rhodamine 6G (R6G) onto polished glass plates. The polymer powders were purchased from Vekton (St. Petersburg, Russia).

The photoisomerizing thioindigo derivative [14] was synthesized and kindly presented by Dr. M. Mostoslavsky and Dr. V. Paramonov (NIOPIK branch, Rubezhnoe, Ukraine) and remained in the possession of our laboratory. Previously, this compound served in 3D holography as a photoswitchable sensitizer of anthracene photooxidation in Reoxan media that helped convert weak amplitude ‘latent image’ into efficient phase holograms [15]. The dye was used in the present work after its absorption and luminescence spectra were found to remain unchanged.

Phenanthrenequinone (PQ), which was purchased from Aldrich, is capable of photoreduction through hydrogen abstraction from surrounding molecules [16] and is known as a key component of light-sensitive materials with postexposure development of holograms by photoattachment and molecular diffusion [17].

Core/shell CdSe/ZnS QDs, with average diameter of 2.5 nm and capped by trioctylphosphineoxide (TOPO), were synthesized and tested in Belarusian State University, Minsk, Belarus. For hexane solutions of the QDs, the maximum luminescence was found at 531 nm, with QY of ~ 13 %.

3. Results and Discussion

3.1. Luminescence of quantum dots

Luminescence quantum yield of QDs in a polycarbonate film was determined by a comparative technique using a similar film with R6G as an intermediate fluorescence reference, whose QY (47 %) was previously determined in turn by comparison with R6G solution in ethanol (QY= 94 %):

$$\phi = \phi_R \frac{I}{I_R} \frac{OD_R n^2}{OD n_R^2}, \quad (1)$$

where ϕ is QY, I is luminescence intensity integrated over the whole spectrum, n is refractive index, OD is optical density and the subscript R stands for reference.

While no spatial inhomogeneity was found in R6G luminescence intensity, the luminescent image of polycarbonate film with QDs (Fig. 3a) manifests their uneven spatial distribution, with apparently uniformly luminescent area with dark holes in the left part and small bright spots on the right. Quantum yields of QD luminescence in these areas were found to differ: 0.4 in the uniform layer and 0.12 in the agglomerates (circle), despite the apparently brighter luminescence in the latter case. The lower QY value within the rounded spot in Fig. 3a can be explained by stronger interaction between agglomerated QDs as compared to less densely distributed QDs in the rectangular area, which also correlates with notably larger red shift of the luminescence spectrum (Fig. 3b) in the latter case with respect to QD luminescence spectrum in liquid (hexane) solution (531 nm). It should be noted that, contrastingly, QD luminescence in a

polyvinylbutyral film was found to be uniform, with QY = 0.23 and maximum luminescence at 534 nm.

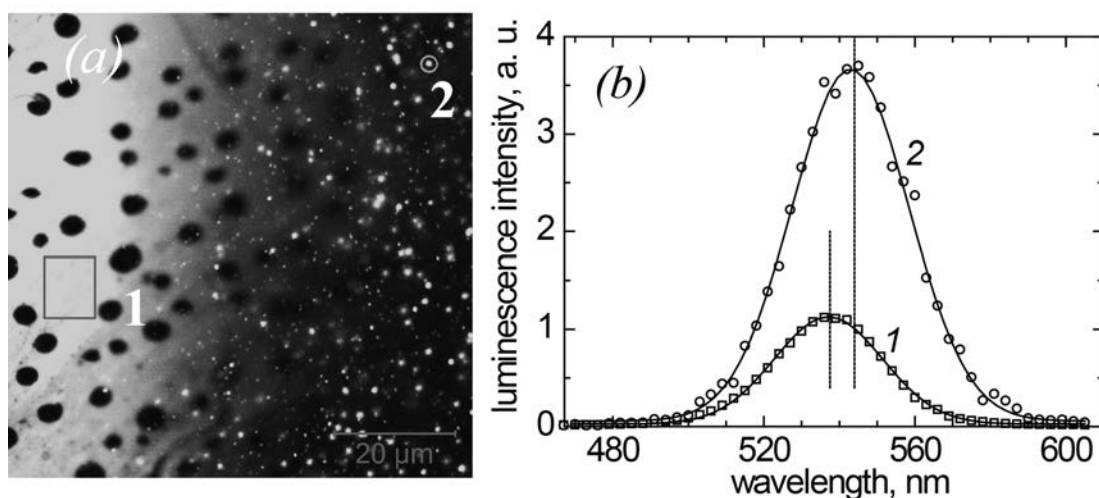


FIG. 3. a) Luminescent image of a $80 \times 80 \mu\text{m}$ part of a polycarbonate film with CdSe/ZnS nanocrystals; excitation wavelength 405 nm; b) luminescence spectra of the film region within the rectangle 1 and the bright spot in the centre of the circle 2 (squares and circles, respectively). Solid lines are best Gaussian fits; dotted lines depict the maxima of luminescence intensity at 537 (1) and 543 nm (2). Notice the lower intensity in the area 1 with QY larger than that in the area 2

3.2. Photoisomerization of thioindigo dye

The thioindigo dye exists in two isomeric forms that can undergo reversible phototransformations accompanied by dramatic spectral changes. In Fig. 4, absorption spectra of the TI-doped PBMA film obtained after exposures to mercury arc light with wavelengths 578 nm (curve 1) and 436 nm (2) are plotted, representing almost pure *trans*-isomer and isomer mixture with predominant contribution of *cis*-isomer, respectively. Only *trans*-TI molecules are capable of fluorescence [14, 18] whose intensity can be then a measure of their concentration. Almost identical fluorescence spectra acquired with LSM and Cary Eclipse spectrofluorimeter are also presented in Fig. 4 (3 and 4, respectively).

To study *trans-cis*-photoisomerization of TI, different exposures of actinic light were applied to small strip-shaped areas of the specimen by scanning them with a He-Ne laser (543 nm) of the microscope, followed by monitoring transmittance and luminescence excited by properly attenuated light of the same laser. The intensities of emitted and transmitted light are shown in Fig. 5 as functions of exposure. Before the measurements, the dye in the film was brought into the *trans*-isomeric form by uniform exposure to 436 nm light of a 120 W high-pressure mercury lamp.

Unlike fluorescence, light absorbance at the excitation wavelength does not exclusively belong to *trans*-isomer. Therefore, the optical density of the film at 543 nm can be taken as a measure of *trans*-isomer concentration only at low degree of *trans-cis* conversion, in the initial stage of the process. Hence, we consider luminescence intensity more reliable for monitoring the dynamics of phototransformation, while the initial value of optical density was used to determine the number of TI molecules.

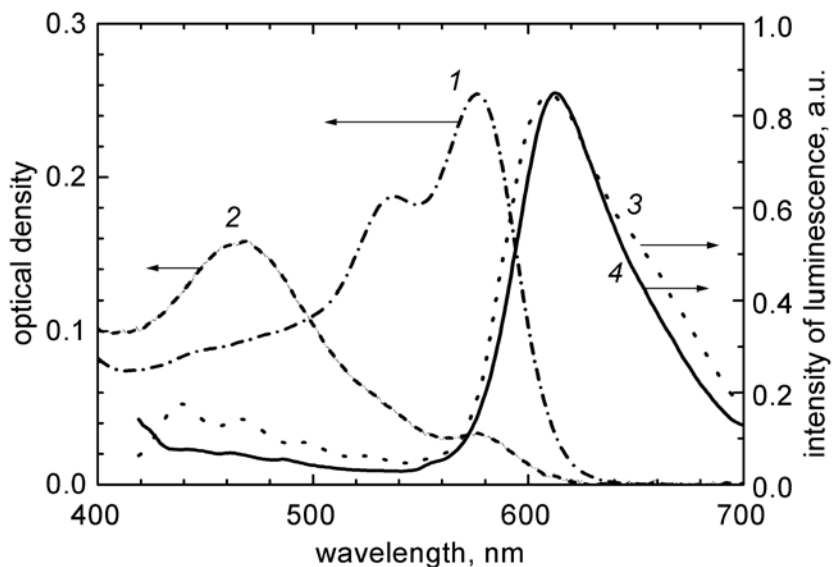


FIG. 4. Absorption spectra of polymer film with thioindigo dye exposed to light with wavelength 436 nm (1, dash-dotted line, almost pure *trans*-isomer) and 578 nm (2, dashed line, predominantly *cis*-isomer with small contribution of *trans*-isomer); fluorescence spectra measured with LSM (3, dotted line) and Cary Eclipse spectrofluorimeter (4, solid line; excitation at 405 nm)

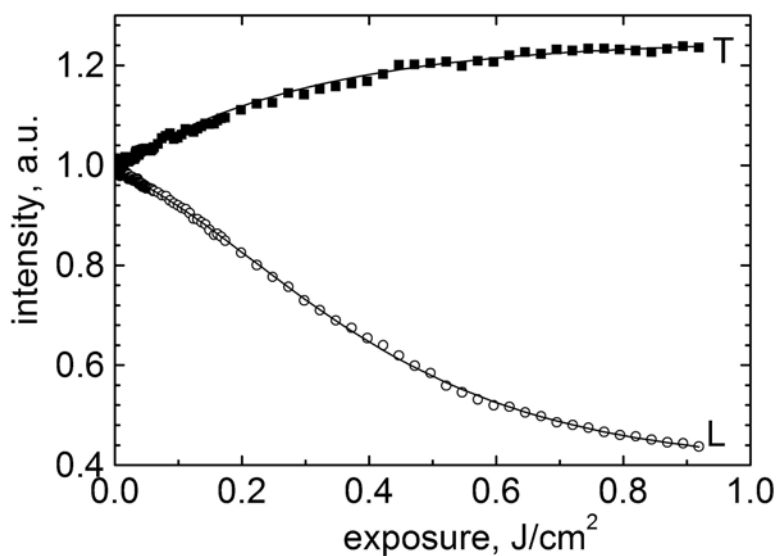


FIG. 5. Photoisomerization of thioindigo in PBMA film monitored with LSM: intensities of transmitted excitation light (543 nm, solid line, T) and luminescence of the *trans*-isomer (dashed line, L) as functions of exposure

The QY of the *trans-cis* photoisomerization can be calculated as ratio of the number $\Delta DN_A S/\alpha$ of molecules within the illuminated area S converted from *trans*- to *cis*-isomer divided by the number $E(1 - T)/h\nu$ of absorbed photons with energy $h\nu$:

$$\phi_{tc} = \frac{\Delta D S N_A h\nu}{E \alpha (1 - T)}, \quad (2)$$

with ΔD - the small photoinduced change of optical density caused by exposure to light energy E , N_A - Avogadro number, $a = 8700 \text{ Lmol}^{-1} \cdot \text{cm}^{-1}$ - molar absorption coefficient of *trans*-TI calculated using the spectroscopic data available from [14], T - transmittance of the doped film at 543 nm.

The initial (measured when almost all the dye was in *trans*-isomeric form) value of $\phi_{tc} = 0.006$ is between the values previously reported for QY of *trans-cis* isomerization of TI in more rigid PMMA and in liquid butyl acetate solution, 0.001 and 0.06, respectively [19]. During photoisomerization, ϕ_{tc} dramatically decreased after about 30 - 35 % of *trans*-molecules had been converted to the *cis*-isomer (Fig. 6). This was presumably due to the significantly heterogeneous distribution of free volume needed for restructuring dye molecules in the bulk polymer, even though glass transition temperature of PBMA is quite close to the measurement temperature. Contrastingly, QY of fluorescence that apparently does not require much free volume did not significantly vary from its initial value (0.15).

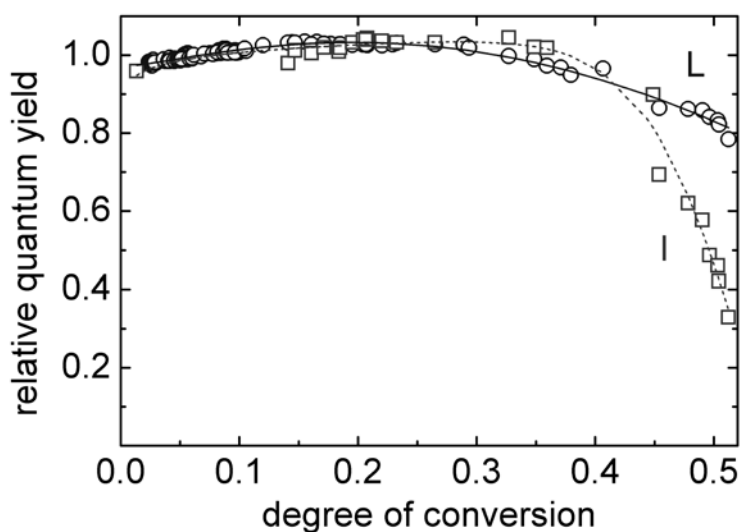


FIG. 6. Quantum yields of isomerization (squares, I) and luminescence (circles, L) as functions of degree of dye conversion from *trans*- to *cis*-isomeric form in the course of isomerization. Lines are guides to the eye

3.3. Photoreduction of phenanthrenequinone

Photoreduction of PQ provided another example of a photochemical process for this study. Different doses of laser light (488 nm) were applied to $50 \times 50 \mu\text{m}$ squares of PQ-doped PMMA film using the scanning microscope (Fig. 7a). As a result of the exposure, PQ was partially bleached and the film transmittance has grown, as well as its luminescence intensity (Fig. 7b) - the situation contrary to that of photoisomerization (cf. Figs. 5 and 8). This means that the luminescence belongs to the photoproduct, despite the latter is known to have almost negligible absorption in the visible range. Because absorbance of the photoproduct at the wavelength of excitation remained unknown, no QY of its luminescence could be calculated.

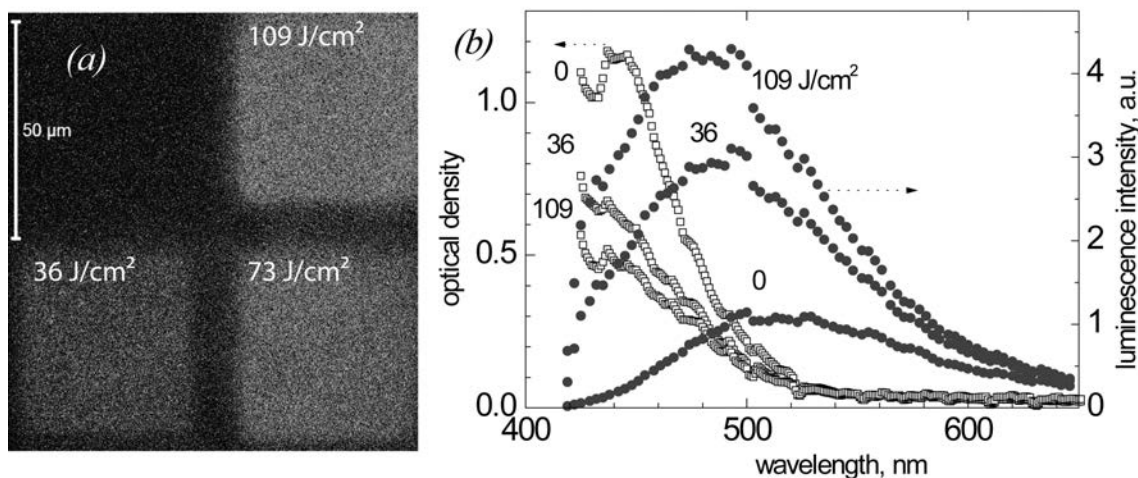


FIG. 7. Phototransformation of phenanthrenequinone in PMMA: a) luminescent image of a $100 \times 100 \mu\text{m}^2$ part of a PMMA film with PQ; the lighter square areas were exposed to 36, 73 and 109 J/cm^2 of laser light at 488 nm before scanning for imaging; (b) local optical density (open symbols) and luminescence spectra (full symbols) of the film in its intact state (0) and after 36 and 109 J/cm^2 exposure at 488 nm

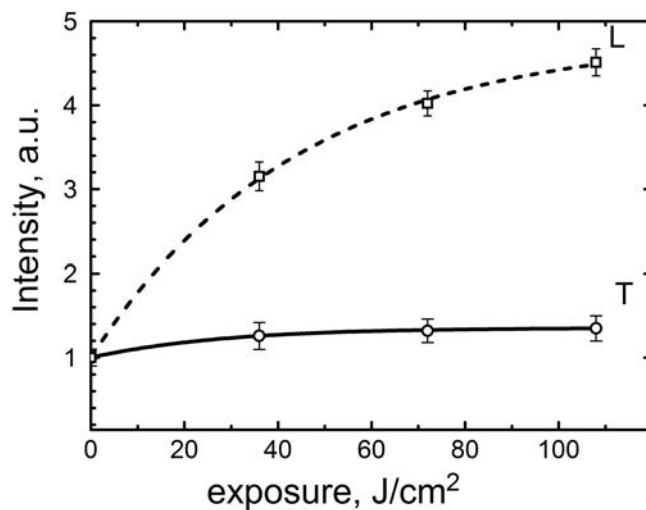


FIG. 8. Relative intensities of transmitted light (T, 488 nm) and luminescence of the film at 500 nm (L, excitation wavelength 405 nm) measured with LSM, as functions of exposure

The QY of PQ phototransformation was calculated similar to that of photoisomerization and was approximately 10 percent.

4. Conclusions

In this study, we gave three examples of using a confocal scanning microscope as a convenient tool for measuring local quantum yields of luminescence and photochemical transformations. This application of the precision imaging instrumentation is based on its ability to measure the spatial distributions and the intensities of sample-related transmitted and emitted

light, obtain local luminescence spectra, and expose small regions of interest to photochemically active light. Such measurements can provide important information on microstructure of composite materials, their spatial heterogeneity, and can also be helpful if only a small amount or small area of a specimen is available for study.

Acknowledgments

The authors gratefully acknowledge the financial support of this work from the Ministry of Education and Science of the Russian Federation (Grant No. 14.B25.31.0002) and the Russian Foundation for Basic Research (Grants No. 12-02-01263 and No. 12-02-00938).

References

- [1] Rajeshwar K., de Tacconi N.R., Chenthamarakshan C.R. Semiconductor-Based Composite Materials: Preparation, Properties, and Performance. *Chem. Mater.*, **13**, P. 2765–2782 (2001).
- [2] Tomczak N., Janyczewski D., Han M., Vancso G.J. Designer polymer-quantum dot architectures. *Progr. Polymer Sci.*, **34**, P. 393–430 (2009).
- [3] Bukowski T.J., Simmons J.H. Quantum Dot Research: Current State and Future Prospects. *Critical Reviews in Solid State and Materials Sciences*, P. 119–142 (2002).
- [4] Demas J.N., Crosby G.A. The Measurement of Photoluminescence Quantum Yields. *Review, J. Phys. Chem.*, **75**, P. 991–1024 (1971).
- [5] Williams A.T.R., Winfield S.A., Miller J.N. Relative fluorescence quantum yields using a computer controlled luminescence spectrometer. *Analyst*, **108**, P. 1067–1071 (1983).
- [6] Lakowicz J.R. *Principles of Fluorescence Spectroscopy*, 3rd ed. Springer, 954 p. (2006).
- [7] Carlson L., Krauss T.D. Direct measurement of the fluorescence quantum yield for individual single-walled carbon nanotubes. *Proc. Conf. Electrochem. Soc. 'Carbon Nanotubes and Nanostructures: Fundamental Properties and Processes'*, Abstr. 1018 (2007).
- [8] Brouwer A.M. Standards for photoluminescence quantum yield measurements in solution (IUPAC Technical Report). *Pure Appl. Chem.*, **83**, P. 2213–2228 (2011).
- [9] Wuerth C., Grabolle M., et al. Relative and absolute determination of fluorescence quantum yields of transparent samples. *Nature Protocols*, **8**, P. 1535–1550 (2013).
- [10] Kuhn H.J., Braslavsky S.E., Schmidt R. Chemical Actinometry (IUPAC Technical Report). *Pure Appl. Chem.*, **76**, P. 2105–2146 (2004).
- [11] Gaigalas A.K., Wang L. Measurement of the fluorescence quantum yield using a spectrometer with an integrating sphere detector. *J. Res. Natl. Inst. Stand. Technol.*, **113**, P. 17–28 (2008).
- [12] Bindhu C.V., Harilal S.S., et al. Measurement of the absolute fluorescence quantum yield of rhodamine B solution using a dual-beam thermal lens technique. *J. Phys. D: Appl. Phys.*, **29**, P. 1074–1079 (1996).
- [13] Ebenstein Y., Mokari T., Banina U. Fluorescence quantum yield of CdSe/ZnS nanocrystals investigated by correlated atomic-force and single-particle fluorescence microscopy. *Appl. Phys. Lett.*, **80**, P. 4033 (2002).
- [14] Mostoslavskii M.A. Photochromic Thioindigoid Dyes. In: *Organic Photochromes*, ed. by Eltsov A.V., Springer, New York and London, P. 45–104 (1990).
- [15] Lashkov G.I., Popov A.P., Ratner O.B. Three-dimensional phase-recording reoxan media with physical development of a latent image. *Opt. Spectrosc.*, **52**, P. 350–352 (1982).
- [16] P.A. Carapellucci, H.P. Wolf, K. Weiss. Photoreduction of 9,10-Phenanthrenequinone. *J. Amer. Chem. Soc.*, **91**, P. 4635–4639 (1969).
- [17] Veniaminov A.V., Mahilny U.V. Holographic Polymer Materials with Diffusion Development: Principles, Arrangement, Investigation, and Applications. *Opt. Spectrosc.*, **115**, P. 902–925 (2013).
- [18] Haucke G., Paetzold R. *Photophysikalische Chemie Indigoide Farbstoffe*. *Nova Acta Leopoldina*. Deutsche Akademie der Naturforscher Leopoldina, Halle (Saale), 123 p. (1978).
- [19] Veniaminov A.V., Lashkov G.I. Photochemical isomerization of thioindigo derivatives embedded in poly(methylmethacrylate). *Polymer Sci. USSR*, **28**, P. 963–971 (1986).

HYDROGEN ADSORPTION PROPERTIES OF METAL-ORGANIC FRAMEWORKS WITHIN THE DENSITY-FUNCTIONAL BASED TIGHT-BINDING APPROACH

Bassem Assfour*, Thaeer assaad, adnan odeh

Department of Chemistry, Atomic Energy Commission of Syria (AECS),
P.O. Box 6091, Damascus, Syrian Arab Republic,
Tel.: +963 11 213 2580, Fax: +963 11 611 2289

*cscientific@aec.org.sy

PACS 87.15.ag

Practical methods for hydrogen storage are still a prime challenge in the realization of an energy economy based on Hydrogen. Metal organic frameworks (MOFs) are crystalline ultra-porous materials with ability to trap and store voluminous amounts of gas molecules. MOFs represent an encouraging storage method relying on their enormous surface area. However, MOFs show reduced hydrogen uptake at room temperature due to low adsorption energy of hydrogen. To increase the adsorption uptake of MOFs at room temperature, the adsorption energy must be increased. In this contribution, materials exhibiting higher adsorption energy and enhanced hydrogen adsorption, namely MIL-53 (Al) and MOF-74, have been investigated using molecular dynamics (MD) simulation. MD simulations were performed within the density functional based tight binding method (DC-SCC-DFTB). Our results demonstrate that DC-SCC-DFTB method predicts structural parameters, adsorption sites, adsorption energies and diffusion factors with a very good accuracy, making this method a very powerful tool to investigate various types of MOF. Moreover, results show that the adsorption energy can be increased by incorporation of transition metals in MOF structures.

Keywords: Hydrogen storage, Metal Organic Frameworks, Molecular dynamics, DFTB, adsorption energy.

Received: 29 October 2014

Revised: 10 November 2014

1. Introduction

Hydrogen storage in metal organic framework materials (MOFs) attracts significant attention because these materials have enormous specific surface area, low density and a crystalline structure that can be tailored and chemically functionalized to maximize the adsorption uptake. MOFs are constructed from metal oxides interconnected by different organic linkers. Thousands of MOFs have been synthesized (only some of them are stable and porous), categorized and carefully studied over the last decade [1,2]. Some MOFs showed exceptional gas storage capacity and selectivity [3–5]. The essential issues for hydrogen adsorption in MOFs are both the strength of adsorption interaction (adsorption energy), and the number and surface of adsorption sites. The former determines the operation temperature and pressure, and the latter determines the storage capacity. The hydrogen adsorption energies on MOFs are ranging from 3 to 5 kJ/mol [6,7]. This small adsorption energy is sufficient for H₂ adsorption below 80K, but not at room temperature because an extremely high pressure is needed to make the adsorption possible [8]. To store the hydrogen reversibly at room temperature and moderate pressures, the

adsorption energy should be about 0.3 – 0.4 eV/molecule (30 – 40 kJ/mol), according to the estimations of Li *et al.* [9]. According to the estimations of another authors, the adsorption energy should be about 0.15 eV/molecule (15 kJ/mol) [10] according to Myers *et al.* and 20 kJ/mol according to Snurr *et al.* [11].

Several strategies have been proposed in order to enhance the adsorption energy of hydrogen such as incorporation of transition metals, fullerene impregnation and lithium doping [12,13]. Another method to improve the storage capacity is reducing the framework density. This requires investigating the MOFs formed by light metal ions such as Li^+ , Mg^{2+} , and Al^{3+} . One expects that the large polarizing power of Al^{3+} should give rise to relatively strong coordination bonds [14]. From structural point of view, a large number of different Al-based MOFs have been synthesized and studied [15–17]. Some compounds are highly porous and promising for gas storage, separation and adsorption applications [18,19]. The MIL-53 [20,21] are porous materials synthesized by the group of Férey, first reported to store significant amount of hydrogen at 77 K [22]. These structures are made up of chains of corner-sharing metal octahedral (Al^{3+} , Cr^{3+}) interconnected by benzene dicarboxylate (BDC) groups, forming 1D diamond-shaped channels and a porous solid with pores of 8.5 Å (see Fig. 1).

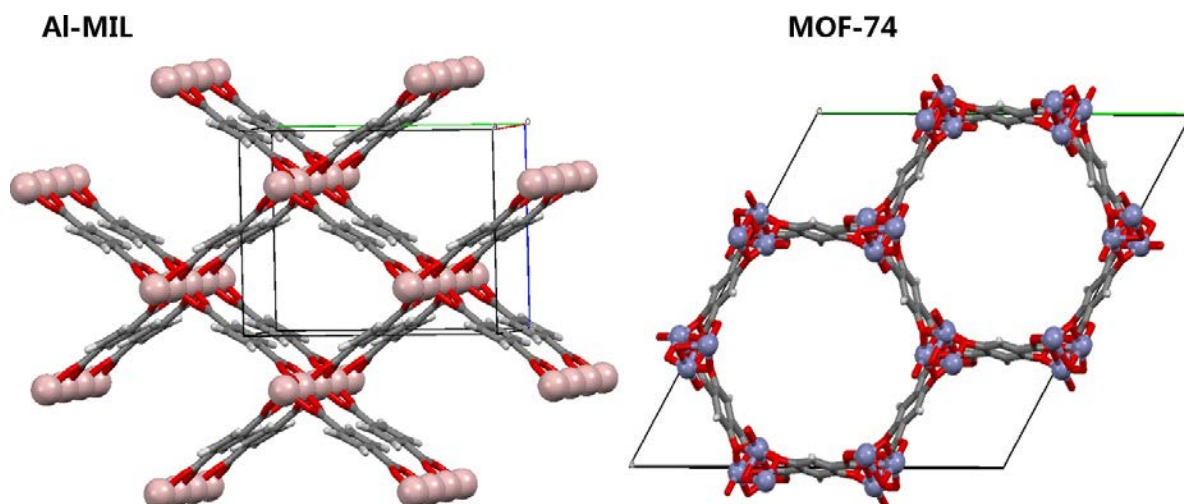


FIG. 1. Crystal structures of the MOFs studied in this work. (Zn, dark blue; O, red; C, gray; H, white; Al, pink). (For interpretation of the references to colour in this fig legend, the reader is referred to the web version of this article)

MOF-74 is constructed from rod-shaped secondary building units; the rod is constructed from 6-coordinated Zn^{2+} centers, where each Zn has three carboxyl and hydroxy groups to produce one-dimensional channels of section area $10.3 \times 5.5 \text{ \AA}^2$ (see Fig. 1). MOF-74 is especially interesting, because it shows the highest surface density for physisorbed hydrogen in framework structures [23], which leads to enhanced hydrogen capacity.

From a modeling point of view, hydrogen binding in MOFs has been extensively investigated in the last few years [24]. Most of studies focus on prediction of hydrogen storage properties of these compounds [25], and trying to optimize chemical structure, pore volume and surface area to enhance hydrogen uptake [26,27].

In this contribution, we report a comprehensive theoretical study comparing the H_2 adsorption in the MIL-53(Al) and MOF-74 materials. We performed molecular dynamics (DFTB MD) simulation on the full crystal structures with hydrogen molecules adsorbed in them. The adsorption sites and energies as well as the values for the hydrogen diffusion coefficients will be presented. The results are compared to experimental data in the literature.

2. Molecular dynamics simulation and calculations of H₂ binding energies

The pore surfaces of MOFs contain numerous distinct sites at which hydrogen might be adsorbed. To investigate the preferable sites for hydrogen adsorption, we performed MD simulations within the dispersion-corrected self-consistent density functional based tight binding method (DC-SCC-DFTB) [28–31], as implemented in the deMonNano program package [32]. DFTB is an approximate version of the DFT method that was later extended to account for the London dispersion energy. This technique showed exceptional performance and ability to study large biological and supramolecular systems [33, 34]. The DC-SCC-DFTB method was successfully used to study the structural, energetic, electronic, and mechanical properties of variety of MOF materials [35, 36]. Recently, DC-SCC-DFTB has been shown to describe the structural properties, formation energies and hydrogen adsorption sites of covalent organic frameworks (COFs) in rather good accuracy [37, 38].

Two sets of Slater-Koster parameters have been used: the standard SCC-DFTB parameter set optimized by Seifert *et al.* for MOF-74 [39], and for Al-MIL we have used materials science parameter set developed by Heine *et al.* [40].

Initially, the structures for Al-MIL and MOF-74 from X-ray diffraction data were optimized with the DC-SCC-DFTB method. In order to obtain the possible adsorption sites, up to 11 and 22 H₂ molecules (corresponding to 2.67 and 1.56 wt. %) were added randomly to the optimized Al-MIL and MOF-74 unit cells, respectively. First, the structures were equilibrated for 4 ps at 100 K. A 16 ps DFTB MD simulation was performed starting at temperatures of 100 K with a step size of 0.25 fs; the temperature was gradually decreased by simulated annealing down to 5 K. The DFTB MD trajectories were generated in the NVT ensemble using the Berendsen thermostat. Such procedure allows determination of the preferred adsorption sites in a rather unbiased manner, because the H₂ molecules were free to diffuse between the different sites, and by decreasing the temperature were first trapped in the strongest adsorption sites.

The H₂ binding energy at each of the revealed adsorption sites (EB) was calculated from the energy difference between the relaxed structure with adsorbed hydrogen and the same structure after specific hydrogen molecule was removed plus the free hydrogen molecule in the same but empty unit cell. i.e. The binding energy was calculated using:

$$EB = E(\text{MOF} + \text{H}_2) - E(\text{MOF}) - E(\text{H}_2). \quad (1)$$

The mean square displacements (MSDs) for the H₂ molecules were evaluated at 25 K, using the following equation where N corresponds to the number of H₂ molecules considered:

$$MSD(t) = \langle \Delta r_i^2(t) \rangle = \frac{1}{N} \sum_{i=1}^N (r_i(t) - r_i(0))^2. \quad (2)$$

We note that MSDs present a reasonably linear profile after 2 ps simulation time and over a broad time domain. The self-diffusion coefficients (Ds) were then obtained by fitting the MSDs plots as a function of time in the region, 2 – 6 ps and assuming the well-known Einstein formula:

$$D = \frac{1}{6} \lim_{t \rightarrow \infty} \frac{\langle \Delta r^2 \rangle}{t}, \quad (3)$$

where $\langle \Delta r^2 \rangle$ is the mean square displacement of the particles averaged on trajectories of duration t .

3. Results and discussion

The optimized structure of empty Al-MIL has a shape similar to that reported in the literature [21], the calculated lattice parameters: ($a = 6.76 \text{ \AA}$, $b = 16.91 \text{ \AA}$, $c = 12.59 \text{ \AA}$) are well comparable with those reported from experiment ($a = 6.6085 \text{ \AA}$, $b = 16.6750 \text{ \AA}$, $c = 12.8130 \text{ \AA}$) at 548 K [21]. The fact that the minimized structure at zero temperature is not exactly the same, but closely related to the experimental one is not surprising in light of the presence of thermal motion at 548 K.

The results of the DFTB MD simulation at $T = 25 \text{ K}$ for Al-MIL loaded with molecular hydrogen are shown in Fig. 2. The three sites with the largest adsorption energies are numbered 1 – 3 and listed in Table 1. Two of them with the highest adsorption energies (site 1 and 2) are near the AlO_6 clusters at the corners of the pore. Site 3 is located over to the benzene ring (the organic linker); site 3 has the lowest adsorption energy so it is the least preferred adsorption site for the hydrogen molecules. The average adsorption energy for 11 hydrogen molecules was found to be 6.35 kJ/mol, and this value was consistent with experimental results where the average heat of adsorption was found to be 5.6 kJ/mol [41]. The maximum total hydrogen uptake, i.e. when the three adsorption sites are fully occupied, was found to be 3.87 wt.%, which compared favorably with 3.8 and 3.1 wt.% measured at 77 K and 16 and 20 bar, respectively [22,41].

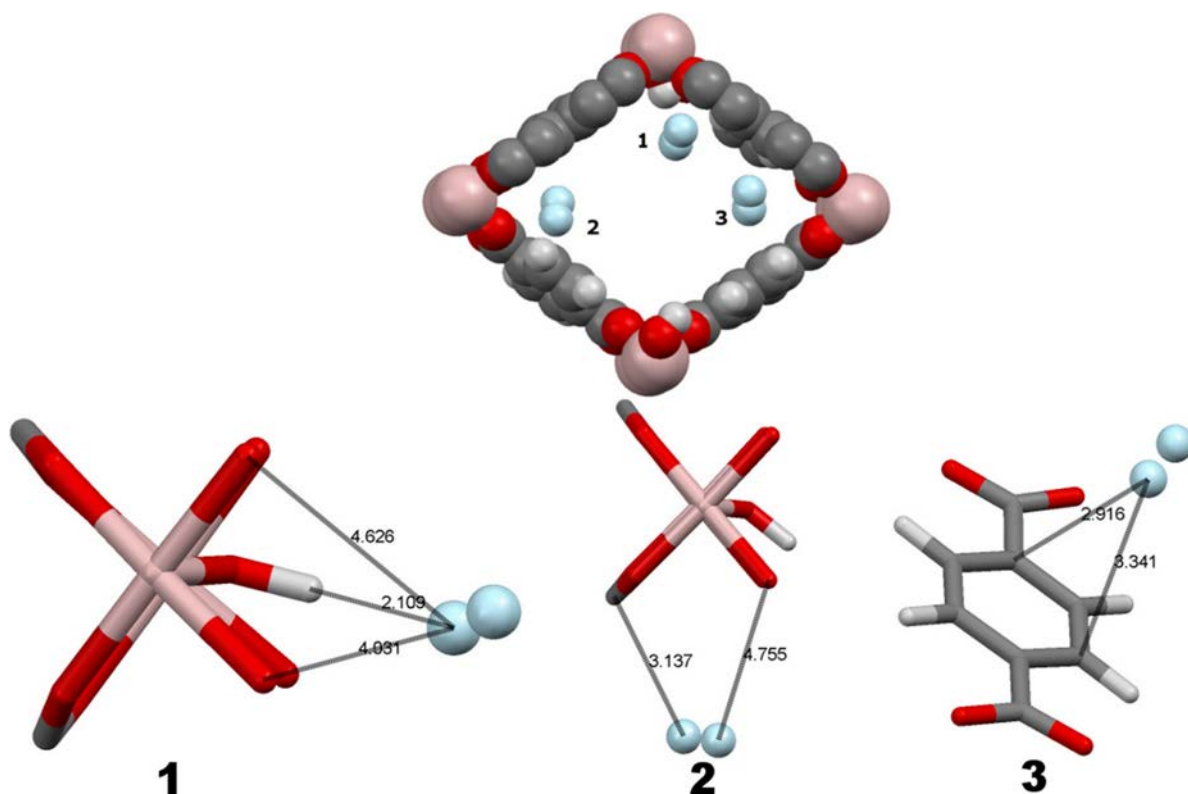


FIG. 2. The main three hydrogen adsorption sites in Al-MIL-53 obtained from DFTB MD simulations. White: hydrogen, dark gray: carbon, red: oxygen, pink: Aluminum. The Hydrogen molecule is plotted in light blue

The optimized structure of empty MOF-74 has a shape similar to that reported in the literature [23], the optimized ($a = 25.987 \text{ \AA}$, $b = 25.981 \text{ \AA}$, $c = 6.846 \text{ \AA}$) and the experimental ($a = b = 25.887 \text{ \AA}$, $c = 6.816 \text{ \AA}$) lattice parameters are in good agreement. The DFTB MD

TABLE 1. Adsorption energy per H₂ of different adsorption sites in MIL-53(Al) and MOF-74. Multiplicity indicates the number of available similar sites in the unit cell, the Max. wt.% indicates the maximum weight percentage reached when the site would be fully occupied.

Material	Adsorption site number	Adsorption energy (kJ/mol)	Multiplicity	Max. wt.%
Al-MIL-53	1	9.41	4	0.97
	2	5.88	4	0.97
	3	3.76	8	1.94
MOF-74	1	9.56	18	1.23
	2	6.13	18	1.23
	3	4.09	18	1.23

simulations of MOF-74 loaded with molecular hydrogen revealed three adsorption sites with the largest adsorption energies. The adsorption sites are presented in Fig. 3 and the corresponding adsorption energies are listed in Table 1. Site 1 is located directly above the Zn²⁺ ions with distance of ≈ 2.5 Å, site 2 is located above a triangle of oxygen atoms with distance of ≈ 3.1 Å, and site 3 is located vertically on the side of the benzene ring with a closest distance to the framework atoms of 2.7 Å.

The calculated adsorption sites are in very good agreement with the neutron diffraction results reported by Channing *et al.* [23], in which 4 adsorption sites were found. Three of them, with the highest adsorption energy are consistent with the calculated adsorption sites. The short distance between the unsaturated metal and H₂ molecules is not a surprising finding and has been observed in other framework structures, where the distance varied between 2.3 – 2.5 Å [42–44]. A recent theoretical calculation has also implicated such short distances [45]. This confirms that the DC-SCC-DFTB method used in this simulation is appropriate to investigate the adsorption of hydrogen in MOF materials. The inelastic neutron scattering (INS) experiments indicate that the H₂ adsorption energy for site 1 is ≈ 8.8 kJ/mol, for site 2 is ≈ 5 kJ/mol and it drops to ≈ 4 kJ/mol with increasing H₂ uptake. Such values are comparable to the calculated adsorption energy for the adsorption sites found from DFTB MD simulation (see Table 1).

The theoretical maximum total hydrogen uptakes, i.e. sites 1 – 3 are fully occupied, is found to be 3.69 wt.%, such value compares favorably with 3.6 wt.% achievable at $T \approx 30$ K and a very low pressure, i.e. with the complete population of the first three adsorption sites found experimentally [23]. Lower experimental H₂ adsorption capacities, ≈ 1.7 wt.% and ≈ 2.5 wt.% at 77 K and 1 and 30 bars respectively, have been reported in literature [45]. The higher maximum calculated capacity could be attributed to the fact that each site is assumed to be fully occupied, but actually, there may be steric hindrance from the different hydrogen molecules which may prevent all the sites from being occupied simultaneously. Another source of error may arise when one considers that the real material has nanoporous artifacts, while the DFTB MD simulations were carried out in under perfect crystal conditions, which can lead to a difference in hydrogen uptake.

Our theoretical calculations for the H₂ binding energies in MIL-53(Al) and MOF-74 demonstrate that such MOFs have at least one adsorption site, located next to the metal cluster with stronger H₂ binding energy than classical MOFs, due to the direct H₂-metal interaction.

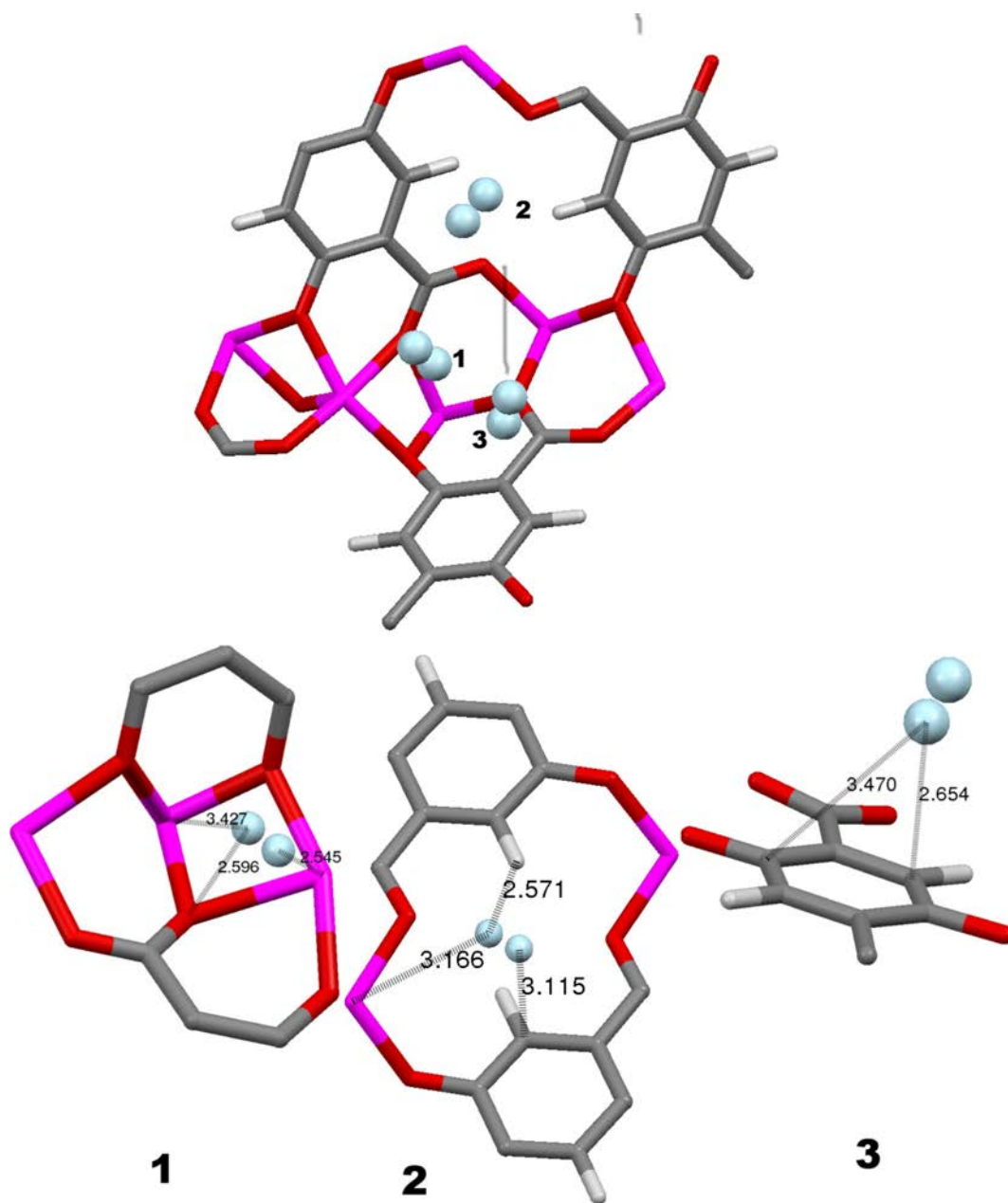


FIG. 3. The main three hydrogen adsorption sites in MOF-74 obtained from DFTB *metal clusters* simulations. The colours are like in Fig. 1.

From DFTB MD simulation at 25 K, the values of the diffusion coefficients can be obtained (Fig. 4). The simulation results for the self-diffusion coefficients of Al-MIL were found to be 4.36×10^{-10} m²/s. At 25 K, the values of the diffusion coefficients appear to be much smaller than those reported at 77 K for such MOF systems [46,47]. This indicates that at such a low temperature only a few H₂ molecules left the site in which they were adsorbed. Clearly, this will also depend on the loading of the sample with hydrogen. To compare our results with the other results in the literature, we have performed an extra 8 ps DFTB MD simulation for Al-MIL at 77 K. The diffusion coefficient at this temperature is calculated to be 5.2×10^{-9} m²/s. This value is also smaller than the values reported for other MOFs [46]. For instance, for Cr-MIL and MIL-47 loaded with 5 H₂ per unit cell the diffusion coefficient

is around 1.0×10^{-8} m²/s. This is due to the difference in the loading of the material with hydrogen, whereas in our simulations, the unit cell was loaded with 11 H₂ molecules. Apart from that, it appears that the order of magnitude of the diffusion coefficient is comparable to that found experimentally for hydrogen adsorbed onto nanostructured carbon, like nanotubes. For instance, at 38 K, a diffusion coefficient of 2.0×10^{-8} m²/s is reported [48]. However, the higher adsorption energy for MILs when compared to the nanocarbon does not limit the diffusion. Perhaps the reason for this is that the differences in adsorption energy between the different sites are not large, and the H₂ molecules can easily diffuse between the different sites in which they can be temporarily trapped.

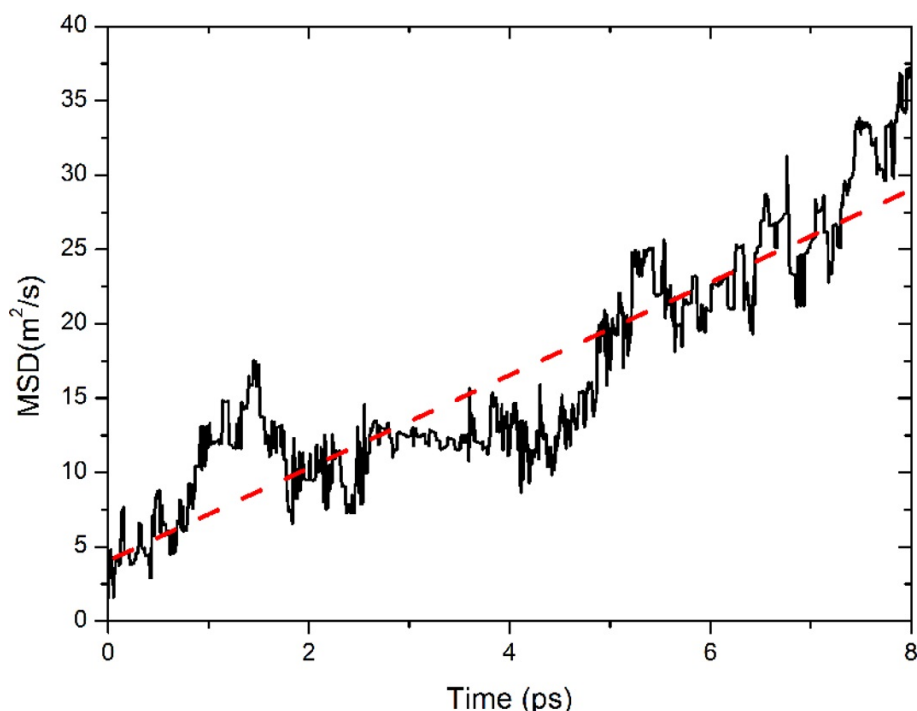


FIG. 4. Example of MSD fits of Al-MIL at 77 K. The simulated MSD curve is represented in thin black; the least square fits of the MSD curve are represented with thick dash red

4. Conclusion

Molecular dynamics (DFTB MD) simulations were used to investigate the hydrogen adsorption in MIL-53 (Al) and MOF-74. DFTB MD simulations were performed within the density functional based tight binding method (DC-SCC-DFTB). Our results demonstrate that DC-SCC-DFTB predicts structural parameters, adsorption sites, adsorption energies and diffusion factors with a very good accuracy, which makes this method a very powerful tool to investigate various types of MOFs. Moreover, the results show that the adsorption energy can be increased by the incorporation of transition metals into MOFs. However, further investigation is required to focus on the design of new MOFs with optimal metal coordination environment.

Acknowledgements

The authors thank Prof. I. Othman, Director General and Prof. Z. ajji, Head of Chemistry Department for their support and encouragement.

References

- [1] Furukawa H., Cordova K.E., O’Keeffe M., Yaghi O.M. The Chemistry and Applications of Metal-Organic Frameworks. *Science*, **341**, 6149 (2013).
- [2] Tranchemontagne D.J., Park K.S., et al. Hydrogen Storage in New Metal-Organic Frameworks. *The Journal of Physical Chemistry C*, **116**(24), P. 13143–51 (2012).
- [3] Furukawa H., Ko N., et al. Ultrahigh Porosity in Metal-Organic Frameworks. *Science*, **329** (5990), P. 424–8 (2010).
- [4] Jiang J. Molecular simulations in metal-organic frameworks for diverse potential applications. *Molecular Simulation*, **40** (7–9), P. 516–36 (2014).
- [5] Keskin S. Gas adsorption and diffusion in a highly CO₂ selective metal-organic framework: molecular simulations. *Molecular Simulation*, **39** (1), P. 14–24 (2012).
- [6] Kuc A., Heine T., Seifert G., Duarte H.A. On the nature of the interaction between H₂ and metal-organic frameworks. *Theoretical Chemistry Accounts*, **120** (4–6), P. 543–50 (2008).
- [7] Dangi G.P., Pillai R.S., et al. A density functional theory study on the interaction of hydrogen molecule with MOF-177. *Molecular Simulation*, **36** (5), P. 373–81 (2010).
- [8] Bae Y-S, Snurr RQ. Molecular simulations of very high pressure hydrogen storage using metal-organic frameworks. *Microporous and Mesoporous Materials*. **135** (1–3), P. 178–86 (2010).
- [9] Li J., Furuta T., et al. Theoretical evaluation of hydrogen storage capacity in pure carbon nanostructures. *The Journal of Chemical Physics*, **119** (4), P. 2376–85 (2003).
- [10] Bhatia S.K., Myers A.L. Optimum Conditions for Adsorptive Storage. *Langmuir*, **22** (4), P. 1688–700 (2006).
- [11] Bae Y.-S., Snurr R.Q. Optimal isosteric heat of adsorption for hydrogen storage and delivery using metal-organic frameworks. *Microporous and Mesoporous Materials*, **132** (1–2), P. 300–3 (2010).
- [12] Thornton A.W., Nairn K.M., et al. Metal-Organic Frameworks Impregnated with Magnesium-Decorated Fullerenes for Methane and Hydrogen Storage. *Journal of the American Chemical Society*, **131** (30), P. 10662–9 (2009).
- [13] Rao D., Lu R., et al. Influences of lithium doping and fullerene impregnation on hydrogen storage in metal organic frameworks. *Molecular Simulation*, **39** (12), P. 968–74 (2013).
- [14] Rowsell J.L.C., Yaghi O.M. Strategies for hydrogen storage in metal-organic frameworks. *Angewandte Chemie-International Edition*, **44** (30), P. 4670–9 (2005).
- [15] Ahnfeldt T., Guillou N., et al. [Al₄(OH)₂(OCH₃)₄(H₂N-bdc)₃]_x H₂O: A 12-Connected Porous Metal-Organic Framework with an Unprecedented Aluminum-Containing Brick. *Angewandte Chemie-International Edition*, **48** (28), P. 5163–6 (2009).
- [16] Lin Y., Kong C., Chen L. Facile Synthesis of Aluminum-Based Metal-Organic Frameworks with Different Morphologies and Structures through an OH⁻-Assisted Method. *Chemistry - An Asian Journal*, **8** (8), P. 1873–8 (2013).
- [17] Reinsch H., Kruger M., et al. A new aluminium-based microporous metal-organic framework: Al(BTB) (BTB:1,3,5-benzenetrisbenzoate). *Microporous and Mesoporous Materials*, **157** (0), P. 50–5 (2012).
- [18] Senkowska I., Hoffmann F., et al. New highly porous aluminium based metal-organic frameworks: Al(OH)(ndc) (ndc=2,6-naphthalene dicarboxylate) and Al(OH)(bpdc) (bpdc=4,4’-biphenyl dicarboxylate). *Microporous and Mesoporous Materials*, **122** (1–3), P. 93–8 (2009).
- [19] Couck S., Denayer J.F.M., et al. An Amine-Functionalized MIL-53 Metal-Organic Framework with Large Separation Power for CO₂ and CH₄. *Journal of the American Chemical Society*, **131** (18), P. 6326 (2009).
- [20] Serre C., Millange F., et al. Very large breathing effect in the first nanoporous chromium(III)-based solids: MIL-53 or Cr-III(OH).O₂C-C₆H₄-CO₂.HO₂C-C₆H₄-CO₂H_x. H₂O_y. *Journal of the American Chemical Society*, **124** (45), P. 13519–26 (2002).
- [21] Loiseau T., Serre C., et al. A rationale for the large breathing of the porous aluminum terephthalate (MIL-53) upon hydration. *Chemistry - a European Journal*, **10** (6), P. 1373–82 (2004).
- [22] Ferey G., Latroche M., et al. Hydrogen adsorption in the nanoporous metal-benzenedicarboxylate M(OH)(O₂C-C₆H₄-CO₂) (M = Al³⁺, Cr³⁺), MIL-53. *Chemical Communications*, **24**, P. 2976–7 (2003).
- [23] Liu Y., Kabbour H., et al. Increasing the Density of Adsorbed Hydrogen with Coordinatively Unsaturated Metal Centers in Metal-Organic Frameworks. *Langmuir*, **24** (9), P. 4772–7 (2008).
- [24] Sculley J., Yuan D., Zhou H.-C. The current status of hydrogen storage in metal-organic frameworks-updated. *Energy & Environmental Science*, **4** (8), P. 2721–35 (2011).
- [25] Goldsmith J., Wong-Foy A.G., Cafarella M.J., Siegel D.J. Theoretical Limits of Hydrogen Storage in Metal-Organic Frameworks: Opportunities and Trade-Offs. *Chemistry of Materials*, **25** (16), P. 3373–82 (2013).

- [26] Suraweera N.S., Xiong R., et al. On the relationship between the structure of metal-organic frameworks and the adsorption and diffusion of hydrogen. *Molecular Simulation*, **37** (7), P. 621–39 (2011).
- [27] Xu Q., Liu D., Yang Q., Zhong C. Molecular simulation study of the quantum effects of hydrogen adsorption in metal-organic frameworks: influences of pore size and temperature. *Molecular Simulation*, **35** (9), P. 748–54 (2009).
- [28] Elstner M.P.D. Jungnickel G., et al. A Self-Consistent Charge Density-Functional Based Tight-Binding Method for Predictive Materials Simulations in Physics. *Chemistry and Biology physica status solidi (b)*, **217** (1), P. 41–62 (2000).
- [29] Elstner M., Cui Q., et al. Modeling zinc in biomolecules with the self consistent charge-density functional tight binding (SCC-DFTB) method: Applications to structural and energetic analysis. *Journal of Computational Chemistry*, **24** (5), P. 565–81 (2003).
- [30] Zhechkov L., Heine T., et al. An efficient a Posteriori treatment for dispersion interaction in density-functional-based tight binding. *Journal of Chemical Theory and Computation*, **1** (5), P. 841–7 (2005).
- [31] Oliveira A.F., Seifert G., Heine T., Duarte H.A. Density-functional based tight-binding: an approximate DFT method. *Journal of the Brazilian Chemical Society*, **20**, P. 1193–205 (2009).
- [32] Heine T., Rapacioli M., et al. DeMon-nano: Jacobs University Bremen Bremen. Germany (2009).
- [33] Heine T., Dos Santos H.F., Patchkovskii S., Duarte H.A. Structure and Dynamics of β -Cyclodextrin in Aqueous Solution at the Density-Functional Tight Binding Level. *The Journal of Physical Chemistry A*, **111** (26), P. 5648–54 (2007).
- [34] Zhu X., Koenig P., et al. Establishing effective simulation protocols for β - and α/β -peptides. III. Molecular mechanical model for acyclic β -amino acids. *Journal of Computational Chemistry*, **31** (10), P. 2063–77 (2010).
- [35] Kuc A., Enyashin A., Seifert G. Metal-Organic Frameworks: Structural, Energetic, Electronic, and Mechanical Properties. *The Journal of Physical Chemistry B*, **111** (28), P. 8179–86 (2007).
- [36] Lukose B., Supronowicz B., et al. Structural properties of metal-organic frameworks within the density-functional based tight-binding method. *Physica status solidi (b)*, **249** (2), P. 335–42 (2012).
- [37] Lukose B., Kuc A., Heine T. The Structure of Layered Covalent-Organic Frameworks. *Chemistry - A European Journal*, **17** (8), P. 2388–92 (2011).
- [38] Assfour B., Seifert G. Hydrogen adsorption sites and energies in 2D and 3D covalent organic frameworks. *Chemical Physics Letters*, **489** (1–3), P. 86–91 (2010).
- [39] Kuc A., Enyashin A., Seifert G. Metal-organic frameworks: Structural, energetic, electronic, and mechanical properties. *Journal of Physical Chemistry B*, **111** (28), P. 8179–86 (2007).
- [40] Frenzel J., Oliveira A.F., et al. Structural and electronic properties of bulk gibbsite and gibbsite surfaces. *Zeitschrift Fur Anorganische Und Allgemeine Chemie*, **631** (6–7), P. 1267–71 (2005).
- [41] Schmitz B., Muller U., et al. Heat of Adsorption for Hydrogen in Microporous High-Surface-Area Materials. *Chemphyschem*, **9** (15), P. 2181–4 (2008).
- [42] Dinca M., Dailly A., et al. Hydrogen Storage in a Microporous Metal-Organic Framework with Exposed Mn^{2+} Coordination Sites. *Journal of the American Chemical Society*, **128** (51), P. 16876–83 (2006).
- [43] Dinc M., Han W.S., et al. Observation of Cu^{2+} - H_2 Interactions in a Fully Desolvated Sodalite-Type Metal-Organic Framework. *Angewandte Chemie International Edition*, **46** (9), P. 1419–22 (2007).
- [44] Peterson V.K., Liu Y., Brown C.M., Kepert C.J. Neutron Powder Diffraction Study of D_2 Sorption in $Cu_3(1,3,5\text{-benzenetricarboxylate})_2$. *J. Am. Chem. Soc.*, **128** (49), P. 15578–9 (2006).
- [45] Zhou W., Wu H., Yildirim T.. Enhanced H_2 Adsorption in Isostructural Metal-Organic Frameworks with Open Metal Sites: Strong Dependence of the Binding Strength on Metal Ions. *Journal of the American Chemical Society*, **130** (46), P. 15268–15269 (2008).
- [46] Salles F., Kolokolov D.I., et al. Adsorption and Diffusion of H_2 in the MOF Type Systems MIL-47(V) and MIL-53(Cr): A Combination of Microcalorimetry and QENS Experiments with Molecular Simulations. *Journal of Physical Chemistry C*, **113** (18), P. 7802–12 (2009).
- [47] Mulder F.M., Dingemans T.J., Wagemaker M., Kearley G.J. Modelling of hydrogen adsorption in the metal organic framework MOF5. *Chemical Physics*, **317** (2–3), P. 113–8 (2005).
- [48] Narehood D.G., Pearce J.V., et al. Diffusion of H_2 adsorbed on single-walled carbon nanotubes. *Physical Review B*, **67** (20), P. 205409 (2003).

NEW ROUTE TO POLY (2,6-DIIMIDAAZO(4,5-b: 4',5'-e) PYRIDINELENE-1,4(2,5-DIHYDROXY)-PHENYLENE) (PIPD) AND HIGH MODULUS FIBER ON IT BASIS

Jun Li¹, Zhen Hu¹, Yuanjun Song¹, Yudong Huang^{1*}, V. V. Zuev^{2,3**}

¹School of Chemical Engineering and Technology, State Key Laboratory of Urban Water Resource and Environment, Harbin Institute of Technology, 150001 Harbin, China

²ITMO University, Kronverkskiy pr. 49, 197101 Saint Petersburg, Russia

³Institute of Macromolecular Compounds of the Russian Academy of Sciences, Bolshoi pr. 31, 199004 Saint Petersburg, Russia

*yudonghuang@163.com, **zuev@hq.macro.ru

PACS 81.07.Lb

A novel entry toward poly(2,6-diimidazo(4,5-b: 4',5'-e)pyridinylene-1,4(2,5-dihydroxy)-phenylene) (PIPD) has been elaborated. A strategy based on a new route to monomers: a sequential nitration of 2,6-diaminopyridine with $\text{KNO}_3/\text{H}_2\text{SO}_4$ gives 2,6- diamino- 3,5-dinitro pyridine (DNDAP) in moderate yield and its hydrogenation with Raney nickel as catalyst leads to 2,3,5,6-tetraaminopyridine (TAP) in high yield. The second monomer 2,5-dihydroxyterephthalate (DHTA) was synthesized in high yield as product of sulfur-mediated aromatization of dimethyl succinoyl succinate with subsequent base hydrolysis. PIPD was synthesized by step-by-step heating in polyphosphoric acid with molecular weights of 19 – 25 kilodaltons. The macromolecule of PIPD can be seen as lap-join chain form nano-sized rigid fragment. The as-polymerized liquid crystalline PIPD solution was used for fiber spinning. The tensile strength of PIPD fibers were 1.28 – 1.99 GPa and depended on the molecular weight of the polymer used for spinning.

Keywords: Nano-sized rigid polymer, synthesis, fiber spinning, mechanical properties, liquid crystallinity.

Received: 13 October 2014

Revised: 5 November 2014

1. Introduction

The development of polymer composites over the last 50 years has seen the emergence of new materials that are lightweight and have exceptional mechanical properties. The composite properties depend on filler fiber properties. Traditional inorganic fiber (glass, metal etc) composites deliver exceptional stiffness and stress but can often have a limited extensibility and poor damage tolerance, especially at low operating temperatures. Unlike carbon and inorganic fibers, rigid-rod polymeric fibers do not show catastrophic failure under compressive stress. That fact stimulated researchers to create stiffer rigid-rod-like polymeric materials. The best result was been obtained with synthesis of poly (p-phenylene benzobisoxazole) (PBO) [1]. PBO has very impressive tensile properties but its performance under compression is disappointing [2]. The traditional way to solve this problem in polymer chemistry is cross-linking macromolecules in the fiber by introducing double bonds into the macromolecule or Υ -irradiation [2]. An alternative route to increase the lateral strength of the PBO fiber is introducing intermolecular hydrogen bonds [3]. This choice was realized by the synthesis of poly(2,6-diimidazo(4,5-b: 4',5'-e)pyridinylene-1,4(2,5-dihydroxy)-phenylene) (PIPD) [4]. This polymer forms in fiber intermolecular bonds in two dimensions and has the highest compressive strength (1 – 1.7 GPa) of

any polymeric fiber to date [5]. However, the synthetic pathway to this polymer is laborious and expensive in preparation and purification. The aim of present work is to optimize a procedure for PIPD synthesis with a view to enhancing of monomer yield, improve the polymerization to increase the polymer molecular mass, spin a fiber directly from the polymerization solution without polymer precipitation or redissolution by dry-jet wet spinning method, and investigate the performance of the obtained nano- and macro-sized fibers.

2. Materials and Methods

All used reagents are commercial products were purchased from National medicine Co. Ltd., China, and were used without additional purification. Prior to use, all solvents were distilled. Hydrogen was purified by passing through columns with a nickel/chromium catalyst and molecular sieves.

2.1. Nitration 2,6-diaminopyridine

7 g of KNO_3 was mixed with 25 ml of conc. sulfuric acid, and to this was added 3 g of 2,6-diaminopyridine. The mixture was stirred at 80 °C for 2 h and then at 120 °C for 1 h. The reaction mixture was then poured into 500 ml of water and cooled to 5 °C. The solution was neutralized by 20% NaOH, and precipitated 2,6-diamino-3,5-dinitro pyridine (DNDAP) was collected after 24 h at 5 °C as yellow powder. DNDAP was recrystallized from water-DMSO (7:1 v/v). Yield 4.2 g (76.7%). Purity by HPLC 95.8% IR, cm^{-1} : 3473/3359, 1621, 1554, 1508, 1371, 1322. ^1H NMR, (DMSO- d_6), δ , ppm : 8.28; 8.44 (2), 9.00 (4). ^{13}C NMR, (DMSO- d_6), δ , ppm: 155.21 (ortho), 120.66 (meta), 136.03 (para).

2.2. 2,3,5,6-tetraaminopyridine (TAP)

In a 200 ml autoclave, 10 g of DNDAP, 50 ml of water and 10 ml of 85% phosphoric acid with 1 g of Raney nickel were slurried; the air was displaced with nitrogen and 1.3 kPa of hydrogen was supplied; the hydrogen pressure was increased to 0.1 MPa and then to 0.5 MPa; the temperature was kept at RT and stirring was continued with the supply of hydrogen at 0.5 MPa until the hydrogen consumption ceased (10 h). Without the introduction of air, 20 ml of 37% hydrochloric acid was added, and mixture was extruded through the filter from autoclave; to filtrate were added 50 ml of THF and 25 ml of conc. HCl. The precipitate was filtered off and dried, yielding 12.9 g TAP·HCl·H₂O (93%) with HPLC purity of 99.7%. IR, cm^{-1} : 3500 – 2500, 1654, 1610, 1320. ^1H NMR, (D₂O), δ , ppm : 7.70 (1), 8 – 9 (NH₂). ^{13}C NMR, (D₂O), δ , ppm: 147.56 (ortho), 102.77 (meta), 131.22 (para).

2.3. Dimethyl 2,5-dihydroxyterephthalate

In a 2 l four-necked flask with stirrer, reflux head, dropping funnel and thermometer were placed 500 ml of water and 240 ml of glacial acetic acid and in this mixture was dispersed 44 g of dimethyl succinyl succinate. The dispersion was heated in a stepwise manner with stirring to 80, 85 and 110 °C, and 1 g of each iodine and potassium iodine were added. Without external heating was added 20 ml of 30% hydrogen peroxide in a course of 20 min at temperature 110 °C. After ten minutes the 40 ml of warm and then 40 ml of cold water were stirred through reaction mixture. After cooling to RT, the slurry was filtered off and washed twice with water. After drying, yield 32.7 g (75%), m.p. 153 °C.

2.4. 2,5-dihydroxyterephthalate (DHTA)

In a 1 l four-necked flask with stirrer, reflux head, dropping funnel and thermometer were placed 20 g of NaOH dissolved in 160 ml of water. 32.7 g of dimethyl 2,5-dihydroterephthalate was slurried into 100 ml of warm water, and slurry was added to alkali. The solution was heated under stirring to 95 °C and after 2 h, 45 ml of 37% HCl was added to the boiling solution. After cooling to RT, the precipitated DHTA was filtered off and dried to yield 18.5 g (65%) with HPLC purity of 99.8%. IR, cm^{-1} : 3300 – 2500, 1650, 1491, 1429, 1290, 1201, 894, 843, 695, 525. ^1H NMR, (DMSO- d_6), δ , ppm: 7.21 (2), 11.7 (OH). ^{13}C NMR, (DMSO- d_6), δ , ppm: 117.78, 119.95, 152.48. 170.80.

2.5. Preparation of PIPD Fiber

Into a 1 l glass reactor with powerful anchor-type stirrer was step-by-step added 71.5 g of 115% polyphosphoric acid (PPA) and 30.5 g of 85% phosphoric acid in a stepwise manner. The mixture was heated to 100 °C and 40 g of solid $\text{TAP}\cdot\text{HCl}\cdot\text{H}_2\text{O}$ added. The reactor was closed and air was displaced by argon by repeated evacuation and argon blanketing. After homogenization for 1 h, to the mixture was added 29.7 g of DHTA and 88.5 g of P_2O_5 . The reaction mixture was stirred for 48 h at 100 °C, 2.5 h at 150 °C, 2.5 h at 160 °C, and finally 19 h at 185 °C. The reaction mass became opalescent at 150 °C. The bottom part of the reactor was removed and the polymer solution was transferred into the cylinder of a piston-type fiber spinning machine. The intrinsic viscosity of the obtained PIPD polymers ranged from 10.9 to 19.1 dL/g. The obtained PIPD/PPA dopes were directly spun into fibers via dry-jet wet-spinning process. Fibers were completely washed in running water, and dried at 100 °C in vacuum.

2.6. Fiber Properties

Tensile Strength and Young's Modulus of Fibers was tested according to the standard of ASTM C1557-14. A fiber was selected randomly from the fiber bundle and the two ends of the fiber were grasped between the clamps of the tester. Tensile properties were measured using a UTS 10 device (UTStestsyste, Germany). No less than 5 specimens were taken for each sample to obtain an average value. Arithmetical mean measurement error was less than 0.03 GPa for tensile strength and 1.5 GPa for Young's modulus.

3. Techniques

^1H - and ^{13}C NMR spectra were recorded on a Bruker AV400 spectrometer. IR spectra were obtained on a Nexus 670 (Nicolet) infrared spectrometer (liquid on KBr disk or in KBr tablets for powder). HPLC was performed on Agilent 1100 instrument using a phosphate buffer as a solvent on 6890/5973N Agilent column. Scanning electron microscope (SEM) images was obtained using a Carl Zeiss Supra55VP scanning electron microscope.

4. Result and discussion

4.1. Monomer synthesis

The synthesis of PIPD was achieved by polymerization of 2,5- dihydroxyterephthalic acid with 2,3,5,6-tetraaminopyridine (TAP) (see the scheme).

To achieve a fiber with optimal mechanical properties, it is necessary to have a polymer with high molecular weight and without defects in the chemical structure. This necessitates the elaboration of versatile procedures for the synthesis of monomers and optimization of polymerization conditions. The main problem in the synthesis of TAP is their oxidative lability as free base. This problem can be solved if the synthetic route using the salt of TAP (for

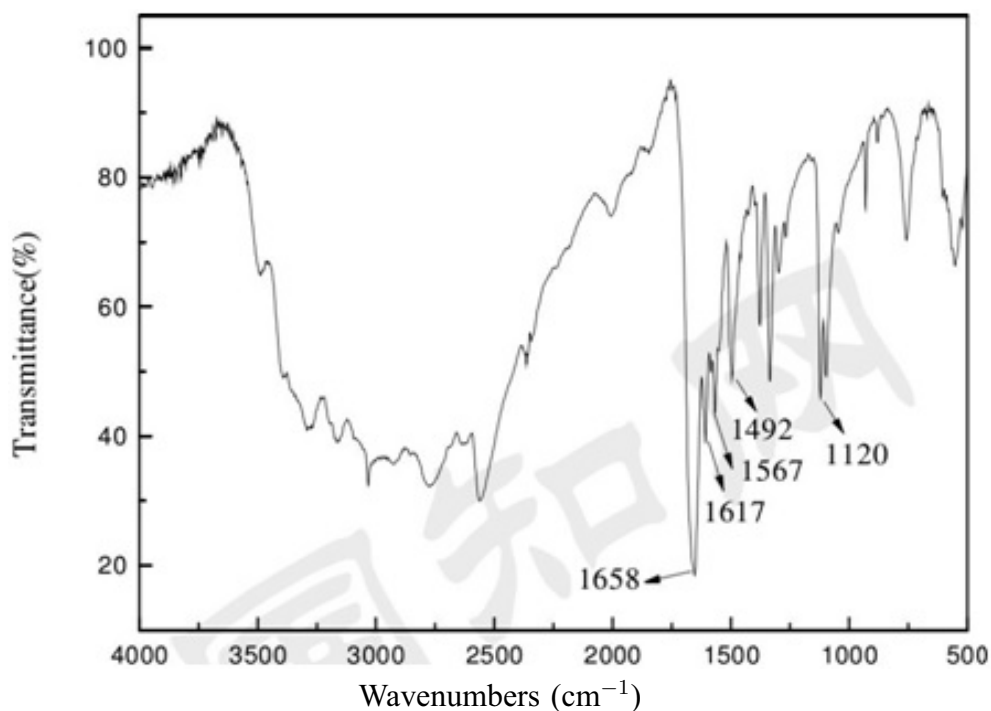


FIG. 1. IR spectrum of PIPD

with polymer contain higher than 18 wt% is lyotropic nematic [6] that contribute any specifics in spinning process. Liquid crystallinity offers desirable properties, which make it possible to efficiently spin a thread from such a rigid macromolecule as PIPD.

4.3. Spinning

Conventional air gap wet spinning of the as-polymerized PIPD solution was performed at 180 °C in a steam bath for fiber production. As result, filaments with diameter 18 – 20 μm (Fig. 2) were obtained, which were further washed to low phosphorus content and dried to produce final, high-modulus fibers. In PIPD solutions used for spinning, a high degree of molecular orientation of the polymer chains with respect to the local director can be expected. During the spinning process the local directors are aligned in the direction of flow by the shear flow in the capillaries of the spinneret and by the elongation flow in the entrance zone above the spinneret and in the air gap. The high degree of the orientation of the director together with the high degree of local molecular order implies that the PIPD macromolecules are highly-oriented. Assuming that this orientation order is merely 'frozen-in' during the coagulation process, the high modulus of PIPD fiber obtained can be predicted. It was supported by our measurements. The average data for tensile strength of three samples with different MW are 1.28, 1.49 and 1.99 GPa. Young's moduli were 101, 120 and 161 GPa correspondingly. Elongation before break for all samples was about 1%. Hence, this strong dependence of tensile strength on MW shows that polymerization grade of our samples is relative low. However, the absolute value of tensile strength is high compared with literature data [15].

5. Conclusion

A novel entry toward PIPD has been elaborated. A strategy based on a new route to monomers: a sequential nitration of 2,6-diaminopyridine with $\text{KNO}_3/\text{H}_2\text{SO}_4$ gives a DNDAP in moderate yield and its hydrogenation with Raney nickel as catalyst leads to TAP in high

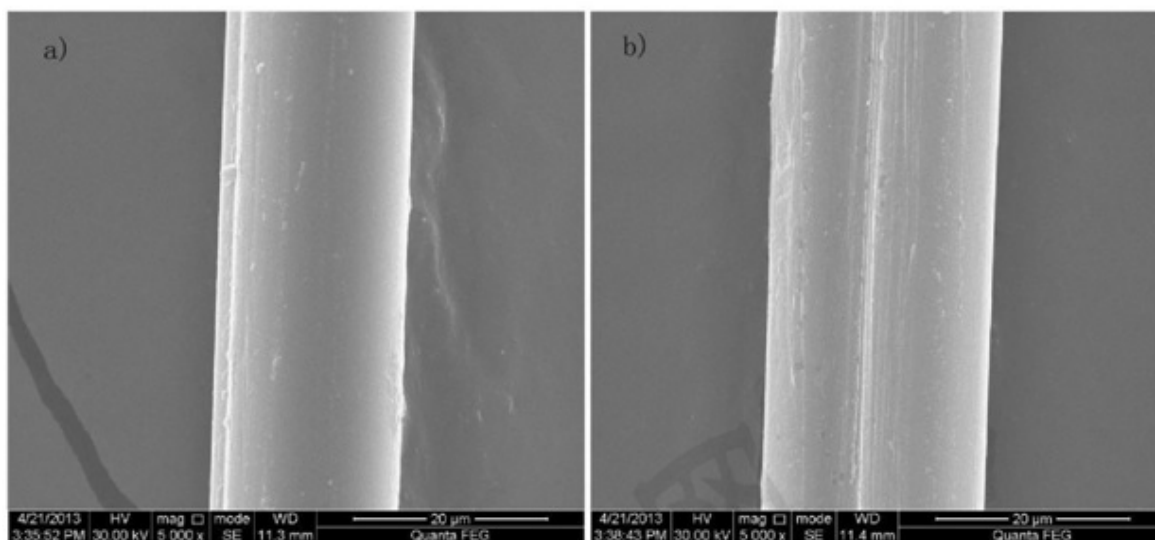


FIG. 2. SEM images of PIPD fiber ($MW = 25.5 \cdot 10^3$) in two directions

yield. Second monomer (DHTA) was synthesized in high yield as product of sulfur-mediated aromatization of dimethyl succinoyl succinate with following base hydrolysis. PIPD was synthesized in a stepwise manner by heating in polyphosphoric acid with $MW 19 - 25 \times 10^3$. The macromolecule of PIPD can be seen as lap-join chain form nano-sized rigid fragment. The as-polymerized liquid crystalline PIPD solution was used for fiber spinning. The tensile strength of PIPD fibers were 1.28 – 1.99 GPa in dependence on MW polymer used for spinning. PIPD is light as well as strong. Its strength approaches and even exceeds that of typical high strength engineering steel (1.3 GPa). However, the PIPD have a significantly lower relative density (1.7) [6] than steel (7.8). Compared on a weight basis, PIPD is thus by far the stronger material.

Acknowledgements

The research reported in this paper was partly supported by RFBR-NNSFC grant No. 14-03-91152-a, by National Natural Science Foundation of China (NNSFC) (grant No. 51203034), Research Fund for the Doctoral Program of Higher Education of China (grant No. 20122302120038), Special Foundation of China Postdoctoral Science (grant No. 2013T60379), Supported by China Postdoctoral Science Foundation (grant No. 2013M541392).

References

- [1] Norcholt M.G., Sikkema D.J. Lyotropic main chain liquid crystal polymers. *Adv. Polym. Sci.*, **98**, P. 115–177 (1991).
- [2] Sweeny W. Improvements in compressive properties of high modulus fibers by crosslinking. *J. Polym. Sci. A*, **30**, P. 1111–1222 (1992).
- [3] Tan L.-S., Arnold F.E., et al. Pseudo-ladder rigid-rod polymers: dihydroxy pendent benzothiazole aromatic heterocyclic polymer and copolymers. *Polymer*, **35**, P. 3091–3101 (1994).
- [4] Sikkema D.J. Design, synthesis and properties of a novel rigid rod polymer, PIPD or ‘M5’: high modulus and tenacity fibres with substantial compressive strength. *Polymer*, **39**, P. 5981–5986 (1998).
- [5] Klop E.A., Lammers M. XRD study of the new rigid-rod polymer fiber PIPD. *Polymer*, **39**, P. 5987–5998 (1998).
- [6] Sikkema D.J., Rodini D.J., Adkins, Q.F. High inherent viscosity polymers and fibers therefrom. US patent 2006/0280,937 (2006).

- [7] Ritter J. Process for the synthesis PIPD. WIPO patent 2008/066825 (2008).
- [8] Dindi H., Schultz J.L. Synthesis of dinitrodiaminopyridine. US patent 2012/8115,007 (2012).
- [9] Balauf M. Rigid-rod polymers having flexible side chain:1. Thermotropic poly(1,4-phenylene 2,5-dialkoxyterephthalate)s. *Macromol. Rapid Commun.*, **7**, P. 407–414 (1986).
- [10] Roitman D.B., Wessling R.A., McAlister J. Characterization of poly(p-phenylene-cis-benzooxazole) in methanesulphonic acid. *Macromolecules*, **26**, P. 5174–5184 (1993).
- [11] Zhang R., Mattice W.L. Evaluation of the persistence length of the rigid-rod polymers poly(benzobisoxazole) and poly(benzobisthiazole) using molecular-dynamics simulations. *Macromolecules*, **25**, P. 4937–5184 (1992).
- [12] Zhang R., Mattice W.L. Persistence length of the ‘rodlike’ molecule poly(p-phenylene-trans-benzobisthiazole) revisited again. *Macromolecules*, **26**, P. 4384–4385 (1993).
- [13] Roitman D.B., McAdon M. Persistence length of the ‘rodlike’ molecule poly(p-phenylene-trans-benzobisthiazole) revisited. *Macromolecules*, **26**, P. 4381–4383 (1993).
- [14] Wong C.-P., Ohnuma H., Berry G.C. Properties of some rodlike polymers in solution. *J. Polym. Sci. Polym. Sym.*, **65**, P. 178–192 (1978).
- [15] Chae H.G., Kumar S. Rigid rod polymeric fibers. *J. Appl. Polym. Sci.*, **100**, P. 791–802 (2006).

DIELECTRIC PROPERTIES OF AURIVILLIUS PHASE $\text{Bi}_{10}\text{Fe}_6\text{Ti}_3\text{O}_{30}$ WITH A NANO-SIZED PSEUDO-PEROVSKITE BLOCKS

N. A. Lomanova

Ioffe Institute, 26 Polytekhnicheskaya Str., Saint Petersburg 194021, Russia

natus@hotmail.ru

PACS 61.66.Fn

Distinctive features of dielectric properties of a ceramic material based on Aurivillius phase $\text{Bi}_{10}\text{Fe}_6\text{Ti}_3\text{O}_{30}$ have been studied.

Keywords: ceramics, Aurivillius phases, dielectric properties.

Received: 20 November 2014

Revised: 3 December 2014

1. Introduction

In general, the structure of Aurivillius phases $\text{Bi}_{m+1}\text{Fe}_{m-3}\text{Ti}_3\text{O}_{3m+3}$ can be regarded as alternating fluorite-like layers $F = \{(\text{Bi}_2\text{O}_2)^{2+}\}_\infty$ and pseudo-perovskite blocks $P = \{(\text{Bi}_{m+1}\text{Fe}_{m-3}\text{Ti}_3\text{O}_{3m+1})^{2-}\}_\infty$ consisting of m pseudo-perovskite layers [1, 2]. According to experimental data from papers [3-5], the number of octahedral layers in a pseudo-perovskite block of Aurivillius phases $\text{Bi}_{m+1}\text{Fe}_{m-3}\text{Ti}_3\text{O}_{3m+3}$ may reach $m=9$, which corresponds to the compound $\text{Bi}_{10}\text{Fe}_6\text{Ti}_3\text{O}_{30}$. The thickness of the pseudo-perovskite block in this compound is ~ 3.7 nm [3]. In this context, the Bi_2O_3 - TiO_2 - Fe_2O_3 system represents a unique object, since for the majority of layered pseudo-perovskite compounds, m cannot exceed 6 (E.g., see [6, 7]). The extremely high stability of compounds $\text{Bi}_{m+1}\text{Fe}_{m-3}\text{Ti}_3\text{O}_{3m+3}$ with a great number of pseudo-perovskite layers in the structure was analyzed in papers [4, 5, 8].

Following the data of papers [9-11], Aurivillius phases Bi_2O_3 - TiO_2 - Fe_2O_3 possess multiferroic properties. Compounds $\text{Bi}_{m+1}\text{Fe}_{m-3}\text{Ti}_3\text{O}_{3m+3}$ experience high-temperature phase conversion (Curie point) accompanied by transition from an orthorhombic structure to a tetragonal one [13-15], for $\text{Bi}_{10}\text{Fe}_6\text{Ti}_3\text{O}_{30}$, this occurs at 953 K [3, 16, 17].

Papers [3, 16] describe the preparation of $\text{Bi}_{10}\text{Fe}_6\text{Ti}_3\text{O}_{30}$ using solid-state chemical reactions. As shown in papers [4, 17], given the limiting value of m , multilayered Aurivillius phases will be in a state close to indifferent equilibrium. Such objects are of interest when regarded as transition nanostructures from a chemical compound to a heterogeneous system.

The study of the properties of Aurivillius phases with a great number of pseudo-like layers in the structure is of particular interest. The physical and chemical properties of compounds $\text{Bi}_{m+1}\text{Fe}_{m-3}\text{Ti}_3\text{O}_{3m+3}$, including $\text{Bi}_{10}\text{Fe}_6\text{Ti}_3\text{O}_{30}$, are described in papers [3-8, 16, 17]. Dielectric properties of some compounds $\text{Bi}_{m+1}\text{Fe}_{m-3}\text{Ti}_3\text{O}_{3m+3}$ are described in papers [15, 18-23], however, only papers [24, 25] provide a system-oriented approach.

This paper aims to study the nature of the electric relaxation for a ceramic material $\text{Bi}_{10}\text{Fe}_6\text{Ti}_3\text{O}_{30}$ using electric modulus formalism for analyzing dielectric data. Combined

with the data on composition and structure of the compound $\text{Bi}_{10}\text{Fe}_6\text{Ti}_3\text{O}_{30}$, the said research is required to forecast a possibility for preparing new multiferroic materials using that compound.

2. Experimental

For the synthesis of $\text{Bi}_{10}\text{Fe}_6\text{Ti}_3\text{O}_{30}$, solid-state chemical reactions were employed. The purity of initial reagents Bi_2O_3 , TiO_2 and Fe_2O_3 was 99.9% or higher. Papers [3, 26] describe the procedure in detail. Phase state was studied using the X-ray diffractometry (XRD) employing XRD-7000 Shimadzu. The elemental composition of the samples was determined by the energy dispersive X-ray microanalysis (FEI Quanta 200 SEM with the EDAX attachment).

Electrical measurements were taken for samples in tablet form, 7 mm in diameter, 3 mm thick, with platinum electrodes on the end face. Investigation was carried out in the open air using RCL-meter Fluke PM6063 (USA), within the temperature range 70–470°C, in the range f 10 kHz to 1MHz. Temperature was regulated using a tube furnace SNOL (Latvia) containing a double-pin cell with a sample. Toward that end, resistance R , module Z , and impedance phase shift angle φ were measured, and these values subsequently served as a basis for the determination of real and imaginary parts of the complex electrical module \overline{M} , complex specific conductivity $\overline{\sigma}$, complex dielectric permeability $\overline{\varepsilon}$ and loss-angle tangent $\text{tg}\varphi = \varepsilon''/\varepsilon'$ according to the following ratios:

$$\overline{M} = i\omega\varepsilon_0 \frac{S}{l} \overline{Z} = M' + jM'', \quad (1)$$

$$\overline{\sigma} = \frac{l}{S} \overline{Z}^{-1} = \sigma' + j\sigma'', \quad (2)$$

$$\overline{\varepsilon} = \frac{1}{j\varepsilon_0\omega} \cdot \frac{l}{S} \overline{Z}^{-1} = \varepsilon' - j\varepsilon'', \quad (3)$$

where M' and M'' are real and imaginary constituents of \overline{M} ; σ' and σ'' are real and imaginary constituents of $\overline{\sigma}$; $\omega = 2\pi f$ is circular frequency, ε_0 is vacuum dielectric permeability, S and l are the sample area and thickness, correspondingly. The measuring procedure is described in papers [24, 25].

3. Results and discussion

Fig. 1 a, b present an X-ray diffraction pattern and a microstructure of a $\text{Bi}_{10}\text{Fe}_6\text{Ti}_3\text{O}_{30}$ sample, correspondingly. The data obtained testify to a single phase of the tested material and to good agreement between real chemical composition and stoichiometric one. At room temperature, Aurivillius phase has a rhombic elementary cell (space group $D_{4h}^{17}\text{-}14/\text{mmm}$), with parameters $a=4.7 \text{ \AA}$, $b=5.2 \text{ \AA}$, $c=81.8 \text{ \AA}$.

The dielectric properties of $\text{Bi}_{10}\text{Fe}_6\text{Ti}_3\text{O}_{30}$ were studied using electric modulus formalism. Such an approach is informative for studying volumetric response from ceramic materials in a case when increased conductivity of a sample complicates analysis of dielectric relaxation processes [27, 28]. As shown in papers [24, 25], Aurivillius phases' conductivity will increase with an increase in the number of pseudo-perovskite layers in the structure.

Fig. 2 shows typical frequency dependencies for the overall specific electric conductivity $\sigma_{ac}(f)$ for $\text{Bi}_{10}\text{Fe}_6\text{Ti}_3\text{O}_{30}$ at different temperatures. This behavior reflects the interrelation between the relaxation process in charge carriers and conductivity in grain volume. The nature of the curves $\sigma_{ac}(f)$ corresponds to the "universal dynamic response" [29]:

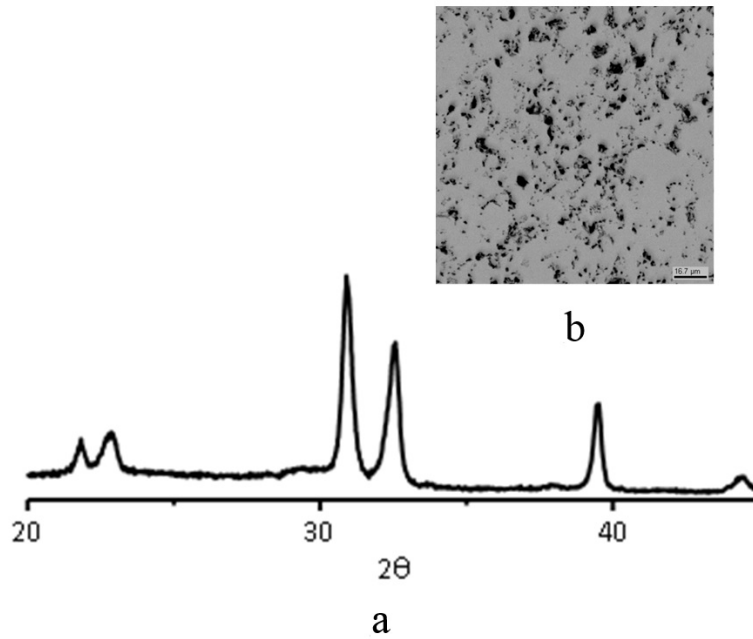


FIG. 1. X-ray diffractograms ($\lambda = 1.54056 \text{ \AA}$) (a) and electron micrographs (b) for $\text{Bi}_{10}\text{Fe}_6\text{Ti}_3\text{O}_{30}$

$$\sigma(f) = \sigma_{dc} + Af^\alpha, \quad (4)$$

where σ_{dc} – direct current specific conductivity, A – pre-exponential factor, f – frequency, α – an index denoting the degree of interrelation between charge carriers and crystal lattice ($0 < \alpha < 1$).

For Aurivillius phases, this type of $\sigma_{ac}(f)$ dependency characterizes slow relaxation mechanisms for polarization and polaron “hopping” movement [20], for which a hop frequency (f_p) between self-localization states corresponds to the change in the slope of $\sigma_{ac}(f)$ curves, it being $< 100 \text{ kHz}$ at temperatures $< 400^\circ\text{C}$. As the temperature rises, the curves enter a plateau phase.

Fig. 3 a, b represent frequency dependencies between a real (ε') and imaginary (ε'') constituent parts of complex dielectric permeability of the compound $\text{Bi}_{10}\text{Fe}_6\text{Ti}_3\text{O}_{30}$ at different temperatures. The $\varepsilon', \varepsilon''(f)$ dependencies are given as smooth curves with a single peak at temperatures $\geq 370^\circ\text{C}$, and with different dispersion in areas of low and high frequencies, increasing with increased temperature. Peaks of curves $\varepsilon', \varepsilon''(f)$ for temperatures exceeding 370°C are apparently beyond the frequency range of measurements. In the low frequency range, ε' values are reasonably high, while they sharply decrease when frequencies exceed 100 kHz . The $\varepsilon''(f)$ dependency is of a similar nature, however, at lower frequencies ($< 100 \text{ kHz}$), its value is an order of magnitude greater, which points to conductivity contribution towards direct current [27, 31]. Within the low frequency range, a rise in temperature will cause extreme dispersion of dielectric permeability determined by the presence of thermally activated charges (e.g. volume charge, charged defects, etc.) [9].

Dielectric losses within the temperature range under consideration are relatively insignificant (loss tangent is $\text{tg}\varphi = \varepsilon''/\varepsilon' < 0.15$). Frequency dependencies of $\text{tg}\varphi(f)$ are characterized by dispersion within the low frequency range, they sharply decrease at higher frequencies (Fig. 3c). Increased $\text{tg}\varphi$ values in the low frequency range testify to the presence

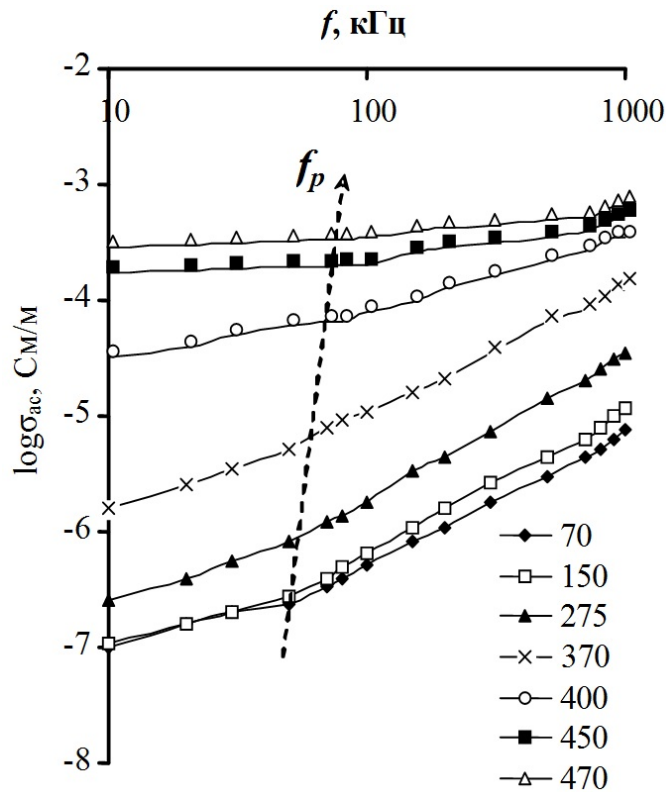


FIG. 2. Frequency dependence of the ac-conductivity $\text{Bi}_{10}\text{Fe}_6\text{Ti}_3\text{O}_{30}$

of direct current electric conductivity (σ_{dc}) [31]. Dielectric losses will increase as temperature rises, which, apparently, are determined by recrystallization processes in the sample volume, or by reduced oxygen vacancies.

To analyze relaxation processes of the electric field, the frequency dependencies of the imaginary part of the electric module $M''(f)$ was examined (Fig. 4a). At the temperatures specified, for dependencies $M''(f)$, single peaks of the same height are recorded, which differ in the position with respect to the frequency axis. Their nature points to a single relaxation process in the sample volume and for an increase in electric conductivity with temperature rise. This is also proved by the nature of diagram $M''-M'$ (Fig. 4b), represented by semi-circles centered on the X-axis, which agrees with Debye relaxation [29]. As the temperature rises, peaks of the curves $M''(f)$ will shift to higher frequencies. The frequency range below the peak will determine the range where the charge carriers are mobile at long distances, while the frequency range above the peak means that the carriers are in a “trap”, in a potential pit, with mobility at short distances preserved. The frequency range, where peaks are recorded on the curves $M''(f)$ are characterized by a change in the movement of charge carriers from long to short distances. In this case, the asymmetry of the peak, denoting relaxation processes with different time responses, is not observed [32].

According to the position of the high-frequency peak on the $M''(f)$ curves, the relaxation time of dielectric polarization, $\tau_M = \frac{1}{2\pi f_m}$, was determined, with temperature dependence following the Arrhenius law:

$$\tau_M = \tau_0 \exp\left(\frac{\Delta E_M}{kT}\right), \quad (5)$$

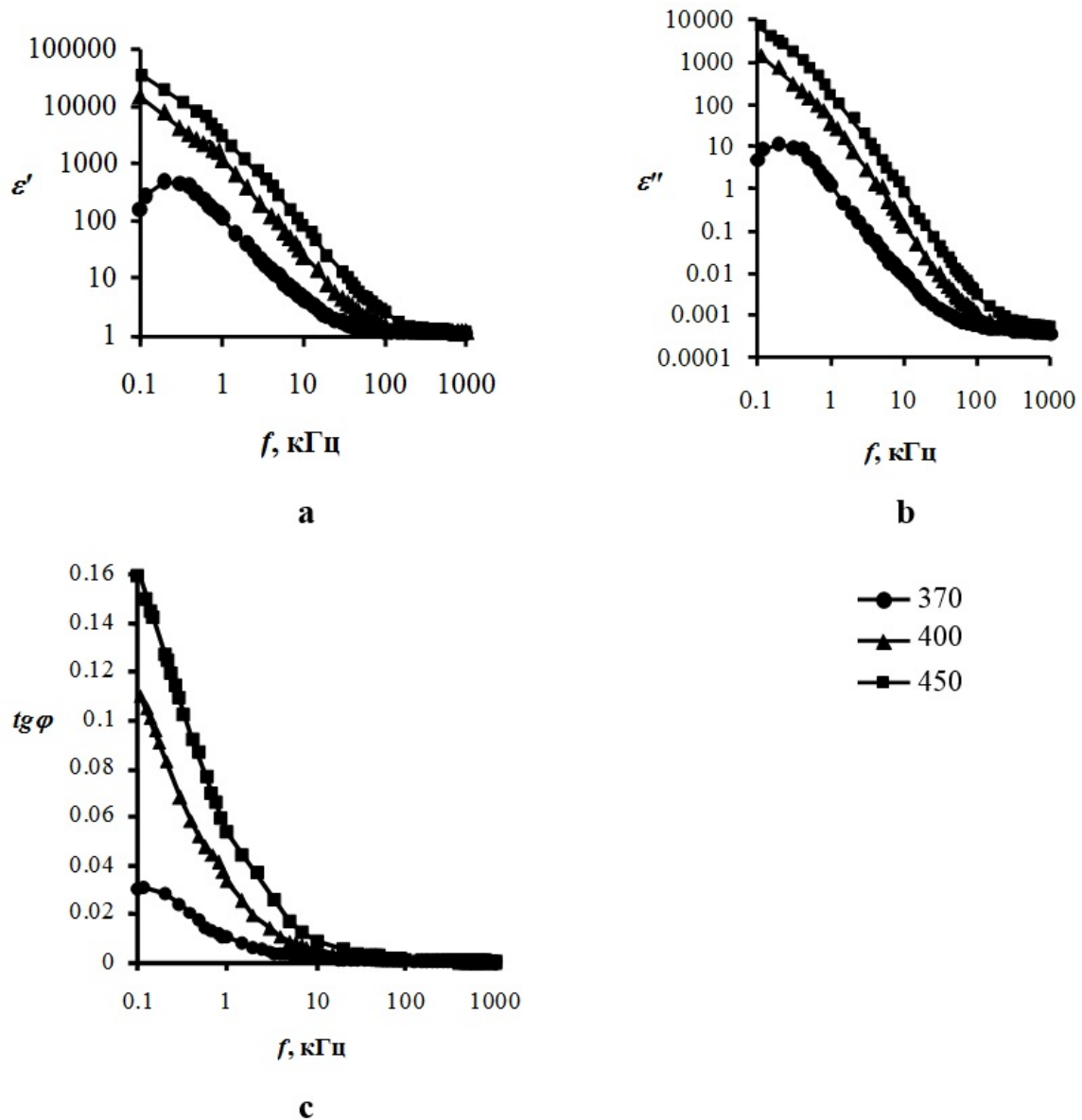


FIG. 3. Frequency dependence of the real, ε' (a) and imaginary, ε'' (b) parts of the dielectric permittivity (a, b) and dielectric, $\operatorname{tg}\varphi$, for $\text{Bi}_{10}\text{Fe}_6\text{Ti}_3\text{O}_{30}$, measured at various temperatures

where τ_M is relaxation time in the grain volume determined by the peak of the curves $M''(f)$, τ_0 is a pre-exponential factor, E_M is energy of activation of the charge carriers in the grain volume determined by the curve slope $\tau_M(1/T)$, k is Boltzmann constant, and T is absolute temperature.

The relaxation time τ within the temperature range under consideration ranged from $5 \cdot 10^{-4}$ – $1 \cdot 10^{-3}$ s. The activation energy E_M of the charge carriers in the grain volume, estimated by ratio (5), was 0.8 ± 0.1 eV, which is a typical value for compounds of Aurivillius phases type [18-25], with electric conductivity determined, primarily, by oxygen vacancy movement. The presence of oxygen vacancies in the structure of bismuth-containing Aurivillius phases is caused by the partial evaporation of Bi^{3+} ions under the high synthetic temperatures of these materials. This contributes to the overall electric conductivity, along

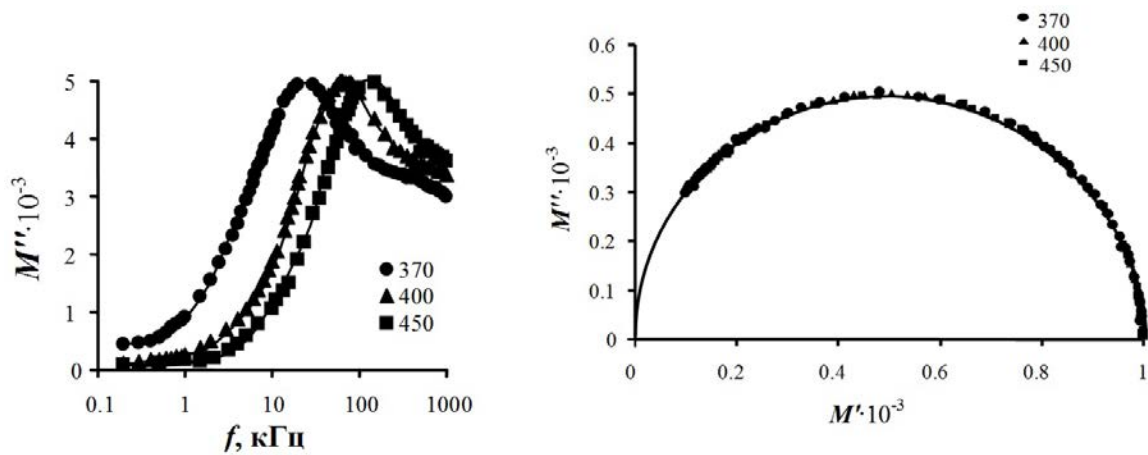


FIG. 4. Frequency dependence of the imaginary part of the electric modulus, M'' (a), and the $M''-M'$ diagram (b) for $\text{Bi}_{10}\text{Fe}_6\text{Ti}_3\text{O}_{30}$ measured at various temperatures

with the phenomenon of hopping polarons between the $\text{Fe}^{3+}-\text{O}-\text{Fe}^{2+}$ positions at elevated temperatures [3, 26].

4. Conclusion

Based on the Aurivillius phase $\text{Bi}_{10}\text{Fe}_6\text{Ti}_3\text{O}_{30}$, distinctive features of dielectric behavior of a ceramic material prepared using solid-state chemical reactions have been studied. The presence of a single process of Debye-type dielectric relaxation in a bulk sample ($E_M=0.8\pm 0.1$ eV) has been shown.

Acknowledgments

The author would like to acknowledge Victor.V. Gusarov (Ioffe Institute) for his help in this work.

References

- [1] Aurivillius B. Mixed bismuth oxides with layer lattices. I. *Ark. Kemi.* **1**(1), P. 463–471 (1949).
- [2] Smolenskii G.A., Isupov V.A., Agranovskaya A.I. A New Group of Ferroelectrics (with Layered Structure) I. *Fiz. Tverd. Tela.*, **1**(1), P. 169–170 (1959).
- [3] Lomanova N. A., Morozov M. I., Ugolkov V. L., Gusarov V. V. Properties of Aurivillius phases in the $\text{Bi}_4\text{Ti}_3\text{O}_{12}-\text{BiFeO}_3$ system. *Russ. J. Inorganic Materials*, **42**(2), P. 189–195 (2006).
- [4] Lomanova N.A., Gusarov V.V. On the limiting thickness of the perovskite-like block in the Aurivillius phases in the $\text{Bi}_2\text{O}_3-\text{TiO}_2-\text{Fe}_2\text{O}_3$ system. *Nanosystems: physics, chemistry, mathematics*, **2**(3), P. 93–101 (2011).
- [5] Lomanova N.A., Semenov V.G., Panchuk V.V., Gusarov V.V. Structural features and stability of the Aurivillius phases $\text{Bi}_{n+1}\text{Fe}_{n-3}\text{Ti}_3\text{O}_{3n+3}$. *Dokl. Chem.*, **447**(2), P. 293–295 (2012).
- [6] Yu W. J., Kim Y. I., Ha D. H., Lee J. H., Park Y. K., Seong S., Hur N. H. A new manganese oxide with the Aurivillius structure: $\text{Bi}_2\text{Sr}_2\text{Nb}_2\text{MnO}_{12-\delta}$. *Solid State Commun.*, **111**(12), P. 705–709 (1999).
- [7] Miyayama M., Yi I.-S. Electrical anisotropy in single crystals of Bi-layer structured ferroelectrics. *Ceramics International*, **26**, P. 529–533 (2000).
- [8] Lomanova N.A., Semenov V.G., Panchuk V.V., Gusarov V.V. Structural changes in the homologous series of the Aurivillius phases $\text{Bi}_{n+1}\text{Fe}_{n-3}\text{Ti}_3\text{O}_{3n+3}$. *J. Alloys and Compounds.*, **528**, P. 103–108 (2012).

- [9] Bai W., Chen G., Zhu J. Y., Yang J., Lin T., Meng X.J., Tang X.D., Duan C.G., Chu J.H. Dielectric responses and scaling behaviors in Aurivillius $\text{Bi}_6\text{Ti}_3\text{Fe}_2\text{O}_{18}$ multiferroic thin films. *Appl. Phys. Lett.* **100**(8), P. 082902–082906 (2012).
- [10] Jiang P.P., Zhang X.L., Chang P., Hu Z. G., Bai W., W. Li Y., Chu J.H. Spin-phonon interactions of multiferroic $\text{Bi}_4\text{Ti}_3\text{O}_{12}$ - BiFeO_3 ceramics: Low-temperature Raman scattering and infrared reflectance spectra investigations. *J. Appl. Phys.*, **115**, P. 144101–144106 (2014).
- [11] Keeney L., Maity T., Schmidt M., Amann A., Deepak N., Petkov N., Roy S., Pemble M. E., Whatmore R. W. *J. Am. Ceram. Soc.*, **96**(8), P. 2339–2357 (2013).
- [12] Isupov V.A. Curie Temperatures of $\text{A}_{m-1}\text{Bi}_2\text{MmO}_{3m+3}$ layered ferroelectrics *Russ. J. Neorg. Mater.*, **33**(9), . 1106–1110 (1997).
- [13] Snedden A., Hervoches Ch. H., Lightfoot Ph. Ferroelectric phase transition in $\text{SrBi}_2\text{Nb}_2\text{O}_9$ and $\text{Bi}_{15}\text{Ti}_3\text{FeO}_{15}$: a powder neutron diffraction study. *Phys. Rev.*, **67**, P. 092102 (2003).
- [14] Krzhizhanovskya M., Filatov S., Gusarov V., Paufer P., Bubnova R., Morozov M., Meyer D. C. Aurivillius phases in the $\text{Bi}_4\text{Ti}_3\text{O}_{12}$ / BiFeO_3 system: thermal behaviour and crystal structure. *Z. Anorg. Allg. Chem.*, **631**, P. 1603–1608 (2005).
- [15] Subbanna G.N., Guru Row T.N., Rao C.N.R. Structure and dielectric properties of recurrent intergrowth structures formed by the Aurivillius family of bismuth oxides of the formula $\text{Bi}_2\text{A}_{n-1}\text{BnO}_{3n+3}$. *J. Solid State Chem.*, **86**(2), P. 206–211 (1990).
- [16] Lomanova N.A., Ugolkov V. L., Gusarov V. V. Thermal behavior of layered perovskite-like compounds in the $\text{Bi}_4\text{Ti}_3\text{O}_{12}$ - BiFeO_3 system. *Glass Physics and Chemistry*, **33**, P. 608–612 (2007).
- [17] Lomanova N.A., Gusarov V.V. Phase states in the $\text{Bi}_4\text{Ti}_3\text{O}_{12}$ - BiFeO_3 section in the Bi_2O_3 - TiO_2 - Fe_2O_3 system. *Russ. J. Inorg. Chem.*, **56**, P. 616–620 (2011).
- [18] Srinivas A., Kumar M., Suryanarayana S.V., Bhimasankaram T. Investigation of dielectric and magnetic nature of $\text{Bi}_7\text{Fe}_3\text{Ti}_3\text{O}_{21}$. *Mater. Res. Bull.*, **34**(6), P. 989–996 (1999).
- [19] Srinivas A., Kima Dong-Wan, Honga Kug Sun, Suryanarayana S.V. Study of magnetic and magnetoelectric measurements in bismuth iron titanate ceramic- $\text{Bi}_8\text{Fe}_4\text{Ti}_3\text{O}_{24}$. *Mater. Res. Bull.*, **39**, P. 55–61 (2004).
- [20] Srinivas K., Sarah P., Suryanarayana S.V. Impedance spectroscopy study of polycrystalline $\text{Bi}_6\text{Fe}_2\text{Ti}_3\text{O}_{18}$, *Bull. Mater. Sci.*, **26**(2), P. 247–253 (2003).
- [21] Bucko M. M., Polnar J., Kozielski L. Dielectric Properties of Some Aurivillius Phases in the $\text{Bi}_4\text{Ti}_3\text{O}_{12}$ - BiFeO_3 System. *Materials Science Forum.*, **730**, P. 88–93 (2013).
- [22] Patwe S. J., Achary S. N., Manjanna J., Tyagi A. K., Deshpande S. K., Mishra S. K., Krishna P. S. R., Shinde A. B. Observation of a new cryogenic temperature dielectric relaxation in multiferroic $\text{Bi}_7\text{Fe}_3\text{Ti}_3\text{O}_{21}$. *Appl. Phys. Lett.*, **103**, P. 12290–112296 (2013).
- [23] Dercz J., Starczewska A., Dercz G. Dielectric and structural properties of $\text{Bi}_5\text{Ti}_3\text{FeO}_{15}$ ceramics obtained by solid-state reaction process from mechanically activated precursors. *Int. J. Thermophys.*, **32**, P. 746–761 (2011).
- [24] Lomanova N.A., Gusarov V.V. Electrical properties of perovskite-like compounds in the Bi_2O_3 - TiO_2 - Fe_2O_3 system. *Russ. J. Inorg. Mater.*, **47**, P. 420–425 (2011).
- [25] Lomanova N.A., Gusarov V.V. Impedance spectroscopy of polycrystalline materials based on the Aurivillius phase system $\text{Bi}_4\text{Ti}_3\text{O}_{12}$ - BiFeO_3 . *Nanosystems: physics, chemistry, mathematics*, **3**, P. 112–122 (2012).
- [26] Morozov M. I., Gusarov V.V. Synthesis of $\text{A}_{m-1}\text{Bi}_2\text{MmO}_{3m+3}$ compounds in the $\text{Bi}_4\text{Ti}_3\text{O}_{12}$ - BiFeO_3 system. *Russ. J. Inorg. Mat.*, **38**, P. 723–729 (2002).
- [27] Molak A., Paluch M., Pawlus S., Klimontko J., Ujma Z., Gruszka I. Electric modulus approach to the analysis of electric relaxation in highly conducting $(\text{Na}_{0.75}\text{Bi}_{0.25})(\text{Mn}_{0.25}\text{Nb}_{0.75})\text{O}_3$ ceramics. *J. Phys. D: Appl. Phys.*, **38**, P. 1450–1460 (2005).
- [28] Yi Z. G., Li Y. X., Wang Y., Yin Q. R. Spectroscopies of mixed-layer Aurivillius phase $\text{Bi}_5\text{Ti}_{1.5}\text{W}_{1.5}\text{O}_{15}$ dielectric, impedance, and electric modulus. *J. Electrochem. Soc.*, **153**(6), P. F100–F105 (2006).
- [29] Jonscher A.K. The ‘universal’ dielectric response. *Nature*, **267**, P. 673–679 (1977).
- [30] Jonscher A.K. Dielectric relaxation in solids. *J. Phys. D: Appl. Phys.*, **32**, P. R57–R70 (1999).
- [31] Gerhardt R. Impedance and dielectric spectroscopy revisited: Distinguishing localized relaxation from long-range conductivity. *J. Phys. Chem. Solids.*, **55**, P. 1491–1506 (1994).
- [32] Pattanayak S., Parida B.N., Das P. R., Choudhary R.N.P. Impedance spectroscopy of Gd-doped BiFeO_3 multiferroics. *Appl. Phys. A.*, **112**, P. 387–395 (2013).

SYNTHESIS AND STUDIES ROOM TEMPERATURE CONDUCTIVITY, DIELECTRIC ANALYSIS OF LaF_3 NANOCRYSTALS

Sidheshwar G. Gaurkhede

Department of Physics, Bhavan's College of ASC,
Andheri (W) Mumbai-400058. India

s.gaurkhede@gmail.com

PACS 61.05.cp, 77.22.d

Lanthanum fluoride (LaF_3) was synthesized using LaCl_3 and NH_4F as starting materials in de-ionized water as solvent via a microwave-assisted technique. The structure of LaF_3 nanocrystals, analyzed by XRD and TEM, was found to be hexagonal with an average crystalline particle size of 20 nm (JCPDS standard card (32-0483) of pure hexagonal LaF_3 crystals). The resistivity and conductivity at room temperature for LaF_3 was verified and found to depend on the applied DC field. At an applied voltage of 20 V/cm – 30 V/cm, the resistivity and conductivity changes rapidly due to the liberation of extra fluoride (F^-) ions, whereas the conductivity of LaF_3 nanocrystals depends upon temperature. The variation of dielectric constant (ϵ') and dielectric loss (ϵ'') with applied frequency shows normal dielectric behavior, attributable to the space charge formation. The observed peak in the plot of tangent loss ($\tan \delta$) vs. $\log F$ around 2.6 KHz can be attributed to interface charge relaxation at the grain boundaries.

Keywords: Microwave radiation, Hexagonal shape, X-ray diffraction, Dielectric materials.

Received: 24 November 2014

Revised: 28 November 2014

1. Introduction

Lanthanum fluoride based chemical sensors have potential to be widely used in applications such as the detection of fluorine, oxygen, and carbon monoxide, due to its high chemical stability and ionic conductivity [1]. The ionic conducting nature of the rare earth fluorides (solid electrolyte) is exploited as sensor materials to construct various electrochemical sensors like gas sensors, biosensors, and ion selective electrodes [2]. Lanthanum fluoride is an excellent F^- ionic conductor among other rare earth fluorides [3]. Miura et al. reported the use of lanthanum fluoride film in biosensor and room-temperature oxygen sensor based on its high F^- ion-conducting properties. The working principle of LaF_3 based biosensors and oxygen sensors is explained as the movement of F^- ion conduction [4, 5]. Fedorov P. P. [6] et al. review the major aspects of inorganic chemistry of nanofluorides, methods of synthesis, including nanochemical effects, preparation of 1D, 2D, and 3D nanostructures, surface modification of the nanoparticles, fluoride nanocomposites and applications of nanofluorides. The orthorhombic $\beta\text{-YF}_3$ structure and ionic conductivity of rare earth fluorides and of tysonite-structured were investigated by Trnovcova et al. [7, 8]. At room temperature, the ionic conductivity of single crystals of tysonite-type solid solutions $\text{La}_{1-x}\text{Ba}_x\text{F}_{3-x}$ has been studied and no exchange occurs between different types of anion sites in the tysonite structure [9, 10]. Very recently, Kumar et al. [11, 12] attempted to synthesize lanthanum fluoride nanoparticles by the simple method of direct precipitation in aqueous solution. The impedance, modulus and dielectric spectra analysis

of the prepared LaF₃ nanoparticles has been studied using AC impedance spectroscopy. The ionic conductivity of LaF₃ nanoparticles were reported to be significantly increased by an order of magnitude, from 10⁻⁶ S cm⁻¹ to 10⁻⁵ S cm⁻¹. The modulus and dielectric spectra analysis confirmed the non-Debye type behavior in the material. The synthesized LaF₃ nanoparticles exhibited hexagonal shape and red luminescence. In the present case, LaF₃ nanoparticles have been synthesized using a conventional microwave radiation technique for first time.

2. Experimental

2.1. Synthesis of Nanocrystals

Synthesis of LaF₃ nanocrystals follows an aqueous route and uses a microwave heating at low power range. The method is simple and cost effective. Water soluble LaCl₃ and NH₄F are mixed to obtain a solution in 1:3 molar ratio [13]. To a 10 ml homogenous solution of 0.64 mol LaCl₃ in de-ionized water in a 100 ml beaker was added a 10 ml solution of 0.192 mol NH₄F in a drop-wise manner via a funnel fitted with a stopper to control the rate of dripping, and placed the whole set up inside a conventional microwave set at low power range (in on-off mode set at 30 sec) for around 30 min. The low power range setting largely helped us avoid spill-over of the solution. A white ultrafine crystalline precipitate identified as doped LaF₃ nanocrystals appeared almost instantly, having settled to the bottom of the beaker. The white precipitate was then washed several times with de-ionized water and absolute methanol, and was then dried in a microwave oven for approximately 15 minutes. The dried sample was then stored in sealed ampoules for further characterization and analysis.

2.2. Characterization

Powder X-ray diffraction (XRD) measurements have been performed using a PANALYTICAL X'PERT PROMPD diffractometer model using CuK α radiation $\lambda = 1.5405$ Å. U with a scanning rate of 2 ° per min in the 2θ range from 0 ° to 80 °. Transmission electron microscope (TEM) analysis was performed at different magnification by PHILIPS (CM 200) 0.24 nm resolution, operating at 200 kV. The dielectric constants of the sample have been measured using sophisticated Hioki 3532 LCR Meter. The capacitance and dissipation factor of the parallel plate capacitor formed by sample as a dielectric medium was measured.

3. Result and Discussion

The XRD pattern obtained from the LaF₃ nanocrystals shown in Fig. 1. The results of the XRD are in good agreement with the hexagonal LaF₃ structure as described in the reports LaF₃ (JCPDS card No. 32-0483) [14]. The average crystallite size was estimated from the Scherrer equation, $D = 0.90\lambda/\beta \cos \theta$, where D is the average crystallite size, λ is the X-ray wavelength (0.15405 nm), θ and β being the diffraction angle and full width at half maximum of an observed peak, respectively. The strongest peak (111) at $\theta = 27.84$ ° for LaF₃ samples were used to calculate the average crystallite size (D) of the nanoparticles [15]. The average crystallite sizes of LaF₃ nanoparticles are 20 nm, which is in agreement with the TEM and SEM results. The XRD pattern of the LaF₃ nanoparticles is nearly similar to that of LaF₃: Ce³⁺, Tb³⁺ [16]. No XRD signals are observed for impurity phases.

Figure 2 shows the transmission electron microscopy (TEM) image of LaF₃ nanocrystals. Hexagonal, assorted and spherical shape nanocrystals with average particle size of about 21 nm were found. Fig. 3 shows the selected area electron diffraction (SAED) pattern. Three strong diffraction rings, corresponding to the (002), (111) and (300) reflections were observed, which

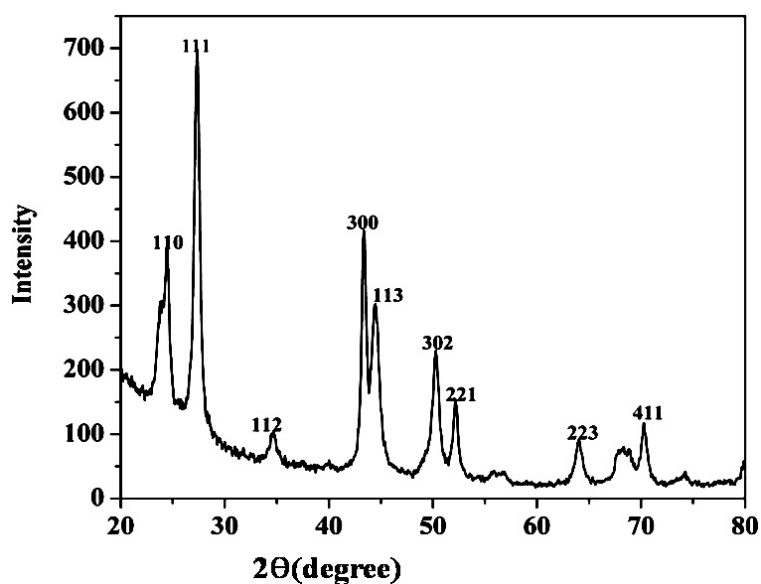


FIG. 1. X-ray diffraction pattern of LaF_3 nanocrystals

is in close agreement with the hexagonal LaF_3 structure [17]. This shows that the original structure of LaF_3 may be retained even after modification.

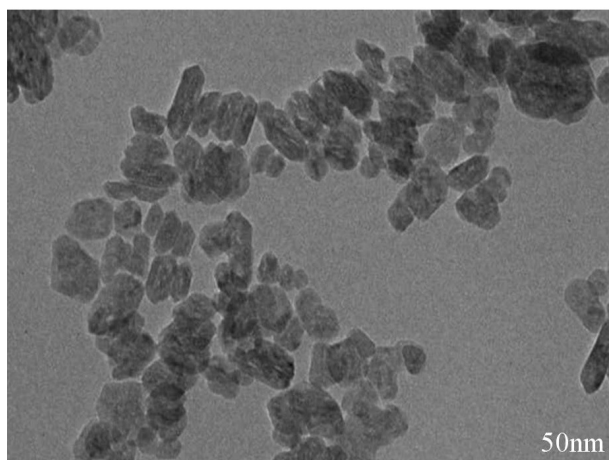


FIG. 2. TEM image of LaF_3 nanocrystals

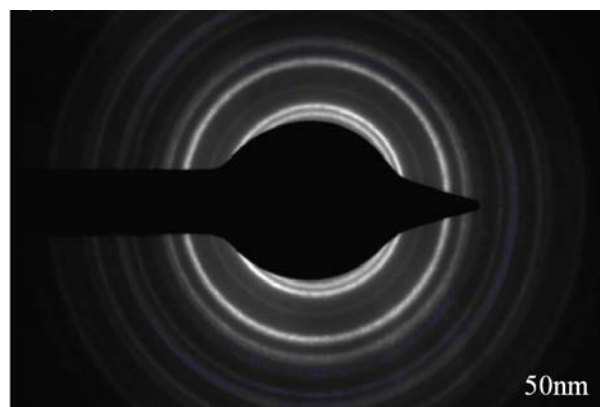


FIG. 3. Selected area electron diffraction (SAED) pattern image of LaF_3 nanocrystals

$I - V$ characteristic of LaF_3 nanocrystals synthesis in deionized water and methanol is shown in Fig. 4. Conductivity / resistivity depended on the applied DC field. The ionic conductivity was calculated using the relation $\sigma_{dc} = t/RA$. Where, R is the measured resistance, t be the thickness of the pellet (cm) and A is the area of the pellet (cm^2) in contact with the electrode. The conductivity at room temperature of the sample prepared in deionized water was found to be $2.7 \times 10^{-6} \text{ S cm}^{-1}$, in agreement with previously-reported work. The conductivity was found to be $8.0 \times 10^{-6} \text{ S cm}^{-1}$, nearly four times higher in methanol than in de-ionized water samples at room temperature. The current was found to increase with the applied field [11]. The conductivity and resistivity were thus found to depend on the applied field. At an applied voltage of about 20 V/cm – 30 V/cm the conductivity / resistivity was found to change rapidly due to liberation of extra fluoride (F^-) ions [12].

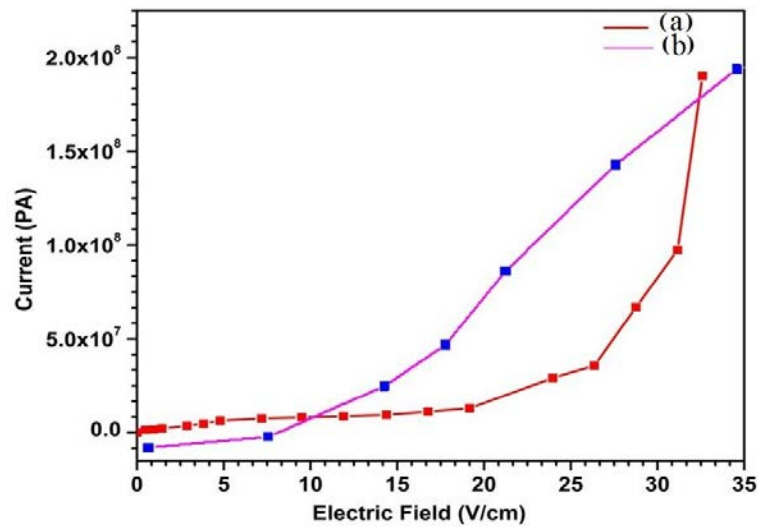


FIG. 4. Current vs. Voltage graph of LaF_3 nanocrystals prepared in (a) de-ionized water (b) methanol

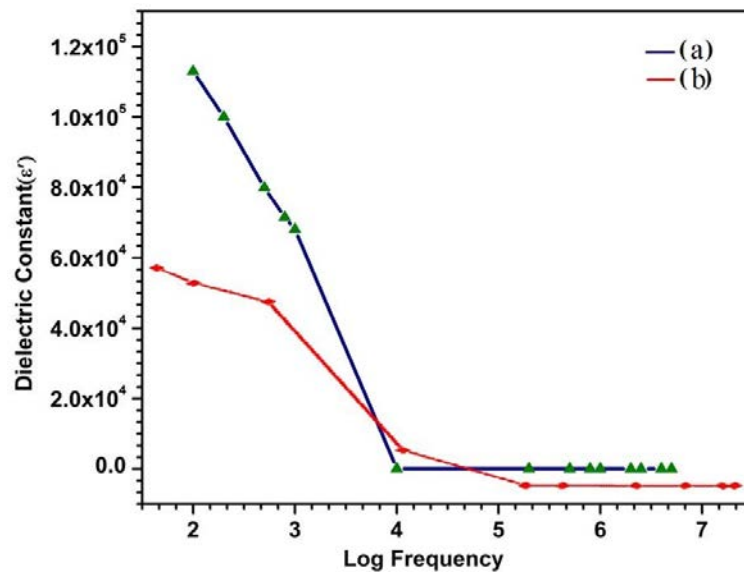


FIG. 5. Variation of dielectric constant with $\log F$ for LaF_3 nanocrystals prepared in (a) de-ionized water (b) methanol

The variations of dielectric constant in log frequency at room temperature for LaF_3 nanocrystals prepared in de-ionized water and methanol have been studied. Fig. 5 and Fig. 6 shows the plot of dielectric constant ϵ' as a function of log frequency and the plot of dielectric loss ϵ'' as a function of log frequency for LaF_3 nanocrystals. Both dielectric constant and dielectric loss exhibited similar variation with frequency, both being inversely proportional to frequency. This is normal dielectric behavior, that both ϵ' and ϵ'' decrease with increasing frequency. The dielectric constant was found to fall more rapidly as compared to dielectric loss with applied frequency.

A plot of $\tan \delta$ against $\log F$ is shown in Fig. 7. The relaxation peaks were found to lie near 2.6 KHz. From the figure, the peak in the low frequency region indicates the contribution of the real dielectric constant of the material due to the polarization [18].

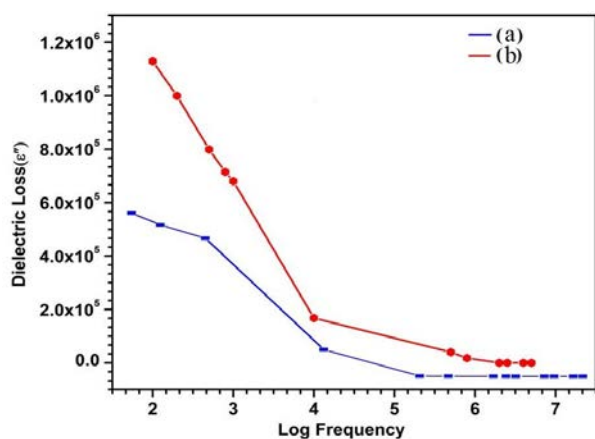


FIG. 6. Variation of dielectric loss with $\log F$ for LaF_3 nanocrystals prepared in (a) methanol (b) de-ionized water

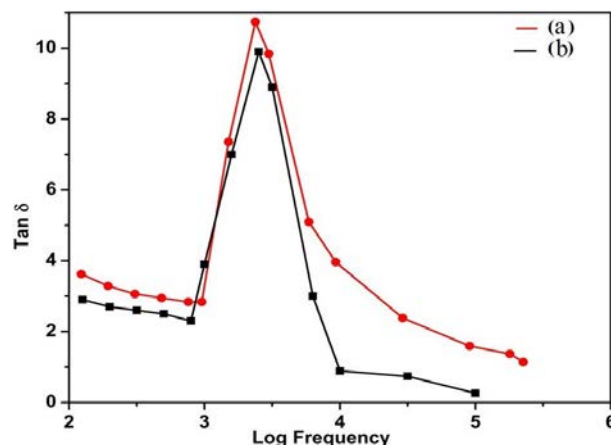


FIG. 7. $\log F$ versus $\text{Tan } \delta$ for LaF_3 nanocrystals prepared in (a) de-ionized water (b) methanol

4. Conclusions

LaF_3 nanocrystals were successfully synthesized using LaCl_3 & NH_4F in deionized water. Elongated & assorted size hexagonal geometry of LaF_3 nanocrystals were observed. XRD and TEM studies indicated that the average particle size was 20 nm. The conductivity at room temperature for LaF_3 sample prepared in deionized water was found to be in close agreement with reported values. This is the first report of conductivity varying with the applied field. With an applied frequency, the variation of ϵ' and ϵ'' shows normal dielectric behavior, attributable to space charge formation. A very sharp peak in the plot of tangent loss ($\text{tan } \delta$) vs. $\log F$ has been noted around 2.6 KHz which can be attributed to interface change relaxation at grain boundaries.

References

- [1] Yamazoe N., Miura N. Environmental gas sensing. *Sensors Actuators*, **20** (2), P. 95–102 (1994).
- [2] Fergus J.W. The Application of Solid Fluoride Electrolytes in Chemical Sensors. *Sensors Actuators*, **42** (2), P. 119–130 (1997).
- [3] Schoonman J., Oversluizen G., Wapenaar K.E.D. Solid electrolyte properties of LaF_3 . *Solid State Ionics*, **1** (3), P. 211–221 (1980).
- [4] Miura N., Hisamoto J., Yamazoe N., Kuwata S. LaF_3 sputtered film sensor for detecting oxygen at room temperature. *Appl. Surf. Sci.*, **33/34**, P. 1253–1259 (1988).
- [5] Miura N., Hisamoto J., et al. Solid-state oxygen sensor using sputtered LaF_3 film. *Sensors Actuators*, **16** (4), P. 301–310 (1989).
- [6] Fedorov P.P., Luginina A.A., Kuznetsov S.V., Osiko V.V. Nanofluorides. *J. Fluorine Chem.*, **132** (12), P. 1012–1039 (2011).
- [7] Trnovcova V., Garashina L.S., et al. Structural aspects of fast ionic conductivity of rare earth fluorides. *Solid State Ionics*, **157** (1–4), P. 195–201 (2003).
- [8] Trnovcova V., Fedorov P.P., Furara I. Fluoride Solid Electrolytes. *Russian Journal of Electrochemistry*, **45** (6), P. 630–639 (2009).
- [9] Duvel A., Bednarcik J., Sepelk V., Heitjans P. Mechano-synthesis of the Fast Fluoride Ion Conductor $\text{Ba}_{1-x}\text{La}_x\text{F}_{2+x}$ From the Fluorite to the Tysonite Structure. *J. Phys. Chem. C*, **118** (13), P. 7117–7129 (2014).
- [10] Roos A., Pol F.C.M. van de, Keim R., Schoonman J. Ionic Conductivity in Tysonite-type Solid Solutions $\text{La}_{1-x}\text{Ba}_x\text{F}_{3-x}$. *Solid State Ionics*, **13**, P. 191–203 (1984).

- [11] Selvasekarapandiana S., Vijayakumara M., et al. Ion conduction studies on LaF_3 thin film by impedance spectroscopy. *Physica B*, **337** (5), P. 52–57 (2003).
- [12] Kumar D.A., Selvasekarapandian S., Nithya H., Hema M. Synthesis, micro-structural, and electrical analysis on lanthanum fluoride. *Ionics*, **18** (5), P. 461–471 (2012).
- [13] Meng J., Zhang M., Liu Y. Hydrothermal preparation and luminescence of $\text{LaF}_3:\text{Eu}^{3+}$ nanoparticles. *Spect. Acta A*, **66** (1), P. 81–85 (2007).
- [14] Daihua T., Liu X., Zhen Z. Oleic acid (OA)-modified LaF_3 : Er, Yb nanocrystals and their polymer hybrid materials for potential optical-amplification applications. *J. Mater. Chem.*, **17** (1), P. 1597–1601 (2007).
- [15] Daqin C., Yuansheng W., En Ma, Yunlong Y. Influence of Yb^{3+} content on microstructure and fluorescence of oxyfluoride glass ceramics containing LaF_3 nano-crystals. *Mater. Chem. Phys.*, **101** (9), P. 464–469 (2007).
- [16] Pi D., Wang F., et al. Polyol-mediated synthesis of water-soluble $\text{LaF}_3:\text{Yb,Er}$ upconversion fluorescent nanocrystals. *Materials Letters*, **61** (6), P. 1337–1340 (2007).
- [17] Yuanfang L., Wei C., et al. X-ray Luminescence of $\text{LaF}_3:\text{Tb}$ and $\text{LaF}_3:\text{Ce, Tb}$ Water Soluble Nanoparticles. *J. Appl. Phys.*, **103** (6), P. 1–7 (2008).
- [18] Kumar D.A., Selvasekarapandian S., et al. Dielectric, modulus and impedance analysis of LaF_3 nanoparticles. *Physica B: Condensed Matter*, **405** (17), P. 3803–3807 (2010).

POROUS STRUCTURE OF CARBON NANOPARTICLES PREPARED BY CHLORINATION OF NANOPARTICLES OF SILICON CARBIDE

V. V. Sokolov, N. A. Petrov, M. V. Tomkovich, V. V. Gusarov

Ioffe Institute, 26 Polytekhnicheskaya Str., Saint Petersburg 194021, Russia

mariya.tom83@gmail.com

PACS 81.05.Uw; 61.46.-w

Specific features of the structure of nanoporous carbon, prepared by chlorinating silicon carbide nanoparticles followed by treatment thereof by hydrogenation have been studied. A considerable number of microscopic pores in carbon nanoparticles have been shown.

Keywords: nanoporous carbon, carbon nanoparticles.

Received: 20 November 2014

Revised: 5 December 2014

1. Introduction

Properties of carbon materials with effective surface are attributable both to the quantity of specific surface, and to their structure, including morphology, size, and porous structure of nanoparticles.

Carbon materials with high surface area having micro-, meso-, and macropores based on particles of micron and submicron dimensions are known and widely applied.

The synthesis of new substances, based on highly-porous carbon opens promising prospects for the use of these materials and carbon-based nanocomposites as sorbents and gas accumulators, catalysts in producing super-condensers, electrodes for electric-chemical generators, etc. One of the promising classes of porous carbon materials is based on nanoporous carbon prepared by high-temperature chlorination of carbides [1, 2]. In papers devoted to the synthesis and study of nanoporous carbon, carbide powders of micron or submicron dimensions were chlorinated [1-4].

The study of the porous structure of carbon nanoparticles synthesized by chlorinating carbide powders is of interest. This article analyzes the porous structure of carbon nanoparticles synthesized by high-temperature chlorination of silicon carbide nanoparticles of cubic modification (SiC).

2. Experimental

For the synthesis of carbon nanoparticles, silicon carbide nanopowder primarily consisting of particles SiC (maximum content of amorphous phase 3-15%), with specific gravity 3.22 g/cm^3 , spherical shape, 45–55 nm in diameter produced by Aldrich (USA) was employed. Silicon carbide was chlorinated in a Tamman furnace under chlorine atmosphere at 700 to 1000°C for 10 and 60 minutes. To remove chlorine impurities from the sample according to the procedure described in [3], after chlorination, the sample was exposed to thermal hydrogenation at 800°C for 60 minutes.

Reliable data on the structure of nanoscale objects can only be obtained by employing a comprehensive approach [5]. This requirement also applies to the analysis of the formed materials' porous structure. Therefore, to define the structure and dimensions of nanoparticles, as well as parameters for their porous structure, a variety of techniques were employed.

Parameters for the crystal structure of the sample were determined based on powder X-Ray diffraction data using a Shimadzu XRD-7000. Crystallites dimensions were calculated according to Scherrer formula based on data from X-Ray diffraction line broadening.

Pycnometric specific gravity of powders was measured using a helium pycnometer AccuPyc 1330 (Micromeritics, USA).

Adsorption and structural analysis of powders were carried out using an analyzer ASAP 2020 (Micromeritics, USA). Specific gravity of nanoparticles, cumulative pore volume, and distribution of pores by dimensions were calculated according to the model BET using DFT method [6], included in the analyzer software. These methods, like others, suggest that the pores have a particular shape. Therefore, the results obtained for spherical, cylindrical, and slot-like pores or pore space of mixed type may vary widely [7].

This paper suggested that slot-like pores are most prevalent. Despite ambiguity, this model was chosen following the results of papers [2-4].

3. Results and discussion

Diffraction patterns of the samples under investigation (Fig. 1) show that for the initial silicon carbide, consisting of nanocrystals SiC with diameters of $d=20\pm 2$ nm (Table 1), the carbon synthesized by high-temperature chlorination will be amorphous. On the contrary, for the carbon prepared by chlorination of macrocrystalline σ SiC, the diffraction patterns show the broadened lines similar in position to the graphite pattern lines [4].

Table 2 provides elemental composition of samples of nanoporous carbon prepared by chlorination of nanopowder SiC under different conditions. The data obtained show that the samples contain insignificant quantities of oxygen and chlorine. In the sample chlorinated at 700°C, low silicon content was observed. Silicon is apparently present as SiO₂. The presence of silicon dioxide is likely attributable to the presence of impurities of silicon dioxide in the initial sample, and to the stability of SiO₂ under a chlorine atmosphere at 700°C. To remove chlorine impurities, the samples were treated under hydrogen atmosphere. The treatment ensured almost complete chlorine removal, see Table 2. Then, the nanoporous carbon samples, once dechlorinated via hydrogenation, were then analyzed.

Table 3 gives the values for the specific surface area and parameters of porous structure for nanoporous carbon samples prepared under different conditions for the chlorination of SiC nanopowder. It should be noted that the results of the structural and adsorption analysis obtained for models BET and DFT vary widely (Table 3). The difference is most pronounced in nanoporous carbon samples synthesized at higher temperatures, i.e. at 850 and 1000°C. This can be proved by the data on micropore volumes and cumulative pore volumes provided in Table 3, as well as by the data on distribution of pores by dimensions in nanoporous carbon prepared at different temperatures. Note that the presence of pores with dimensions of 37 nm is apparently attributable to interparticle porosity. The pores share dimensions for all chlorination conditions, because initial nanoparticles SiC were of 50–60 nm in size (Table 1), chlorination did not cause considerable change in the dimensions of the carbon particles as compared to the particles of the initial silicon carbide [7].

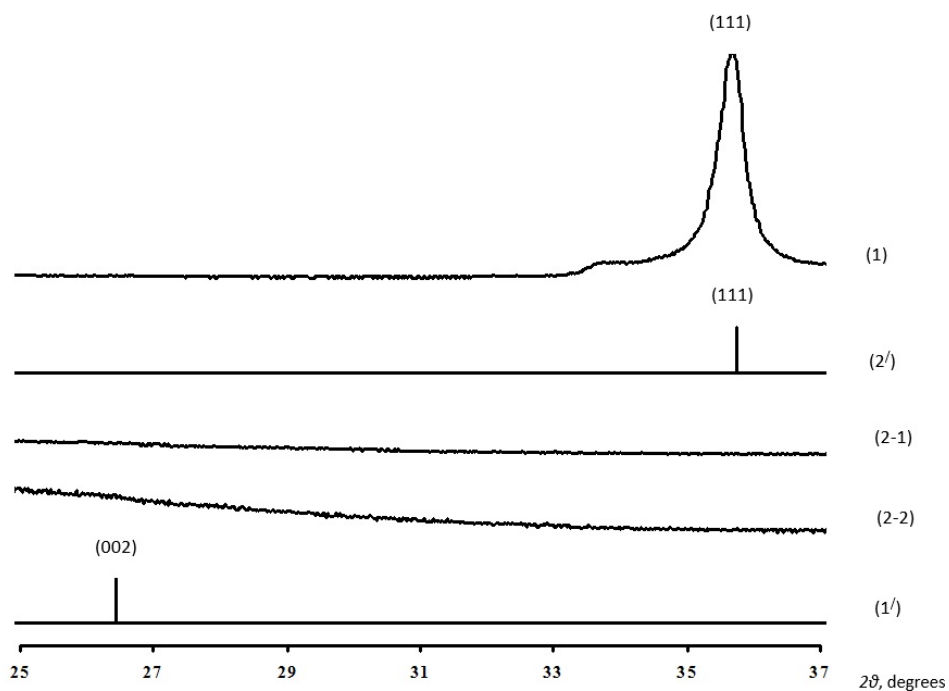


FIG. 1. X-Ray diffraction patterns of silicon carbide (1), carbon prepared by chlorination (2-1), and carbon sample treated in vacuum (2-2). Line diagrams of powder patterns show the peaks corresponding to phases -SiC (1') and graphite (2')

TABLE 1. Characteristics of silicon carbide nanopowder

Substance	Crystal structure	Specific density, g/cm ³		size (d), nm		Specific surface	
		X-Ray	Pycno-metric	Crystallites	Particles	Per unit of volume, m ² /cm ³	Per unit of weight, m ² /g
Silicon carbide	Cubic, primarily -phase (3-15% of amorphous one)	3.219	3.220 ⁽¹⁾ 3.217 ⁽²⁾	$d_{111}=20\pm 2$	45-50 ⁽¹⁾ 59 ⁽³⁾	100.7 ⁽³⁾	70-90 ⁽¹⁾ 31.3 ⁽³⁾

Notes:

- (1) characteristics of the powder provided by company Aldrich, USA (CAS Number 409-21-2);
- (2) helium pycnometry data;
- (3) following the data of adsorption and structural analysis

TABLE 2. Elemental analysis of nanoporous carbon synthesized from -SiC

Chlorination conditions	Elemental composition, At. %	
	After chlorination	After treatment in hydrogen flow
1,000°C, 10 min	C – 96.99 O – 1.58 Cl – 1.43	C – 97.31 O – 2.69
850°C, 60 min	C – 94.22 O – 2.68 Cl – 3.10	C – 98.42 O – 1.58
700°C, 100 min	C – 91.67 O – 3.36 Si – 0.77 Cl – 4.20	C – 98.68 O – 1.05 Si – 0.24 Cl – 0.03

TABLE 3. Specific surface and porous structure of carbon synthesized from nanoparticles β -SiC

Chlorination conditions	Pycnometric density g/cm ³	Pore volume (<2 nm), cm ³ /g	Cumulative pore volume (DFT), cm ³ /g	Specific surface (BET), m ² /g	Specific surface (DFT), m ² /g	Size in the peak points of the size distribution curve, nm
1000°C, 10 min	2.17	0.403	Pores sizes ≤ 86 nm 0.564	1472	1126	<0.45 0.68 0.8 1.3 37
850°C, 60 min	2.11	0.470	Pores sizes ≤ 93 nm 0.599	1529	1270	0.5 0.66 0.8 1.3 37
700°C, 100 min	1.98	0.527	Pores sizes ≤ 86 nm 0.612	1538	1550	0.54 0.8 1.3 37

4. Conclusion

The results obtained show great potential for the synthesis of nanoporous carbon from nanoparticles of silicon carbide, as the prepared carbon nanopowder had effective specific surface areas and high micropore content.

References

- [1] Fedorov N.F., Ivakhnyuk G.K., Gavrilov D.N. Porous structure of carbon adsorbents from titanium carbide. *Zh.Prikladnoi Khimii*, **55**(1), P. 46–50 (1982).
- [2] Nikitin A., Gogotsi Y. Nanostructured carbide-derived carbon. *Encyclopedia of Nanoscience and Nanotechnology*, **7**, P. 553-74 (2003).
- [3] Kravchik A.E., Kukushkina Y.A., Sokolov V.V., Tereshchenko G.F., Ustinov E.A. Structure of nanoporous carbon produced from titanium carbide and carbonitride. *Russ. J. Appl. Chem.*, **81**(10), P. 1733–1739 (2008).
- [4] Kukushkina J.A., Sokolov V.V., Tomkovich M.V. *Russian Journal of Applied Chemistry*, **87**(10), P. 1466–1473 (2014).
- [5] Almjasheva O.V., Fedorov B.A., Smirnov A.V., Gusarov V.V. Size, morphology and structure of the particles of zirconia nanopowder obtained under hydrothermal conditions. *Nanosystems: physics, chemistry, mathematics*, **1**(1), P. 26–37 (2010).
- [6] Evans R., Marconi U.M.B., Tarazona P. J. Capillary condensation and adsorption in cylindrical and slit-like pores. *Chem. Soc. Faraday Trans. II*, **82**, P. 1763–1787 (1986).
- [7] Smirnov A.V., Fedorov B.A., Petrov N.A., Sokolov V.V. et al. Structural features of carbon nanoparticles produced by chlorination of β -SiC nanopowder. *Doklady Physical Chemistry*, **458**(2), P. 153–157 (2014).

NANOCRYSTALLINE PEROVSKITE-LIKE OXIDES FORMATION IN $\text{Ln}_2\text{O}_3 - \text{Fe}_2\text{O}_3 - \text{H}_2\text{O}$ (Ln = La, Gd) SYSTEMS

E. A. Tugova, O. N. Karpov

Ioffe Physical Technical Institute of RAS, Saint Petersburg, Russia

katugova@inbox.ru

PACS 61.46.-w; 82.80.Ej

Nanocrystalline LnFeO_3 (Ln = La, Gd) ferrites have been prepared by the co-precipitation method followed by heat treatment in air. The formation mechanisms for LaFeO_3 and GdFeO_3 in $\text{Ln}_2\text{O}_3 - \text{Fe}_2\text{O}_3 - \text{H}_2\text{O}$ (Ln = La, Gd) systems under the mentioned conditions are investigated. The phase interaction scheme, reflecting ways which lead to the target, synthesis product yield, as well as the common tendency of LaFeO_3 and GdFeO_3 formation mechanisms, are constructed. The mean sizes of coherent scattering regions of LaFeO_3 and GdFeO_3 were determined to be 30 ± 3 and 40 ± 4 nm, respectively.

Keywords: LnFeO_3 , ferrites, nanostructures, precipitation technique, phase formation, X-Ray diffraction.

Received: 5 November 2014

Revised: 27 November 2014

1. Introduction

Perovskite-like oxides, produced by different synthetic methods and having a variety of structural peculiarities, possess a complex array of electric, magnetic, catalytic, thermal, and other properties being of interest, in terms of practical applications [1-20]. Conventionally, the most common technique for obtaining complex oxides, including perovskite-like phases, is the method of solid-state synthesis [21-23]. Usually, for solid-state synthesis, simple oxides, carbonates, nitrates, oxalates, citrates or other salts of proper metals can be used as reagents. To ensure stoichiometry of the compounds synthesized, definite composition of gaseous medium can be prescribed, i.e. air, nitrogen, oxygen, hydrogen, etc. Despite a great number of papers devoted to the solid-state synthesis of perovskite-like oxides and to research into the peculiarities of their structure and properties [12, 17-21], limited data on the formation processes for perovskite-like oxides are available. There is also insufficient data on state equilibria for $\text{Ln}_2\text{O}_3 - \text{Fe}_2\text{O}_3$ (Ln = La, Gd) systems, which include perovskite-like oxides. Additionally, since the composition of the substances determines their basic properties, the lack of the mentioned data may affect the preparation of materials based on perovskite-like oxides with function-oriented characteristics.

Recently, the preparation of perovskite-like oxides using “soft chemistry” techniques has become of greater interest [24-25]. This is determined by the practical application of nanomaterials with unique structure and properties prepared using “soft chemistry” techniques [26]. However, mechanisms for the formation of the considered compounds remain mostly unstudied, which is associated, inter alia, with a lack of reliable generalized data on stability regions, processes of decomposition of intermediate substances, typically, *p*-, *d*- and *f*-elements hydroxides resulting from the reactions of precipitation, hydrolysis, etc., i.e. those proceeding, primarily, in aqueous media. Shafer and Roy attempted to determine stability of

rare-earth oxides and hydroxides in studying the state equilibria of $\text{Ln}_2\text{O}_3 - \text{H}_2\text{O}$ ($\text{Ln} = \text{La}, \text{Nd}, \text{Sm}$) systems [27]. Lanthanum oxide was found to differ from neodymium and samarium, primarily, in its greater tendency towards hydration. The authors were not able to determine whether LaOOH monohydrate or La_2O_3 forms via the decomposition of lanthanum hydroxide, or its crystal structure. The authors of [28] studied the dehydration kinetics for $\text{Gd}(\text{OH})_3$ obtained via hydrothermal conditions. The chemical transformations within the $\text{Fe}_2\text{O}_3 - \text{H}_2\text{O}$ system within media of different pH and with different P - T -conditions were investigated in [29, 30]. Papers [2, 5, 31] also discussed the formation of LaFeO_3 during the dehydration of components of the $\text{La}_2\text{O}_3 - \text{Fe}_2\text{O}_3 - \text{H}_2\text{O}$ system. It has been reported that for the preparation of GdFeO_3 nanoparticles using polyol technique, the authors obtained an until-then unknown compound corresponding to the formula Gd_3FeO_6 , extending the number of compounds formed in the Gd_2O_3 - Fe_2O_3 - H_2O system [32].

Thus, in literature, there are a number of works concerning the study of nanocrystalline perovskite-like oxides using “soft chemistry” techniques. However, to describe the mechanisms of perovskite-like oxides formation using “soft chemistry” techniques requires application of a comprehensive approach, taking into account information about phase equilibria in the systems where perovskite-like oxides could form, and analysis of the impact chemical background could have on the formation of the synthetic targets.

Therefore, the data investigation aims at studying of the formation processes of nanoscale perovskite-like oxides in $\text{Ln}_2\text{O}_3 - \text{Fe}_2\text{O}_3 - \text{H}_2\text{O}$ ($\text{Ln} = \text{La}, \text{Gd}$) systems differing in synthetic prehistory.

2. Experimental

2.1. Synthesis procedure

LnFeO_3 ($\text{Ln} = \text{La}, \text{Gd}$) samples were prepared by precipitation method from aqueous solutions of stoichiometric amounts of 1M $\text{Ln}(\text{NO}_3)_3 \cdot 6\text{H}_2\text{O}$ and $\text{Fe}(\text{NO}_3)_3 \cdot 9\text{H}_2\text{O}$. Aqueous 10 wt.% NH_4OH was used as the precipitating medium. To the NH_4OH medium, the aqueous solutions of lanthanum, gadolinium and iron nitrates were added in a drop-wise manner by adjusting the pH value to 8–9. The co-precipitated mixtures were filtered immediately after preparation to remove traces of NO_3^- ions. Samples were then dried at room temperature in air. These initial mixtures were then pressed and calcined in air at 500–900°C for 3 h.

2.2. Characterization of prepared nanocrystalline perovskite-related oxides

The purity and crystal structure of LnFeO_3 ($\text{Ln} = \text{La}, \text{Gd}$) samples were characterized by powder X-ray diffraction (XRD) using Shimadzu XRD-7000 with monochromatic $\text{CuK}\alpha$ radiation ($\lambda = 154.178$ pm). $\alpha\text{-Al}_2\text{O}_3$ was used as an internal standard. Crystallite sizes of the obtained powders were calculated by the X-ray line broadening technique based on Scherer’s formula.

The elemental composition and the composition of separate phases were analyzed by means of scanning electron microscopy (SEM) using Quanta 200, coupled with EDAX microprobe analyzer. The error in determining the elements content by this method varies with the atomic number and equals to 0.3 mass% on average.

The IR spectroscopic investigations of samples were carried out on an FSM-1202 Fourier-transform spectrometer from 400–4000 cm^{-1} . Samples were prepared as KBr pellets.

3. Results and discussion

X-ray phase analysis of precipitated mixtures testifies to their X-ray amorphous condition. Elemental analysis showed that the stoichiometric ratio of Ln:Fe is 1.00:1.06, which is close to that of the synthetic targets, LnFeO_3 (Ln = La, Gd). Furthermore, the obtained samples were exposed to thermal treatment from 500 to 900° in air ($p_{\text{O}_2} = 0.21$ atm.).

Fig. 1a shows the data obtained from X-ray phase analysis for samples corresponding to the stoichiometry of LaFeO_3 after thermal treatment from 500 to 900°C in air. According to the X-ray phase analysis, when the initial mixture was exposed to thermal treatment at 500°C for 3 hours, $\text{La}_2\text{O}_2\text{CO}_3$ is crystallized as a monoclinic structure. The IR spectrometric analysis of this sample showed presence of bandwidths at 3,650-3,300; 2,936; 2,862; 1,774; 1,639; 1,500; 1,450-1,400; 1,388; 1,057-1,076; 856-900; 700-725 cm^{-1} (see table), which can be attributed to valence and deformation vibrations of crystallization water, Fe-O groups typically found in $\text{Fe}(\text{OH})_3$, Fe_2O_3 , $\text{La}_2\text{O}_2\text{CO}_3$ (Fig. 1b) spectra. Raising the initial mixture processing temperature to 600°C will lead to a decrease in the bandwidth intensity, associated with the removal of crystallization water (3,500–3,200; 1,630 cm^{-1}), and with initiation of decarbonation of $\text{La}_2\text{O}_2\text{CO}_3$, forming La_2O_3 . According to the data presented (see Fig. 1, table) the reaction mixture thermally treated at 600 and 900°C contained a wide bandwidth at frequency 670–530 cm^{-1} , which can be referred to as a band corresponding to La-O-Fe vibrations in perovskite structure, by analogy with [33, 34]. The data obtained agree with the results of X-ray phase analysis for samples exposed to thermal processing at 600°C when the formation of LaFeO_3 is recorded. The size of the regions of coherent scattering for LaFeO_3 , prepared by thermal treatment of the co-precipitated mixture at 600°C, was 30 ± 3 nm.

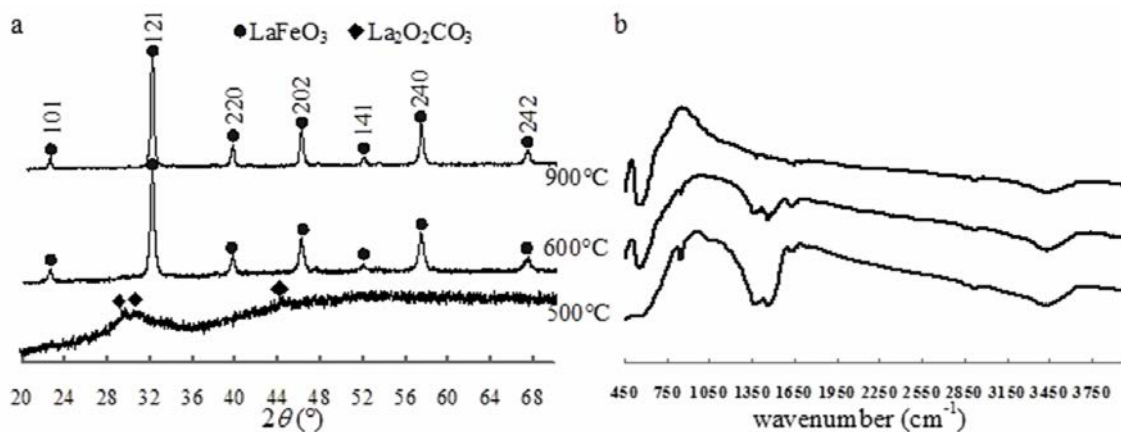


FIG. 1.) X-Ray diffraction patterns and b) IR transmission spectra of initial mixture corresponding with stoichiometry of LaFeO_3 heat treated in the air

Thus, the activation temperature for the formation of LaFeO_3 is connected with the decarbonation of $\text{La}_2\text{O}_2\text{CO}_3$, proceeding from 500 – 600°C, with La_2O_3 thus formed, initiating the generation of nanoscale perovskite-like lanthanum ferrite from 600°C.

Fig. 2 shows the X-ray phase analysis for samples corresponding to a stoichiometry of GdFeO_3 , prepared after thermal treatment of the initial mixture from 500 to 900°C in air. According to the presented X-ray phase analysis data (Fig. 2), the samples thermally treated from 500 to 600°C contain Gd_2O_3 and $\text{Gd}_2\text{O}_2\text{CO}_3$ phases. The appearance of $\text{Gd}_2\text{O}_2\text{CO}_3$ in the reaction mixture may be caused by utilizing synthetic precursors that were previously

TABLE. IR spectroscopic data of the initial mixture on stoichiometry closed to LaFeO₃, heat treated at 500, 600, 900°C temperatures versus reference data [33-34]

Experimental data			Reference data [33-34]				
wavenumber (cm ⁻¹)			wavenumber (cm ⁻¹)				
500°C	600°C	900°C	H ₂ O	La ₂ O ₂ CO ₃	La(OH) ₃	Fe(OH) ₃	α-Fe ₂ O ₃
515-670	530-670	530-670	650	660-680-730	655		500-620
858	860-875			860-870-880			
1075	1080			1050-1060-1080		1080	
1382	1375	1388		1380		1353	1388
1473	1468-1500			1470-1500		1500	
1638	1645	1650	1600-1630			1634	1656
2862	2859	2859					2865
2928	2934	2934	2930				2951
3350-3600	3350-3600	3400-3600	3200-3550		3420, 3600		

dried in air (and thus exposed to CO₂). According to [35], Gd₂O₂CO₃ exists in layered structures consisting of alternating (Ln₂O₂²⁺)_n and carbonate groups (CO₃)_n²⁻ layers. Raising the thermal treatment temperature will result in decarbonation, leading to the formation of cubic crystallized active-reactive Gd₂O₃. According to [35], Gd₂O₂CO₃ decomposes as follows: Gd₂O₂CO₃ $\xrightarrow{650^\circ\text{C}}$ Gd₂O₃ + ↑CO₂. According to the presented data of X-ray phase analysis (Fig. 2), starting from 700°C, the GdFeO₃ phase is formed. The mean size of coherent scattering regions, calculated from reflex with 111 index for the GdFeO₃ sample obtained after thermal treatment of the initial mixture at 700°C, was 40±4 nm.

Thus, the activation temperature for the formation of GdFeO₃, in the case when one of the reagents is Gd₂O₂CO₃, shall be determined by its decarbonation temperature at 600–700°C, leading to the formation of active-reactive Gd₂O₃. In such a case, the formation of nanoscale perovskite-like gadolinium ferrite will be recorded as starting from 700°C.

Thus, in case when initial compositions were obtained by the co-precipitation method, the processes for LnFeO₃ nanoparticle formation can be represented as a scheme depicted in Fig. 3, exemplified by the formation of GdFeO₃ nanocrystals. The diagram is given with experimental and literature data [27-30, 33-35] taken into consideration. The formation of FeO(OH) and Gd(OH)₃ hydroxides, mixed on the molecular level at the initial stages of synthesis, apparently, may lead to the formation of GdFeO₃ nanoparticles, with simultaneous dehydration of both components. The second mechanism is connected with both dehydration and decarbonation processes, the latter proceeding at a higher temperature. In connection with this, localized in space Fe₂O₃ and Gd₂O₃ will interact at the next stage. This will lead to a rise in the synthesis temperature for GdFeO₃ and to an increase in the size of the formed crystals. The obtained results correlate with the previous conclusions [22]. Note that if GdFeO₃ nanocrystals are prepared via hydrothermal methods, the initial mixture obtained according to the technique described in this paper, we also record a difference in the nature of intermediate products, despite carrying out the synthesis in an aqueous medium [1].

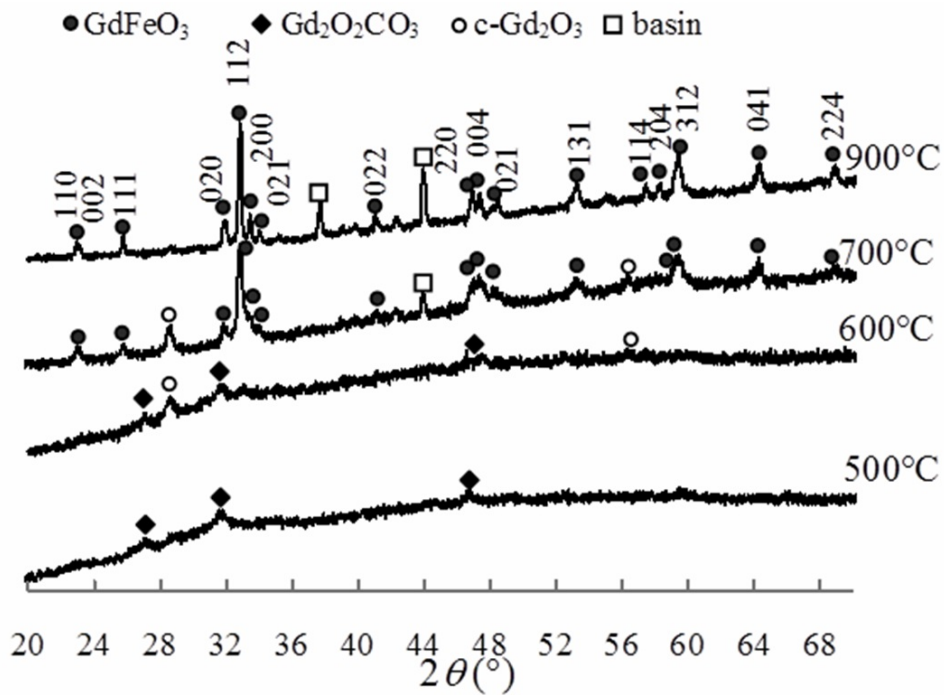


FIG. 2. X-Ray diffraction patterns of initial mixtures corresponding with stoichiometry of GdFeO_3 after sintering within the temperature range 500 to 900°C in the air

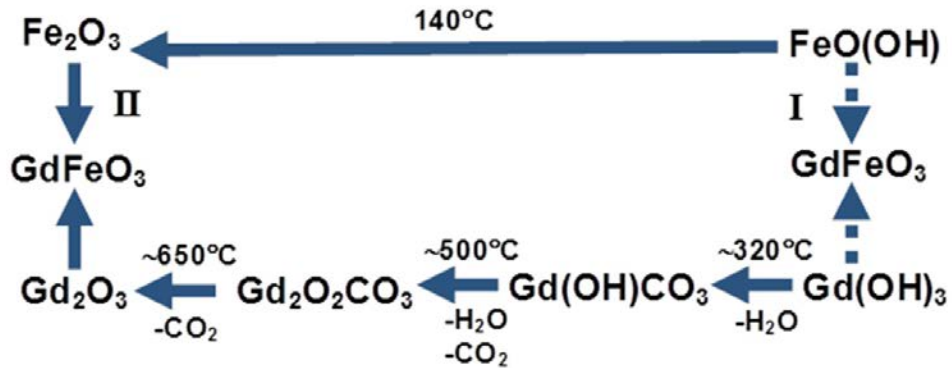


FIG. 3. LnFeO_3 nanocrystals formation scheme exemplified by the forming of GdFeO_3 under the heat treatment of co-precipitated initial mixture in air. Remarks: I - the mechanism of co-precipitated hydroxides simultaneous dehydration with GdFeO_3 formation; II - the scheme of step-by-step transformations of co-precipitated components with spatial-isolated Fe_2O_3 and Gd_2O_3 nanoparticles formation followed by solid state interaction for GdFeO_3 production

4. Conclusion

Therefore, the mechanism for perovskite-related lanthanum and gadolinium ferrites formation depends heavily on chemical processes resulting in the spatial separation of components of a target product. In particular, these processes may determine the temperature at which perovskite-related ferrite begins to form, as well as the size of the formed nanocrystals.

Acknowledgments

The authors would like to thank Prof. V.V. Gusarov very much for useful discussions and valuable advice.

References

- [1] Tugova E.A., Zvereva I.A. Formation mechanism of GdFeO_3 nanoparticles under the hydrothermal conditions. *Nanosystems: physics, chemistry, mathematics*, **4**(6), P. 851–856 (2013).
- [2] Nakayama S. LaFeO_3 perovskite type oxide prepared by oxide mixing co-precipitation and complex synthesis methods. *J. Mater. Sci.*, **6**, P. 5643–5648 (2001).
- [3] Tang P., Chen H., Cao F., Pan G. Magnetically recoverable and visible light driven nanocrystalline YFeO_3 photocatalysts. *Catal. Sci. Technol.*, **1**(7), P. 1145–1148 (2011).
- [4] Nguyen A.T., Mittova I.Ya., Al'myasheva O.V. Influence of the synthesis conditions on the particle size and morphology of yttrium orthoferrite obtained from aqueous solutions. *Russ. J. Appl. Chem.*, **82**(11), P. 1915–1918 (2009).
- [5] Nguyen A.T., Mittova I.Ya., Almjasheva O.V., Kirillova S.A., Gusarov V.V. Influence of the preparation conditions on the size and morphology of nanocrystalline lanthanum orthoferrite. *Glas. Phys. Chem.*, **34**(6), P. 756–761 (2008).
- [6] Shang M., Zhang C., Zhang T., Yuan L., Ge L. Yuan H., Feng S. The multiferroic perovskite YFeO_3 . *Appl. Phys. Lett.*, **102**(6), 062903(3 pages) (2013).
- [7] Zhou Z., Guo L., Yang H., Liu Q., Ye F. Hydrothermal synthesis and magnetic properties of multiferroic rare-earth orthoferrites. *J. Alloys Compd*, **583**, P. 21–31 (2014).
- [8] Tang P., Sun H., Chen H., Cao F. Hydrothermal processing-assisted synthesis of nanocrystalline YFeO_3 and its visible-light photocatalytic activity. *Curr. Nanosci.*, **8**, P. 64–67 (2012).
- [9] Nguyen A.T., Almjasheva O.V., Mittova I.Ya., Stognei O.V., Soldatenko S.A. Synthesis and magnetic properties of YFeO_3 nanocrystals. *Inorganic Materials*, **45**(11), P. 1304–1308 (2009).
- [10] Zhang Yu., Yang J., Xu J., Gao Q., Hong Zh. Controllable synthesis of hexagonal and orthorhombic YFeO_3 and their visible-light photocatalytic activities. *Materials Letters*, **81**, P. 1–4 (2012).
- [11] Maiti R., Basu S., Chakravorty D. Synthesis of nanocrystalline YFeO_3 and its magnetic properties. *Journal of Magnetism and Magnetic Materials*, **321**(19), P. 3274–3277 (2009).
- [12] Venugopalan A., Appasamy M., Saravanan S., Kothandaraman K., Kothandaraman J. Structural, electrical and magnetic studies on Y-Fe-O system. *Journal of Rare Earths*, **27**(6), P. 1013–1017 (2009).
- [13] Lu X., Xie J., Shu H., Liu J., Yin Ch., Lin J. Microwave-assisted synthesis of nanocrystalline YFeO_3 and study of its photoactivity. *Materials Science and Engineering B*, **138**, P. 289–292 (2007).
- [14] Zhang W., Fang C.X., Yin W.H, Zeng Y.W. One-step synthesis of yttrium orthoferrite nanocrystals via sol-gel auto-combustion and their structural and magnetic characteristics. *Mater. Chem. Phys.*, **137**(3), P. 877–883 (2013).
- [15] Popkov V.I., Almjasheva O.V. Yttrium orthoferrite YFeO_3 nanopowders formation under glycine-nitrate combustion conditions. *Russian Journal of Applied Chemistry*, **87**(2), P. 167–171 (2014).
- [16] Goswami S., Bhattacharya D., Choudhury P. Particle size dependence on magnetization and noncentrosymmetry in nanoscale BiFeO_3 . *Journal of applied physics D*, **109**(7), P. 737–739 (2011).
- [17] Egorysheva A.V., Volodin V.D., Ellert O.G., Efimov N.N., Skorikov V.M., Baranchikov A.E., Novotortsev V.M. Mechanochemical activation of starting oxide mixtures for solid-state synthesis of BiFeO_3 . *Inorganic Materials*, **49**(3), P. 303–309 (2013).
- [18] Morozov M. I., Lomanova N. A., Gusarov V.V. Specific features of BiFeO_3 formation in a mixture of bismuth (III) and iron (III) oxides. *Russ. J. Gen. Chem.*, **73**(11), P. 1772–1776 (2003).
- [19] Lomanova N.A., Gusarov V.V. Effect of surface melting on the formation and growth of nanocrystals in the Bi_2O_3 - Fe_2O_3 system. *Russ. J. Gen. Chem.*, **83**(12), P. 2251–2253 (2013).

- [20] Lomanova N.A., Gusarov V.V. Influence of synthesis temperature on BiFeO₃ nanoparticles formation. *Nanosystems: physics, chemistry, mathematics*, **4**(5), P. 696–705 (2013).
- [21] Tretyakov Yu. D., Lukashin A.V., Eliseev A. A. Synthesis of functional nanocomposites based on solid-phase nanoreactors. *Russian Chemical Reviews*, **73**(9), P. 899–923 (2004).
- [22] Gusarov V.V. Fast solid-phase chemical reactions. *Russian Journal of General Chemistry*, **67**(12), P. 1846–1851 (1997).
- [23] Schaak R.E., Mallouk Th. E. Perovskites by design: A toolbox of solid-state reactions. *Chemistry of Materials*, **14**, P. 1455–1471 (2002).
- [24] Livage J. Vanadium pentoxide gels. *Chemistry of Materials*, **3**(4), P. 578–593 (1991).
- [25] Sanchez C., Rozes L., Ribot F., Laberty-Robert C., Grosso D., Sassoie C., Boissiere C., Nicole L. “Chimie douce”: A land of opportunities for the designed construction of functional inorganic and hybrid organic-inorganic nanomaterials. *Comptes Rendus Chimie*, **13**(1-2), P. 3–39 (2010).
- [26] Gopalakrishnan J. Chimie. Douce approaches to the synthesis of metastable oxide materials. *Chemistry of Materials*, **7**(7), P. 1265–1275 (1995).
- [27] Shafer M.W., Roy R. Rare-earth polymorphism and phase equilibria in rare-earth oxide-water systems. *Journal of the American Ceramic Society*, **42**(4), P. 563–570 (1959).
- [28] Chang Ch, Mao D. Thermal dehydration kinetics of a rare earth hydroxide Gd(OH)₃. *International Journal of Chemical Kinetics*, **39**(2), P. 75–81. (2007)
- [29] Tareen J.A.K., Krishnamurthy K.V. Hydrothermal stability of hematite and magnetite. *Bulletin Materials Science*, **3**(1), P. 9–13 (1981).
- [30] Popov, V.V., Gorbunov, A.I. Hydrothermal Crystallization of iron (III) hydroxide. *Inorg. Materials*, **42**(3), P. 275–281 (2006).
- [31] Xu H., Hu X., Zhang L. Generalized low-temperature synthesis of nanocrystalline rare earth orthoferites LnFeO₃ (Ln=La, Pr, Nd, Sm, Eu, Gd). *Cryst. Growth Des.*, **8**(7), P. 2061–2065 (2008).
- [32] Söderlind S., Fortin M.A., Petoral Jr R.M., Klasson A., Veres T., Engström M., Uvdal K., Käll P.-O. Colloidal synthesis and characterization of ultras-small perovskite GdFeO₃ nanocrystals. *Nanotechnology*, **19**(8), P. 085608-(8pp) (2008).
- [33] Tugova E.A. A comparative analysis of the formation processes of Ruddlesden-Popper phases in the La₂O₃-SrO-M₂O₃ (M = Al, Fe) systems. *Glas. Phys. Chem*, **35**(4), P. 416–422 (2009).
- [34] Bernal S., Blanco G., Gatica J.M., Perez-Omil J.A., Pintado J.M., Vidal H. Chemical reactivity of binary rare earth oxides. *Binary Rare Earth Oxides*, Kluwer Academic Publishers, P. 9–55 (2004).
- [35] Sheu H. Sh., Shih W.-J., Chuang W.-T., Li I.-F., Yeh Ch.-Sh. Crystal structure and phase transitions of Gd(CO₃)OH studied by synchrotron powder diffraction. *Journal of the Chinese Chemical Society*, **57**(4), P. 938–945 (2010).



NANOSYSTEMS:

PHYSICS, CHEMISTRY, MATHEMATICS

INFORMATION FOR AUTHORS

The journal publishes research articles and reviews, and also short scientific papers (letters) which are unpublished and have not been accepted for publication in other magazines. Articles should be submitted in English. All articles are reviewed, then if necessary come back to the author to completion.

The journal is indexed in Chemical Abstract Service of the American Chemical Society and in Russian Scientific Citation Index.

Author should submit the following materials:

1. Article file in English, containing article title, the initials and the surname of the authors, Institute (University), postal address, the electronic address, the summary, keywords, MSC or PACS index, article text, the list of references.
2. Files with illustrations, files with tables.
3. The covering letter in English containing the article information (article name, MSC or PACS index, keywords, the summary, the literature) and about all authors (the surname, names, the full name of places of work, the mailing address with the postal code, contact phone number with a city code, the electronic address).
4. The expert judgement on possibility of publication of the article in open press (for authors from Russia).

Authors can submit a paper and the corresponding files to the following addresses: nanojournal.ifmo@gmail.com, popov1955@gmail.com.

Text requirements

Articles should be prepared with using of text editors MS Word or LaTeX (preferable). It is necessary to submit a pdf copy. In the name of files the English alphabet is used. The recommended size of short communications (letters) is 4-6 pages, research articles – 6-15 pages, reviews – 30 pages.

Recommendations for text in MS Word:

Formulas should be written using Math Type. Figures and tables with captions should be inserted in the text. Additionally, authors present separate files for all figures and Word files of tables.

Recommendations for text in LaTeX:

Please, use standard LaTeX without macros and additional style files. The list of references should be included in the main LaTeX file. Single LaTeX file of the paper with the corresponding pdf file should be submitted.

References in the article text are given in square brackets. The list of references should be prepared in accordance with the following samples:

- [1] N. Surname. *Book Title*. Nauka Publishing House, Saint Petersburg, 281 pp. (2000).
- [2] N. Surname, N. Surname. Paper title. *Journal Name*, **1**(5), P. 17-23 (2000).
- [3] N. Surname, N. Surname. Lecture title. In: Abstracts/Proceedings of the Conference, Place and Date, P. 17-23 (2000).
- [4] N. Surname, N. Surname. Paper title (2010). URL: <http://books.ifmo.ru/ntv>.
- [5] N. Surname, N. Surname. Patent Name. Patent No. 11111, Bul. No. 33, 5 pp. (2010).
- [6] N. Surname, N. Surname. Thesis Title. Thesis for full doctor degree in math. and physics, Saint Petersburg, 105 pp. (2000).

Requirements to illustrations

Illustrations should be submitted as separate black-and-white files. Formats of files – jpeg, eps, tiff.



2ND NORTH COUNTRIES UNIVERSITIES MATHEMATICAL COMPETITION (NCUMC - 2015)

ST. PETERSBURG, UNIVERSITY ITMO, APRIL 20-22, 2015

For university students of any countries!

Personal and team competition.

April 20 — Registration;

April 21 — Registration, Competition and Marking session;

April 22 — Complain session and Closing ceremony.

KEEP THE MATHEMATICS ALIVE!

Registration payment: free.

Registration deadline: April 14, 2015.

Competition language: English.

Location: Saint Petersburg National Research University of Informational Technologies, Mechanics and Optics: Kronverkskij, 49.

More information about NCUMC and registration: <http://mathdep.ifmo.ru/ncumc/>
or Department of High Mathematics, University ITMO,
Igor Yu. Popov: +7 (812) 232-67-65, popov1955@gmail.com.



NANOSYSTEMS:

PHYSICS, CHEMISTRY, MATHEMATICS

Журнал зарегистрирован

Федеральной службой по надзору в сфере связи, информационных технологий и массовых коммуникаций

(свидетельство ПИ № ФС 77 - 49048 от 22.03.2012 г.)

ISSN 2220-8054

Учредитель: федеральное государственное автономное образовательное учреждение высшего образования

«Санкт-Петербургский национальный исследовательский университет информационных технологий, механики и оптики»

Издатель: федеральное государственное автономное образовательное учреждение высшего образования

«Санкт-Петербургский национальный исследовательский университет информационных технологий, механики и оптики»

Отпечатано в Учреждении «Университетские телекоммуникации»

Адрес: 197101, Санкт-Петербург, Кронверкский пр., 49

Подписка на журнал НФХМ

На второе полугодие 2015 года подписка осуществляется через

ОАО Агентство «Роспечать»

Подписной индекс 57385 в каталоге «Издания органов научно-технической информации»